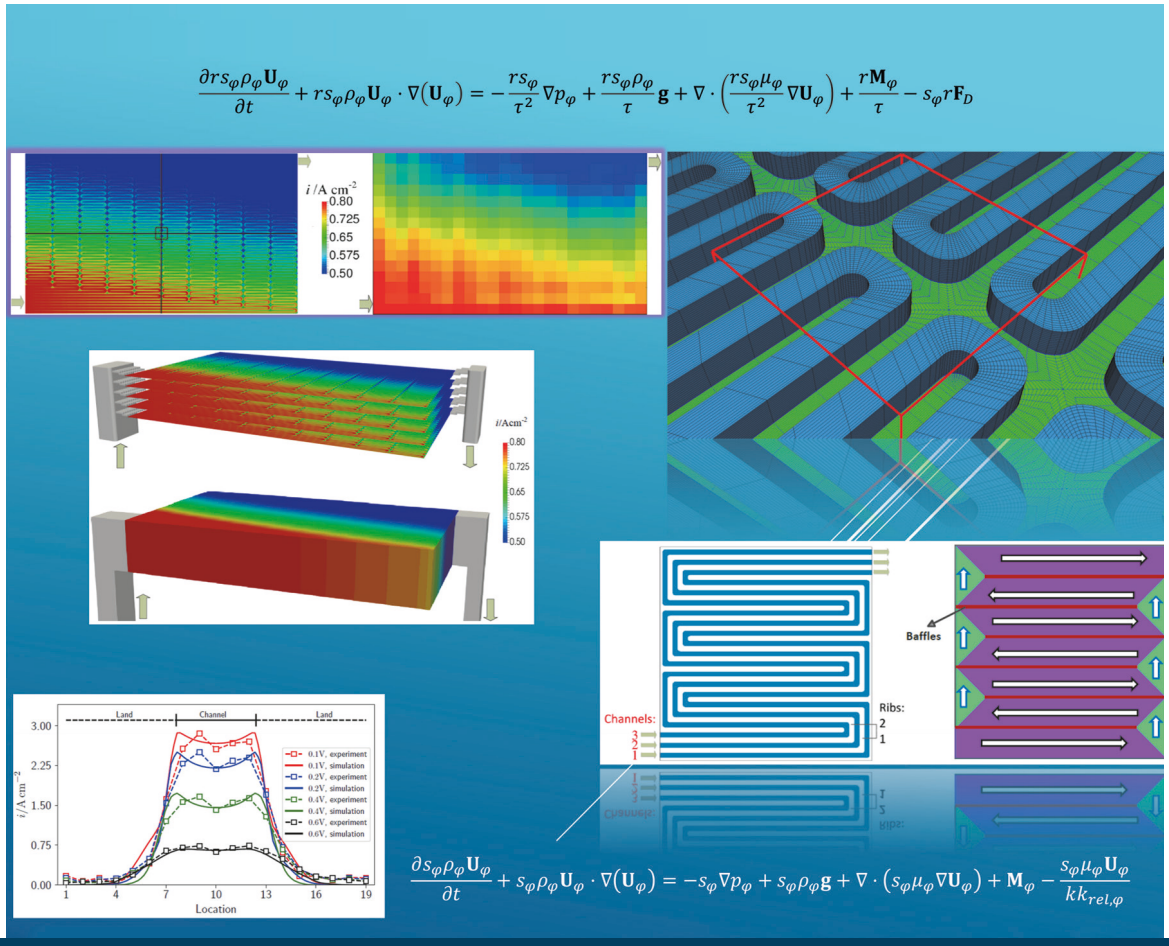

Modeling and Simulation of Polymer Electrolyte Fuel Cells

Shidong Zhang

Energie & Umwelt / Energy & Environment
Band / Volume 493
ISBN 978-3-95806-472-0

Mitglied der Helmholtz-Gemeinschaft

JÜLICH
Forschungszentrum

Schriften des Forschungszentrums Jülich
Reihe Energie & Umwelt / Energy & Environment Band / Volume 493

Forschungszentrum Jülich GmbH
Institut für Energie- und Klimaforschung
Elektrochemische Verfahrenstechnik (IEK-14)

Modeling and Simulation of Polymer Electrolyte Fuel Cells

Shidong Zhang

Schriften des Forschungszentrums Jülich
Reihe Energie & Umwelt / Energy & Environment Band / Volume 493

ISSN 1866-1793 ISBN 978-3-95806-472-0

Bibliografische Information der Deutschen Nationalbibliothek.
Die Deutsche Nationalbibliothek verzeichnet diese Publikation in der
Deutschen Nationalbibliografie; detaillierte Bibliografische Daten
sind im Internet über http://dnb.d-nb.de abrufbar.

Herausgeber und Vertrieb:	Forschungszentrum Jülich GmbH Zentralbibliothek, Verlag 52425 Jülich Tel.: +49 2461 61-5368 Fax: +49 2461 61-6103 zb-publikation@fz-juelich.de www.fz-juelich.de/zb
Umschlaggestaltung:	Grafische Medien, Forschungszentrum Jülich GmbH
Druck:	Grafische Medien, Forschungszentrum Jülich GmbH
Copyright:	Forschungszentrum Jülich 2020

Schriften des Forschungszentrums Jülich
Reihe Energie & Umwelt / Energy & Environment, Band / Volume 493

D 82 (Diss. RWTH Aachen University, 2019)

ISSN 1866-1793
ISBN 978-3-95806-472-0

Vollständig frei verfügbar über das Publikationsportal des Forschungszentrums Jülich (JuSER)
unter www.fz-juelich.de/zb/openaccess.

Abstract

Polymer electrolyte fuel cells are efficient and clean devices that convert chemical energy directly into electricity. Great attention has been received during the past decade on experimental and numerical studies. Comprehensive experimental investigations of fuel cells are still very expensive and challenging considering various parameters in fuel cell operations, designs, and optimizations. The numerical procedure provides an alternative way for fuel cell analysis. With the development of computational power, e.g. high-performance computing facility, the limitation of numerical applications on the analysis of PEFCs is decreasing. The numerical method may serve as an easy and fast tool nowadays.

The major transport phenomena involved in PEFCs includes fluid flow, heat and mass transfer, species and charge transfer, electrochemical reaction. Numerical models need to take some or all of the major physical processes into account. Therefore, in the present study, two PEFC models are developed and implemented into an open-source library OpenFOAM ®, which allows large scale parallel calculations. These models, a detailed model and a homogeneous model, consider cell-level and stack-level applications. The detailed model is based on the conventional computational fluid dynamics, whereas the homogeneous model is derived from the detailed model and applies a distributed resistance analogy. Both models enable simulations concerning three-dimensional, single-phase and two-phase, multi-region, multi-physics, and nonisothermal situations. An Eulerian-Eulerian approach is applied to describe two-phase flow.

Both models are numerically verified and experimentally validated via in-house designed HT-PEFCs and LT-PEFCs, including prototypes with nominal active area of (4.2×4.2) 16 cm^2 and (11.2×19) 200 cm^2. The detailed and homogeneous models are applied on both HT-PEFCs and LT-PEFCs respectively: 1. The local variations of current density and gas mole fractions are large in fuel cells with serpentine flow paths. The serpentine flow path leads to higher pressure drop, however, contributes to better reactants redistribution and higher local current density. 2. The homogeneous model is compared with a previously developed detailed model with good agreement. Simulation results are presented; both models provide finer-scale results than experimental measurements. 3. The catalyst layer cracks and MEA failure are numerically simulated via the detailed model. Cracks present slight effects on cell performance, however, significant on local values. The MEA failure is found resulted from the high local temperature and/or mechanical damage. 4. A LT-PEFC is simulated via the homogeneous model. The results are also presented. Therefore, the present models are ready to be applied in other PEFC designs.

Kurzfassung

Polymerelektrolyt-Brennstoffzellen (PEFC) sind effiziente und saubere elektrochemische Wandler, die chemische Energie direkt in Elektrizität umwandeln. Sowohl experimentelle als auch numerische Arbeiten erlangten in den letzten Jahren vermehrt große Aufmerksamkeit. Umfassende experimentelle Charakterisierungen von Brennstoffzellen sind teuer und zeitaufwendig. Dies gilt insbesondere wenn Design- und Betriebsvariationen im Sinne einer Optimierung durchgeführt werden. Numerische Verfahren bieten hierzu eine Alternative. Mit steigender Computerleistung eröffneten sich neue Möglichkeiten in Bezug auf die Simulation von Polymerelektrolyt-Brennstoffzellen, und rechnergestützte Verfahren kommen als Entwicklungswerkzeug zum Einsatz. Diese bieten die Möglichkeit den Einfluss von Betriebs- und Designvariationen schnell und kostengünstig auf das Zell- und Stackverhalten zu bewerten.

Neben Stoff-, Wärme- und Ladungstransport sind elektrochemische Reaktionen wesentliche Phänomene, die im Rahmen der Modellentwicklung zu beachten sind. In der vorliegenden Arbeit werden zwei PEFC-Modelle entwickelt und in die Open Source Bibliothek OpenFOAM ® implementiert. Diese Modelle, ein detailliertes Modell und ein sogenanntes homogenes Modell, zielen auf verschiedene Anwendungen. Das detaillierte Modell basiert auf konventioneller numerischer Strömungsmechanik. Das homogene Modell leitet sich aus dem detaillierten Modell ab und berücksichtigt die wesentlichen Effekte im Rahmen einer Widerstandsanalogie.

Beide Modelle ermöglichen dreidimensionale, ein- und zweiphasige, multiphysikalische und nicht-isotherme Simulationen. Die Zweiphasenströmung wird mit einem Euler-Euler-Ansatz beschrieben. Beide Modelle sind numerisch verifiziert und experimentell validiert. Für die experimentelle Validierung wurden im IEK-3 entwickelte Hochtemperatur- (HT-PEFC) und Niedertemperatur- Polymerelektrolyt-Brennstoffzellen (LT-PEFC) mit elektrochemisch aktiven Flächen von 16 beziehungsweise 200 cm^2 verwendet. Sowohl das detaillierte als auch das homogene Modell wurden zur Beschreibung des Betriebsverhaltens von HT- und LT-PEFCs verwendet. 1. Die lokalen Stromdichtevariationen sind bei Brennstoffzellen mit serpentinenartigen Strömungskanälen groß. Diese Strömungsführung führt zu einem hohen Druckabfall, trägt jedoch zu einer guten Verteilung der Reaktanten und einer hohen lokalen Stromdichte bei. 2. Die Simulationsergebnisse des homogenen Modells stimmen gut mit den Ergebnissen des detaillierten Modells überein. Beide Modelle liefern Ergebnisse die mit experimentellen Methoden nur schwer zugänglich sind. 3. Der Einfluss produktions- oder betriebsbedingter Rissstrukturen in den Membran-Elektroden-Einheiten wird mit dem detaillierten Modelle untersucht. Die Risse wirken sich geringfügig auf die gesamte Zellleistung aus. Lokale Stromdichte- und Potentialvariationen sind jedoch signifikant. 4. Mit dem homogenen Modell wird eine LT-PEFC simuliert und die Ergebnisse werden dargestellt.

Contents

1 Introduction **1**
- 1.1 Motivations and objectives . . . 1
- 1.2 Research objectives . . . 4
- 1.3 Methodology . . . 5
- 1.4 Outline of the thesis . . . 6
- 1.5 Work principle of PEFCs . . . 8
  - 1.5.1 Water transport in the membrane . . . 10
  - 1.5.2 Water transport in porous media . . . 13
  - 1.5.3 Water transport in gas channels . . . 16
- 1.6 Literature review . . . 16
  - 1.6.1 HT-PEFC: cell level modeling research . . . 17
  - 1.6.2 HT-PEFC: homogeneous/stack modeling research . . . 21
  - 1.6.3 LT-PEFC: cell level modeling research . . . 23
  - 1.6.4 LT-PEFC, homogeneous/stack modeling research . . . 33
- 1.7 Summary . . . 36

2 Methodology **37**
- 2.1 Detailed model . . . 38
  - 2.1.1 Computational domain . . . 38
  - 2.1.2 Assumptions . . . 39
  - 2.1.3 Governing equations . . . 39
- 2.2 Homogeneous model . . . 49
  - 2.2.1 Assumptions . . . 51
  - 2.2.2 Governing equations . . . 52
- 2.3 Summary . . . 59

3 Numerical Procedure **61**
- 3.1 Discretization of domains . . . 61
  - 3.1.1 Discretization of space . . . 62
  - 3.1.2 Discretization of time . . . 63
- 3.2 Discretization of general equations . . . 63
  - 3.2.1 Transient term . . . 64
  - 3.2.2 Convection term . . . 64

3.2.3 Diffusion term . . . 65
3.2.4 Source term . . . 65
3.2.5 Boundary and initial conditions . . . 66
3.2.6 Temporal discretization . . . 68
3.3 Discretization of governing equations . . . 69
3.3.1 Continuity equations . . . 69
3.3.2 Momentum equations . . . 71
3.3.3 Other equations . . . 72
3.4 Solution procedures . . . 72
3.4.1 Methods . . . 72
3.4.2 Algorithms . . . 75
3.5 Summary . . . 80

4 HT-PEFC detailed models 81
4.1 Introduction . . . 81
4.2 Numerical analysis . . . 83
4.2.1 Model 1 . . . 83
4.2.2 Computational domain . . . 83
4.2.3 Operating and boundary conditions . . . 85
4.2.4 Grid independence . . . 87
4.3 Results . . . 87
4.3.1 Analytical verification for *model 1* . . . 87
4.3.2 Experimental validation for *model 1* . . . 89
4.3.3 Simulation results of *model 1* . . . 93
4.3.4 Simulation results of *model 2* . . . 104
4.4 Discussion . . . 110
4.5 Conclusion . . . 111

5 HT-PEFC homogeneous model 113
5.1 Introduction . . . 113
5.2 Numerical . . . 115
5.3 Model validation . . . 115
5.4 Results . . . 118
5.4.1 Polarization curves . . . 118
5.4.2 Local current density distribution . . . 119
5.4.3 Reaction mole fractions . . . 121
5.4.4 Nernst potential . . . 123
5.5 Discussion . . . 123
5.6 Conclusion . . . 124

6 LT-PEFC detailed model 125
6.1 Introduction . . . 125
6.2 Numerical analysis . . . 126
6.2.1 Verification . . . 127

6.2.2 Validation 129
6.2.3 Geometry and model parameters 131
6.3 Results 133
6.3.1 Catalyst cracks 133
6.3.2 MEA failure 144
6.4 Discussion 154
6.5 Conclusion 156

7 LT-PEFC homogeneous model 159
7.1 Introduction 159
7.2 Verification 160
7.2.1 Results 161
7.3 Validation 163
7.3.1 Results 164
7.4 Discussion 172
7.5 Conclusion 173

8 Discussion 175

9 Conclusion 179

10 Outlook 183

List of Figures

1.1 The concept of present thesis. The differences between each model are listed in Table 1.1. Note: *model 1* is derived from the OpenFuelCell package [36]. 7
1.2 Schematic of a PEFC. 10
1.3 The state of water in different sites of a PEFC. (Reprinted from [42]) 11
1.4 Liquid water behaviors in small pores with hydrophilic and hydrophobic surface wettabilities 15

2.1 Computational domains: master domain and sub-domains . . 38
2.2 Interfacial momentum transfer: drag, lift, and virtual mass . 40
2.3 Interface between two phases, phase 1 and phase 2. 44
2.4 Schematic of a fuel cell and computational domain applied in the homogeneous model (manifolds are not shown). 51

3.1 Schematic of two control volumes with points P and N as the cell centers. Face F is the interface between cell P and cell N. 62
3.2 Schematic of variable discretization at a boundary 66

4.1 Bipolar plate used in the HT-PEFC stack. (Reproduced from [98]) 82
4.2 Flow channel configuration, with 10 channel-24 pass serpentine geometry: (a) active area and number of channels, from 1-10; (b) sub-region; (c) grid at local area; (d) sub-region mesh. (Reproduced from [98]) 84
4.3 Analytical solution (void) and simulation results (solid), oxygen mole fraction (right) and current density (left) distributions along the channel, $\lambda = 2, 4, 10$. (Reproduced from [97]) . 88
4.4 Diagram of fuel cell composition and flow path used in the verification and validation. (a) Straight geometry; (b) Serpentine geometry. (Reproduced from [97]) 89
4.5 Deassembled view of the cell. (Reproduced from [97]) 90
4.6 Schematic of the fuel cell test station used for the experiments. (Reproduced from [97]) 91

4.7 Comparisons of polarization curves from numerical and experimental results, $\lambda = 2/2$. (Reproduced from [97]) 92
4.8 Comparisons of polarization curves from numerical and experimental results, $\lambda = 2/6$. (Reproduced from [97]) 92
4.9 Polarization curves comparison between the present results [98], past numerical result [99] and experimental data [215]. (Reproduced from [98]) 93
4.10 Local current density distribution, $i = 0.6\,\mathrm{A\,cm^{-2}}$: (a) results of present simulation [98]; (b) results from past simulation [99]; (c) experimental measured data [99], by S++ [63] current scan shunt. (Reproduced from [98]) 95
4.11 Current density relative frequency of present ($N = 727\times10^3$), previous ($N = 10\times10^3$) [99] numerical results and experimental ($N = 0.39 \times 10^3$) data [215], $i = 0.6\,\mathrm{A\,cm^{-2}}$. (Reprinted from [98]) 95
4.12 Current density distributions in sub-region, marked in Figure 4.2, of: (a) present and (b) previous [99] numerical results, $i = 0.6\,\mathrm{A\,cm^{-2}}$. (Reproduced from [98]) 96
4.13 Current density distribution along sections XX′ and YY′, $i = 0.6\,\mathrm{A\,cm^{-2}}$. (Reproduced from [98]) 97
4.14 Current density distribution along channel 1 and channel 10, $i = 0.6\,\mathrm{A\,cm^{-2}}$. Analytical solution from Kulikovsky et al. [214] is also plotted. NB: $\bar{i}$ is for the whole cell, whereas i is located at the channel central line and therefore higher than at the rib location. (Reproduced from [98]) 98
4.15 Global (a) oxygen (c) water vapor and local (b) oxygen (d) water vapor mole fractions distributions, $i = 0.6\,\mathrm{A\,cm^{-2}}$. NB: the distributions in sub-regions are relegend for better observation. (Reproduced from [98]) 99
4.16 Oxygen (a) and water (b) mole fraction distribution along sections XX′ and YY′, $i = 0.6\,\mathrm{A\,cm^{-2}}$. (Reproduced from [98]) 101
4.17 Oxygen (a) and water (b) mole fraction distribution along channel 1 and channel 10, $i = 0.6\,\mathrm{A\,cm^{-2}}$. (Reproduced from [98]) 102
4.18 Pressure coefficient along the channels, $i = 0.6\,\mathrm{A\,cm^{-2}}$. (Reprinted from [98]) 103
4.19 Streak lines in the sub-region, colored by the pressure coefficient magnitude: (a) gas channels; (b) GDL, $i = 0.6\,\mathrm{A\,cm^{-2}}$. (Reprinted from [98]) 103
4.20 Polarization curves of experimental data [99] and numerical results [98]. 104
4.21 Global current density distributions, $i = 0.6\,\mathrm{A\,cm^{-2}}$. 105
4.22 Current density distributions, $i = 0.6\,\mathrm{A\,cm^{-2}}$. (a) cathode side; (b) anode side. 106

4.23 Local current density distributions on sub-zone, $i = 0.6\,\mathrm{A\,cm^{-2}}$. (a) Model 2, membrane; (b) Model 1 results, membrane [98]; (c) Model 2, cathode side; (d) Model 2, anode side. 107
4.24 Current density along the horizontal (left to right) line, $i = 0.6\,\mathrm{A\,cm^{-2}}$. (Note: the current density and the distance are normalized). 108
4.25 Current density along the vertical (bottom to top) line, $i = 0.6\,\mathrm{A\,cm^{-2}}$. (Note: the current density and the distance are normalized). 108
4.26 Current density distributions in through-plane direction, $i = 0.6\,\mathrm{A\,cm^{-2}}$. (a) slice CD; (b) slice AB. (Shown in Fig. 4.2(b)) 109
4.27 Current density in the MEA, $i = 0.6\,\mathrm{A\,cm^{-2}}$. 110

5.1 Jülich HT-PEFC stack showing (Reproduced from [103]). (a) Gas flow channels; (b) Oil cooling passages machined in BPPs; (c) Schematic of air flow; (d) Schematic of fuel flow; (e) Entire stack/manifold assembly. 114
5.2 The computational mesh in DRA simulations. (a) Cathode side; (b) Anode side; (c) Local grid marked in (a); (d) Local grid marked in (b). (The green regions represent the 'core' region, and the red regions is the manifolds.) 116
5.3 The computational mesh in DNM simulations. (a) Cathode side; (b) Anode side; (c) Local grid marked in (a); (d) Local grid marked in (b). 116
5.4 Temperature distribution, $i = 0.6\,\mathrm{A\,cm^{-2}}$. (a) Numerical prediction by the DRA method; (b) Experimental measurements [99]. (Reproduced from [103]) 117
5.5 Pressure distribution, $i = 0.6\,\mathrm{A\,cm^{-2}}$. (a) Numerical prediction by the DRA method; (b) Numerical prediction by the DNM method. (Reproduced from [103]) 118
5.6 Polarization curves from experimental data, the DNM and DRA. (Reproduced from [103]) 119
5.7 Current density distribution, $i = 0.6\,\mathrm{A\,cm^{-2}}$. (a) DNM, the third cell; (b) DRA; (c) Experimental data [99]. (Reproduced from [103]) 120
5.8 Current density distribution from (a) the DNM and (b) the DRA, $i = 0.6\,\mathrm{A\,cm^{-2}}$. (Reprinted from [103]) 120
5.9 Current density distribution in each cell, $i = 0.6\,\mathrm{A\,cm^{-2}}$. (a) Cell 1; (b) Cell 2; (c) Cell 4; (d) Cell 5. 121
5.10 Oxygen mole fraction distributions from (a) the DNM (cell 3) and (b) the DRA, $i = 0.6\,\mathrm{A\,cm^{-2}}$. (Reprinted from [103]) . 121
5.11 Water vapor mole fraction distributions from (a) the DNM (cell 3) and (b) the DRA, $i = 0.6\,\mathrm{A\,cm^{-2}}$. (Reproduced from [103]) 122

5.12 Mole fraction distributions for oxygen in (a) the whole stack and (b) in local region, and water vapor in (c) the whole stack (d) in local region, predicted by the DNM, $i = 0.6\,\mathrm{A\,cm^{-2}}$. . . 122
5.13 Nernst potentials distribution from (a) the DNM and (b) the DRA, $i = 0.6\,\mathrm{A\,cm^{-2}}$. (Reproduced from [103]) 123

6.1 The cracks in catalyst region. 126
6.2 One type of MEA broken in the experiment. (CCM: catalyst coated membrane) 127
6.3 Geometry in model verification (1-D). 128
6.4 The comparison of liquid water saturation variations between the present numerical simulation and analytical model [137] results. 128
6.5 The comparison of polarization curves for numerical prediction and experimental measurement. 129
6.6 The flow configuration for numerical validation. 130
6.7 Comparison of local current density variation under different cell voltages [226]. 131
6.8 The prototype of a LT-PEFC. 133
6.9 Locations and orientations of cracks in the MEAs. 133
6.10 Polarization curves comparison of the cases with cracks and without cracks. 134
6.11 Current density distributions at the center of membrane, $i = 1.4\,\mathrm{A\,cm^{-2}}$. (left: inlet; right: outlet) (a) Case without crack; (b) Case with horizontal cracks; (c) Case with vertical cracks. 134
6.12 Potential distributions at the center of membrane, $i = 1.4\,\mathrm{A\,cm^{-2}}$. (left: inlet; right: outlet) (a) Without crack; (b) With horizontal cracks; (c) With vertical cracks. 135
6.13 Liquid water saturation at the cathodic surface of membrane, $i = 1.4\,\mathrm{A\,cm^{-2}}$. (left: inlet; right: outlet) (a) Without crack; (b) With horizontal cracks; (c) With vertical cracks. 135
6.14 Current density on the cross-line from inlet to outlet, $i = 1.4\,\mathrm{A\,cm^{-2}}$. 136
6.15 Potential on the cross-line from inlet to outlet, $i = 1.4\,\mathrm{A\,cm^{-2}}$. 137
6.16 Liquid water saturation on the cross-line from inlet to outlet, $i = 1.4\,\mathrm{A\,cm^{-2}}$. 137
6.17 (a) Current density, (b) Liquid water saturation, and (c) Potential distributions for case with 3 horizontal cracks, $i = 1.4\,\mathrm{A\,cm^{-2}}$. 138
6.18 Current density along the cross-line as marked in Fig. 6.17, $i = 1.4\,\mathrm{A\,cm^{-2}}$. 139
6.19 Potential along the cross-line as marked in Fig. 6.17, $i = 1.4\,\mathrm{A\,cm^{-2}}$. 139

6.20 Liquid water saturation along the cross-line as marked in Fig. 6.17, $i = 1.4\,\mathrm{A\,cm^{-2}}$. 140
6.21 The voltage variations for different crack sizes, $i = 1.4\,\mathrm{A\,cm^{-2}}$. 141
6.22 Current density distributions, crack size = 0.06 mm, $i = 1.4\,\mathrm{A\,cm^{-2}}$. 141
6.23 Potential distributions, crack size = 0.06 mm, $i = 1.4\,\mathrm{A\,cm^{-2}}$. 141
6.24 The liquid water saturation distributions, crack size = 0.06 mm, $i = 1.4\,\mathrm{A\,cm^{-2}}$. 142
6.25 Current density distributions on the cross-line from inlet to outlet, crack size = 0.06 mm. 142
6.26 Current density distributions on the cross-line from inlet to outlet, crack size = 0.06 mm. 143
6.27 Liquid water saturation distributions on the cross-line from inlet to outlet, crack size = 0.06 mm. 143
6.28 The sketch of fuel cells in which the CCM (MEA) is partially covered by the GDL (not to scale). 144
6.29 The cross section of the geometry (not to scale). 145
6.30 The comparison of polarization curves for normal cell and cell with GDL shortage. 145
6.31 The current density and liquid water saturation distributions, $i = 1.4\,\mathrm{A\,cm^{-2}}$. (a) Current density for normal cell. (b) Current density for cell with GDL shortage. (c) Liquid water saturation for normal cell. (d) Liquid water saturation for cell with GDL shortage. 146
6.32 The in-plane protonic conductivity distributions, $i = 1.4\,\mathrm{A\,cm^{-2}}$. (a) Normal cell. (b) Cell with GDL shortage. 147
6.33 The through-plane protonic conductivity distributions, A – B, $i = 1.4\,\mathrm{A\,cm^{-2}}$. (a) Normal cell. (b) Cell with GDL shortage. 147
6.34 The oxygen mole fraction distributions, $i = 1.4\,\mathrm{A\,cm^{-2}}$. (a) Complete cell. (b) Cell with GDL shortage. 148
6.35 The temperature distributions on the center plane of membrane, $i = 1.4\,\mathrm{A\,cm^{-2}}$. (A cross line, AB, was marked in the middle). (a) Normal cell. (b) Cell with GDL shortage. 148
6.36 Voltage variations for various distances, $i = 1.4\,\mathrm{A\,cm^{-2}}$. . . . 149
6.37 Water content variations along AB for various distances, $i = 1.4\,\mathrm{A\,cm^{-2}}$. 150
6.38 Temperature variations along AB for various distances, $i = 1.4\,\mathrm{A\,cm^{-2}}$. 150
6.39 Temperature deviations at point A or B under various distances, $i = 1.4\,\mathrm{A\,cm^{-2}}$. 151
6.40 Voltage variations under various distances for cases with GDL shortage at both anode and cathode sides, $i = 1.4\,\mathrm{A\,cm^{-2}}$. . . 151
6.41 (a) Current density and (b) liquid water saturation distributions, $d = 0.08$ mm and $i = 1.4\,\mathrm{A\,cm^{-2}}$. 152

6.42 Temperature variations along AB under various distances, $i = 1.4\,\mathrm{A\,cm^{-2}}$. 153
6.43 Temperature deviation at point A/B under various distances, $i = 1.4\,\mathrm{A\,cm^{-2}}$. 153
6.44 Electric conductivity along AB under various distances, $i = 1.4\,\mathrm{A\,cm^{-2}}$. 154

7.1 The geometry applied in the calculation of the homogeneous model. 160
7.2 The comparison of polarization curves predicted by the detailed and homogeneous models. 162
7.3 The current density distribution in the membrane. (a) Detailed model. (b) Homogeneous model. 162
7.4 Liquid water saturation distribution at interface of membrane and catalyst electrode. (a) Detailed model. (b) Homogeneous model. 163
7.5 The geometry and the computational domains. (a) The flow path design [97]. (b) The present simplification (Baffles are marked with red lines). 164
7.6 The comparison of polarization curves between experimental measurement and numerical simulation. 165
7.7 The current density distribution, $i = 0.8\,\mathrm{A\,m^{-2}}$. 166
7.8 The protonic conductivity distribution in the membrane, $i = 0.8\,\mathrm{A\,m^{-2}}$. 166
7.9 Activation overpotential distributions, $i = 0.8\,\mathrm{A\,cm^{-2}}$. (a) Cathode side. (b) Anode side. 167
7.10 Liquid water saturation distribution at interface of membrane and catalyst electrode, $i = 0.8\,\mathrm{A\,cm^{-2}}$. 168
7.11 (a) Oxygen and (b) water vapor mole fraction distributions at the interface between membrane and cathode catalyst electrode, $i = 0.8\,\mathrm{A\,cm^{-2}}$. 169
7.12 (a) Oxygen and (b) water vapor mole fraction distributions in cathode gas channels, $i = 0.8\,\mathrm{A\,cm^{-2}}$. 169
7.13 Hydrogen mole fraction at (a) the interface between membrane and anode catalyst electrode and (b) gas channels, $i = 0.8\,\mathrm{A\,cm^{-2}}$. 170
7.14 Pressure distribution in cathode side gas channels, $i = 0.8\,\mathrm{A\,cm^{-2}}$. 171
7.15 Temperature distribution in cathode side gas channels, $i = 0.8\,\mathrm{A\,cm^{-2}}$. 171

8.1 Skematic of liquid water distribution in a channel cross section. (a) Homogeneous. (b) Condensed. (c) Merged. 177

List of Tables

1.1 Basic difference between models in Fig. 1.1. 8
1.2 Enthalpies and entropies of formation in PEFCs (298.15 K, 1 atm) [40] 9

2.1 Source/sink terms: two phase flow, detailed model 49
2.2 Source/sink terms: single phase flow, detailed model 50
2.3 Source/sink terms: two phase flow, homogeneous model . . . 60
2.4 Source/sink terms: Single phase flow, homogeneous model . . 60

3.1 Finite volume notations 69

4.1 Operating conditions and properties 85
4.2 Model parameters for *model 1* [99] 86
4.3 Material properties and model parameters for *model 2* [98]. . 86
4.4 Grid dependence study 87
4.5 Geometry and operating conditions in validations 90
4.6 Model parameters in validations, *model 1* 91

5.1 Model parameters 117

6.1 Parameters 128
6.2 Operating condition in validations 129
6.3 Model parameters and operating conditions 132
6.4 Cell performance variation with number of cracks, $i = 1.4\,\mathrm{A\,cm^{-2}}$ 138

7.1 Model parameters in verification 161
7.2 Model parameters in validation 165

Chapter 1

Introduction

1.1 Motivations and objectives

Fossil fuels, like coal, petroleum, natural gas etc., have been widely used nowadays. However, the green-house gases emission and pollution due to the consumption of fossil fuels become more and more serious. Nevertheless, fossil fuels are not renewable in a short period, therefore, the storage of them is fixed and they will be used out in the near future. Clean and renewable energy alternatives are attracting attention.

The fuel cell, which converts chemical energy directly into electricity, shows great potential in dealing with the issues mentioned above. The origin of fuel cell dates back to more than 150 years ago and was invented by William Robert Grove. The research of fuel cell done by Friedrich Wilhelm Ostwald provided the groundwork for the following fuel cell investigations [1]. Nowadays, the most well-known fuel cells can be classified into several types based on the electrolyte/membrane and operating temperature:

- PEFC: polymer electrolyte fuel cell
- DMFC: direct methanol fuel cell
- AFC: alkaline fuel cell
- MCFC: molten carbonate fuel cell
- SOFC: solid oxide fuel cell

Fuels that can be supplied for these fuel cells include hydrogen, methanol, and reformat. The products consist of water, heat, and/or carbon dioxide: CO_2. If pure hydrogen is utilized in the fuel cell, only water and heat are produced; meanwhile, the hydrogen can be obtained from water electrolysis [2] and current technology shows the ability of hydrogen storage in the form of compression in cylinders [3].

Considering the operating temperature, the PEFC can be divided into two types: low-temperature PEFC (LT-PEFC) and high-temperature PEFC (HT-PEFC). The LT-PEFCs, which are the conventional PEFCs, represent the fuel cells that operate at temperatures lower than 100 °C. The HT-PEFCs are developed due to the fact that the reaction kinetics, catalyst activity and the resistance to fuel impurities are higher at improved operating temperature, ranging from 140 - 180 °C.

The PEFC has primary advantages compared with other types of fuel cells, including no risk of electrolyte leakage, shorter warm-up time, and higher specific power. Therefore, the PEFC is considered as a candidate for small stationary, portable, automotive and other transportation applications [4–6]. However, the commercialization of PEFCs is still largely limited by the performance, durability and cost [7].

A PEFC is consisted of several components, interconnect/bipolar plate (BPP), the gas diffusion layer (GDL), and membrane electrode assembly (MEA). The central part of a fuel cell is the MEA that includes proton transfer membrane, and catalyst layers (CLs) for both anode and cathode sides.

BPP: The BPP provides path ways for supplied gases, conduct electricity and heat during electrochemical reaction. Various kinds of flow fields need to be machined on either one or both sides of the BPPs. The selection of a BPP depends on many aspects, including [8]:

- Impermeability to gases: avoiding gas leakage.
- High electrical and thermal conductivities: promoting electricity and heat transfer.
- High corrosion resistance: preventing acid corrosion.
- Mechanical strength: protecting key components in the fuel cells.
- Low cost...

Considering all of these requirements, the graphite bipolar plate seems to be a reliable option. However, the application is limited to stationary and laboratory conditions, where the weight and volume are not critical. Besides, the cost during flow channels machining and material brittleness hinder the utilization in mobile and transport fields [9]. Meanwhile, metallic plates attract more attention as a superior alternative due to the lower cost, increased volumetric power density, and higher mechanical strength [10]. Some disadvantages also appear, e.g. chemical instability, which should be well addressed [11].

GDL: The GDL is formed by randomly oriented carbon fibers that are either woven or non-woven [12]. The typical thickness is in the range of 200 to 400 μm. In an operating LT-PEFC, liquid water may be formed in

the pores of GDL and CL, which contributes to better humidification of the membrane, or on the other hand, leads to the flooding problem. The GDL, therefore, needs to have a proper wetting characteristic. Researches have shown that a certain amount of coating by the hydrophobic agent, like polytetrafluoroethylene (PTFE) [13][14] and fluorinated ethylene propylene (FEP) [15][16], is beneficial for cell performance in terms of higher liquid water removal capability. In an HT-PEFC, the scenario is different as no liquid water can be produced in a relatively high operating temperature. The GDL provides mechanical support for CL and membrane, which also facilitates gas diffusion in/out of catalyst sites, and/or water removal. As a connection between the BPPs and MEA, the GDLs should be highly electronic and thermal conductive. During fuel cell assembly, mechanical pressure applied from the BPPs compresses the GDLs. The compression varies from under-channel and under-land regions, which is crucial in PEFC designs [17]. It leads to non-uniformly distributed porosity and tortuosity of GDLs. Gas diffusion and fluid flow may, therefore, be affected.

CL: The CL consists of the carbon and platinum particles, and part of the ionomer (polymer electrolyte), which are mixed together to provide reaction sites for reactant species. The carbon and platinum particles contacts with the GDL, which offer paths for electron transfer; the ionomer presents proton and/or water transfer through the membrane. Besides, these components would fill up the CL, the porosity of which ranges from 0.2 to 0.5. This may give higher platinum loading, allow reactants to reach reaction sites, and prevent starvation. The CL is usually very thin with approximately 10μm for a LT-PEFC, and 20 - 120 μm [18] for a HT-PEFC. The preparation, function, and performance of CLs in PEFCs can be found in [19–21].

Membrane: The membrane in PEFCs must present relatively high proton conductivity that it can transfer proton from the anode side to the cathode side effectively. It needs to prevent gases (fuel and oxygen) mixing. Also, it should be chemically and mechanically stable under various operating conditions. Nowadays, the well-developed membranes are based on perfluorocarbon-sulfonic acid (PFSA) ionomer. Among them, the most widely used membrane material is Nafion that is made by Dupont, with perfluoro-sulfonyl fluoride ethyl-propyl-vinyl ether (PSEPVE) [22]. The proton conductivity of the PFSA membrane is related to the dissolved water with the sulfonic acid groups. Therefore, the reasonable working temperature is limited to approximately 60 - 80 ℃, which corresponds to the operating temperature of an LT-PEFC. However, they are not suitable for HT-PEFCs, due to the loss of proton conductivity and membrane stability when the operating temperature is higher than 80 °C [23]. A polybenzimidazole (PBI)/phosphoric acid (H_3PO_4) system was firstly introduced by Wainright et al. [24], the applicability of which on HT-PEFCs was tested by Li et al. [25]. In addition to the traditional PBI membrane, an alternative

(poly(2,5-benzimidazole): ABPBI, membrane) was also used and fabricated. This membrane was employed in many Jülich HT-PEFC prototypes, studies and achievements of which have been published [26–28].

In PEFCs, air or oxygen is supplied at the cathode side, whereas reformat or hydrogen are supplied at the anode side. The (humidified) gases transfer in the grooved flow fields, diffuse through the GDLs and finally reach CLs where electrochemical reactions take place. At the anode side, hydrogen is oxidized: protons transfer through the membrane and combine with oxygen ions to form water; in the meantime, electrons transfer through the external circuit. At the cathode side, oxygen is reduced. The transport processes in the PEFCs are very complicated, including three-dimensional heat and mass transfer, species and charge transfer, electrochemical reactions, multi-phase flows, and so on.

It is quite expensive and nearly impossible to conduct experimental measurements in a PEFC. Meanwhile, almost all of the transport processes are multi-scale phenomena, as indicated in the review of Andersson et al. [29] and the work of He and Tao [30]. For example, the sizes of catalyst particles are at the sub-micron scale, whereas the liquid water droplets are at a micro scale, and the flow in flow paths is at a continuum scale. Numerical models need to be developed to represent some of the major transport processes and predict the cell performance based on reasonable simplifications and assumptions Siegel [4]. It is not necessary for the model to present precise values of every variable in the computational domain, however, correctly represent the general trends in a wide range of operating conditions.

With the development of materials and optimization of design, the power density of a fuel cell is compatible with the internal combustion engines. However, a single cell is not sufficient for many applications due to the active area and output voltages. Therefore, single cells are combined in series or parallel to form a stack with the aim of gaining higher voltage and power output. A fuel cell stack is normally a combination of dozens or hundreds of unit cells. The ideal output of a stack is the sum output from each individual fuel cell. However, this is usually not obtainable due to the failure of one or more single cells, material degradation, and poor-design flow fields, etc. [31].

1.2 Research objectives

The numerical approach provides an alternative for the diagnosis and optimization of fuel cells and stacks. Depending on the operating temperature of a cell/stack, the two-phase flow phenomena need to be modeled in a LT-PEFC and only single-phase flow is considered in a HT-PEFC. The aim of the present thesis lies in the development of PEFC models, including a detailed and a homogeneous models. Both models are able to account for LT-

and HT-PEFC applications. Therefore, the main purposes can be outlined as:

- Detailed modeling work:
  The model considers all of the major three-dimensional transfer phenomena, in which all sub-components: MEA, CLs, GDLs, gas channels [1] and bipolar-plates (BPPs) are taken into account. A multiple region technique is used to solve various coupled transport equations simultaneously. The model is developed by considering the major transport processes, including single-phase and two-phase flows, charge transfer, electrochemical reaction, species transfer, and heat and mass transfer. An Eulerian-Eulerian two-phase model is applied to describe two-phase flow in the gas channels. The Leverett Function is selected to represent liquid water transfer in porous media, like GDLs and CLs. A local time stepping approach is used to obtain faster convergences. In addition, a specific HT-PEFC model is derived from an existing SOFC model [32]. The local Nernst equation for open-circuit potential, Kirchhoff-Ohm relation for the local current density, the local electrochemical reaction, fluid flow equations, species transport equations are considered and solved.

- Homogeneous modeling work:
  The transport processes are the same as in corresponding detailed and homogeneous models. The distributed resistance analogy (DRA) is selected for general transport phenomena. A multi-shared space (MUSES) method is applied, which allows for simultaneous solutions for concentration, heat and momentum equations for different 'phases' occupying 'same' physical spaces. Therefore, the grids used in the stack models would be very coarse compared to the detailed models. The model is derived from the detailed model, with considerations from the work of Beale and Zhubrin [33] and Nishida et al [34]. An Eulerian-Eulerian two-phase model is applied to describe two-phase flow in the gas channels.

1.3 Methodology

All of the transport equations are discretized and solved via an open-source library, OpenFOAM ® [35], which is based on the finite volume method and enables fully parallel simulations. Both the detailed and the homogeneous models are readily implemented into OpenFOAM. Source codes of

[1] It is usually named as 'channel' in fuel cell community, while 'duct' is widely used in fluid mechanics. However, both refer to the same object.

both models are based on an OpenFOAM multi-phase solver, reactingTwoPhaseEulerFoam, and a fuel cell solver [36]. They both enable consideration of three-dimensional, multi-region, multi-phase, multi-physics, and multi-scale simulations on fuel cells. The grids, which consist of only hexahedral elements, are constructed through a commercial software ANSYS-ICEM CFD [37] in the present thesis. The computational domains are decomposed manually using a contiguous multi-block mesh that is body-fitted and concentrated near the solid ribs.

All of the large simulations were performed on the Jülich Aachen Research Alliance (JARA) high-performance computing facility. Post-processing, including data analysis and visualization of the results, were conducted by OpenFOAM utilities, a python package matplotlib [38], and an open-source software Paraview [39].

1.4 Outline of the thesis

The present thesis is organized as follows (also shown in Fig. 1.1):

1. Chapter 1. The background and motivation of studies in this thesis are described. Afterward, the state-of-art literature review of PEFC cell and stack modeling work is presented.

2. Chapter 2. The physical processes and the corresponding governing equations are introduced. Two models are provided: a detailed model (*model 2* and *model 4*) and a homogeneous model (*model 3* and *model 5*), see Fig. 1.1.

3. Chapter 3. The numerical processes for implementation of physical models are presented. The computational grid, boundary conditions, and discretization method are exhibited.

4. Chapter 4. The numerical results of two in-house designed HT-PEFCs are shown by using the detailed models (*model 1* and *model 2*).

5. Chapter 5. The application of the homogeneous model on an in-house designed HT-PEFC short stack (*model 3*) is provided.

6. Chapter 6. This chapter describes the application of the detailed model (*model 4*) on LT-PEFCs.

7. Chapter 7. This chapter includes the numerical results of an in-house designed LT-PEFC by utilizing the homogeneous model (*model 5*).

8. Chapter 8. A discussion concerning the present models is given.

9. Chapter 9. A conclusion is presented.

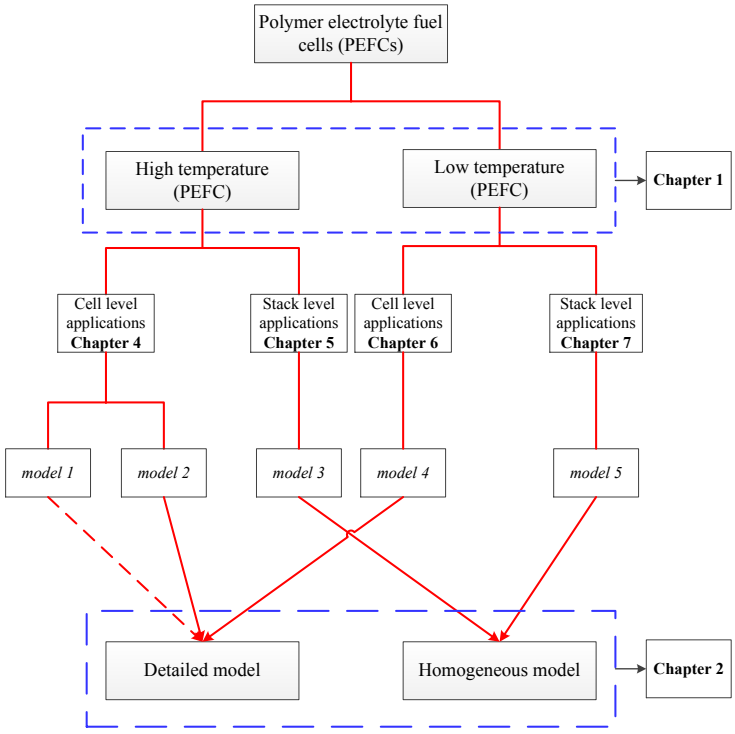

Figure 1.1: The concept of present thesis. The differences between each model are listed in Table 1.1. Note: *model 1* is derived from the OpenFuelCell package [36].

10. Chapter 10. The outcome and further applications of the present models (source codes).

Table 1.1: Basic difference between models in Fig. 1.1.

	Level	Electrochemistry	Multi-phase	Potentials
model 1	Detailed	Tafel	Single-phase	Kirchhoff relation
model 2	Detailed	Butler-Volmer	Single-phase	Two-potential model
model 3	Homogeneous	Butler-Volmer	Single-phase	Kirchhoff relation
model 4	Detailed	Butler-Volmer	Two-phase	Two-potential model
model 5	Homogeneous	Butler-Volmer	Two-phase	Kirchhoff relation

1.5 Work principle of PEFCs

A schematic of PEFC structure is shown in Fig. 1.2. The electrochemical reactions in LT-/HT-PEFCs are almost identical:

At the anode side, hydrogen is oxidized (hydrogen oxidation reaction (HOR)),

$$\mathrm{H_2} \rightarrow 2\mathrm{H^+} + 2\mathrm{e^-} \tag{1.1}$$

At the cathode side, oxygen is reduced (oxygen reduction reaction (ORR)),

$$\frac{1}{2}\mathrm{O_2} + 2\mathrm{H^+} + 2\mathrm{e^-} \rightarrow \mathrm{H_2O} \tag{1.2}$$

The overall reaction,

$$\mathrm{H_2} + \frac{1}{2}\mathrm{O_2} \rightarrow \mathrm{H_2O} \tag{1.3}$$

The water may either be in the vapor phase (HT-PEFC) or the liquid and vapor phase (LT-PEFC). During the electrochemical reactions, heat and electricity are generated besides water. From the thermodynamic point of view, the enthalpy change during the reaction is expressed as:

$$\Delta H = \Delta G + T\Delta S \tag{1.4}$$

where H is enthalpy, G is Gibbs free energy, T means temperature, and S is entropy. Among these, only the portion of Gibbs free energy, ΔG, can be converted into electricity in a PEFC. ΔH represents the difference between the heats of formation of products and reactants, which yields,

$$\Delta H = (h_\mathrm{f})_{\mathrm{H_2O}} - (h_\mathrm{f})_{\mathrm{H_2}} - 0.5(h_\mathrm{f})_{\mathrm{O_2}} \tag{1.5}$$

where the subscript f means formation. Similarly, the entropy difference, ΔS, refers to,

$$\Delta S = (s_{\mathrm{f}})_{\mathrm{H_2O}} - (s_{\mathrm{f}})_{\mathrm{H_2}} - 0.5(s_{\mathrm{f}})_{\mathrm{O_2}} \tag{1.6}$$

Table 1.2: Enthalpies and entropies of formation in PEFCs (298.15 K, 1 atm) [40]

Species	h_{f} (kJ mol^{-1})	s_{f} (kJ mol^{-1} K^{-1})
H_2	0	0.13066
O_2	0	0.20517
H_2O (l)	-286.02	0.06996
H_2O (g)	-241.98	0.18884

The enthalpies and entropies of formation for H_2, O_2, and H_2O at standard conditions are shown in Table 1.2. Considering the electrical work of a PEFC, it gives,

$$W = qE = nFE \tag{1.7}$$

where W is the electrical work, q is charge in electrochemical reaction, n means number of electrons per molecule, F represents the Faraday's constant, and E is the theoretical potential. In addition, the electricity generated from reaction corresponds to the Gibbs free energy, ΔG,

$$E = \frac{W}{nF} = \frac{-\Delta G}{nF} \tag{1.8}$$

Taking the effects of temperature and pressure into account, the Nernst potential can be obtained as,

$$E = E_0 + \frac{R_g T}{nF} \ln\left(\frac{P_{\mathrm{H_2}} P_{\mathrm{O_2}}^{0.5}}{P_{\mathrm{H_2O}}}\right) \tag{1.9}$$

where E_0 refers to the potential at standard condition, as in Eq. 1.8, P means dimensionless reference pressure, R_g is the universal gas constant. The Nernst potential is the ideal potential for a PEFC, which is always higher than the potential measured experimentally [41]. Besides the thermodynamics in PEFCs, water management is another key issue that needs to be well-posed.

In LT-PEFCs, the membrane needs to be well humidified to obtain high electric conductivity; however, extra humidification leads to the flooding problem in fuel cells. Liquid water may fill in the pores in GDLs, CLs, and even flow channels and prevent reactants reaching reacting sites. It is produced at the cathode side, however, two-phase phenomena may also

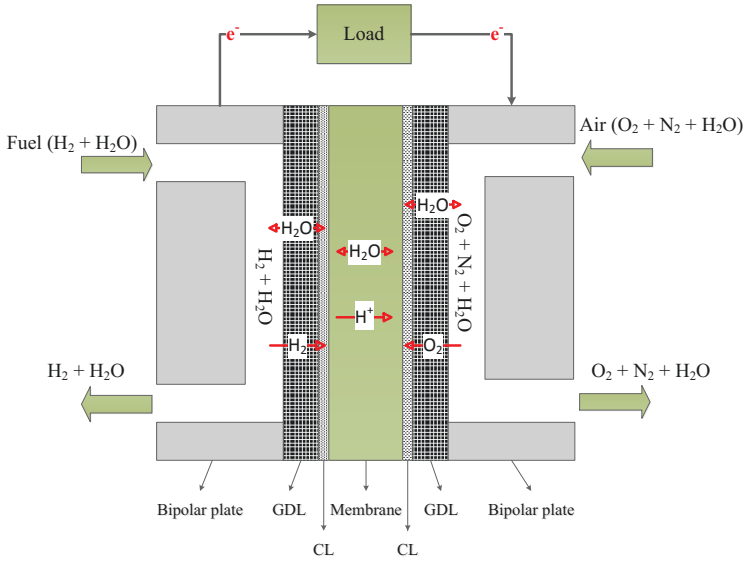

Figure 1.2: Schematic of a PEFC.

happen at the anode side, depending on the water cross-over through the membrane and partial pressure of water vapor.

For HT-PEFCs, the electric conductivity of the acid-doped PBI membrane is a strong function of the doping level and temperature [25]. That is to say, it is not necessary to supply humidified gases from inlets to maintain high humidification of the membrane. Water transfer in the membrane mainly depends on diffusion processes, as the Electro-osmotic drag (EOD) can be neglected in PBI membranes [25]. Considering the operating temperature of HT-PEFCs, water mainly exists in the vapor phase, whereas the phosphoric acid in the PBI membrane contains some water in the dissolved phase. However, the dissolved water in the PBI membrane/electrolyte is beyond the scope of this thesis.

Water management in both types of PEFCs is critical and important [42]. As shown in Fig. 1.3, water may exist in different states. Water management in a PEFC can be divided into three main groups: in the membrane, in the porous media, and in gas channels.

1.5.1 Water transport in the membrane

Diffusion processes: generally, the water concentration gradient exists in the membrane, which leads to water diffusion from higher concentration

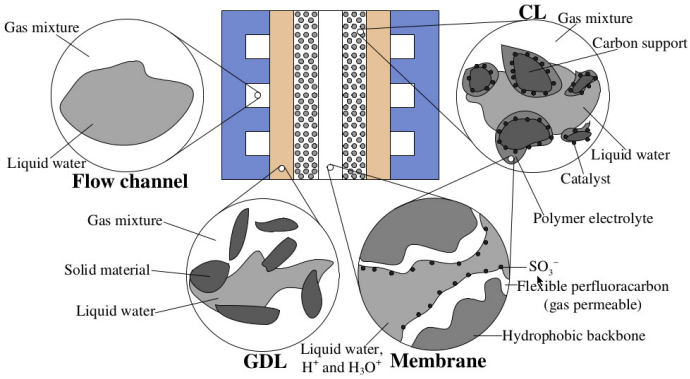

Figure 1.3: The state of water in different sites of a PEFC. (Reprinted from [42])

sites to lower sites. The diffusion flux can be described as:

$$\mathbf{J} = -D\nabla c_{\text{water}} \tag{1.10}$$

In a LT-PEFC, it can be further written as,

$$\mathbf{J} = -D\nabla c_{\text{water}} = -\frac{\rho_{\text{mem}}}{\text{EW}} D\nabla\lambda \tag{1.11}$$

where D represents the diffusion coefficient, c is water concentration, EW is the Nafion membrane equivalent weight, and λ means water content in the Nafion membrane.

In this process, the diffusion coefficient is a function of Nafion membrane hydration. Experimental study [43] was performed to measure the coefficient by assuming the membrane hydration is uniform and homogeneous. Mathematical formulations can be derived from the experimental data, described as either [44]:

$$D = \begin{cases} 2.692661843 \times 10^{-10} & \lambda < 2 \\ 10^{-10}\exp[2416(\frac{1}{303} - \frac{1}{T})][0.87(3-\lambda) + 2.95(\lambda - 2)] & 2 < \lambda <= 3 \\ 10^{-10}\exp[2416(\frac{1}{303} - \frac{1}{T})][2.95(4-\lambda) + 1.642454(\lambda - 3)] & 3 < \lambda <= 4 \\ 10^{-10}\exp[2416(\frac{1}{303} - \frac{1}{T})](2.563 - 0.33\lambda + 0.0264\lambda^2 - 0.000671\lambda^3) & \lambda > 4 \end{cases} \tag{1.12}$$

or [45]:

$$D = \begin{cases} 3.1 \times 10^{-7}\lambda[\exp(0.28\lambda) - 1]\exp^{\frac{-2346}{T}} & 0 < \lambda < 3 \\ 4.17 \times 10^{-8}\lambda[161\exp(0.28\lambda) + 1]\exp^{\frac{-2346}{T}} & 3 < \lambda < 17 \end{cases} \tag{1.13}$$

A comparison of these two corrections indicates deviations under different water content λ; however, the maximum value of the diffusion coefficient at $\lambda = 3$ is captured by both. Which one performs better in LT-PEFC simulations has not been concluded yet.

In a HT-PEFC, the membrane is based on phosphoric acid doped PBI. The diffusion of water through the membrane is related to the properties of the phosphoric acid. In a study of Reimer et al. [46], the diffusion coefficient D of a PBI based HT-PEFC was experimentally measured with an averaged value of $2.7 \times 10^{-7} \mathrm{m}^2\mathrm{s}^{-1}$.

Electro-osmotic drag (EOD): in a LT-PEFC, when protons transfer through pores in the membrane, water molecules are dragged with them; proton transfer in the membrane may be in the form of hydronium complexes (H_3O^+) or similar forms. In a HT-PEFC, the water transfer mechanism is different and it can be neglected for PBI membranes [25]. The drag coefficient can be defined as several water molecules dragged by protons for simplification. In this case, the water flux due to EOD is written as:

$$\mathbf{J} = n_d \frac{\mathbf{I}_{\text{proton}}}{F} \tag{1.14}$$

where n_d is the drag coefficient, and $\mathbf{I}_{\text{proton}}$ represents proton transfer flux.

One experimental measurement [47] showed $n_d = 2.5$ (2.0 – 2.9) when $\lambda = 22$, and $n_d = 0.9$ when $\lambda = 11$. Experimental data [45] also showed that $n_d = 1.4$ when $\lambda = [5 - 14]$, and n_d decreases to 0 when λ decreases from 5 to 0. The formulation of n_d from experimental data is shown as either [44]:

$$n_d = \frac{2.5\lambda}{22} \tag{1.15}$$

or a step-wise form [48]:

$$n_d = \begin{cases} 1 & \lambda < 14 \\ 0.1875\lambda - 1.625 & other \end{cases} \tag{1.16}$$

These two formulations are widely used in PEFC modeling and simulations, although deviations exist.

Hydraulic permeation: pressure gradient may exist in the membrane from anode side to cathode side. Water permeates from one side to the other, which can be described via:

$$\mathbf{J} = -\lambda \frac{\rho_{\text{mem}}}{\text{EW}} \frac{K}{\mu} \nabla p \tag{1.17}$$

where K is the permeability of water in the membrane and μ is dynamic viscosity of water. The value of permeability as shown in [49] is in the magnitude of 10^{-14}, which is negligibly small. Considering the mechanical strength of the membrane and the parasitic power, the pressure difference

between anode and cathode is generally not large. The predominant processes of water transfer in the membrane are diffusion and EOD, which can be described by several models: diffusive model, and chemical potential model, individually or in combinations [42].

1.5.2 Water transport in porous media

In PEFCs, the porous regions include the GDL and CL.

GDL: The water vapor transfer in the GDLs mainly depends on diffusion, and/or convection, considering the microstructure, such as pores, fiber diameter, etc. Diffusion refers to transport processes due to the concentration gradient, and convection represents transportation due to fluid motion/velocity. Convection processes contribute better reactants distribution. Diffusion processes mainly result from reactants consumption and product production. In different flow field designs, the transportation mechanism also varies. For parallel flow field design, water transport is dominated by diffusion. For serpentine flow field design, water transport is dominated by both convection and diffusion. For the interdigitated flow field design, water transport is dominated by convection.

In a HT-PEFC, water transported in the GDL refers to the water vapor. Various parameters, including fiber diameter, GDL thickness, porosity, tortuosity, etc., have been investigated on the GDL performance [50]. Nevertheless, the flow in the HT-PEFC GDL is a single-phase, which is much simpler compared to the cases in the LT-PEFC GDL where two-phase flow appears. To consider liquid water transport in GDL, several non-dimensional numbers can be defined to evaluate the significance of each parameter:

$$\text{Reynolds number: } \mathrm{Re} = \frac{\rho_l U_l L}{\mu_l} = \frac{\text{ineria force}}{\text{viscous force}} \tag{1.18}$$

$$\text{Capillary number: } \mathrm{Ca} = \frac{\mu_l U_l}{\sigma_{l-a}} = \frac{\text{viscous force}}{\text{surface tension}} \tag{1.19}$$

$$\text{Weber number: } \mathrm{We} = \frac{\rho_l U_l^2 L}{\sigma_{l-a}} = \mathrm{Re} \cdot \mathrm{Ca} = \frac{\text{interia force}}{\text{surface tension}} \tag{1.20}$$

$$\text{Bond number: } \mathrm{Bo} = \frac{(\rho_l - \rho_a) g L^2}{\sigma_{l-a}} = \frac{\text{gravitational force}}{\text{surface tension}} \tag{1.21}$$

$$\text{Dynamic viscosity ratio: } \mathrm{M} = \frac{\mu_{\text{liquid}}}{\mu_{\text{gas}}} = \frac{\text{Liquid viscosity}}{\text{Gas viscosity}} \tag{1.22}$$

where σ is the surface tension, g is the gravity, and L represents a characteristic length. Then, the corresponding values for typical liquid water transfer in GDLs are [42]: Re = 0.0023, Ca = 5.6×10^{-8}, We = 1.3×10^{-10}, Bo = 9.9×10^{-4}, and M = 20. It can be seen that surface tension, which is a force and only acts on the interface between liquid and liquid or liquid and gas, is dominant compared to other factors (capillary dominant). Due to the surface tension, a pressure jump/difference appears across the interface. If the pressure difference is zero, the interface is a flat surface, otherwise, the surface will be curved to the side with lower pressure. If a surface tension coefficient is defined to represent the surface tension effect, the relation between pressure difference and surface curvature can be expressed by the Young-Laplace equation [51]:

$$\delta p = \sigma(\frac{1}{R_1} + \frac{1}{R_2}) \tag{1.23}$$

where R_1 and R_2 represent the surface curvature at both sides. If the interface is identical to a sphere, as shown in Fig. 1.4, $R_1 = R_2$, a simplified expression is:

$$\delta p = \frac{2\sigma}{R} \tag{1.24}$$

If the pore diameter d is known, the pressure difference, or capillary pressure, can be calculated as:

$$p_c = p_g - p_l = \frac{4\sigma cos(\alpha)}{d} \tag{1.25}$$

where α is the contact angle.

The Leverett J-function is usually applied to relate the GDL properties (porosity ϵ, intrinsic permeability K, contact angle α), liquid water surface tension coefficient σ, and water volume saturation s:

$$p_c = \sigma cos(\alpha)\sqrt{\frac{\epsilon}{K}}J(s) \tag{1.26}$$

Many studies presented the formulation of $J(s)$. There are different formulations of $J(s)$ [52]. The Leverett–Udell [53] correlation is very widely used,

$$J(s) = \begin{cases} 1.42(1-s) - 2.12(1-s)^2 + 1.26(1-s)^3 & \alpha < 90^o \\ 1.42s - 2.12s^2 + 1.26s^3 & \alpha > 90^o \end{cases} \tag{1.27}$$

As shown in the work of Wang et al. [54], applying this correlation in quantitative modeling is not recommended; however, qualitatively, it can present preliminary predictions in cell design and performance optimization.

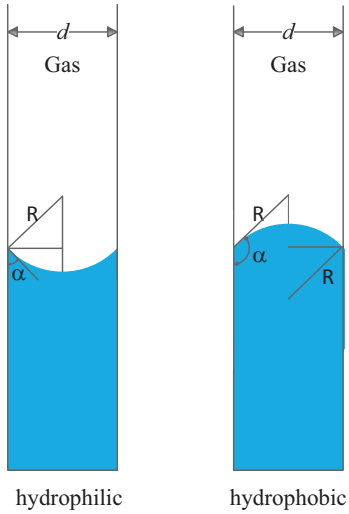

Figure 1.4: Liquid water behaviors in small pores with hydrophilic and hydrophobic surface wettabilities

The overall transportation of liquid and gas phases is governed by Darcy's law:

$$\nabla p = -\frac{U_i \mu_i}{K \cdot k_{rel,i}} + \rho_i \mathbf{g} \tag{1.28}$$

where the relative permeability factor $k_{rel,i}$ is still challenging to measure nowadays, and it has many formulations, which are functions of liquid water saturation and/or GDl properties. In the article by Liu et al. [54], various formulas of Leverett J-function and relative permeability are reviewed.

CL: Water transport in the CL can be described with the same approach as in the GDL. However, water management in the CL can be much more complex compared to that in the GDL. As the regions where reactions take place, water is produced in the vapor phase or liquid phase depending on the operating temperature. The amount of water production can be obtained from Faraday's law. Water desorption and adsorption from the electrolyte is computed from the difference between the real water content λ and the equivalent water content, λ_e:

$$R_\lambda = \psi \frac{\rho_m}{EW}(\lambda - \lambda_e) \tag{1.29}$$

where ψ represents the water desorption/adsorption rates, and λ_e can be

calculated as:

$$\lambda_{\mathrm{e}} = \begin{cases} 0.043 + 17.81a - 39.85a^2 + 36.0a^3 & 0 \leq a \leq 1 \\ 14.0 + 1.4(a - 1.0) & 1 < a \leq 3 \\ 15.8 & 3 < a \end{cases} \tag{1.30}$$

where a is water activity, defined as:

$$a = \frac{p_{\mathrm{H_2O}}}{p} + 2s \tag{1.31}$$

where s is the liquid water saturation. In a HT-PEFC, $s = 0$.

1.5.3 Water transport in gas channels

Gas channels provide pathways for reactants distribution in PEFCs. The widely used flow field designs include parallel, serpentine, interdigitated, and combined ones. The flow fields are designed to facilitate the distribution of the reactants over the entire area; The flow fields need to be well optimized to fulfill the basic requirement. For HT-PEFCs, water only exists in the vapor phase in flow fields where water management is simpler. In LT-PEFCs, the situation is different. The flow field design should be able to remove excess water from both the anode and cathode sides to reduce the possibility of flooding. As shown in the work of Ferreira et al. [55], liquid water enters the flow field from the GDLs, and forms droplets on the surface of GDL or attach to the walls of flow fields [56, 57]. The liquid water droplets may flow away due to flowing gas or remain attached. Numerical studies [58–60] have shown that the locations, where liquid droplets emerged on the GDL surfaces, are randomly distributed. It is still a challenge to capture the formation sites with numerical methods considering a large amount of computational power. In such a case, the mist state assumption is usually applied in the flow channel to incorporate other transport processes.

1.6 Literature review

The development of PEFCs has gained greatly during the past decades. Experimental work offered many possibilities for researchers to understand the physical processes in PEFCs. Meanwhile, modeling work studies were promoted due to the development of experimental technologies, such as magnetic resonance imaging (MRI) [61], neutron radiography [62], S++ ® current scan shunt [63, 64] and X-ray computed tomography [65].

The origin of PEFC modeling researches dates back to the 1990s. Springer et al. [44] and Bernardi and Verbrugge [49] developed the first PEFC models. One dimensional (1-D) steady-state simulations were considered: Springer

et al. [44] analyzed the water transfer through the Nafion membrane, where liquid water diffusion and EOD were considered; Bernardi and Verbrugge [49] investigated the overall performance of PEFCs, in terms of polarization curves. This work provided a fundamental framework and formulations for subsequent PEFC modeling studies. Afterward, many models were developed by following the earlier work by Springer et al. [44] and Bernardi and Verbrugge [49]. Nguyen and White [66] and Fuller and Newman [67] derived 2-D models, which provided the analysis of water and heat management in the 2-D scenario. Yi and Nguyen [68, 69] further developed their earlier model [66] and explored the effects of various designs and different operating conditions, e.g. inlet humidity and cooling techniques. Gurau et al. [70] developed a 2-D mathematical model for the whole fuel cell. In this work, the major transport processes were taken into consideration and the solution procedure was described in detail. Djilali and co-workers [71–73] derived PEFC models to capture 3-D transport phenomena. These models were implemented into the computational fluid dynamics (CFD) software, Fluent [37], via user-defined functions (UDFs). Fimrite et al. [74] applied a binary friction model to predict transport phenomena in the membrane and the model may act as a physically consistent modeling framework. Kulikovsky and co-workers [75–78] carried out the analytical solutions of simple PEFC models. They provided salient information to understand fuel cells. The earlier models provided the basic descriptions of physical processes in PEFCs. Due to the limitations of computational power, the 3-D and large scale simulations were almost impossible. During the past years, the development and application of various models attracted much attention. In the following sections, an overview of recent PEFC cell and stack models these models and applications are presented.

1.6.1 HT-PEFC: cell level modeling research

In HT-PEFCs, water only exists in the vapor phase, except for the dissolved water in the membrane, which means the flooding issue disappears. The proton conductivity of a HT-PEFC depends on the membrane phosphoric acid doping level and temperature [25]. The relative humidity of gases may alter phosphoric acid concentrations in the PBI membrane, the behavior of which also varies greatly [26–28, 79, 80]. The properties differences between Nafion and PBI membranes indicate that additional membrane/electrolyte models will be necessary and important. The study of phosphoric acid behavior is beyond of this thesis, literature review of which will not be covered in this part.

Korsgaard et al. [81] performed experimental measurements and numerical simulations. A self-derived semi-empirical model was applied on a PEFC with a commercial PBI membrane. It was found that the cell showed excellent resistance to gas with high CO concentrations at a temperature of

160 ℃ and a CO content of up to 2%. The comparison of numerical results and experimental data showed that the predicted overpotential was within 4 mV deviation for temperature from 120 - 180 ℃ with air stoichiometric factor from 2 to 5.

Cheddie and Munroe [82–84] were among the first to develop mathematical models for PBI based PEFCs. The work [82] investigated the porous electrodes properties effects on cell performance. It was found that the performance was always satisfactory if the CL was sufficient porous; otherwise, mass transfer limitations deteriorated the cell performance as the extremely low permeability hindered reactants reaching reaction sites. Higher membrane conductivity and cathode catalyst activity contributed to better performance. The study [83] revealed voltage loss sources: the activation overpotential was the largest contributor and the ohmic overpotential was the second. The authors also found the PBI membrane presented a lower heat dissipation rate than that of Nafion membrane. The work [84] considered the reactant and temperature distributions in the PEFC. The results elucidated that oxygen depletion firstly occurred in the cathode CLs just under ribs/lands. The hottest temperature region, similar to the oxygen depletion region, was located in the membrane under ribs/lands.

Jiao and Li. [85] developed a 3-D, nonisothermal PEFC model to analyze the effects of temperature, phosphoric acid doping level, stoichiometric factor, operating pressure, and inlet RHs. In this model, a semi-empirical correlation was derived for proton conductivity in the membrane, which was based on Arrhenius Law and previous experimental data. They found that higher operating temperature and phosphoric acid doping level resulted in better cell performance. It was proposed that the humidification of supplied gases was not recommended, but higher operating pressure and supplement of pure oxygen showed significant improvements in cell performance. Higher stoichiometric only performed better in high operating current densities. Jiao et al. [86] then provided a CO poisoning model to investigate CO poisoning in PEFCs. It was found that CO adsorption/desorption processes in HT-PEFCs were described by Langmuir kinetics rather than Temkin kinetics that was well-known to describe LT-PEFCs. The limit CO concentrations in this study for operating temperatures of 130 ℃, 160 ℃, and 190 ℃, were found to be 0.1%, 2%, and 10%, respectively. It was indicated that HT-PEFC operated with a sufficiently good performance at 130 ℃ or higher temperature with CO. Under high current density loads, severe performance degradation due to CO poisoning was observed only if the volume-averaged hydrogen coverage ratio was lower than 0.1 at the anode CL. Jiao et al. [87] conducted a numerical investigation on the combined effects of CO poisoning and flow channel design, including parallel-Z, parallel-U, serpentine, and interdigitated, via their previous model. It was found that the interdigitated design showed the best performance when pure hydrogen was supplied, and the serpentine design, parallel designs showed the worst. However, the

degradation due to CO poisoning was significant for interdigitated design and insignificant for parallel designs. When the CO concentration was high, parallel designs showed the highest power output, and interdigitated design provided the highest output at low CO concentration condition. It was also revealed that general distributions of absorbed hydrogen and CO coverage fractions in the anode CL were similar for different flow channel designs.

Lobato et al. [88] carried out a 3-D, half-cell PEFC model with a focus on the effects of various flow channel geometries: 4-step serpentine, parallel and pin-type. Comparison of current density distributions from different flow channels indicated that the current density was directly related to how the reactants spread over the electrode surface. From the polarization curves, it was found that parallel flow channels generated the lowest voltage, while the other two types showed similar voltages. The serpentine and pin-type flow channels contributed to better reactant and product redistribution. Also, it was essential for flow channel design to achieve better performance by avoiding the preferential paths of gases Úbeda et al. [89] provided a parameter estimation procedure for a PEFC model. In this study, they found that kinetic parameters showed the most significant influence on cell performance, followed by ionic and electronic conductivity. The mass transfer parameter, like permeability, exhibited a very slight impact.

Sousa et al. [90] applied a 2-D, isothermal PEFC model to study the influence of the CL properties on cell performance, in which the CL was treated as the combination of spherical catalyst agglomerates and porous inter-agglomerate spaces. The porous space was filled with a mixture of phosphoric acid and PTFE. It was found that the catalyst utilization was very low even under high current density operation, as the electrochemical reactions only took place on the agglomerate surfaces. The optimum value of phosphoric acid loading was found to be 30% - 50% of the total CL volume. Sousa et al. [91] applied their previous model to investigate the effects of various flow field designs, including straight, serpentine, pin-in, and interdigitated. The numerical results showed that the interdigitated flow channel design provided the highest output power. Due to the heterogeneous current density distribution of interdigitated flow channel design, as well as the strong convection in the porous electrode, the pin-in flow channel design was found to be the desired one, which generated higher voltage compared to the straight and serpentine designs. Besides, the cell performance can be improved by optimizing the catalyst parameters, like phosphoric acid loading, effective factor, etc.

Chippar et al. [92] combined the stress analysis and CFD methodology to investigate the GDL compression effect on the PBI based PEFCs. The finite element method was used to predict GDL compression/deformation and the CFD was applied to represent various transport phenomena. They found that the maximum deformation of the GDL was located at the edge of ribs/lands, where the GDL was preferentially damaged. It was indicated

that the species and current density distributions were spatially non-uniform due to the GDL compression, in which case the cell performance was reduced. The studies of Chippar et al. [92, 93] numerically analyzed the influence due to gas cross over through the membrane, the first of which assumed uniform gas crossover throughout the entire membrane, and the second of which considered several pinholes where gas crossover took place. In the first study, they found gas crossover was insignificant in fresh membranes. When a degraded membrane was used, the gas diffusivity through the membrane increased, and the reactant and current density distributions were non-uniform, which led to lower performance. In the second study, they also found the non-uniformity of reactants and current density distributions, especially near the pinholes. However, the cell performance was insensitive to the pinhole location and the pinhole size. Oh et al.[94] conducted a numerical study of stress analysis on the thermal effects in PEFCs. A fluid-structure interaction method was coupled to simulate cell expansion/compression and fluid transport simultaneously. The results showed that the membrane and CL had tensile and compressive deformation, because of the combined effects of the undeformed structure and GDL intrusion. In the heat-up process from room temperature to fuel cell operating temperature, it was found that in-plane stress was the dominant stress component responsible for the membrane deformation. Besides, the thermal stress variation due to the thermal gradient during the cell operating was slight.

Sun et al. [95] applied a 2-D, nonisothermal HT-PEFC model to investigate the approaches, employing various designs and operating parameters, to enhance the cell performance. Additionally, experiments were conducted to validate the numerical results. It was found that: lower PBI loading, higher operating temperature, thinner CL thickness, smaller CL porosity, and higher acid doping level contributed to enhanced cell performance, which was captured by both experiments and simulations.

Singdeo et al. [96] conducted numerical simulations on a new modified-serpentine flow field. The new design remained some features from serpentine designs, utilizing multiple bends, while the in-plane flow path was modified to obtain more uniform distributions of reactant and product. Besides, a new design fuel cell was fabricated and a low-cost current density mapping device was developed. The spatial deviation of current density between experimental data and simulated results was 4%. It was elucidated that the new design showed great capability of achieving high uniform distribution of current density in the whole active area.

The present author and others [97] developed a 3-D, nonisothermal PEFC model. The model was verified with an analytical model by performing simulation on a cell with a straight channel. Validation was conducted by the comparison of polarization curves between experiment and simulations, on an in-house design. The local variations of current density, as well

as oxygen mole fraction, was shown for under channel regions and rib/land regions, while the under channel regions presented higher values and under rib/land regions provided lower values. This model was applied in a cell with a relatively large active area of 200 cm^2 in another study [98] with a focus on high precision analysis. The cell was part of a short stack, for which the experimentally measured polarization curve and current density distribution were already available. The local values of current density, oxygen and water mole fraction, and pressure were presented. It was observed that local variations for current density, and oxygen and water mole fraction were large, changing significantly from under channel to under rib/land regions. Also, the serpentine flow paths led to higher pressure drop compared to that of straight flow paths. It was concluded that the serpentine flow channels contributed to better reactant distributions. Detailed numerical simulations on stack level fuel cell were also possible.

1.6.2 HT-PEFC: homogeneous/stack modeling research

A unit cell cannot satisfy the requirement for industrial applications, in terms of voltage and power output. Therefore, fuel cells are built in stacks, which include dozens or hundreds of unit cells, combined in series or parallel. In a stack, cooling system and manifold are important in maintaining stable operation. Detailed numerical simulations on HT-PEFC stacks are complicated, considering the heat transfer in the cooling system and turbulent/laminar or transition flow in the manifolds, and expensive, due to the number of cells and CFD models. In such a case, various homogeneous/stack models were developed.

Kvesić et al. [99] developed a 3-D stack model, in the form of a multi-domain and multi-scale model, to simulate transport phenomena in a five-cell HT-PEFC short stack. In-situ measurements were conducted via an S++ ® [63] device to obtain current density and temperature distributions in the stack. The local current density distributions were compared between numerical results and experimental data, the maximum deviations of which was within 10%. It was found that the current density distribution in the active area was not uniform, the maximum and minimum values of which were found near the inlet and the outlet, respectively, with a ratio of 2. The temperature variations in the stack were mainly governed by the cooling system. Numerical predictions showed good agreement with experimental data for temperature distribution. It was also found that the temperature variation in this short stack was minor, within 6 K. A later study by Kvesić et al. [100] described a CFD model that considered transport phenomena in a stack with reformat gas. The current density and temperature distributions were also measured via an S++ device. It was observed that the deviations between simulation and experiment were slight when the mean current density was low, $i <= 0.4 A\,cm^{-2}$. Under a high current density load,

experimental data showed a more uniform current density distribution than the numerical prediction. An optimal flow configuration, using counter-flow of gas supplement and co-flow of anode gas and coolant, provided the most homogeneous current density distribution.

Bezmalinović et al. [101] considered the water transport in a PEFC stack experimentally and numerically. Dry air was supplied at the cathode side and humidified hydrogen was supplied from the anode side. It was found that the water transfer through the membrane was significant as the water vapor partial pressure at the anode outlet was almost always higher than that at the cathode outlet. They found that the water transport coefficient was a strong function of current density, as well as stoichiometry and humidity level. The membrane water permeability coefficient was determined as $2.4 \times 10^{-13}\,\mathrm{mols^{-1}\,cm^{-1}Pa^{-1}}$, which was one magnitude higher than previous reported values. Simulations were conducted to study the effects of flow rate on reactants distribution along the flow channels. Deviations between numerical results and experimental data were slight; however, the model slightly overestimated the water transport at low current density condition, while it underestimated the water transport at high current density conditions.

Drakselová et al. [102] developed a macro-homogeneous stack model, which considered the complex geometry of flow channels and electrochemical reaction in each unit cell. Numerical simulations were performed on 100-cell stacks with serpentine flow channels or parallel flow channels, both of which have an active area of 180 cm^2. Experimental validation was conducted on an 80-cell stack with an active area of 187 cm^2. The polarization curves of predicted results and experimental data showed good agreement. The numerical simulations on cases with serpentine flow channels and parallel flow channels showed that the latter case performed better by means of polarization curves, due to the fact that the nonuniformly distributed oxygen in serpentine case decreased the stack performance. It was revealed that the flow channel design was important not only for stack performance but also for local variations of parameters. Higher stoichiometric factors at cathode mitigated the effects from various flow channel designs and showed positive effects on stack performance in short term operation.

The present author and others developed a stack level HT-PEFC model [103] based on the DRA approach for a 5-cell short stack. In addition, detailed numerical simulations were performed. The DAR predicted results were compared with experimental data, including the polarization curves, temperature distribution, and current density variation, with good agreement. The pressure, oxygen/water mole fraction, and Nernst potential distributions were compared to detailed numerical simulation results with minor deviations.

Zero-dimensional models are usually applied in system/stack level simulations. Considering the 2-D and 3-D model simulation results, it can be seen

that 0-D or 1-D models cannot reflect the local and internal distributions of key parameters, like temperature, pressure, current density, reactants concentrations, etc. Therefore, in terms of stack optimization, models with 2-D or above are necessary.

1.6.3 LT-PEFC: cell level modeling research

During the past several years, there have been various reviews considering LT-PEFC modeling studies, including water transport [4, 6, 42, 104], theoretical modeling with atomistic methods [105], multiphase flow models [29, 106–109], and microstructure modeling [50] etc. Water management, like water transport and multiphase flow in LT-PEFCs, is one of the most important issues in current PEFC researches and a key point in the present study. This study applies macroscopic models, hence the review mainly focuses on water management in this range.

Water transfer in the membrane

The membrane is the core part of a PEFC. It enables proton transfer from the anode to the cathode side if sufficient protonic conductivity is guaranteed. Higher protonic conductivity results from reasonable hydration/humidification, therefore water adsorption and desorption processes in membranes are important in studying the cell performance.

Verma and Pitchumani [110] developed a 2-D, single-phase, transient, isothermal model to capture the transient water content in the membrane. A case with single-channel was considered and the transient behavior was achieved by step-changing of the current density. Under various membrane properties, including diffusion coefficients, equivalent weights (EWs), EOD coefficients, ionic conductivity, and gradient factors, they found sudden current density increase can lead to anode dry out, causing voltage reversal and may contribute to cell degradation. Results also showed that the voltage reversals can be averted by employing a graded membrane approach.

Chaudhary et al. [111] derived a two-phase, transient and 2-D model. Two membrane water uptake approaches were investigated by considering Schroeder's paradox and individual contributions of water vapor and liquid water to the membrane water uptake. The approach that considered two different membrane equilibrium water concentrations showed better agreement with the experimental data than that took identical membrane equilibrium water concentrations. The transient studies, including responses from current density, liquid water saturation, and water content in the membrane, were performed. The transient rate of adsorption and desorption of water from the membrane can better represent the response of the water content of the membrane.

Karpenko-Jereb et al. [112] carried out a 1-D model to describe water

and charge transport through the membrane in PEFCs. They considered electrical potential, concentration, and pressure gradients. Water diffusion and EOD coefficients, water sorption and ion conductivity were defined as temperature-dependent functions. The simulation results, in terms of polarization curves, were in fairly good agreement with experimental data under various inlet humidification.

Water transfer in the porous media

Due to the complex microstructures in the porous media, accurate prediction of water transport properties is still challenging. Considering the fiber diameter and pore diameter in the typical porous media, where the Knudsen number is usually lower than 0.01 [109], the continuous media assumption is valid. When it comes to the MPL/CL, the pore diameters are so small that typical Navier-Stokes equations cannot be applied for numerical simulations. The volume of fluid (VOF) method [51, 113–115] and the Lattice Boltzmann Method (LBM) [58, 60, 116–118], which is a mesoscopic model that considers the dynamics of individual particles, are usually used to capture water dynamics in the porous media, while only LBM can be applied in the MPL/CL. The gas-liquid interface is tracked in both models.

However, both LBM and VOF are too computation expensive to perform large cell-level simulations. Besides, it is difficult to incorporate other transport phenomena, like water and thermal management, electrochemical reaction, and charge transfer. In macroscopic models, GDLs are usually treated as homogeneous materials that can be described by porosity, permeability, tortuosity, etc. In such a case, two macroscopic models were developed to simulate two-phase flow in the GDLs.

M2 model

The multiphase mixture model, also called a M2 model, was developed by Wang et al. [119, 120]. In this model, two phases were treated as one mixture phase. Therefore, only one set of governing equations was solved. The liquid water saturation was obtained from the mixture properties. Water condensation and evaporation were not considered explicitly, as phase equilibrium was always guaranteed. Readers may refer to references [121–123] for the debating of the M2 model on the applicability to PEFCs.

You and Liu [124] developed a unified two-phase flow mixture model, which was similar to the work of Wang et al. [120], to analyze flow transport at the cathode side of PEFCs. In this model, two-phase flow in the gas channel and GDL were treated as a two-phase mixture. The results indicated that water transport through the membrane was related to current density, water activities, water partial pressure, and membrane properties. They also found that two-phase flow characteristics at the cathode side depended on current density, operating temperature, and cathode and anode relative humidification. You and Liu [125] presented a two-phase flow

and multi-component mathematical model, which considered a complete set of governing equations that were valid in different components of PEFCs. The results predicted by this model were compared with experimental data. Under various operating conditions, the comparisons of polarization curves showed reasonable agreements.

Wang et al. [126] derived their previous model [120] to analyze two-phase flow transport at the cathode side of a PEFC, including liquid water formation and its effects on the electrochemical kinetics at the membrane/cathode interface. In this work, they considered a threshold current density that represented the transition from single-phase flow to two-phase flow. It was indicated that capillary action was the dominant mechanism for water transport inside the two-phase zone of the hydrophilic structure. Wang and Wang [127] extended the M2 model to simulate two-phase flow, species transport, heat transfer, and electrochemical reactions and their effects on liquid water transportation under nonisothermal condition. The authors performed a theoretical analysis and found that water transport due to vapor-phase diffusion under temperature gradients was comparable to water production in PEFCs. The vapor-phase diffusion enhanced water removal from GDL to flow channels. The vapor-phase diffusion resulted in better thermal dissipation in the heat pipe effect. Meng and Wang [128] developed a mathematical model for two-phase flow and flooding dynamics in PEFCs based on experimental data. The M2 model was used to describe liquid water transfer in the GDLs and the mist flow model was taken to consider flow transport in gas channels. In addition, an interfacial coverage model was developed to represent liquid water droplet emergence on the GDL surface. This work showed the capability of predicting liquid water flooding effect and stoichiometric factor on cell performance. In this study, two flooding mechanisms were presented: bulk transportation of liquid water through the GDL, and interfacial processes occurring at the GDL surface.

In the study of Wang [129], a 3-D, two-phase model was applied to investigate multiphase flows, species transport, electrochemical processes, and coupling effects. The transition from single-phase to multi-phase flow, and the formation of condensation/evaporation front for co-flow and counter-flow, were also analyzed. It was found that the two-phase flow phenomena occurred at both anode and cathode side, and single-phase and two-phase flows coexisted when the cell was operated under low-humidity operation condition. In the co-flow configuration, liquid water firstly appeared at the downstream of the cell, whereas severe flooding was observed in the middle of the cell when counter-flow configuration was applied. Liquid water saturation under the land was always larger compared to that under the channel in both co-flow and counter-flow configurations.

Mahmoudi et al. [130] studied the effects of nonhomogeneous compression of GDLs at the cathode side of PEFCs with interdigitated flow field. In this study, a 2-D, isothermal, two-phase, and multi-component model was

considered, where the CL was treated as an ultra-thin layer. The simulation results proved the influence due to GDL compression, which decreased water removal, reactant gases transport, limiting current density, and maximum power output. A compression of 35% on GDL deformation had no significant impacts under single-phase conditions. However, the considerable influence was observed under the two-phase condition with 25% decrease of limiting current density and maximum power output. Under a higher compression level of GDL, the cell performance losses mainly resulted from a higher saturation level in GDLs.

The study of Wang and Chen [131] presented an advanced control approach for liquid water region in GDLs, which was related to a dimensionless parameter, Da_0 that was introduced in their previous study [132]. This represented the relative importance of water addition rate to water removal rate. A 3-D, nonisothermal, and two-phase model was applied to explore transport phenomena in PEFCs, where phase change was incorporated. It was found that a liquid-free region near the channel central line existed in part of the gas channels under a two-phase flow regime when $Da_0 < 1$. The value of Da_0 was greatly affected by GDL thermal conductivity and operating temperatures. They observed that a larger liquid-free region can be found under high current density operating conditions. The liquid-free region was adjacent to the two-phase flow region, which contributed better water management in terms of avoiding severe flooding and dehydration.

The applications of the M2 model in water management for GDLs of PEFCs are not limited. Part of the steady-state simulations is considered here. The transient behaviors, including cold-start, degradation, etc., are also highly interested for researchers, however, out of the scope in the present work.

Two fluid models

The other model, usually named as two-fluid model, was derived by Berning et al. [71–73] and Nguyen et al. [133–135], as well as the work of Gurau et al. [70, 136]. They considered the gas phase and liquid phase separately. A non-equilibrium phase change model was applied and the water phase change rate can be defined as finite values. Considering the flow type in the GDL, the two-phase momentum equations can be reduced to two-phase Darcy's equations, which is an empirical extension from single-phase Darcy's equation. Further simplification can be obtained as shown in the work of Pasaogullari and Wang [137] and Beale et al. [138].

Lin et al. [139] applied a two-phase, 1-D steady-state, isothermal model to consider transport phenomena in PEFCs, especially liquid water flooding in CLs and GDLs. In addition, a thin film-agglomerate approach was taken to model CLs. It was found that liquid water accumulated in the CLs and GDLs if it was not removed effectively. Much more severe flooding problem was found in the CLs. Cell performance decreased with liquid water accumulation in CLs and GDLs, which was confirmed by experimental data. The

results suggested that excessive catalyst loading would not help to improve the overall cell performance, conversely, cell performance may be reduced from the extra thickness due to the effect on species, liquid water, and proton transfers. In the work of Ye and Nguyen [140], a single-domain, 3-D, and two-phase transport model were developed by considering an experimentally measured capillary pressure function. In this case, the liquid water saturation in the GDLs and CLs can be easily predicted. It was found that liquid water saturation was higher under channels for cathode CL, and lower for cathode GDLs. Wang and Nguyen [141] developed a 1-D, steady-state, two-phase model for the cathode side of PEFCs, in which the effects of capillary properties of GDL and CL, as well as saturation-level jump condition at the interface between GDL and CL, on liquid water transfer rate and saturation level, were investigated. The results revealed that compared to the capillary properties of CL, that of GDL showed a more significant effect on fuel cell performance. Higher capillary diffusion capability and lower hydrophilic porosity of GDL and CL contributed to better cell performance. This model was used in a later study by the same authors [142], where the impacts of MPL on the rate of liquid water transfer through the membrane were analyzed. The results indicated that the presence of MPL partially blocked the liquid water generated at CL and hindered the liquid water transfer to GDL, which contributed to a higher back-diffusion rate in the membrane. Therefore, the liquid water saturation in GDLs was lower, contributing to a higher oxygen transport rate from flow channels to reaction sites. As a result, the cell performance can be enhanced by applying MPL in PEFCs. In addition, more hydrophobic MPL further mitigated the requirement of water humidification at the anode side and water removal at the cathode side.

Weber and Newman [143] combined their previous model [144] and a catalyst-layer model to study the effects of MPLs on PEFCs. It was found that cell performance was enhanced by adding a MPL, due to the better contact, higher structural stability, higher catalyst-layer utilization, and longer durability and cell reproducibility for pinhole formation in the membrane. The MPL served as a valve to push water away from the GDLs and through the membrane, which mitigated flooding problems. The results also indicated that a thin, compact, mainly hydrophobic MPL contributed to the highest maximum power output. The study of Weber and Hickner [145] applied the model developed by Weber and Newman [146] to investigate water content in the MEA. The corresponding experiments were conducted. It was observed that the membrane contained considerably more water than other MEA components at low operating temperatures, 40 and 60 ℃. Due to water vapor transportation and heat-pipe effect, the water content in MEA decreased dramatically under high operating temperature, 80 ℃. The water content profile presented local maxima and minima values in the GDL due to the strong heat-pipe effect, which was deteriorated when more humidified

feeds existed.

Meng [147] developed a multi-dimensional, two-phase model to study water transport in the cathode side of PEFCs, with consideration of MPLs. Compared to 1-D models, this model was able to distinguish different effects of the current-collector and the gas channel on the liquid water transport and distribution. It was found that liquid water saturation was highest inside the catalyst layer and lowest inside the MPL. The MPL acted as a barrier for liquid water transport in cathode GDLs, comparing with the results that neglected the MPLs. Another study done by Meng [148] considered liquid water transport through the GDLs with a focus on coupling effects of two-phase flow and heat transfer phenomena. The results indicated that increasing operating temperature promoted liquid water evaporation, decreased liquid water saturation in the GDLs, altered the sites where liquid water was condensed/evaporated. Increasing gas inlet humidification and/or operating current can offset the temperature effect.

He et al. [149] carried out a 3-D two-phase model to investigate the influence of anisotropic GDL thermal conductivity on heat transfer and liquid water removal in a PEFC with a serpentine flow channel and semi-counter flow condition. The results showed that the anisotropic GDL resulted in higher temperature variations compared to the isotropic case; in-plane thermal conductivity normal to flow channels was more important than that along flow channels considering the larger temperature difference. Water saturation decreased due to the anisotropic GDL; however, water vapor may condense in the region neighbor to the rib/land. The anisotropic thermal conductivity in through-plane and in-plane direction, normal to flow channels, resulted in lower membrane conductivity. It was also found that the cell with anisotropic GDL provided more nonuniform current density distribution than that with the isotropic GDL.

Kang et al. [150] analyzed the effects of spatial variation of GDL wettability on through-plane water distribution in PEFCs via a macroscopic two-phase model. It was found that the centrally located liquid saturation peak in the GDL resulted from incomplete PTFE treatment of the GDL. The PTFE distribution was not uniform in the through-plane direction. Liquid water more easily accumulated in the relatively hydrophilic GDL pores. The simulation results confirmed the observation by previous experiments.

Kong et al. [151] investigated the application of multi-layer GDLs and the effects on water removal. The multi-layer GDL consisted of a single-layer MPL, and a double-layer GDL, where the porosity and/or wettability can be varied. A 1-D, steady-state, two-phase model, based on capillary pressure saturation, was used to conduct numerical simulations. It was found that the double-layer GDL with different porosity in positive direction, one with lower porosity near the MPL and the other with higher porosity near the channel, and/or different hydrophobicity in negative direction, higher hydrophobicity near the MPL and higher hydrophilicity near the channel,

resulted in better water removal ability comparing to the single-layer GDL with uniform properties. The results suggested that liquid water saturation in GDLs can be further decreased by the proper arrangement of the double-layer GDLs.

The two-fluid model was widely applied in macroscopic models of PEFCs in considering liquid water transport in GDLs. In addition to the above mentioned approaches in liquid water transport in GDLs, full morphology models and pore-network models have also been used to investigate liquid water dynamics in GDLs [52].

Water transfer in flow channels

To investigate liquid water transport inflow channels, the VOF method has been usually applied [56, 57, 152, 153], especially when it comes to the possibility of tracking liquid waterfront [29, 108]. Although the VOF method offers the opportunity to capture the interface between gas and liquid phases, it should be kept in mind that the time step for general VOF simulations is in the range of 10^{-6} to 10^{-3} s. It is too computationally expensive to couple with other related transport phenomena in fuel cell simulations. Macroscopic two-phase models are usually coupled with water transfer in the GDLs and MEA to represent water transport in the whole cell. Considering the number of sets of governing equations, the two-phase models can be categorized as a multi-fluid model and a mixture model. Similar to the M2 model and two-fluid model in GDLs, the mixture model considers the multi/two-phase flow as a single-phase flow with mixture properties, whereas the multi-fluid model treats each phase separately.

Mixture model

Yuan et al. [154] developed a 3-D, multi-phase, steady-state PEFC model to investigate the effects of operating parameters, including operating pressure, fuel cell temperature, relative humidity (RH), and stoichiometric factor. This model treated the full cell as nine sub-layers: current collectors, flow channels, GDLs, CLs, and membranes. It was found that cell performance can be improved via higher operating pressure and temperature if both sides were reasonably humidified, as better liquid water removal and faster electrochemical reaction were achieved. Humidification of supplied gases was more important at the anode side, and the best performance was achieved by applying high hydrogen humidification and low air humidification. Increasing the air stoichiometric factor contributed to the elevation of water removal; however, too high values led to serious membrane dry out. Additionally, increasing inlet velocity resulted in a high-pressure drop.

A recent numerical study conducted by Kim et al. [155] was performed on a PEFC with complex flow-fields that was developed by Toyota Mirai. The design aimed to improve water management and mass transport and suggested the potential for robust and high-power stack performance. To

simulate such complex flow channels, a two-phase flow model was developed by considering Forchheimer's inertial effect. They found that Forchheimer's inertial effect contributed to better liquid water removal and improvement of interfacial water and mass transport. The results confirmed the substantial improvement of cell performance at high current density operating conditions and stability, therefore the applications of this kind of complex geometry were promising.

Multi-fluid model

Lin and Nguyen [156] carried out a 2-D, two-phase, steady-state, isothermal PEFC model. In this work, the authors aimed to investigate the effects that were related to ratios of widths of shoulders and channels on cell performance. They found that the cell performance increased via higher in-plane liquid water permeability of the GDLs and smaller shoulder width. The variation of in-plane electronic conductivity exhibited insignificant influence on cell performance, however, a smaller value resulted in highly nonuniform distribution of electronic current.

He et al. [157] introduced a two-fluid, two-phase model, where drag and lift forces between gas and liquid phase were considered with the Navier-Stokes equations, to investigate two-phase behavior in PEFCs. A simplified model was implemented to consider the liquid water droplet detachment diameter on the surface of GDL. It took into account the properties of the GDL/channel interface, including contact angle and surface tension. It was found that a higher contact angle for liquid water at the GDL/channel interface resulted in smaller detaching droplets and better water removal. Additional results related to surface tension showed that lower surface tension led to smaller detaching droplets. It can be proposed that higher contact angles and lower surface tensions were beneficial for better cell performance.

In the work of Sui et al. [158, 159], a 3-D, non-isothermal, two-phase PEFC model was developed and implemented into the software CFD-ACE. The authors aimed to illustrate physical features, transport, and species distribution along the flow channels by coupling the heat and mass transfer. A phenomenological model was also implemented for water transport in the membrane. The model was introduced in two parts. (i) A test case simulations were also performed and good agreement was achieved with an analytical solution. The results indicated that for unit cells with only parallel flow channels, the reduced dimensional model was a useful and easy tool for fuel cell design and optimization. (ii) The authors performed systematic experimental validation for this model, including various operating conditions, like current density, humidification, and coolant temperature. Values of model parameters, including the EOD coefficient, capillary diffusion coefficient, and catalyst specific area, were fitted via experimental data. It was found that the predicted net water flux from the anode side increased when anodic humidification water flow rate was increased. In this study, various adjustment methods were applied to improve the overall fit between

experimental data and simulation results.

Wu et al. [160] derived a 3-D model by coupling multi-species, multi-phase, electrochemical kinetics, and heat transfer processes, with a focus on non-equilibrium membrane water absorption/desorption, as well as non-equilibrium condensation/evaporation. This model was also capable of predicting transient phenomena in the cell. Three different water generation mechanisms were compared: vapor production, liquid production, and dissolved production. The results showed comparable deviations in non-equilibrium situations. The deviations were mitigated when the processes in the cell approached the equilibrium state. If the final equilibrium state was reached, cell performance was independent of the water generation mechanism. The transient simulations indicated that the cell response time was greatly prolonged if the water was produced in the vapor phase due to the slow condensation processes.

Kim and Kim [161] applied a 3-D, multi-phase, nonisothermal PEFC model to study the effects of inlet humidity on cell performance. Cases with different levels of inlet relative RH were simulated, which were randomly imposed at the inlets of anode and cathode sides. The ohmic and activation polarization were selected to represent the cell performance. It was found that the cell performance was mainly impacted by the ohmic resistance in low RH conditions. Excessive humidification for cathode inlets caused flooding problems in the cathode CL. Flow humidity can be controlled by adjusting the temperature at bi-polar plates. When the temperature of the bipolar plate was increased along the flow direction, concentration losses were decreased due to the lower liquid water saturation.

Xing et al. [162] provided a 2-D, two-phase, nonisothermal model for PEFCs. The water transfer between different phases, including vapor, liquid and dissolved, was considered. The liquid water effects, by applying traditional Butler-Volmer (BV), corrected BV, and agglomerate kinetics were numerically investigated. In addition, mathematical expressions of liquid water saturation and current density at both sides were statistically regressed. It was found that three mechanisms predicted reasonable current density compared with experimental data in low current density conditions. Under the high current density load, the current density predicted by the agglomerate kinetics method showed more accurate values compared with experimental data. The flooding issue, represented via the liquid water saturation, was observed to appear at the downstream of both anode and cathode channels. With the statistical regression, liquid water saturation at anode and cathode side was found to increase linearly at both low and high current density conditions, whereas exponential relation was found to be more accurate at medium current densities. This model was then applied in another study by Xing et al. [163] to investigate the effects of electrode properties and channel geometries on liquid water profile and cell performance. In addition, the parametric study was conducted to find out the optimal electrode

and channel designs. It was revealed that larger GDL thickness and channel depth resulted in a monotonic decrease of cell performance in a very large range of current density; in contrast, the contact angle and channel length showed negligible effects under low current density condition. The optimal length of the gas channel in this study was found to be 1 cm, in which maximum current density was obtained. A novel design of flow channel with multiple inlets and outlets were proposed to provide better water removal ability and cell performance. Further study was conducted by Xing et al. [164] to analyze the effects of RH, stoichiometric factor, channel length, and their interactive influence. It was found that higher anode RH contributed better cell performance. If anode RH was decreased and channel length was increased, the optimal RH at cathode also increased. By slightly increasing the stoichiometric factor, the limiting current density was also increased; however, further, increasing showed neglected effects. It was also indicated that convection was insignificant on the liquid water transport in the GDLs, which was dominated by the capillary diffusion.

Fan et al. [165] developed a 3-D, multiphase, nonisothermal numerical model for PEFCs to investigate the fuel cell performance and water management at low external humidification. In addition, the case with no external humidification at the anode side was studied and the effects of co-flow/counter-flow configurations on cell performance and water transport were discussed. It was indicated that external humidification was not necessary at high current densities. The water produced from the electrochemical reaction and transferred from the cathode side was sufficient to humidify the membrane. It was important to maintain cell performance at low current densities. In the case of no external humidification at the anode side, the water produced at the cathode side firstly transferred to the anode side and water moved back to the cathode side at the downstream of the flow channel. It was also found that water distribution was more uniform under a counter-flow configuration. Zhang and Jiao [166] developed a 3-D, multi-phase, nonisothermal PEFC model, which applied a Eulerian-Eulerian algorithm (except for temperature, which was shared by both phases) for two-phase flow phenomena. The authors analyzed the two-phase flow in the fuel cells with wave-like, serpentine and parallel flow-path configurations, under high current densities. It was found that neglecting water phase change resulted in much higher water vapor concentration in the cathode channel than the water vapor saturation concentration, especially at high inlet humidity. The generated liquid water due to condensation attached to both the GDL surface and sidewalls, the amount of which was minor considering the high gas velocity. The wave-like case showed better water removal capability compared to straight channels. The comparison of serpentine and parallel cases indicated that the serpentine flow channel contributed to higher cell performance.

The study by Wang et al. [167] considered numerically a novel cath-

ode flow channel design, by adding a sub-channel for parallel flow channels. Moist air was supplied from the main channel to maintain the humidity of the membrane, while dry air was supplied from sub-channel to improve water removal ability. Influence of sub-channel inlet location and flow rates on the distribution of reactants on liquid water saturation and cell performance were investigated with a 3-D, multi-phase, nonisothermal model. It was found that reactant distribution, liquid water removal, and cell performance were greatly affected by the sub-channel location and sub-channel flow rate. It was proposed that when the sub-channel inlet was located at 30% along the length of the flow channel, and the sub-channel flow rate was 70% of the total air inlet, the performance gained greatly compared with the conventional design without sub-channels.

Liquid water in gas channels is always treated as in the mist state to mitigate the computation requirement. During the past years, macroscopic models were developed and applied to investigate water management in gas channels, for example, inlet humidity, gas supply stoichiometric factor, operating temperature, operating pressure, novel channel designs, etc. The work reviewed in this part cannot cover all the relevant studies. Most of the previous studies did not account for the inter-phase reaction between the gas phase and the liquid phase. It was usually assumed that flow velocity was shared by liquid phase and gas phase or an algebraic slippery velocity was defined between the gas phase and liquid phase. From the work of Zhang and Jiao [166], which applied the Eulerian-Eulerian algorithm for two-phase flow, it can be seen that the velocity difference between gas and liquid phases existed, and may not be simply expressed by an algebraic relation. Under low humidification and/or low current density conditions, liquid water saturation was very low, in which case, many studies [168–170] assumed the liquid water in gas channels can be neglected or blown away, only single-phase flow was considered. Further simplifications [171–178] assumed that two phase flow can be neglected in both flow channels and porous electrodes.

1.6.4 LT-PEFC, homogeneous/stack modeling research

Similar to the HT-PEFC stacks, LT-PEFCs are also required to fulfill the industrial requirement. However, the situation is much more critical in a LT-PEFC stack than that of a HT-PEFC stack. The designs of the manifold, bipolar plates, cooling system are important issues related to the stack performance. Various numerical models and simulations have been performed during the past years.

Karimi et al. [179] conducted numerical investigations on a PEFC stack performance and optimization. The authors applied a flow network model to represent the pressure and molar flow rate distributions of fuel and gas in the stacks. In addition, a single cell model was used to evaluate the stack

performance, by means of cell voltage. Various inlet-outlet flow configurations were numerically simulated to examine reactants distributions in the stack, in which humidified fuel and air were supplied. It was found that the flow configuration, a double-inlet/single-outlet design, presented an optimal stack performance by decreasing compressor power requirement for reactant supplement and minimizing cell to cell voltage variations. The stack performance was sensitive to the size and number of flow channels on the bipolar plates. Park and Li [180] used the previous model to investigate the effects of flow variance and temperature distribution. They found temperature was a dominant factor for stack voltage variance when the flow variance was small enough to guarantee sufficiently uniform distributed reactant flow among the cells of the stack. By applying a larger manifold or smaller flow channel diameter, sufficient flow uniformity can be obtained. Temperature and flow distributions were important, a judicial matching of which can present uniform cell voltage distribution.

Zhang et al. [181] developed a 2-D, nonisothermal, multi-component CFD model for an air-breathing PEFC stack, which was fed with pressurized hydrogen and air provided by natural convection . It was observed that the optimal performance of the stack was achieved when a critical minimum clearance between the cell cartridges and the bottom substrate, and a minimum inter-cartridge spacing was satisfied. It was demonstrated that the model was viable for the air-breathing fuel cell in practical applications.

Wang [182] applied an analytical model to analyze the flow and pressure distribution in U-type arrangement fuel cell stacks. This model was based on mass and momentum conservation and considered wall friction and inertial effects. The analytical solution was given for the U-type stacks. It took both flow conditions and geometrical parameters into account. It was found that wall friction led to higher pressure drop and momentum effects contributed to a lower pressure drop. An optimal design with less non-uniformity pressure distribution can be obtained by properly balancing these two effects. This model was then applied to the Z-type arrangement fuel cell stack by the same author [183].

Le and Zhou [184] applied a previously developed, cell-level, 3-D, and multi-phase PEFC model to investigate liquid water transport phenomena and the presence of liquid water, as well as flooding in the gas channels and GDLs, in a 3-cell short stack. This model considered all of the major transport phenomena, including fluid dynamics, multi-component, heat transfer, phase change, and electrochemical reaction. The VOF method was also applied to track the liquid water dynamic behavior in the flow channels of the stack. It was found that the flooding cell contained lower reactant concentration compared to the cell without flooding. The overall stack performance was diminished if one cell was flooded since the mean current densities in each cell were identical.

Chernyavsky et al. [185] conducted numerical studies on the flow field of

a model distribution header manifold in a PEFC stack. The model headers included the inlet and outlet sections that were connected to a plate with a series of holes to represent unit cells. The large eddy simulation (LES) simulations were conducted to investigate the complex/turbulent flow under counter-flow configuration. In addition, corresponding experiments were conducted with Particle Image Velocimetry. It was found that the flow showed unsteady and highly turbulent nature in the header with a complex 3-D structure. The numerical simulations were confirmed by the experimental results. It was proposed that the pressure drop and effective cross-section area may be impacted by the flow structures.

The work done by Amirfazli et al. [186] described an analytical model, including two sub-models: coolant flow distribution model and thermal model, to investigate the coolant flow and temperature distributions in a water-cooled PEFC stack (65 unit cells). The coolant flow distribution model provided the coolant flow distribution in each unit cell. The thermal model considered the heat generation and coolant flow distribution in each cell to obtain temperature distribution in the stack. Two flow configurations: U-type and Z-type, were considered numerically and experimentally. It was found that the Z-type configuration contributed to more uniform temperature distribution compared to that of U-type configuration when the stack manifolds cross-section area was small. When the cross-section area was large, both configurations resulted in similar uniformity of temperature distributions. Smaller cross-section area led to a higher flow rate, which increased the parasitic losses; therefore, a balance between temperature distribution uniformity and parasitic losses were necessary.

Robin et al. [187] developed a 2-D + 1-D model to investigate heterogeneous distributions of parameters at the surface a cell, and the effects of operating condition on stack performance. The model was validated by the experiment measurements under three different inlet humidity: dry, half-hydrated, and full-hydrated, on a 6-cell stack. Local temperature and current density distributions were measured with an in-situ device. The measured current density distribution showed that three temperature hot spots were observed on the cell surface, where the coolant fluid had the lowest velocity. It was found that increasing the porosity of the first third of the MEA contributed to better stack performance if dry air was supplied. By varying the GDL properties, the performance can be optimized. Nandjou et al. [188] [189] then developed a pseudo-3D model to investigate heat and water transport, temperature, humidity, and current density heterogeneities, in a PEFC stack. This model treated the stack as a multi-layer system and each layer was discretized only in the in-plane direction to obtain the local heterogeneities of parameters. It was found that the Darcy-Forchheimer approach captured heterogeneous velocity distribution in different channels, with good agreements with the solutions from 3-D Navier-Stocks equations. The model was validated via experimental data on temperature and current

distributions. In the latter study, the model was applied on an automotive driving cycle test. The serpentine flow channels were used at both anode and cathode sides. The simulation results showed the impacts of BPP design on temperature and humidity distribution heterogeneities during the automotive cycle. It was also found that the maximum temperature in the membrane was much higher than nominal value under high current density conditions. Results indicated that the improvement of fuel cell load resulted in larger variation of temperature and humidity between the channel region and rib/land region. The water content in the stack was measured with a neutron imaging technique, which validated the simulation results on liquid water saturation.

1.7 Summary

In this chapter, several points are presented:

1. Motivation of the present study was described.
2. Research objectives were introduced.
3. The procedure and outline of this thesis were given.
4. Previous studies related to the present work were reviewed.

Numerical procedures offer alternative ways to understand physical processes in PEFCs. Meanwhile, CFD tools play important roles in performing the numerical simulations, especially with the increasing of computational power.

Chapter 2

Methodology

In the last chapter, previous modeling studies were reviewed. It can be seen that few studies concerned the two-phase interaction in the macroscopic two-phase models. Zhang and Jiao [166] was the most recent who applied a Eulerian-Eulerian algorithm in two-phase simulations of PEFCs. In the present study, the Eulerian-Eulerian algorithm is applied with the implementation of a phase change model, which considers the interface temperature that guarantees the heat balance and derives the mass transfer rate between each phase. The interface temperature is computed such that the latent heat due to the mass transfer through the interface is equal to the net rate that the heat is transferred to the interface, In addition, the drag, lift forces, and virtual mass can be taken into account. A multi-region technique, also seen in the work of Beale et al. [32], is applied to treat transport phenomena in different regions separately. A local time-stepping (LTS) [190] approach is used to obtain faster convergence in two-phase simulations. In addition, the electrochemical reaction is described by the Butler-Volmer or Tafel relation; species diffusion, water transfer in the membrane, heat transfer and charge transfer are also considered.

The fuel cell stack is a complex system. It is possible to apply the detailed numerical model to predict the transport phenomena in a LT-PEFC short stack. However, the simulations of larger stacks are still challenging. The flow in the manifold is very complicated [185], therefore, analytical models may not be able to qualitatively represent pressure drop and/or flow distribution. In the previously developed stack level models, liquid water presence is usually not taken into account. However, it is important for stack performance. In the present work, a pseudo-3-D stack model, which takes Eulerian-Eulerian two-phase model for two-phase flow in the manifold and unit cell flow channel regions, is developed based on a DRA [33][34] methodology. All of the physical processes are inherited from the cell level model, which considers all of the major transport phenomena, including heat and mass transfer, and electrochemical reaction. As much coarser grid

can be used, an easier and faster solution is possible.

The detailed and homogeneous HT-PEFC models are simplified versions of LT-PEFC models, except for two-phase flow. Water transfer in the membrane for LT-PEFC and HT-PEFC are described by slightly different mechanisms. In this chapter, the detailed (*model 2* and *model 4*, Fig. 1.1) and homogeneous (*model 3* and *model 5*, Fig. 1.1) PEFC models are described sequentially.

2.1 Detailed model

2.1.1 Computational domain

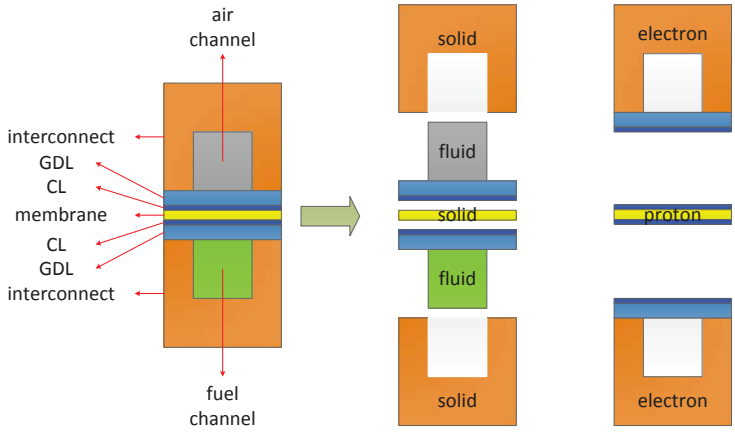

Figure 2.1: Computational domains: master domain and sub-domains

The schematic of the computation domains is shown in Fig. 2.1, on each of which corresponding transport process(es) take place. The master domain represents the whole full cell, in which the overall heat transfer is considered. The sub-domains can be categorized into three different types: solid, fluid, and electron-proton transfer regions (additional types of sub-domains are possible). In the present work, the solid part only provided the material properties, including thermal conductivity, density, and specific heat, for heat transfer. In the fluid region, the fluid flow, species transport, and/or heat transfer, depending on the flow type, are considered and solved. In

electron-proton transfer region, charge transfer is taken into account; dissolved water transfer (water transfer in the membrane) is only considered in the proton region. Transport phenomena in every sub-domains are coupled. All of the related transport phenomena are solved simultaneously. Further studies may be conducted on the cooling system (fluid) and stress analysis (solid).

2.1.2 Assumptions

In the present study, several assumptions are presumed in the model. They include:

1. The model is steady state.
2. The gas and liquid phases are in laminar flow regimes.
3. Liquid and gas phases are incompressible and gases follow the ideal gas law.
4. Fick's law will be used for two/multi-component species transfer.
5. The porous materials, including GDLs and CLs, are homogeneous and isotropic.
6. The membrane is only permeable to water. No gas cross over of gases is considered.
7. Produced water is in liquid form for LT-PEFCs and vapor form for HT-PEFCs.
8. Liquid water (if present) may be treated as if it is composed of spherical droplets.

2.1.3 Governing equations

Fluid region

Continuity and momentum equations

In the Eulerian-Eulerian two phase algorithm, phases are treated separately, with one phase as continuous phase and the other as dispersed. The Eulerian-Eulerian model, also called as two-fluid model or multi-fluid model, was introduced by Harlow and co-workers [191, 192], Spalding [193], Ishii and Hibiki [194], Rusche [195], and Marschall [196], etc., in detail. Based on the assumptions in the present study and reasonable averaging techniques, the conditionally averaged continuity and momentum equations are:

$$\frac{\partial \rho_\phi s_\phi}{\partial t} + \nabla \cdot (s_\phi \rho_\phi \mathbf{U}_\phi) = R_\phi \tag{2.1}$$

$$\frac{\partial \rho_\phi s_\phi \mathbf{U}_\phi}{\partial t} + \nabla \cdot (s_\phi \rho_\phi \mathbf{U}_\phi \mathbf{U}_\phi) + \nabla \cdot (s_\phi \tau^\phi) = -s_\phi \nabla p + s_\phi \rho_\phi \mathbf{g} + \mathbf{M}_\phi \quad (2.2)$$

where the subscript ϕ indicates each phase; s means the phase volume fraction, ρ is the mixture/pure phase density, $\mathbf{U}$ represents phase velocity, R means the mass source/sink term, p is the pressure shared by gas and liquid phases, and $\mathbf{g}$ is the gravity force. The term τ, combined Reynolds (turbulent) and viscous stress, can be expressed for laminar flow in present study as:

$$\tau^\phi = \mu_\phi \nabla \mathbf{U}_\phi \quad (2.3)$$

μ_ϕ is dynamic viscosity of phase ϕ and the term $\mathbf{M}_\phi$ represents the interaction between each phase, see Fig. 2.2, including interfacial drag force, lift force, virtual mass, etc.

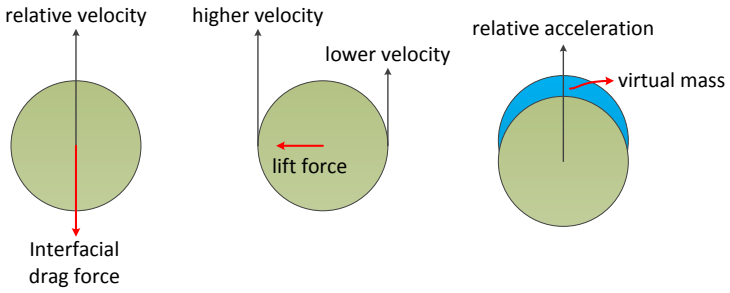

Figure 2.2: Interfacial momentum transfer: drag, lift, and virtual mass

$$\mathbf{M}_\phi = \frac{s_\phi}{V}(\mathbf{F}_\mathrm{d} + \mathbf{F}_\mathrm{l} + \mathbf{F}_\mathrm{vm}) \quad (2.4)$$

where V represents the volume of the droplets, $\mathbf{F}_\mathrm{d}$, $\mathbf{F}_\mathrm{l}$, and $\mathbf{F}_\mathrm{vm}$ are the drag force, lift force, and virtual mass. The drag force works only if relative velocity exists between phases:

$$\mathbf{F}_\mathrm{d} = \frac{1}{2}\rho_\phi A C_\mathrm{d} |\mathbf{U}_\mathrm{r}| \mathbf{U}_\mathrm{r} \quad (2.5)$$

where A is the projected area of water droplet, normal to the relative velocity, $\mathbf{U}_r$ is the relative velocity,

$$\mathbf{U}_r = \mathbf{U}_\phi - \mathbf{U}_\mathrm{other} \quad (2.6)$$

and C_d means the drag coefficient that can be obtained empirically and depends on the properties of droplets. The Schiller and Naumann drag model is usually used with the expression as:

$$C_d = \frac{24}{\mathrm{Re}}(1 + 0.15\mathrm{Re}^{0.687}) \tag{2.7}$$

where Re represents the particle Reynolds number based on the particle diameter d and relative velocity $\mathbf{U}_r$:

$$\mathrm{Re} = \frac{\mathbf{U}_r d}{\nu_\phi} \tag{2.8}$$

where ν_ϕ is the kinematic viscosity of phase ϕ.

The lift force term, $\mathbf{F}_\mathrm{l}$, has an expression as:

$$\mathbf{F}_\mathrm{l} = C_\mathrm{l}\rho_\phi V \mathbf{U}_\mathrm{r} \times (\nabla \times \mathbf{U}_\mathrm{r}) \tag{2.9}$$

where C_l represents the lift force coefficient, which is a function of droplet Reynolds number and Eötvös number:

$$\mathrm{Eo} = \frac{\rho_r g d^2}{\sigma} \tag{2.10}$$

where ρ_r is the relative density, $\rho_\phi - \rho_\mathrm{other}$, and σ is the surface tension coefficient.

And the virtual mass term, $\mathbf{F}_{vm}$, can be computed as:

$$\mathbf{F}_\mathrm{vm} = C_\mathrm{vm}\rho_\phi(\frac{D\mathbf{U}_\phi}{Dt} - \frac{D\mathbf{U}_\mathrm{other}}{Dt}) \tag{2.11}$$

where C_{vm} means the virtual mass coefficient, and

$$\frac{D}{Dt} = \frac{\partial}{\partial t} + \mathbf{U} \cdot \nabla \tag{2.12}$$

In the fuel cell, fluid needs to flow through the porous media before reaching the catalyst surface. In such a case, a Darcy modified Navier-Stokes equation is applied:

$$\frac{\partial \rho_\phi s_\phi \mathbf{U}_\phi}{\partial t} + \nabla\cdot(s_\phi\rho_\phi\mathbf{U}_\phi\mathbf{U}_\phi) + \nabla\cdot(s_\phi\mu_\phi\nabla\mathbf{U}_\phi) = -s_\phi\nabla p_\phi + s_\phi\rho_\phi\mathbf{g} + \mathbf{M}_\phi + s_\phi S_{\mathrm{Darcy},\,\phi} \tag{2.13}$$

Note: the porosity ϵ is removed from both left and right sides. where $S_{\mathrm{Darcy},\,\phi}$ is the Darcy term, which can be computed as:

$$S_{Darcy,\,\phi} = -\frac{s_\phi \mathbf{U}_\phi \mu_\phi}{K K_{\mathrm{r},\,\phi}} \tag{2.14}$$

where K is the absolute permeability, and $K_{\mathrm{r},\,\phi}$ represents the relative permeability. (NB: the velocity $\mathbf{U}_\phi$ in the porous media is superficial velocity.)

It should be noted that, in Eq. 2.13, the correlation for p_ϕ is expressed as:

$$p_\phi = \begin{cases} p_{\text{other}} & \text{in the channel} \\ p_{\text{other}} \pm p_c & \text{in the porous region} \end{cases} \tag{2.15}$$

where p_c is the capillary pressure that represents the pressure difference between gas phase and liquid phase in porous media.

Species transfer

Liquid phase in PEFCs is usually considered as pure water. The multi-component species transfer is solved in the gas phase, which can be described by:

$$\frac{\partial \rho_\phi s_\phi Y_\text{i}}{\partial t} + \nabla(s_\phi \rho_\phi \mathbf{U}_\phi Y_\text{i}) = \nabla \cdot (s_\phi \rho_\phi D_\text{i}^\text{eff} \nabla Y_\text{i}) + s_\phi R_\text{i} \tag{2.16}$$

where the subscript i indicates the species component, Y represents the mass fraction, R is the species mass source/sink term, and D^eff is the effective species diffusion coefficient.

A binary gas diffusion coefficient, can be calculated from the correlation of Fuller et al. [197] and Poling et al. [198]:

$$D_\text{ij} = \frac{10^{-7} T^{1.75} (1/M_\text{i} + 1/M_\text{j})^{1/2}}{p(V_\text{i}^{1/3} + V_\text{j}^{1/3})^2} \tag{2.17}$$

where the subscript i and j represent two different species, T is the gas phase temperature, V is the species diffusion volume with the unit of cm^3, M means the molar mass.

When it comes to the porous media, the diffusion coefficient is reduced from the open channel by a ratio of the porosity, ε, and the tortuosity factor, τ [199]. In addition, the binary diffusion and Knudsen diffusion coefficients are combined harmonically [200]:

$$D_\text{ij}^\text{eff} = s_\text{g}^\beta \frac{\varepsilon}{\tau} \left(\frac{1}{D_\text{ij}} + \frac{1}{D_{\text{kn, i}}}\right)^{-1} \tag{2.18}$$

where β is the power component, the Kundsen diffusion coefficient, $D_{\text{kn, i}}$, is expressed as:

$$D_{kn,i} = \frac{1}{3} d_\text{cl} < v_T >_i \tag{2.19}$$

where d_cl is the characteristic length of the pore domain, and $< v_T >$ represents the thermal molecular velocity of each species as:

$$< v_T >_\text{i} = \sqrt{\frac{8 R_g T}{\pi M_\text{i}}} \tag{2.20}$$

where R_g is the universal gas constant.

For multi-component gas mixture, the diffusion coefficient can be estimated from the individual binary coefficients or the effective binary diffusion coefficients in Wilkes approach [201]:

$$D_{\mathrm{i}} = (1 - X_{\mathrm{i}}) \left(\sum_{\mathrm{j} \neq \mathrm{i}} \frac{X_{\mathrm{j}}}{D_{\mathrm{ij}}^{\mathrm{eff}}} \right)^{-1} \tag{2.21}$$

where X is the molar fraction of each species, which can be computed as:

$$X_{\mathrm{i}} = \frac{Y_{\mathrm{i}}}{M_{\mathrm{i}}} \left(\sum_{\mathrm{i}} \frac{Y_{\mathrm{i}}}{M_{\mathrm{i}}} \right)^{-1} \tag{2.22}$$

Heat transfer

In the present solution algorithm, temperature is solved globally in the whole fuel cell domain. In case of two phase regime, the temperature of continuous phase is solved globally, whereas, heat transfer for the dispersed phase is computed in the specific sub-domain.

$$\frac{\partial s_\phi \rho_\phi h_\phi}{\partial t} + \nabla(s_\phi \rho_\phi \mathbf{U}_\phi h_\phi) = \nabla \cdot (s_\phi \chi_\phi^{\mathrm{eff}} \nabla h_\phi) + s_\phi Q_\phi \tag{2.23}$$

where h represents the enthalpy, χ^{eff} is the effective thermal diffusivity, and Q means the thermal heat source/sink, due to phase change, interface heat transfer, and/or electrochemical reaction.

Phase change

Considering the two phase flow in LT-PEFCs, water exists in both vapor and liquid phases, due to condensation and evaporation between water vapor and liquid water. As shown in Fig. 2.3, an interface is assumed between phase 1 (gas) and phase 2 (liquid). Due to phase change, there exists heat and mass transfer between these two phases, which happens at the phase interface.

From a physical point of view, the heat balance and mass balance must be guaranteed due to the conservation of heat and mass. The equations are as following:

$$\mathbf{j} = m''_{21} = -(\rho \mathbf{U} Y - \Gamma \nabla Y)_1 = (\rho \mathbf{U} Y - \Gamma \nabla Y)_2 \tag{2.24}$$

$$\mathbf{q}'' = m''_{21} h_{21} = -(\rho \mathbf{U} h - \chi \nabla h)_1 = (\rho \mathbf{U} h - \chi \nabla h)_2 \tag{2.25}$$

where Eq. 2.24 represents the mass balance between phase 1 and phase 2, and Eq. 2.25 means the heat balance. (NB: $\rho \mathbf{U} = m''$)

In order to obtain the heat transfer and mass transfer through the interface, the interface mass fraction or interface temperature should be prescribed.

Prescribe interface temperature

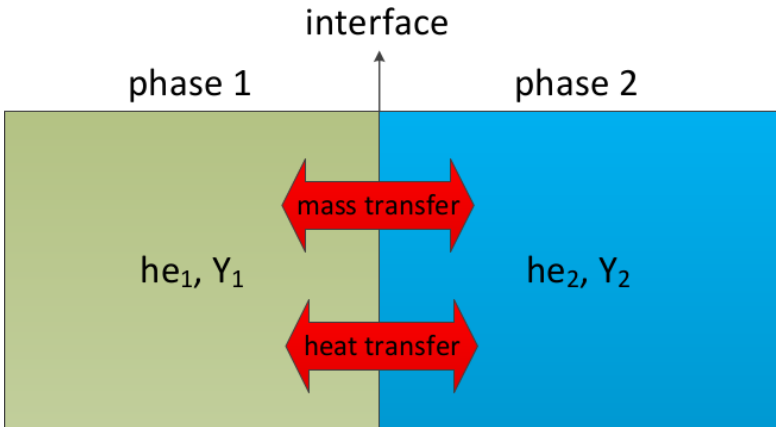

Figure 2.3: Interface between two phases, phase 1 and phase 2.

Prescribing the interfacial temperature, T_{int}, the interface mass fraction of the saturated species i can be obtained as:

$$Y_{\text{int, i}} = \frac{M_{\text{i}}}{M_{\text{mix}}} \frac{p_{\text{Sat}}(T_{\text{int}})}{p} \tag{2.26}$$

where $Y_{\text{int, i}}$ indicates the interface mass fraction of species i, M_{mix} represents the mixture molar mass, and p_{Sat} is the saturation pressure that is a function of temperature, which can be described by [202],

$$p_{\text{Sat}}(T) = 611.21 \exp\left(\left(18.678 - \frac{T}{234.5}\right)\left(\frac{T}{257.14 + T}\right)\right) \tag{2.27}$$

For other species without phase change, the interface mass fraction is computed as:

$$Y_{\text{int, j}} = \frac{1 - Y_{\text{int, i}}}{1 - Y_{\text{i}}} Y_{\text{j}} \tag{2.28}$$

where Y_{j} is the bulk mass fraction of species j.

The mass transfer can be expressed as:

$$m''_{21} = -(\rho \mathbf{U} Y - \Gamma \nabla Y)_1 \simeq m_{21} Y_{\text{int}} + \Gamma/\delta (Y_{\text{int}} - Y_1) \tag{2.29}$$

$$m''_{21} = \frac{\Gamma}{\delta} \frac{Y_1 - Y_{\text{int}}}{Y_{\text{int}} - 1} \tag{2.30}$$

where δ is the distance (the length between the finite volume center to the surface center).

From the heat balance,

$$(\rho \mathbf{U} h - \chi \nabla h)_2 + (\rho \mathbf{U} h - \chi \nabla h)_1 = 0 \tag{2.31}$$

a new expression can be obtained:

$$(\chi \nabla h)_2 + (\chi \nabla h)_1 = m''_{21} h_{21} \tag{2.32}$$

Then (central difference scheme):

$$\chi_2 \frac{h_{\text{int, 2}} - h_2}{\delta_2} + \chi_1 \frac{h_{\text{int, 1}} - h_1}{\delta_1} = m''_{21} h_{21} \tag{2.33}$$

or

$$k_2 \frac{T_{\text{int}} - T_2}{\delta_2} + k_1 \frac{T_{\text{int}} - T_1}{\delta_1} = m''_{21} h_{21} \tag{2.34}$$

where k represents the phase thermal conductivity.

In Eq. 2.34, all of the values, except T_{int} is prescribed, are known. Therefore, T_{int} can be solved based on Newton's method in iteration: (NB: m''_{21} is a function of T_{int}, see Eqs. 2.26 and 2.30).

$$T_{\text{int}}^{n+1} = T_{\text{int}}^{n} - \frac{k_2 \frac{T_{\text{int}}^n - T_2}{\delta_2} + k_1 \frac{T_{\text{int}}^n}{\delta_1 - T_1} - m''_{21} h_{21}}{\frac{k_2}{\delta_2} + \frac{k_1}{\delta_1} - \frac{d(m''_{21})}{dT_{\text{int}}}|_{T_{\text{int}}^n} h_{21}} \tag{2.35}$$

where n represents the iteration step.

Prescribe interfacial mass fraction

Prescribing the saturated species mass fraction at the interface, $Y_{\text{int, i}}$, the saturation pressure can be obtained by inverting Eq. 2.26:

$$p_{\text{Sat}} = \frac{Y_{\text{int, i}} M_{\text{mix}}}{M_{\text{i}}} p \tag{2.36}$$

As $pSat$ is a function of temperature, the interface temperature T_{int} can be computed by inverting this function:

$$T_{\text{int}} = T^{-1}(p_{\text{Sat}}) \tag{2.37}$$

The mass flux can be easily obtained from Eqs. 2.33 and 2.34, as:

$$m''_{21} = \frac{\chi_2}{\delta_2} \frac{h_{\text{int, 2}} - h_2}{h_2 - h_1} + \frac{\chi_1}{\delta_1} \frac{h_{\text{int, 1}} - h_1}{h_2 - h_1} \tag{2.38}$$

or

$$m''_{21} = \frac{k_2}{\delta_2} \frac{T_{\text{int, 2}} - T_2}{h_2 - h_1} + \frac{k_1}{\delta_1} \frac{T_{\text{int, 1}} - T_1}{h_2 - h_1} \tag{2.39}$$

In such case, the mass balance is taken into account from Eq. 2.24:

$$(\rho \mathbf{U} Y - \Gamma \nabla Y)_1 + (\rho \mathbf{U} Y - \Gamma \nabla Y)_2 = 0 \tag{2.40}$$

and

$$\frac{\Gamma_1}{\delta_1}(Y_{\text{int}} - Y_1) + \frac{\Gamma_2}{\delta_2}(Y_{\text{int}} - Y_2) = 0 \tag{2.41}$$

Therefore, the interfacial species mass fraction Y_{int} can be easily solved as:

$$Y_{\text{int}} = \frac{\frac{\Gamma_1}{\delta_1}Y_1 + \frac{\Gamma_2}{\delta_2}Y_2}{\frac{\Gamma_1}{\delta_1} + \frac{\Gamma_2}{\delta_2}} \tag{2.42}$$

The overall heat and mass transfer during phase change can be computed after Y_{int} and T_{int} are obtained. The mass and heat source/sink terms due to phase change are:

$$R_{\text{i}} = \rho C_K D(Y_{\text{int}} - Y_{\text{i}}) \tag{2.43}$$

and

$$Q_\phi = R_{\text{i}} h e_\phi \tag{2.44}$$

where C_K represents the mass transfer coefficient, and D is the mass transfer diffusivity. If the Lewis number, Le, defined as the ratio of thermal diffusivity to mass diffusivity, is known, then,

$$D = \frac{\chi}{\text{Le}} \tag{2.45}$$

Single phase flow

In case of single phase flow, the governing equations are reduced by neglecting the interfacial momentum transfer, heat transfer and phase change. Only governing equations for gas or liquid phase need considering. In addition, the phase volume fractions, s_ϕ, in Eqs. 2.1 ,2.13, and 2.16 are always 1.

Electron-proton transfer regions

In electron-proton transfer regions, charge transfers are considered, in which electron transfers in BPPs, GDLs and CLs and proton transfers in the membrane/electrolyte phase. Water in the membrane exists in dissolved phase.

Electron and proton transfer

The governing equations for electron and proton are:

$$\nabla \cdot (\sigma_{\text{E}} \varphi_{\text{E}}) = J_{\text{E}} \tag{2.46}$$

$$\nabla \cdot (\sigma_{\text{P}} \varphi_{\text{P}}) = J_{\text{P}} \tag{2.47}$$

where the subscripts E and P represent electron and proton, respectively, φ is potential, σ is the electric conductivity, and J is the source/sink term due to electrochemical reaction. The proton conductivity of membrane can be calculated:

$$\sigma_{\mathrm{P}} = \begin{cases} (0.514\lambda - 0.326)\exp(1268.(\frac{1}{303} - \frac{1}{T})) & 1 \leq \lambda \\ 0.1879\lambda\exp(1268.(\frac{1}{303} - \frac{1}{T})) & other \end{cases} \tag{2.48}$$

where λ is the water content in the membrane/electrolyte (Eq. 2.57).

Considering the CL at the cathode side, the electrochemical reaction is ORR. The electrochemical reaction is described via Butler-Volmer relation as:

$$j_{\mathrm{ca}} = i_{\mathrm{ca},\,0}(1-s)^{\beta}\prod_{i}\left(\frac{C_{\mathrm{i}}}{C_{\mathrm{ref}}}\right)^{\gamma}\left[\exp(\frac{-\alpha_{\mathrm{ca}}zF\eta_{\mathrm{ca}}}{R_gT}) - \exp(\frac{(1-\alpha_{\mathrm{ca}})zF\eta_{\mathrm{ca}}}{R_gT})\right] \tag{2.49}$$

where $i_{\mathrm{ca},\,0}$ is the exchange current density, s represents the liquid water saturation, z is the number of electrons transfer, F is Faraday's constant, C_{i} means the reactants concentration, C_{ref} is the corresponding reference concentration (inlet species concentration), α_{ca} is the transfer coefficient, β is the power exponent, γ is the reaction order, and η_c is the activation overpotential that are computed as:

$$\eta_c = \varphi_E - \varphi_P - E_{\mathrm{Nernst,\,ca}} \tag{2.50}$$

where $E_{\mathrm{Nernst,\,ca}}$ is the Nernst potential that has the expression of:

$$E_{\mathrm{Nernst,\,ca}} = \sum_{\mathrm{i}}\frac{-G_{\mathrm{i}}\omega - R_gT\ln p_{\mathrm{i}}^{\omega}}{zF} = \sum_{\mathrm{i}}\frac{-(H_{\mathrm{i}} - T\,S_{\mathrm{i}})\omega - R_gT\ln p_{\mathrm{i}}^{\omega}}{zF} \tag{2.51}$$

where G is Gibbs free energy of a species, p_{i} represents the partial pressure of species i, H is the enthalpy, S here means the entropy, and ω represents the consumption (negative) and production (positive) mass corresponding to the transfer of z electrons. For example, 0.5 O_2 is consumed, and 1 H_2O is produced with 2 e^- transfer during the reaction, $\omega = -0.5$ for oxygen, $\omega = 1$ for water and $z = 2$.

The source/sink terms result from the electrochemical reaction at cathode side can be calculated as:

$$J_{\mathrm{E}} = -j_{\mathrm{ca}} \tag{2.52}$$

and

$$J_{\mathrm{P}} = j_{\mathrm{ca}} \tag{2.53}$$

Similarly, the electrochemical reaction at anode CL is HOR, the reaction rate of which can be obtained by:

$$j_{\text{an}} = i_{\text{an, 0}}(1-s)^{\beta}\prod_{\text{i}}\left(\frac{C_{\text{i}}}{C_{\text{ref}}}\right)^{\gamma}\left[\exp(\frac{\alpha_{\text{an}}zF\eta_{\text{an}}}{R_gT}) - \exp(-\frac{(1-\alpha_{\text{an}})zF\eta_{\text{an}}}{R_gT})\right] \tag{2.54}$$

The activation overpotential and Nernst potential at anode side share the same formulations with Eqs. 2.50 and 2.51:

The source/sink terms due to the electrochemical reaction at anode side are as following:

$$J_{\text{E}} = j_{\text{an}} \tag{2.55}$$

and

$$J_{\text{P}} = -j_{\text{an}} \tag{2.56}$$

Water transfer through membrane

As described in Chapter 1, three mechanisms of water transfer in the membrane exist, including diffusion, EOD and hydraulic permeation. Usually, diffusion and EOD are considered in PEFCs since the hydraulic permeability coefficient is usually very small. A non-equilibrium form of water transfer in membrane can be written as:

$$\frac{\rho_{\text{m}}}{\text{EW}}\frac{\partial\lambda}{\partial t} + \nabla(\frac{\mathbf{i}_{\text{P}}}{F}n_d) = \frac{\rho_{\text{m}}}{\text{EW}}\nabla\cdot(D_{\text{m}}^{\text{eff}}\nabla\lambda) + R_{\lambda} \tag{2.57}$$

where ρ_{m} means membrane density, EW is the equivalent weight, λ represents the water content, $\mathbf{i}_{\text{P}}$ is the proton current density, n_d is the EOD coefficient, D_{m}^{eff} means water diffusion coefficient in the membrane, and R_{λ} is the source/sink for water desorption/adsorption.

The computation of water desorption and adsorption source/sink terms can be found in Eq. 1.29.

Master domain

Heat transfer is solved globally in the whole full cell. The governing equation is written as:

$$\frac{\partial\rho CpT}{\partial t} + \rho Cp\mathbf{U}\cdot\nabla T = \nabla\cdot(k^{\text{eff}}\nabla T) + Q \tag{2.58}$$

where Cp means the specific heat, k^{eff} is the effective thermal conductivity, Q represents the heat source/sinks from all sub-regions, and $\mathbf{U}$ is the velocity that is always zero in solid regions.

The effective thermal conductivity in porous media is calculated as,

$$k^{\text{eff}} = \varepsilon s_{\text{l}}k_{\text{l}} + \varepsilon s_{\text{g}}k_{\text{g}} + (1-\varepsilon)k_{\text{solid}} \tag{2.59}$$

Source/sink terms

The source/sink terms concerning mass, charger, and heat transfer in the master domain and sub-domains are summarized in Table 2.1. These terms are presented for the general two phase flow condition. In single phase case, the formulations of source/sink terms vary slightly, which are listed in Table 2.2. The electron and proton transfers are not affected by the flow types.

Table 2.1: Source/sink terms: two phase flow, detailed model

Regions	Description	Calculation	Units
Fluid	R_{i} (Eq. 2.16)	$\begin{cases} \frac{j\omega M_{\mathrm{i}}}{zF} & \text{CLs} \\ 0 & \text{other} \end{cases}$	$\mathrm{kg\,m^{-3}\,s^{-1}}$
	$R_{\mathrm{H_2O}}$ (Eq. 2.16)	R_{ce}	$\mathrm{kg\,m^{-3}\,s^{-1}}$
	R_{gas} Eq. 2.1	$\sum_{\mathrm{i}} R_{\mathrm{i}}$	$\mathrm{kg\,m^{-3}\,s^{-1}}$
	R_{liquid} Eq. 2.1	$\begin{cases} \frac{j\omega M_{\mathrm{H_2O}}}{zF} - R_\lambda - R_{\mathrm{ce}} & \text{CLs} \\ -R_{\mathrm{ce}} & \text{other} \end{cases}$	$\mathrm{kg\,m^{-3}\,s^{-1}}$
	Q_q Eq. 2.23	$Q_{\mathrm{ce,\,d}}$	$\mathrm{W\,m^{-3}}$
Electron-proton	J_{E} Eq. 2.46	$\begin{cases} j_{\mathrm{an}}\,, -j_{\mathrm{ca}} & \text{CLs} \\ 0 & \text{other} \end{cases}$	$\mathrm{A\,m^{-3}}$
	J_{P} Eq. 2.47	$\begin{cases} -j_{\mathrm{an}}\,, j_{\mathrm{ca}} & \text{CLs} \\ 0 & \text{other} \end{cases}$	$\mathrm{A\,m^{-3}}$
	R_λ Eq. 2.57	$\begin{cases} \text{Eq. 1.29} & \text{CLs} \\ 0 & \text{other} \end{cases}$	$\mathrm{kg\,mol^{-1}\,s^{-1}}$
Solid	Q	0	$\mathrm{W\,m^{-3}}$
Master	Q Eq. 2.58	$\begin{cases} \frac{i_{\mathrm{E}}^2}{\sigma_{\mathrm{E}}} & \text{BPPs} \\ -Q_{\mathrm{ce,\,d}} & \text{channels} \\ \frac{i_{\mathrm{E}}^2}{\sigma_{\mathrm{E}}} - Q_{\mathrm{ce,\,d}} & \text{GDLs} \\ j(\eta - \frac{\Delta ST}{zF}) + \frac{i_{\mathrm{E}}^2}{\sigma_{\mathrm{E}}} + \frac{i_{\mathrm{P}}^2}{\sigma_{\mathrm{P}}} - Q_{\mathrm{ce,\,d}} & \text{CLs} \\ \frac{i_{\mathrm{P}}^2}{\sigma_{\mathrm{P}}} & \text{membrane} \end{cases}$	$\mathrm{W\,m^{-3}}$

2.2 Homogeneous model

The homogeneous model is derived from the detailed model in the previous section based on the DRA method [33, 34]. The variations of numerous

Table 2.2: Source/sink terms: single phase flow, detailed model

Regions	Description	Calculation	Units
Fluid	R_{i} Eq. 2.16	$\begin{cases} \frac{j\omega M_{\mathrm{i}}}{zF} & \text{CLs} \\ 0 & \text{other} \end{cases}$	$\mathrm{kg\,m^{-3}\,s^{-1}}$
	$R_{\mathrm{H_2O}}$ Eq. 2.16	$\begin{cases} \frac{j\omega M_{\mathrm{H_2O}}}{zF} - R_\lambda & \text{CLs} \\ 0 & \text{other} \end{cases}$	$\mathrm{kg\,m^{-3}\,s^{-1}}$
	R_{gas} Eq. 2.1	$\sum_{\mathrm{i}} R_{\mathrm{i}}$	$\mathrm{kg\,m^{-3}\,s^{-1}}$
Electron-proton	J_{E} Eq. 2.46	$\begin{cases} j_{\mathrm{an}}\,, -j_{\mathrm{ca}} & \text{CLs} \\ 0 & \text{other} \end{cases}$	$\mathrm{A\,m^{-3}}$
	J_{P} Eq. 2.47	$\begin{cases} -j_{\mathrm{an}}\,, j_{\mathrm{ca}} & \text{CLs} \\ 0 & \text{other} \end{cases}$	$\mathrm{A\,m^{-3}}$
	R_λ Eq. 2.57	$\begin{cases} \text{Eq. 1.29} & \text{CLs} \\ 0 & \text{other} \end{cases}$	$\mathrm{kg\,mol^{-1}\,s^{-1}}$
Solid	Q	0	$\mathrm{W\,m^{-3}}$
Master	Q Eq. 2.58	$\begin{cases} \frac{i_{\mathrm{E}}^2}{\sigma_{\mathrm{E}}} & \text{BPPs} \\ \frac{i_{\mathrm{E}}^2}{\sigma_{\mathrm{E}}} & \text{GDLs} \\ j(\eta - \frac{\Delta ST}{zF}) + \frac{i_{\mathrm{E}}^2}{\sigma_{\mathrm{E}}} + \frac{i_{\mathrm{P}}^2}{\sigma_{\mathrm{P}}} & \text{CLs} \\ \frac{i_{\mathrm{P}}^2}{\sigma_{\mathrm{P}}} & \text{membrane} \end{cases}$	$\mathrm{W\,m^{-3}}$

variable in the through-plane direction of each unit cell are averaged, while those in the in-plane direction are resolved.

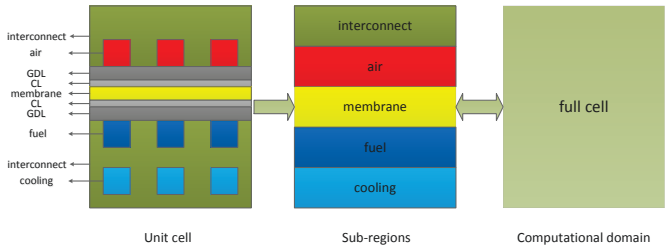

Figure 2.4: Schematic of a fuel cell and computational domain applied in the homogeneous model (manifolds are not shown).

2.2.1 Assumptions

In developing the model, the following assumptions are presumed.

1. The model is steady state.
2. The gas and liquid phases are in laminar flow regimes.
3. The liquid and gas phases are incompressible and the gas phase obeys the ideal gas law.
4. Fick's law will be used for two/multi-component species transfer.
5. The porous materials, including GDLs and CLs, are homogeneous and isotropic.
6. The membrane is only permeable to water. No gas cross over of gases is considered.
7. Produced water is in liquid phase for LT-PEFCs and in vapor form for HT-PEFCs.
8. Liquid water exists in spherical droplets.
9. Flow in flow channels can be described via Darcy's law.
10. Parameter variations in the through direction of a unit cell are negligible.

2.2.2 Governing equations

Following the principle of DRA [33, 34], the unit cell can be simplified as shown in Fig. 2.4. The computational domain is shared by various sub-regions via a multi-shared space (MUSES) method. The MUSES method allows for simultaneous consideration of concentration, heat and momentum equations for various 'region' occupying the 'same' physical space. Similarly to the cell level model, the sub-regions can be categorized into three different types: fluid, solid, and electrolyte. The difference in the homogeneous model is that the heat transfer is solved in specific sub-regions, instead of globally. The fluid region accounts for the species, heat and momentum solutions, including air, fuel, and cooling. The solid region only considers heat transfer, including interconnect. The electrolyte region addresses electrochemical reaction, species transfer through the GDLs and MEA, and heat transfer.

Fluid region

Based on previous work [33, 34, 203], fluid flow in flow channels of unit cell may be described in Darcy's form. Taking the porous properties, porosity, r, and tortuosity, τ, into consideration, the continuity and momentum equations are as following:

$$\nabla(s_\phi \rho_\phi \mathbf{U}_\phi) = r R_\phi \tag{2.60}$$

$$\begin{aligned} &\frac{\partial \rho_\phi s_\phi \mathbf{U}_\phi}{\partial t} + \nabla \cdot (s_\phi \rho_\phi \frac{\mathbf{U}_\phi \mathbf{U}_\phi}{r}) = \\ &-\frac{r s_\phi}{\tau^2}\nabla p + \frac{r s_\phi \rho_\phi}{\tau}\mathbf{g} + \nabla \cdot (\frac{s_\phi \mu_\phi}{\tau^2}\nabla \mathbf{U}_\phi) + \frac{r\mathbf{M}_\phi}{\tau} + s_\phi r \mathbf{F}_D \end{aligned} \tag{2.61}$$

where $\mathbf{U}$ is the superficial velocity, $\mathbf{U} = r\mathbf{u}_c/\tau$, $\mathbf{u}_c$ is the capillary velocity, $\mathbf{F}_D$ is the distributed resistance drag term. NOTE: $\varepsilon = 1$ and $\tau = 1$ in the manifolds, and the interfacial momentum transfer term, $\mathbf{M}_\phi$, can be negligible compared with the drag term, $\mathbf{F}_D$.

To consider the pressure drop, the rectangular flow duct covered with the GDL is assumed to be a full rectangular channel, therefore, the pressure drop can be written as, The pressure drop in a rectangular flow channel [1] gives,

$$\frac{dp}{dx} = \frac{2}{D_h^2} f Re_h \mu \mathbf{U} \tag{2.62}$$

[1] The effects of gases by-pass through the GDLs on pressure drop are small, with approximate 1% differences. Therefore, the rectangular flow duct is treated as a full channel.

where D_h is the hydraulic diameter of the rectangular channel, f is the Fanning friction factor, and Re_h represents the Reynolds number based on D_h, which can be calculated as,

$$D_h = \frac{2ab}{a+b} \tag{2.63}$$

where a the cross-section width and b is the height.

The drag term can be obtained via:

$$\mathbf{F}_D = -\frac{r\mu\mathbf{U}}{\tau^2 K} \tag{2.64}$$

where K is the permeability in the volume averaged gas channels, similar to the permeability in GDLs, and it reads,

$$K = \frac{D_h^2}{2fRe_h} \tag{2.65}$$

The continuity and momentum equations can also be expressed by means of interstitial velocity, $\mathbf{u} = \mathbf{u}_c/\tau$,

$$\nabla(s_\phi \rho_\phi \mathbf{u}_\phi) = R_\phi \tag{2.66}$$

$$\begin{aligned} &\frac{\partial \rho_\phi \alpha_\phi \mathbf{u}_\phi}{\partial t} + \nabla \cdot (\alpha_\phi \rho_\phi \mathbf{u}_\phi \mathbf{u}_\phi) = \\ &-\frac{s_\phi}{\tau^2}\nabla p + \frac{s_\phi \rho_\phi}{\tau}\mathbf{g} + \nabla \cdot (\frac{s_\phi \mu_\phi}{\tau^2}\nabla \mathbf{u}_\phi) + \frac{\mathbf{M}_\phi}{\tau} + s_\phi \mathbf{F}_D \end{aligned} \tag{2.67}$$

It is assumed that the liquid phase in LT-PEFC gas channels exists in mist state (spherical droplets). The drag force on liquid phase due to wall friction can be assumed being negligible compared to the interfacial drag force from gas phase. On the other hand, the wall friction drag force applied on the gas phase is dominated compared to the interfacial drag from liquid phase. Therefore, the momentum transfer equation for gas phase is finally solved in the Darcy's formulation ($\mathbf{M}_\phi$ is neglected), whereas, the momentum transfer equation for liquid phase is solved in the Navier-Stokes form ($\mathbf{F}_D$ is neglected).

For the species transfer, the governing equation is written as:

$$\frac{\partial r \rho_\phi s_\phi Y_\mathrm{i}}{\partial t} + \nabla(s_\phi \rho_\phi \mathbf{U}_\phi Y_\mathrm{i}) = \nabla \cdot (s_\phi \rho_\phi \frac{r}{\tau^2} D_\mathrm{i} \nabla Y_\mathrm{i}) + s_\phi r R_\mathrm{i} \tag{2.68}$$

or

$$\frac{\partial r \rho_\phi s_\phi Y_\mathrm{i}}{\partial t} + \nabla(r s_\phi \rho_\phi \mathbf{u}_\phi Y_\mathrm{i}) = \nabla \cdot (s_\phi \rho_\phi \frac{r}{\tau^2} D_\mathrm{i} \nabla Y_\mathrm{i}) + r s_\phi R_\mathrm{i} \tag{2.69}$$

where D_{i} is the diffusion coefficient, which is a tensor depending on the flow direction. The diffusion coefficient calculated in the homogeneous model is the same as that in the detailed model. However, the diffusion coefficient here is only computed in void space, e.g. flow channels.

For heat transfer, the equations are solved separately for gas phase and liquid phase. The general heat transfer equation is described as:

$$\frac{\partial r s_\phi \rho_\phi h e_\phi}{\partial t} + \nabla(s_\phi \rho_\phi \mathbf{U}_\phi h e_\phi) = \nabla\cdot(s_\phi \frac{r}{\tau^2}\chi_\phi \nabla h e_\phi) + r s_\phi^2 \sum_{\mathrm{NB}} \kappa(T_{\mathrm{NB}} - T_{\mathrm{int}}) + r s_\phi Q_{\mathrm{he},\,\phi} \tag{2.70}$$

or

$$\frac{\partial r s_\phi s_\phi h e_\phi}{\partial t} + \nabla(s_\phi r \rho_\phi \mathbf{u}_\phi h e_\phi) = \nabla\cdot(s_\phi \frac{r}{\tau^2}\chi_\phi \nabla h e_\phi) + r s_\phi^2 \sum_{\mathrm{NB}} \kappa(T_{\mathrm{NB}} - T_{\mathrm{int}}) + r s_\phi Q_{\mathrm{he},\,\phi} \tag{2.71}$$

where the subscript NB means the neighbor regions, χ_ϕ is the heat transfer coefficient, which is a tensor depending on the flow direction, κ represents the inter-phase heat transfer coefficient (heat transfer between contacted sub-regions), T_{int} means the interface temperature between two phases, or a mean value of two phase temperatures (for single phase flow, it equals to the phase temperature).

The inter-phase heat transfer coefficient is calculated via:

$$\kappa V = UA \tag{2.72}$$

where V is the volume of the region, A represents the contacted area, and U means the overall heat transfer coefficient. In the work of Nishida et al. [34], an harmonic averaging method can be applied to represent the overall heat transfer coefficient,

$$\frac{1}{U} = \frac{1}{h^*} + \sum_{\mathrm{j}} \frac{L_{\mathrm{j}}}{k_{\mathrm{j}} S_f} \tag{2.73}$$

where k represents the thermal conductivity, S_f is the conduction shape factor, and h^* represents the convective heat transfer coefficient,

$$h^* = \frac{\mathrm{Nu} k_f}{D_h} \tag{2.74}$$

where Nu is the Nusselt number, k_f represents the thermal conductivity of fluid, and D_h is the hydraulic diameter of flow channels.

For the inter-phase heat transfer, it is assumed that heat transfer from other regions to phase ϕ is related to its volume fraction. To make it simple, the amount of heat transfer equals the total heat transfer multiplied by the phase saturation s_ϕ, which is $s_\phi \sum_{\mathrm{NB}} \kappa(T_{\mathrm{NB}} - T_{\mathrm{int}})$.

The phase change model applied in the gas channels is the same as that was introduced in the detailed model.

Single phase flow

For single phase flow, only one set of governing equations are solved. The interfacial heat and mass transfer, phase change are excluded. In addition, the phase saturation for the concerning phase is always 1.

Solid region

In the homogeneous model, only heat transfer needs to be considered, which is described via:

$$\frac{\partial \rho h}{\partial t} = \nabla \cdot (\chi \nabla h) + \sum_{\mathrm{NB}} \kappa (T_{\mathrm{NB}} - T) + Q \tag{2.75}$$

where T is the temperature of the present region. The calculation of heat transfer coefficient κ is obtained via Eqs. 2.72, 2.73, and 2.74.

Electrolyte region

The electrolyte region in the present model represents the MEA, including the CLs and membrane. The CLs are presumed to be ultra-thin, the electrochemical reactions therefore happen on surfaces. The electrochemical reactions at both sides can be described by a Butler-Volmer relation relation, which is same as in the detailed model, see Eqs. 2.49 and 2.54,

$$j_{\mathrm{ca}} = i_{\mathrm{ca},\,0}(1-s)^{\beta} \prod_{\mathrm{i}} \left(\frac{C_{\mathrm{i}}}{C_{\mathrm{ref}}} \right)^{\gamma} \left[\exp(\frac{-\alpha_{\mathrm{ca}} z F \eta_{\mathrm{ca}}}{R_g T}) - \exp(\frac{(1-\alpha_{\mathrm{ca}}) z F \eta_{\mathrm{ca}}}{R_g T}) \right] \tag{2.76}$$

and

$$j_{\mathrm{an}} = i_{\mathrm{an},\,0}(1-s)^{\beta} \prod_{\mathrm{i}} \left(\frac{C_{\mathrm{i}}}{C_{ref}} \right)^{\gamma} \left[\exp(\frac{\alpha_{\mathrm{an}} z F \eta_{\mathrm{an}}}{R_g T}) - \exp(-\frac{(1-\alpha_{\mathrm{an}}) z F \eta_{\mathrm{an}}}{R_g T}) \right] \tag{2.77}$$

where $i_{\mathrm{ca},\,0}$, $i_{\mathrm{an},\,0}$, j_{ca}, and j_{an} are cathode exchange current density, anode exchange current density, cathode current density, and anode current density, respectively, all of which have the unit of $\mathrm{A\,cm^{-2}}$.

The Nernst potential, E_{Nernst}, for both sides are calculated as in Eq. 2.51.

The overall voltage output can be obtained via a Kirchhof-Ohm relation as:

$$V = E_{\mathrm{Nernst}} - \eta_{\mathrm{an}} - \eta_{\mathrm{ca}} - \Omega j \tag{2.78}$$

where V is the cell voltage, Ω represents the overall ohmic resistance, including the ohmic resistance in membrane, GDLs, and BPPs. The proton conductivity, which is inversely related to the ohmic resistance, is a function of membrane water content, λ, which can be obtained from Eq. 2.48. The ohmic resistance in the MEA is calculated as:

$$\Omega_{\mathrm{m}} = \sum_{\mathrm{i}} \frac{L_{\mathrm{i}}}{\zeta_{\mathrm{i}} \sigma_{\mathrm{i}}} \tag{2.79}$$

where L represents the thickness of each component in the MEA, and ζ is a fitting parameter that is usually 1 in the membrane and larger than 1 in the CLs.

From Eqs. 2.76, 2.77, and 2.78, the current density may be calculated as following. Define a function,

$$g(\eta) = E_{\mathrm{Nernst}} - \eta_{\mathrm{an}} - \eta_{\mathrm{ca}} - \Omega j - V \tag{2.80}$$

Therefore, Eq. 2.80 at anode and cathode sides can be written as,

$$g(\eta_{\mathrm{an}}) = E_{\mathrm{Nernst}} - \eta_{\mathrm{an}} - \eta_{\mathrm{ca}} - \Omega j_{\mathrm{an}} - V \tag{2.81}$$

$$g(\eta_{\mathrm{ca}}) = E_{\mathrm{Nernst}} - \eta_{\mathrm{an}} - \eta_{\mathrm{ca}} - \Omega j_{\mathrm{ca}} - V \tag{2.82}$$

The activation overpotential at both side should guarantee that both Eqs. 2.81 and 2.82 are smaller than residual values e.g. 1.0×10^{-6}. Newton's method can be applied to solve η_{an} and η_{ca},

$$\begin{aligned} \eta_{\mathrm{an}}^{n+1} &= \eta_{\mathrm{an}}^{n} - \frac{g(\eta_{\mathrm{an}})}{g(\eta_{\mathrm{an}})'} \\ &= \eta_{\mathrm{an}}^{n} - \frac{E_{\mathrm{Nernst}} - \eta_{\mathrm{an}} - \eta_{\mathrm{ca}} - \Omega j_{\mathrm{an}} - V}{-1 - \Omega j'_{\mathrm{an}}} \end{aligned} \tag{2.83}$$

$$\begin{aligned} \eta_{\mathrm{ca}}^{n+1} &= \eta_{\mathrm{ca}}^{n} - \frac{g(\eta_{\mathrm{ca}})}{g(\eta_{\mathrm{ca}})'} \\ &= \eta_{\mathrm{ca}}^{n} - \frac{E_{\mathrm{Nernst}} - \eta_{\mathrm{an}} - \eta_{\mathrm{ca}} - \Omega j_{\mathrm{ca}} - V}{-1 - \Omega j'_{\mathrm{ca}}} \end{aligned} \tag{2.84}$$

it should be noted that η_{an} and η_{ca} are solved simultaneously, instead of in serial.

The current density, j, can be calculated afterwards as,

$$j = \frac{E_{\mathrm{Nernst}} - \eta_{\mathrm{an}} - \eta_{\mathrm{ca}} - V}{\Omega} \tag{2.85}$$

To account for the membrane water content, the water transfer through the membrane should be considered. Similarly, the diffusion and EOD mechanisms are taken to address water transport; unlike the detailed model, an

equilibrium model is selected in the homogeneous model. Therefore, the equivalent water content, λ_{e}, is applied to represent the water content in the membrane. Considering the simplification in homogeneous model, water content in the membrane is obtained via a mean value of those at anode and cathode sides:

$$\lambda_{\mathrm{e,\ m}} = \frac{\lambda_{\mathrm{e,\ an}} + \lambda_{\mathrm{e,\ ca}}}{2} \tag{2.86}$$

where $\lambda_{\mathrm{e,\ an}}$ and $\lambda_{\mathrm{e,\ ca}}$ are the water contents at anode and cathode CLs, respectively. Water contents in the CLs is calculated as shown in Eqs. 1.30 and 1.31.

The water flux through the membrane includes the EOD term,

$$\Phi_{\mathrm{EOD}} = \frac{n_d i M_{\mathrm{H_2O}}}{F} \tag{2.87}$$

and the diffusion term,

$$\Phi_{\mathrm{diff}} = \frac{D_{\mathrm{m}}^{\mathrm{eff}}}{L_{\mathrm{m}}} M_{\mathrm{H_2O}} \frac{\rho_{\mathrm{m}}}{\mathrm{EW}} (\lambda_{\mathrm{e,\ an}} - \lambda_{\mathrm{e,\ ca}}) \tag{2.88}$$

Therefore, the total flux from anode to cathode is: (NB: the total flux from cathode to anode is also possible)

$$\Phi = \Phi_{\mathrm{EOD}} + \Phi_{\mathrm{diff}} \tag{2.89}$$

The heat transfer in electrolyte region is the same as in solid region, Eq. 2.75.

Phase change

The phase change issue in the homogeneous model is described by a simplified formulation, as shown,

$$R_{\mathrm{ce}} = \begin{cases} \Upsilon_{\mathrm{co}} \varepsilon s_{\mathrm{gas}} \frac{p_{\mathrm{H_2O}} - pSat(T)}{R_g T} & p_{\mathrm{H_2O}} > pSat(T) \\ \Upsilon_{\mathrm{ev}} \varepsilon s_{\mathrm{liquid}} \frac{pSat(T) - p_{\mathrm{H_2O}}}{R_g T} & p_{\mathrm{H_2O}} < pSat(T) \end{cases} \tag{2.90}$$

where Υ means the phase change rate, ε represents the porosity of the GDLs. This formulation is applied in the CLs that is the membrane surfaces.

The heat source due to phase change is expressed as,

$$Q_{\mathrm{ce}} = R_{\mathrm{ce}} \Delta H \tag{2.91}$$

where ΔH represents the enthalpy change.

It should be noted that, species fractions, phase saturation, and pressures represent the wall values on the surfaces of membrane in calculations of variables in electrolyte region. Additional relations are necessary to relate the bulk values in flow channels and wall values on the membrane surfaces.

Additional relations

Transport phenomena in the GDLs can be described by 1-D analytical solutions, considering the fact that the thickness of GDL is relatively thin. The species mass transport in fuel cells was comprehensively studied by Beale [204][205], while in the present work, a simple form is applied in describing mass transport of species based on the dilute mixture theory [206].

For a species i,

$$\Phi_{\mathrm{i}} = C_K(Y_{\mathrm{w,\,i}} - Y_{\mathrm{b,\,i}}) \tag{2.92}$$

where C_K represents the averaged mass transfer coefficient, Y_{w} is the mass fraction on the surface of membrane, and Y_{b} means the bulk mass fraction or the mass fraction in flow channels.

As shown in the work of Nishida et al. [34], an harmonic averaging method can be used to calculate the averaged mass transfer coefficient for mass transfer between bulk values (in flow channel) and wall values (on membrane surface):

$$\frac{1}{C_{K,\mathrm{i}}} = \frac{1}{C_K^*} + \sum_{\mathrm{j}} \frac{L_{\mathrm{j}}}{\rho D_{\mathrm{j}} S f_{\mathrm{j}}} \tag{2.93}$$

where C_K^* represents the convective mass transfer coefficient, L is the thickness of each porous layer, D is the diffusion coefficient in each porous layer, and Sf means the conduction shape factor [207].

The convective mass transfer coefficient, C_K^*, can be obtained as:

$$C_K^* = \frac{\mathrm{Sh}^* \rho D_f}{D_h} \tag{2.94}$$

where Sh^* means the Sherwood number, D_f is the diffusion coefficient in flow channel, and D_h represents the hydraulic diameter.

Then wall values of mass fraction can therefore be obtained as:

$$Y_{\mathrm{w,\,i}} = \Phi_{\mathrm{i}}/C_K + Y_{\mathrm{b,\,i}} \tag{2.95}$$

For liquid water transfer in the porous layers, the two-phase Darcy's law for both phases are written as:

$$\nabla p_{\mathrm{g}} = \frac{s_{\mathrm{g}} \mathbf{U}_{\mathrm{g}} \mu_{\mathrm{g}}}{K\, K_{\mathrm{rel,\,g}}} \tag{2.96}$$

$$\nabla p_{\mathrm{l}} = \frac{s_{\mathrm{l}} \mathbf{U}_{\mathrm{l}} \mu_{\mathrm{l}}}{K\, K_{\mathrm{rel,\,l}}} \tag{2.97}$$

As the liquid phase pressure gradient is much larger than that of gas phase, the liquid phase continuity equation, Eq. 2.1, can be rewritten as:

$$\nabla \cdot (\rho_{\text{liquid}} s_{\text{liquid}} \mathbf{U}_{\text{liquid}}) = \nabla \cdot (\frac{\sqrt{K\varepsilon} K_{\text{rel, liquid}} \sigma cos\theta}{\mu_{\text{liquid}}} \nabla J(s)) = R_{\text{liquid}} \quad (2.98)$$

A Laplacian formulation can be derived from the Leverett J function, which is a function of liquid water saturation.

$$\nabla \cdot (\frac{\sqrt{K\varepsilon} K_{\text{rel, liquid}} \sigma cos\theta}{\mu_{\text{liquid}}} \frac{dJ(s)}{ds} \nabla s) = R_{\text{liquid}} \quad (2.99)$$

Assuming the gas and liquid phases are in a phase-equilibrium state in the porous layers, R_{liquid} is a constant value that represents the liquid water flux from the CLs. In addition, considering the 1-D transport in the through-plane direction of porous layers, Eq. 2.99 is readily rewritten as:

$$\frac{\sqrt{K\varepsilon} K_{\text{rel, liquid}} \sigma cos\theta}{\mu_{\text{liquid}}} \frac{dJ(s)}{ds} \frac{ds}{dx} = R_{\text{liquid}} x + C_0 \quad (2.100)$$

where x is the distance from flow channel or the porous layer thickness, and C_0 is a constant that can be obtained when $x = 0$, where $s(x)|_{x=0}$ is in fact the liquid water saturation in flow channel. In such case, $s(L)$ can be calculated and s_{w}, liquid water saturation on the membrane surface, can be computed iteratively for multi-layer GDLs.

Source/sink terms

The source/sink terms related to the governing equations of homogeneous model are listed in Table. 2.3. For the case of single phase, the source/sink terms are also shown in Table. 2.4

2.3 Summary

In this chapter, two macroscopic PEFC models are introduced in detail, namely a detailed model and a homogeneous model. The detailed model is developed based on conventional CFD, whereas the homogeneous model is inherited from the detailed model with additional simplifications. Both models consider all of the major transport phenomena in PEFCs, including electrochemical reactions, species, momentum, and heat and mass transfers. A two-phase Eulerian-Eulerian model is applied for two-phase flow simulations.

Table 2.3: Source/sink terms: two phase flow, homogeneous model

Regions	Description	Calculation	Units
Fluid	R_{i} Eq. 2.68	$\frac{i\omega M_i}{zFL\mathrm{channel}}$	$\mathrm{kg\,m^{-3}\,s^{-1}}$
	$R_{\mathrm{H_2O}}$ Eq. 2.68	R_{ce}	$\mathrm{kg\,m^{-3}\,s^{-1}}$
	R_{gas} Eq. 2.60	$\sum_{\mathrm{i}} R_{\mathrm{i}}$	$\mathrm{kg\,m^{-3}\,s^{-1}}$
	R_{liquid} Eq. 2.60	$\frac{i\omega M_{\mathrm{H_2O}}}{zFL_{\mathrm{channel}}} - \Phi/L_{\mathrm{channel}} - R_{\mathrm{ce}}$	$\mathrm{kg\,m^{-3}\,s^{-1}}$
	Q_d Eq. 2.70	$Q_{\mathrm{ce,\,d}}$	$\mathrm{W\,m^{-3}}$
	Q_c Eq. 2.70	$Q_{\mathrm{ce,\,c}}$	$\mathrm{W\,m^{-3}}$
Electrolyte	Q Eq. 2.75	$-(\frac{\Delta H}{F} + V)\frac{i}{L_{\mathrm{m}}} + Q_{\mathrm{ce,\,w}}$	$\mathrm{W\,m^{-3}}$

Table 2.4: Source/sink terms: Single phase flow, homogeneous model

Regions	Description	Calculation	Units
Fluid	R_{i} Eq. 2.68	$\frac{i\omega M_i}{zFL\mathrm{channel}}$	$\mathrm{kg\,m^{-3}\,s^{-1}}$
	$R_{\mathrm{H_2O}}$ Eq. 2.68	R_{ce}	$\mathrm{kg\,m^{-3}\,s^{-1}}$
	R_{gas} Eq. 2.60	$\frac{i\omega M_{\mathrm{H_2O}}}{zFL_{\mathrm{channel}}} - \Phi/L_{\mathrm{channel}}$	$\mathrm{kg\,m^{-3}\,s^{-1}}$
Electrolyte	Q Eq. 2.75	$-(\frac{\Delta H}{F} + V)\frac{i}{L_{\mathrm{m}}}$	$\mathrm{W\,m^{-3}}$

Chapter 3

Numerical Procedure

Physical models concerning transport phenomena in fuel cells are described as a set of governing equations with various boundary conditions. In the case of 3-D scenario, the governing equations are in fact partial differential equations (PDEs). It is not generally possible to obtain analytical solutions for the PDEs, which promotes the development of approximate solutions with numerical simulation method. The final solutions are distributed into a so-called computational domain, which contains a finite number of computational nodes that represent the space and time. The PDEs are discretized in this computation domain by means of the corresponding algebraic equations via various discretization approaches. The present study is performed on the finite volume method (FVM) based library, OpenFOAM [208]. This chapter provides the numerical procedure in conducting FVM discretizations and simulations.

Normally, there are three steps for the numerical simulation methodology,

- Discretization of domains
- Discretization of equations
- Solution procedure

and in the present study, all of the numerical simulation steps are performed by the Open Source CFD toolbox OpenFOAM.

3.1 Discretization of domains

The computational domain needs to be subdivided into a finite number of sub-entities for space (spatial discretization) and time (temporal discretization). The spatial sub-entities are usually referred as control volumes, while

the temporal sub-entities are called time step or time interval. These sub-entities are contiguous, which means they do not overlap with each other and completely fill the whole domain.

3.1.1 Discretization of space

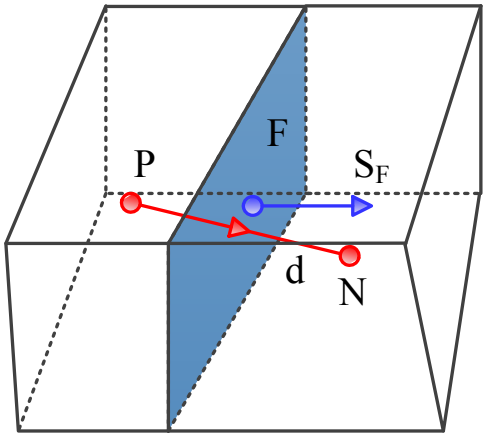

Figure 3.1: Schematic of two control volumes with points P and N as the cell centers. Face F is the interface between cell P and cell N.

The computational domain for spatial discretization is consistent with numerous control volumes, a sketch of which is shown in Fig. 3.1. A control volume is covered by a set of faces, which can be categorized into two groups: boundary faces (computational domain boundaries) and internal faces (between two control volumes). Variables stored on the cell surface are located at the surface center, the position of which is obtained as:

$$\int_S (\mathbf{x} - \mathbf{x}_f) dS = 0 \tag{3.1}$$

where S represents the surface of integration, $\mathbf{x}$ is a reference position, and $\mathbf{x}_f$ means the position of surface center.

Variables and other properties defined for the cell are located at the cell center P, as shown in Fig. 3.1, the position of which is given by:

$$\int_V (\mathbf{x} - \mathbf{x}_P) dV = 0 \tag{3.2}$$

where V represents the volume, and $\mathbf{x}_P$ is the cell center.

A face area vector $\mathbf{S_F}$ is normal to the surface and the magnitude of it equals to the face area. The positive direction of S_F points out to the

neighbor cell N. Hence, a unit normal vector $\mathbf{n}$ for face F can be defined as $\mathbf{n} = \mathbf{S_F}/|\mathbf{S_F}|$. The vector $\mathbf{d} = \mathbf{x}_P - \mathbf{x}_N$ represents the displacement between cell P and cell N. In case $\mathbf{d} \parallel \mathbf{S_F}$ is valid for all of the faces in computational domain, the computational mesh is orthogonal. In OpenFOAM, all the computational mesh is treated as unstructured grids, which means the number of faces in a control volume is not limited. The control volume may have a variable of neighbors. However, only control volume with convex faces can be applied [195] in the calculations.

3.1.2 Discretization of time

The temporal discretization makes sense for transient simulations. The time step or time interval, Δt, is uniform or non-uniform (adaptive time-stepping). A local time-stepping (LTS) approach [190] can be applied in two phase flow simulations, where the time step varies globally. The LTS is only valid for steady state case.

3.2 Discretization of general equations

The PDEs are usually impossible to be solved directly. In the numerical treatment, they are discretized into algebraic formulations on the computation domains. The transport equations can be written in a generic form, e.g. for any tensorial quantity φ, as:

$$\underbrace{\frac{\partial(\rho\varphi)}{\partial t}}_{\text{transient term}} + \underbrace{\nabla\cdot(\rho\mathbf{U}\varphi)}_{\text{convection term}} = \underbrace{\nabla\cdot(\rho\Gamma_\varphi\nabla\varphi)}_{\text{diffusion term}} + \underbrace{S_\varphi}_{\text{source term}} \tag{3.3}$$

where Γ_φ is the diffusion coefficient.

In FVM, the PDE discretizations in space are obtained by integrating Eq. 3.3 over the control volume (V_P),

$$\int_{V_P}\left[\frac{\partial\rho\varphi}{\partial t} + \nabla\cdot(\rho\mathbf{U}\varphi)\right]dV = \int_{V_P}\left[\nabla\cdot(\rho\Gamma_\varphi\nabla\varphi) + S_\varphi\right]dV \tag{3.4}$$

Transforming the integration over the control volume (V_P) into the integration over the cell faces via the generalized form of the Gausss theorem,

$$\int_{V_P}\nabla\bigotimes\varphi dV = \int_S d\mathbf{S}\bigotimes\varphi = \oint_S \mathbf{n}\bigotimes\varphi dS \tag{3.5}$$

where the symbol $\bigotimes$ can represent any tensor product, including inner, outer, and cross, and $d\mathbf{S}$ is the differential of the surface area vector. The

integrated formulation is:

$$\int_{V_P} \frac{\partial \rho\varphi}{\partial t} dV + \oint_S \rho\varphi(\mathbf{n}\cdot\mathbf{U})dS = \oint_S \rho\Gamma_\varphi(\mathbf{n}\cdot\nabla\varphi)dS + \int_{V_P} S_\varphi dV \tag{3.6}$$

3.2.1 Transient term

The integrated form of the transient term in Eq. 3.6 is computed over the control volume. The Euler implicit time differencing scheme is usually applied for time derivative. The variation of φ in a time step Δt can be written with linear interpolation as:

$$\int_{V_P} \frac{\partial \rho\varphi}{\partial t} dV \approx \frac{\rho_P^n \varphi_P^n - \rho_P^o \varphi_P^o}{\Delta t} V_P \tag{3.7}$$

where φ^n represents values at the new time step, and φ^o is values for the old time step.

3.2.2 Convection term

The convection term in integration form is shown in Eq. 3.6. The algebraic equations can be written as:

$$\int_S d\mathbf{S}\cdot\rho\mathbf{U}\varphi \approx \sum_f \mathbf{S}\cdot(\rho\mathbf{U})_f\varphi_f = \sum_f F\varphi_f \tag{3.8}$$

where F donates the mass flux through face 'f', which is defined as $F = \mathbf{S}\cdot(\rho\mathbf{U})_f$, and φ_f means the face value of φ that is interpolated from cell center. The face interpolation can be achieved in several ways:
Central differencing (CD): the face value can be obtained by averaging the values between adjacent cells,

$$\varphi_f = a\varphi_P + (1-a)\varphi_N \tag{3.9}$$

where $a = |\mathbf{x}_f - \mathbf{x}_N|/|\mathbf{x}_f - \mathbf{x}_N| + |\mathbf{x}_f - \mathbf{x}_P|$. The CD scheme has second-order accuracy.
Upwind differencing (UD): the face value depends on the flow direction,

$$\varphi_f = \begin{cases} \varphi_P & F \le 0 \\ \varphi_N & F < 0 \end{cases} \tag{3.10}$$

where $F < 0$ represents the mass flux from cell N to cell P. The UD scheme is first order accurate.
Blending differencing (BD): the face value is calculated via a linear combination of CD and UD schemes.

$$\varphi_f = \omega\varphi_{f,UD} + (1-\omega)\varphi_{f,CD} \tag{3.11}$$

where ω is a blending factor, in the range of 0 to 1.

3.2.3 Diffusion term

The diffusion term, $\nabla \cdot (\rho\Gamma_\varphi \nabla\varphi)$, is discretized via the conversion of volumetric integration to surface integration,

$$\int_{V_P} \nabla \cdot (\rho\Gamma_\varphi \nabla\varphi) dV = \oint_S d\mathbf{S} \cdot (\rho\Gamma_\varphi \nabla\varphi) \approx \sum_f (\rho\Gamma_\varphi)_f (\mathbf{S} \cdot \nabla_f \varphi) \tag{3.12}$$

where $\nabla_f \varphi$ represents the surface normal gradient for φ. This formulation is only valid when Γ_φ is a scalar. For orthogonal meshes, the surface normal gradient can be calculated as:

$$\nabla_f^\perp \varphi = \frac{\varphi_N - \varphi_P}{|\mathbf{D}|} \tag{3.13}$$

where the vector between cell N and cell P, $\mathbf{D}$ is parallel to the surface normal vector, $\nabla_f^\perp$ means the surface normal gradient.

If the meshes are non-orthogonal, an additional correction term is necessary,

$$\mathbf{S} \cdot \nabla_f \varphi = \underbrace{|\mathbf{D}| \nabla_f^\perp \varphi}_{\text{orthogonal term}} + \underbrace{\mathbf{k} \cdot (\nabla\varphi)_f}_{\text{non-orthogonal term}} \tag{3.14}$$

where the vector $\mathbf{k}$ is the correction factor for non-orthogonal meshes.

3.2.4 Source term

Terms that cannot be written as transient, convection, and diffusion, are classified as source, or sink terms. These terms have a generic formulation as:

$$S_\varphi = S_I \varphi + S_E \tag{3.15}$$

where S_I and S_E are the coefficients that can be functions of φ. S_I means the term is usually discretized implicitly, and S_E means the term is explicitly discretized. The integration of the source term gives:

$$\int_{V_P} S_\varphi dV = S_I V_P \varphi_P + S_E V_P \tag{3.16}$$

3.2.5 Boundary and initial conditions

The boundary conditions are important for both steady and transient simulations. Various types of boundary conditions are applied for different situations, the majority of which are derived from either **Dirichlet** or **von Neumann** conditions, or mixed. The initial conditions are important for transient simulations, which will not affect the final solutions in steady state cases. However, appropriate initial conditions may contribute to much faster and more stable steady state simulations.

Dirichlet boundary condition: the values on the boundaries for specific variable are prescribed.

von Neumann boundary condition: the surface normal gradients for specific variable are prescribed.

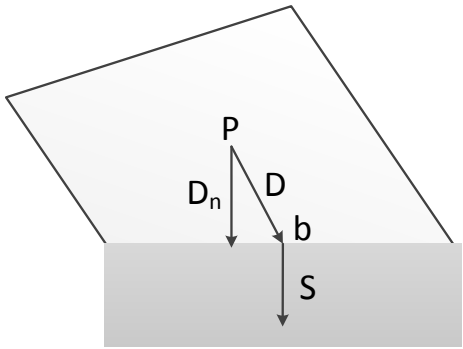

Figure 3.2: Schematic of variable discretization at a boundary

A schematic of the discretization at a boundary cell is presented in Fig. 3.2. No neighbor cells exist on the other side of the boundary face, the vector $\mathbf{D}$ is therefore defined from the cell center P to the boundary face center b. The face normal vector $\mathbf{D}_n$ represents a component of $\mathbf{D}$ that is normal to the boundary face, which can be calculated via:

$$\mathbf{D}_n = \frac{\mathbf{D}\cdot\mathbf{S}}{|\mathbf{S}|}\mathbf{n} = \frac{\mathbf{D}\cdot\mathbf{S}}{|\mathbf{S}|}\frac{\mathbf{S}}{|\mathbf{S}|} \tag{3.17}$$

Dirichlet boundary condition: the boundary value of φ is prescribed as φ_b.

- For the convection term, the integrated form gives,

$$\int_{V_P} \nabla \cdot (\rho \mathbf{U} \varphi) dV = \sum_f F \varphi_f + F_b \varphi_b \tag{3.18}$$

where the term $F_b \varphi_b$ donates the surface integration on the boundary face, and F_b represents the flux through the boundary.

- For the diffusion term, the integrated form is,

$$\int_{V_P} \nabla \cdot (\rho \Gamma \nabla \varphi) dV = \sum_f (\rho \Gamma)_f \mathbf{S} \cdot \nabla_f \varphi + (\rho \Gamma)_b \mathbf{S}_b \nabla_b \varphi \tag{3.19}$$

where term $(\rho \Gamma)_b \mathbf{S}_b \nabla_b \varphi$ is the surface integration over the boundary face, and $\mathbf{S}_b \nabla_b \varphi$ donates the surface normal gradient. As shown in section 3.2.3, a correction treatment is necessary if non-orthogonal mesh is applied.

von Neumann boundary condition, the boundary surface normal gradient for φ is prescribed as g_b.

- For convection term,

$$\int_{V_P} \nabla \cdot (\rho \mathbf{U} \varphi) dV = \sum_f F \varphi_f + F_b \varphi_b = \sum_f F \varphi_f + F_b (\varphi_P + |\mathbf{D}_n| g_b) \tag{3.20}$$

where,

$$\varphi_b = \varphi_P + \mathbf{D}_n \cdot \nabla_b \varphi = \varphi_P + |\mathbf{D}_n| g_b \tag{3.21}$$

- For diffusion term,

$$\begin{aligned} \int_{V_P} \nabla \cdot (\rho \Gamma \nabla \varphi) dV &= \sum_f (\rho \Gamma)_f \mathbf{S} \cdot \nabla_f \varphi + (\rho \Gamma)_b \mathbf{S}_b \nabla_b \varphi \\ &= \sum_f (\rho \Gamma)_f \mathbf{S} \cdot \nabla_f \varphi + (\rho \Gamma)_b g_b \end{aligned} \tag{3.22}$$

3.2.6 Temporal discretization

Although the simulations in the present study are steady state, the discretiation of time is important for further studies concerning transient simulations. Similar to the equation discretization in space, the temporal discretization is introduced by the integration over the time interval Δt,

$$\begin{aligned}&\int_t^{t+\Delta t}\left(\rho_P\frac{\varphi^n-\varphi^o}{\Delta t}V_P+\sum_f F\varphi_f\right)dt\\&=\int_t^{t+\Delta t}\left(\sum_f \Gamma_f\mathbf{S}\cdot\nabla_f\varphi+S_IV_P\varphi_P+S_EV_P\right)dt\end{aligned}\tag{3.23}$$

If the variations of cell values, face values, and gradients within a time step are neglected [195], the temporal discretization for PEDs depends on the selection of new or old cell values, face values, and gradients of φ. In such case, the equations are discretized explicitly with old values or implicitly with new values.

Explicit discretization, the discretized formulation reads,

$$\frac{\varphi^n-\varphi^o}{\Delta t}V_P+\sum_f F\varphi_f^o=\sum_f(\rho\Gamma)_f\mathbf{S}\cdot\nabla_f\varphi^o+S_IV_P\varphi_P^o+S_EV_P\tag{3.24}$$

where φ^o represents the value of φ at previous time step. Therefore, φ^n can be obtained directly from the old values, φ^o, from this formulation. However, it may become unstable if the Courant number, Co, is larger than 1. The Courant number is defined as,

$$Co=\frac{\mathbf{U}_f\cdot\mathbf{S}}{\mathbf{D}\cdot\mathbf{S}}\Delta t\tag{3.25}$$

Implicit discretization, the discretized formulation gives,

$$\frac{\varphi^n-\varphi^o}{\Delta t}V_P+\sum_f F\varphi_f^n=\sum_f(\rho\Gamma)_f\mathbf{S}\cdot\nabla_f\varphi^n+S_IV_P\varphi_P^n+S_EV_P\tag{3.26}$$

where φ^n donates the value of φ at new time step. A linear system of algebraic equations should be formed to solve all of the new values of φ_P and φ_N. This formulation guarantees the boundness of solutions and removes the Courant number limitation, which means the solution is unconditionally stable.

Table 3.1: Finite volume notations

Term description	Terms in equations	Discretized formulation
Transient term	$\left[\!\left[\frac{\partial \varphi}{\partial t}\right]\!\right]$	$\frac{\varphi^n - \varphi^o}{\Delta t} V_P$
Convection term	$[\![\nabla \cdot (\rho \mathbf{U} \varphi)]\!]$	$\sum_f F \varphi_f^n$
Diffusion term	$[\![\nabla \cdot (\rho \Gamma \nabla \varphi)]\!]$	$\sum_f (\rho\Gamma)_f \mathbf{S} \cdot \nabla_f \varphi^n$
Divergence term	$\nabla \cdot \varphi$	$\sum_f \mathbf{S} \cdot \varphi^o$
Gradient term	$\nabla \varphi$	$\sum_f \mathbf{S} \varphi^o$
Implicit source term	$[\![S_I \varphi]\!]$	$S_I V_P \varphi^n$
Explicit source term	S_E	$S_E V_P$

3.3 Discretization of governing equations

The governing equations concerning the transport phenomena in fuel cell were introduced in Chapter 2. The procedure of two phase flow governing equations discretization have been described comprehensively in the thesis of Rusche [195] and others. In this section, a brief introduction of the discretization procedure will be given.

The finite volume notation for various terms in equation discretizations are summarized in Table. 3.1, where the operator $[\![]\!]$ is defined as the finite volume discretization notation.

3.3.1 Continuity equations

For the two phase flow, the conservative form of continuity equations are written as,

$$\frac{\partial s_\mathrm{g} \rho_\mathrm{g}}{\partial t} + \nabla \cdot (s_\mathrm{g} \rho_\mathrm{g} \mathbf{U}_\mathrm{g}) = R_\mathrm{g} \tag{3.27}$$

and

$$\frac{\partial s_\mathrm{l} \rho_\mathrm{l}}{\partial t} + \nabla \cdot (s_\mathrm{l} \rho_\mathrm{l} \mathbf{U}_\mathrm{l}) = R_\mathrm{l} \tag{3.28}$$

where the subscripts g and l donate the gas phase and liquid phase.

Rewriting Eqs. 3.27 and 3.28 reads,

$$\frac{\partial s_\mathrm{g}}{\partial t} + \nabla \cdot (s_\mathrm{g} \mathbf{U}_\mathrm{g}) = \frac{1}{\rho_\mathrm{g}} (R_\mathrm{g} - s_\mathrm{g} \frac{D\rho_\mathrm{g}}{Dt}) \tag{3.29}$$

and

$$\frac{\partial s_\mathrm{l}}{\partial t} + \nabla \cdot (s_\mathrm{l} \mathbf{U}_\mathrm{l}) = \frac{1}{\rho_\mathrm{l}} (R_\mathrm{l} - s_\mathrm{l} \frac{D\rho_\mathrm{l}}{Dt}) \tag{3.30}$$

Considering the fact that, $s_\mathrm{g} + s_\mathrm{l} = 1$, Eq. 3.27 and Eq. 3.28 are not independent with each other in solving phase saturation s. There are various

formulations in rearrangement the two phase continuity equations [195]. In the present study, the equations are rearranged by $s_\mathrm{l}\times$ Eq. 3.29 - $s_\mathrm{g}\times$ Eq. 3.30, which gives,

$$\begin{aligned} &s_\mathrm{l}\frac{\partial s_\mathrm{g}}{\partial t} - s_\mathrm{g}\frac{\partial s_\mathrm{l}}{\partial t} + s_\mathrm{l}\nabla\cdot(s_\mathrm{g}\mathbf{U}_\mathrm{g}) - s_\mathrm{g}\nabla\cdot(s_\mathrm{l}\mathbf{U}_\mathrm{l}) \\ &= \frac{s_\mathrm{l}}{\rho_\mathrm{g}}(R_\mathrm{g} - s_\mathrm{g}\frac{D\rho_\mathrm{g}}{Dt}) - \frac{s_\mathrm{g}}{\rho_\mathrm{l}}(R_\mathrm{l} - s_\mathrm{l}\frac{D\rho_\mathrm{l}}{Dt}) \end{aligned} \tag{3.31}$$

By applying $s_\mathrm{l} = 1 - s_\mathrm{g}$, a new formulation is,

$$\frac{\partial s_\mathrm{g}}{\partial t} + \nabla\cdot(\mathbf{U}s_\mathrm{g}) + \nabla\cdot(s_\mathrm{l}\mathbf{U}_\mathrm{r}s_\mathrm{g}) = \frac{s_\mathrm{l}}{\rho_\mathrm{g}}(R_\mathrm{g} - s_\mathrm{g}\frac{D\rho_\mathrm{g}}{Dt}) - \frac{s_\mathrm{g}}{\rho_\mathrm{l}}(R_\mathrm{l} - s_\mathrm{l}\frac{D\rho_\mathrm{l}}{Dt}) \tag{3.32}$$

where $\mathbf{U}$ is the mixture velocity, defined as $\mathbf{U} = s_\mathrm{g}\mathbf{U}_\mathrm{g} + s_\mathrm{l}\mathbf{U}_\mathrm{l}$, and $\mathbf{U}_\mathrm{r}$ is the relative velocity, defined as $\mathbf{U}_\mathrm{r} = \mathbf{U}_\mathrm{g} - \mathbf{U}_\mathrm{l}$.

Based on Table 3.1, Eq. 3.32 is written as,

$$\left[\!\left[\frac{\partial s_\mathrm{g}}{\partial t}\right]\!\right] + [\![\nabla\cdot(\mathbf{U}s_\mathrm{g})]\!] + [\![\nabla\cdot(s_\mathrm{l}\mathbf{U}_\mathrm{r}s_\mathrm{g})]\!] = [\![S_I s_\mathrm{g}]\!] + [\![S_E]\!] \tag{3.33}$$

where

$$S_I s_\mathrm{g} + S_E = \frac{s_\mathrm{l}}{\rho_\mathrm{g}}(R_\mathrm{g} - s_\mathrm{g}\frac{D\rho_\mathrm{g}}{Dt}) - \frac{s_\mathrm{g}}{\rho_\mathrm{l}}(R_\mathrm{l} - s_\mathrm{l}\frac{D\rho_\mathrm{l}}{Dt}) \tag{3.34}$$

The algebraic equations after discretization read,

$$\frac{s_\mathrm{g}^n - s_\mathrm{g}^o}{\Delta t}V_P + \sum_f F_{m,\,f}s_\mathrm{g}^o + \sum_f (1 - s_\mathrm{g}^o)F_{r,\,f}s_\mathrm{g}^o = S_I s_\mathrm{g}^n V_P + S_E V_P \tag{3.35}$$

where $F_{m,\,f}$ represents the mixture mass flux through the cell faces, and $F_{r,\,f}$ is the mass flux due to relative velocity through cell faces.

The gas phase saturation, s_g, is calculated explicitly as,

$$s_\mathrm{g}^n = \frac{S_E - (\sum_f F_{m,\,f}s_\mathrm{g}^o + \sum_f (1 - s_\mathrm{g}^o)F_{r,\,f}s_\mathrm{g}^o)/V_P + s_\mathrm{g}^o/\Delta t}{1/\Delta t - S_I} \tag{3.36}$$

where the multidimensional universal limiter for explicit solution (MULES) is applied for explicit solutions [208]. The MULES is suitable for convective-only transport equations, which gives bounded solutions.

3.3.2 Momentum equations

The phase-intensive momentum transfer equations are,

$$\begin{aligned}&\frac{\partial s_{\mathrm{g}}\rho_{\mathrm{g}}\mathbf{U}_{\mathrm{g}}}{\partial t}+\nabla\cdot(s_{\mathrm{g}}\rho_{\mathrm{g}}\mathbf{U}_{\mathrm{g}}\mathbf{U}_{\mathrm{g}})\\&=-s_{\mathrm{g}}\nabla p_{\mathrm{g}}+\nabla\cdot(s_{\mathrm{g}}\mu_g\nabla\mathbf{U}_{\mathrm{g}})+s_g\rho_g\mathbf{g}+\mathbf{M}_{\mathrm{g}}+s_{\mathrm{g}}S_{\mathrm{Darcy,\,g}}\end{aligned}\tag{3.37}$$

$$\begin{aligned}&\frac{\partial s_{\mathrm{l}}\rho_{\mathrm{l}}\mathbf{U}_{\mathrm{l}}}{\partial t}+\nabla\cdot(s_{\mathrm{l}}\rho_{\mathrm{l}}\mathbf{U}_{\mathrm{l}}\mathbf{U}_{\mathrm{l}})\\&=-s_{\mathrm{l}}\nabla p_{\mathrm{l}}+\nabla\cdot(s_{\mathrm{l}}\mu_{\mathrm{l}}\nabla\mathbf{U}_{\mathrm{l}})+s_{\mathrm{l}}\rho_l\mathbf{g}+\mathbf{M}_{\mathrm{l}}+s_{\mathrm{l}}S_{\mathrm{Darcy,\,l}}\end{aligned}\tag{3.38}$$

where S_{Darcy} is only valid in porous media, and,

$$p_{\mathrm{l}}=\begin{cases}p_{\mathrm{g}} & \text{channel}\\ p_{\mathrm{g}}-p_c & \text{porous media}\end{cases}\tag{3.39}$$

Then, momentum transfer equation for liquid phase can be rewritten as,

$$\begin{aligned}&\frac{\partial s_{\mathrm{l}}\rho_{\mathrm{l}}\mathbf{U}_{\mathrm{l}}}{\partial t}+\nabla\cdot(s_{\mathrm{l}}\rho_{\mathrm{l}}\mathbf{U}_{\mathrm{l}}\mathbf{U}_{\mathrm{l}})\\&=-s_{\mathrm{l}}\nabla p_{\mathrm{g}}+\nabla\cdot(s_{\mathrm{l}}\mu_{\mathrm{l}}\nabla\mathbf{U}_{\mathrm{l}})+s_{\mathrm{l}}\rho_{\mathrm{l}}\mathbf{g}+\mathbf{M}_{\mathrm{l}}+s_{\mathrm{l}}S_{\mathrm{Darcy,\,l}}+s_{\mathrm{l}}\frac{dp_c}{ds_{\mathrm{l}}}\nabla s_{\mathrm{l}}\end{aligned}\tag{3.40}$$

where the term $\frac{dp_c}{ds_{\mathrm{l}}}\nabla s_{\mathrm{l}}$ due to p_c is treated as a source/sink term for the momentum transfer equation, which is only valid in porous media where capillary pressure dominates.

The finite volume discretizations of momentum transfer equations give,

$$\begin{aligned}&\left[\!\left[\frac{\partial s_{\mathrm{g}}\rho_{\mathrm{g}}\mathbf{U}_{\mathrm{g}}}{\partial t}\right]\!\right]+[\![\nabla\cdot(s_g\rho_{\mathrm{g}}\mathbf{U}_{\mathrm{g}}\mathbf{U}_{\mathrm{g}})]\!]\\&=-s_{\mathrm{g}}\nabla p_{\mathrm{g}}+s_g\rho_g\mathbf{g}+[\![\mathbf{M}_{\mathrm{g}}]\!]+[\![\nabla\cdot(s_{\mathrm{g}}\mu_{\mathrm{g}}\nabla\mathbf{U}_{\mathrm{g}})]\!]+[\![s_{\mathrm{g}}S[\mathbf{U}_{\mathrm{g}}]_{\mathrm{Darcy,\,g}}]\!]\end{aligned}\tag{3.41}$$

and

$$\begin{aligned}&\left[\!\left[\frac{\partial s_{\mathrm{l}}\rho_{\mathrm{l}}\mathbf{U}_{\mathrm{l}}}{\partial t}\right]\!\right]+[\![\nabla\cdot(s_{\mathrm{l}}\rho_{\mathrm{l}}\mathbf{U}_{\mathrm{l}}\mathbf{U}_{\mathrm{l}})]\!]\\&=s_{\mathrm{l}}\nabla p_{\mathrm{g}}+s_{\mathrm{l}}\rho_{\mathrm{l}}\mathbf{g}+[\![\mathbf{M}_{\mathrm{l}}]\!]+[\![\nabla\cdot(s_{\mathrm{l}}\mu_{\mathrm{l}}\nabla\mathbf{U}_{\mathrm{l}})]\!]+[\![s_{\mathrm{l}}S[\mathbf{U}_{\mathrm{l}}]_{\mathrm{Darcy,\,l}}]\!]+s_l\frac{dp_c}{ds_{\mathrm{l}}}\nabla s_{\mathrm{l}}\end{aligned}\tag{3.42}$$

where Darcy's terms are discretized implicitly, and the term due to capillary pressure is discretized explicitly. The interfacial momentum transfer term, $\mathbf{M}$, includes drag force, lift force, virtual mass force etc., all of which are functions of velocity. They are discretized implicitly. The momentum transfer equations are usually not discretized directly considering the strong coupling between velocity and pressure. In the next section, the decoupling procedure will be introduced.

3.3.3 Other equations

Additional governing equations in fuel cell include species, heat, proton, electron, and dissolved water transfer equations. These equations share the same generic formulations, as Eq. 3.3, although the parameters have various meanings depending on specific transport phenomena. The finite volume discretization of the generic transport equation reads,

$$\left[\!\left[\frac{\partial \rho\varphi}{\partial t}\right]\!\right] + [\![\nabla \cdot (\rho \mathbf{U}\varphi)]\!] = [\![\nabla \cdot (\rho\Gamma_{\varphi}\nabla\varphi)]\!] + S_{\varphi} \tag{3.43}$$

these equations are discretized directly over the computational domains. Unlike the MULES method [208] in solving phase saturation, these equations are usually solved implicitly.

3.4 Solution procedures

3.4.1 Methods

The finite volume discretization of governing equations is conducted over each control volume, which gives,

$$a_P\varphi_P + \sum_N a_N\varphi_N = r_P \tag{3.44}$$

where φ_P represents the specific variable, φ_N donates the neighbor values, a_P and a_N are coefficients, and r_P is the source/sink term.

The solution procedure for φ_P from Eq. 3.44 varies for different selection of time integration. If the neighbor values, φ_N, are from previous time step, φ_P can be calculated as,

$$\varphi_P^n = \frac{r_P - \sum_N a_N\varphi_N^o}{a_P} \tag{3.45}$$

and if new values, φ_N^n, are applied, φ_P reads,

$$\varphi_P^n = \frac{r_P - \sum_N a_N\varphi_N^n}{a_P} \tag{3.46}$$

where the first formulation represents the explicit solution procedure, and the second one represents an implicit solution method, which were introduced in section 3.2.6. In the present study, only the solution of phase saturation is conducted explicitly.

To perform implicit solution, the discretized governing equation on unit control volume need to be assembled over the entire computational domain, which gives,

$$\mathbf{A}[\varphi] = \mathbf{r} \tag{3.47}$$

where $\mathbf{A}$ is the coefficient matrix, $[\varphi]$ is a column vector of φ^n over each cell, and $\mathbf{r}$ is a column vector storing the source/sink terms. The coefficients a_P and a_N in Eq. 3.44 are stored as the diagonal and off-diagonal components in matrix $\mathbf{A}$, respectively. The matrix $\mathbf{A}$ is usually so sparse that most of the off-diagonal components are zero.

To solve the algebraic equations, Eq. 3.47, various solution algorithms have been developed, which can be categorized in two types, direct method and iterative method. In direct method, $[\varphi]$ can be calculated via,

$$\mathbf{A}^{-1}\mathbf{A}[\varphi] = [\varphi] = \mathbf{A}^{-1}\mathbf{r} \tag{3.48}$$

where $\mathbf{A}^{-1}$ donates the inverse of matrix $\mathbf{A}$. The inversion of matrix $\mathbf{A}$ leads to a dense matrix $\mathbf{A}^{-1}$, which poses requirement for memory to store all of the non-zero matrix components, especially for large systems. The number of operations in conducting the solution is approximately at a magnitude of cube of the number of $[\varphi]$. Compared to the direct method, iterative method offers a more economic solution.

In iterative method, the solution is obtained by iteratively improving the approximation of the solution until the tolerance is reached. During the iteration, the sparse nature of matrix $\mathbf{A}$ can be preserved by selecting appropriate iteration method. Normally, $\mathbf{A}$ needs to be diagonal dominated to guarantee solution convergence during iteration. To evaluate the diagonal property of $\mathbf{A}$, the matrix can be divided into a diagonal matrix and an off-diagonal matrix,

$$\mathbf{A} = \mathbf{D} + \mathbf{N} \tag{3.49}$$

where $\mathbf{D}$ only includes the diagonal components of $\mathbf{A}$, and $\mathbf{N}$ contains the off-diagonal components.

Diagonally equal: the magnitude of diagonal component for each row/column is equal to the magnitude of off-diagonal components, which is valid for every diagonal component.

$$|\mathbf{D}_{\mathrm{ii}}| = \sum_{\mathrm{j}}^{N} |\mathbf{N}_{\mathrm{ij}}| \tag{3.50}$$

Diagonally dominant: the magnitude of the off-diagonal components for each row/column is equal to or less than that of the diagonal components,

$$|\mathbf{D}_{\mathrm{ii}}| \leq \sum_{\mathrm{j}}^{N} |\mathbf{N}_{\mathrm{ij}}| \tag{3.51}$$

and the magnitude of off-diagonals is less than that of the diagonal components for at least for one row/column.

In addition to the basic requirement of diagonal dominance for $\mathbf{A}$, it is critical to have more diagonal-dominated matrix system, which contributes to better solver convergence. The contributions of each transportation term are considered as below,

Transient term: The discretization of transient term contributes to the diagonal components of $\mathbf{A}$, as well as to the source term.

$$\left[\!\left[\frac{\partial \rho \varphi_P}{\partial t}\right]\!\right] = \underbrace{\frac{\rho}{\Delta t} V_P}_{\text{diagonal}} \varphi_P^n + \underbrace{\frac{\rho}{\Delta t} V_P \varphi_P^o}_{\text{source}} \tag{3.52}$$

Convection term The discretization of convection term contributes to both diagonal and off-diagonal components of $\mathbf{A}$. Besides, the off-diagonal contribution makes the coefficient matrix $\mathbf{A}$ asymmetrical. The convection term does not result in a more diagonal-dominated matrix.

$$[\![\nabla \cdot (\rho \mathbf{U} \varphi_P)]\!] = \sum_f F_f \varphi_f = \underbrace{\sum_f \omega F_f}_{\text{diagonal}} \varphi_P + \underbrace{\sum_f (1-\omega) F_f}_{\text{off-diagonal}} \varphi_N \tag{3.53}$$

where ω can be decided from section 3.2.2.

Diffusion term The discretization of diffusion term contributes equally to the diagonal and off-diagonal components of $\mathbf{A}$.

$$[\![\nabla \cdot (\rho \Gamma \nabla \varphi_P)]\!] = \underbrace{\sum_f (\rho\Gamma)_f \frac{|\mathbf{S}|}{|\mathbf{d}|}}_{\text{diagonal}} \varphi_P + \underbrace{\sum_f (\rho\Gamma)_f \frac{|\mathbf{S}|}{|\mathbf{d}|}}_{\text{off-diagonal}} \varphi_N \tag{3.54}$$

this is valid only for orthogonal mesh. It should be noted that non-orthogonal correction term generally needs to be discretized explicitly, otherwise, it decreases the diagonal dominance.

Source term The discretization of diffusion term varies with the linear term and non-linear term. For linear term,

$$[\![S_E]\!] = \underbrace{S_E V_P}_{\text{source}} \tag{3.55}$$

it is discretized explicitly.

For non-linear term,

$$[\![S_I \varphi]\!] = \begin{cases} \underbrace{S_I V_P}_{\text{diagonal}} \varphi & S_I > 0 \\ \underbrace{S_I V_P \varphi^o}_{\text{source}} & S_I < 0 \end{cases} \tag{3.56}$$

the discretization should increase the diagonal dominance, therefore only if $S_I > 0$, the non-linear term is discretized implicitly.

All of the governing equations in the present fuel cell model can be solved in explicit or implicit method. However, concerning the strong coupling between fluid velocity and pressure, it is difficult to solve them from the momentum and continuity equations. Addition treatment is necessary for momentum transfer equations to guarantee solution process convergence.

3.4.2 Algorithms

The solution of the whole fuel cell system includes the description of transport phenomena for heat, mass and charge. In a fuel cell, they are coupled with each other. The algorithms are supposed to apply a segregated approach on a system of linear algebraic equations, in other word, the governing equations are solved separately while the coupling between them are remained. While the solutions procedures for heat, species, and charge transport equations are straight-forward, the algorithms in this section focus on the decoupling processes of fluid pressure and velocity.

The Pressure Implicit with Splitting of Operators (PISO) algorithm, which was developed by Issa [209], is usually applied for pressure-velocity coupling problems. In this algorithm, a momentum predictor and a correction loop are involved. In the loop, pressure is solved and the the fluid velocity/flux is updated based on the new pressure, which is conducted iteratively.

To perform the PISO algorithm, the Rhie-Chow correction method [210] is widely used (avoiding checkerboard problem) to relate the conservative fluxes and pressure gradient,

$$\mathbf{U}_f = f_x \mathbf{U}_P + (1 - f_x)\mathbf{U}_N + \left(\frac{1}{\mathbf{A}}\right)_f \left[\mathbf{n} \cdot (\nabla p)_f - \frac{p_N - p_P}{|\mathbf{d}|}\right] \tag{3.57}$$

where $\mathbf{n} \perp \mathbf{d}$. This provides the interpolation for velocity at the cell faces.

Momentum correction equation

The velocity correction formulation is formed by semi-discretizing the momentum transfer equations.

$$(\mathbf{A}_\varphi)_D \mathbf{U}_\varphi = (\mathbf{A}_\varphi)_H - s_\varphi \nabla p_g \tag{3.58}$$

where 'D' operator donates the diagonal of matrix $\mathbf{A}$, and 'H' operator represents the off-diagonal of matrix $\mathbf{A}$. $\mathbf{A}$ is obtained by finite volume

discretization of partial momentum transfer equations,

$$\begin{aligned}&\mathbf{A} := \\ &\left[\!\!\left[\frac{\partial s_\varphi \rho_\varphi \mathbf{U}_\varphi}{\partial t}\right]\!\!\right] + [\![\nabla \cdot (s_\varphi \rho_\varphi \mathbf{U}_\varphi \mathbf{U}_\varphi)]\!] \\ &= s_\varphi \rho_\varphi \mathbf{g} + [\![\mathbf{M}_\varphi]\!] + [\![\nabla \cdot (s_\varphi \mu_\varphi \nabla \mathbf{U}_\varphi)]\!] + [\![S_I \mathbf{U}_\varphi]\!] + S_E\end{aligned} \tag{3.59}$$

Rewrite Eq. 3.58, and neglect the pressure influence, the momentum correction equation can be achieved,

$$\mathbf{U}_\varphi = \frac{(\mathbf{A}_\varphi)_H}{(\mathbf{A}_\varphi)_D} - \frac{s_\varphi \nabla p_g}{(\mathbf{A}_\varphi)_D} \tag{3.60}$$

where the velocity/momentum is predicted and corrected via new pressure.

Pressure equation

The phase continuity equations need to be accounted for in constructing the pressure equation. As a mixture/share pressure is applied in the present work, a mixture continuity equation can be formed by considering the summation of phase continuity equations, Eq. 3.29 + Eq. 3.30,

$$\nabla \cdot (s_\mathrm{g} \mathbf{U}_\mathrm{g} + s_\mathrm{l} \mathbf{U}_\mathrm{l}) = R \tag{3.61}$$

where,

$$R = \frac{R_\mathrm{g}}{\rho_\mathrm{g}} + \frac{R_\mathrm{l}}{\rho_\mathrm{l}} - \frac{s_\mathrm{l}}{\rho_\mathrm{l}} \frac{D\rho_\mathrm{l}}{Dt} - \frac{s_\mathrm{g}}{\rho_\mathrm{g}} \frac{D\rho_\mathrm{g}}{Dt} \tag{3.62}$$

The formulation on cell faces gives,

$$\nabla \cdot (s_\mathrm{g} F_\mathrm{g} + s_\mathrm{l} F_\mathrm{l}) = R \tag{3.63}$$

by applying the interpolation of momentum correction equation, Eq. 3.60, on the face centers, the volumetric phase flux, F_φ, reads,

$$F_\varphi = F_\varphi^* - \left(\frac{s_\varphi}{\mathbf{A}_D}\right)_f |\mathbf{S}| \nabla_f^\perp p \tag{3.64}$$

where the central differencing scheme is used. And the flux prediction, F^*, is calculated as,

$$F^* = \left(\frac{\mathbf{A}_H}{\mathbf{A}_D}\right)_f \cdot \mathbf{S} \tag{3.65}$$

In such case, the pressure equation is constructed by substituting Eq. 3.64 into Eq. 3.63,

$$\left[\!\left[\nabla \cdot \left[s_{\mathrm{g}} \left(\frac{s_{\mathrm{g}}}{\mathbf{A}_{\mathrm{g}}} \right)_f + s_{\mathrm{l}} \left(\frac{s_{\mathrm{l}}}{\mathbf{A}_{\mathrm{l}}} \right)_f \right] \nabla [p_g] \right]\!\right] = \nabla \cdot (s_{\mathrm{g}} F_{\mathrm{g}}^* + s_{\mathrm{l}} F_{\mathrm{l}}^*) - R \quad (3.66)$$

PISO loop

Although the Rhie-Chow scheme is important in conducting the PISO or relevent solution procedures for velocity interpolation, a Rhie-Chow error needs to be specifically treated to ensure the stability of the solution. The Rhie-Chow error may lead to unreasonable behavior, including pressure oscillation, spurious currents, etc. Therefore, a modified Rhie-Chow scheme is necessary in solving the two phase flow. The idea is to exclude discontinuous forces, buoyancy force etc., from the momentum predictor, since there forces are finally balanced by the pressure gradient. The excluded forces are treated on face centers and reconsidered in reconstructing phase velocities.

Introducing a hydrostatic pressure for the mixture phase, $\rho \mathbf{g} \cdot \mathbf{h}$, and subtracting it from the total pressure, p, a modified pressure, p_{rgh}, is written as,

$$p_{\mathrm{rgh}} = p - \rho \mathbf{g} \cdot \mathbf{h} \quad (3.67)$$

where ρ donates the mixture density, $s_{\mathrm{g}}\rho_{\mathrm{g}} + s_{\mathrm{l}}\rho_{\mathrm{l}}$.

Substituting the modified pressure into the momentum equation, the momentum equation gives,

$$\begin{aligned} &\frac{\partial s_\varphi \rho_\varphi \mathbf{U}_\varphi}{\partial t} + \nabla \cdot (s_\varphi \rho_\varphi \mathbf{U}_\varphi \mathbf{U}_\varphi) - \nabla \cdot (s_\varphi \mu_g \nabla \mathbf{U}_\varphi) - \mathbf{M}_\varphi - s_\varphi S_{\text{Darcy, g}} \\ &= -s_\varphi \nabla p_{\mathrm{rgh}} + s_\varphi (\rho_\varphi - \rho)\mathbf{g} - s_\varphi \rho_\varphi \mathbf{g} \cdot \mathbf{h} \nabla \rho \end{aligned} \quad (3.68)$$

Momentum correction: The formulations for each phase are shown as Eq. 3.64. However, as a modified Rhie-Chow scheme is applied, the semi-discretization of momentum equations, Eq. 3.58, excludes the buoyancy force and the explicit part of drag force term.

Pressure correction loop: The flux are calculated from the predicted velocities with CD scheme,

$$\begin{aligned} F_{\mathrm{g}}^* = F_{\mathrm{g}}^o &+ \left(\frac{A_{\mathrm{g,\,d}}}{(\mathbf{A}_{\mathrm{g}})_D} \right)_f F_{\mathrm{l}} \\ &+ \left(\frac{s_{\mathrm{g}}(\rho_{\mathrm{g}} - \rho)}{(\mathbf{A}_{\mathrm{g}})_D} \right)_f \mathbf{S} \cdot \mathbf{g} \\ &- \left(\frac{s_{\mathrm{g}} \rho_{\mathrm{g}}}{(\mathbf{A}_{\mathrm{g}})_D} \right)_f (\mathbf{g} \cdot \mathbf{h})_f |\mathbf{S}| \nabla_f^\perp \rho \end{aligned} \quad (3.69)$$

and

$$\begin{aligned} F_{\mathrm{l}}^{*} = F_{\mathrm{l}}^{o} &+ \left(\frac{A_{\mathrm{l,\,d}}}{(\mathbf{A}_{\mathrm{l}})_D}\right)_f F_{\mathrm{g}} \\ &+ \left(\frac{s_{\mathrm{l}}(\rho_{\mathrm{l}} - \rho)}{(\mathbf{A}_{\mathrm{l}})_D}\right)_f \mathbf{S}\cdot\mathbf{g} \\ &- \left(\frac{s_{\mathrm{l}}\rho_{\mathrm{l}}}{(\mathbf{A}_{\mathrm{l}})_D}\right)_f (\mathbf{g}\cdot\mathbf{h})_f |\mathbf{S}| \nabla_f^{\perp}\rho \end{aligned} \tag{3.70}$$

where the term $\left(\frac{A_{\mathrm{g,\,d}}}{(\mathbf{A}_{\mathrm{g}})_D}\right)_f F_{\mathrm{l}}$ and $\left(\frac{A_{\mathrm{l,\,d}}}{(\mathbf{A}_{\mathrm{l}})_D}\right)_f F_{\mathrm{g}}$ represent the flux due to interfacial drag from liquid phase and gas phase, respectively, and F^o represents the flux as,

$$F^o = \mathbf{S}\cdot\frac{\mathbf{A}_H}{\mathbf{A}_D} \tag{3.71}$$

The pressure equation can be constructed as,

$$\left[\!\!\left[\nabla\cdot\left[s_{\mathrm{g}}\left(\frac{s_{\mathrm{g}}}{\mathbf{A}_{\mathrm{g}}}\right)_f + s_{\mathrm{l}}\left(\frac{s_{\mathrm{l}}}{\mathbf{A}_{\mathrm{l}}}\right)_f\right]\nabla[p_{\mathrm{rgh}}]\right]\!\!\right] = \nabla\cdot(s_{\mathrm{g}}F_{\mathrm{g}}^{*} + s_{\mathrm{l}}F_{\mathrm{l}}^{*}) - R \tag{3.72}$$

Conservative fluxes: The volumetric face fluxes are corrected based on the pressure solved from the pressure equation.

$$F_{\mathrm{g}}^{**} = F_{\mathrm{g}}^{*} - \frac{\frac{s_{\mathrm{g}}}{(\mathbf{A}_{\mathrm{g}})_D}}{\frac{s_{\mathrm{g}}}{(\mathbf{A}_{\mathrm{g}})_D} + \frac{s_{\mathrm{l}}}{(\mathbf{A}_{\mathrm{l}})_D}} |\mathbf{S}| \nabla_f^{\perp} p_{\mathrm{rgh}} \tag{3.73}$$

and

$$F_{\mathrm{l}}^{**} = F_{\mathrm{l}}^{*} - \frac{\frac{s_{\mathrm{l}}}{(\mathbf{A}_{\mathrm{l}})_D}}{\frac{s_{\mathrm{g}}}{(\mathbf{A}_{\mathrm{g}})_D} + \frac{s_{\mathrm{l}}}{(\mathbf{A}_{\mathrm{l}})_D}} |\mathbf{S}| \nabla_f^{\perp} p_{\mathrm{rgh}} \tag{3.74}$$

The total conservative flux is the summation of corrected gas phase flux and liquid phase flux,

$$F^{**} = F_{\mathrm{g}}^{**} + F_{\mathrm{l}}^{**} \tag{3.75}$$

Velocity correction: The phase velocities can be calculated by reconstructing the corrected phase fluxes.
Pressure correction: The final pressure is calculated from Eq. 3.67.

Solution sequence

Detailed model: The solution processes for the detailed model is summarized as below,

1. Define regions, reading material properties, and selecting solution procedure.

2. Fuel cell iteration loop:
   (a) Mapping temperature from master region to sub-regions.
   (b) Updating properties/fields in sub-regions.
   (c) Fluid region:
      i. Calculate the interfacial momentum transfer coefficients.
      ii. Semi-discretizing the momentum transfer equation(s) and predicting velocities.
      iii. PISO loop:
         - Predict phase fluxes, with Eqs. 3.69 and 3.70.
         - Construct and solving the pressure equation, Eq. 3.72.
         - Correct phase fluxes, with Eqs. 3.73 and 3.74.
         - Reconstruct phase velocities from phase fluxes.
      iv. Solve phase saturation, with Eq. 3.36.
      v. Solve heat transfer for the dispersed phase.
      vi. Solve species transfer.
   (d) Solid region:
   (e) Electron-proton region:
      - Apply Butler-Volmer or Tafel relation for electrochemical reactions.
      - Solve electron transfers.
      - Solve proton transfer.
      - Solve the dissolved water transfer.
   (f) Mapping heat source/sink from sub-regions to master region.
   (g) Master region: Solving heat transfer.

3. Output: write out the simulation results.

Homogeneous model: The solution processes for homogeneous model is summarized as below,

1. Define regions, reading material properties, and selecting solution procedure.

2. Fuel cell iteration loop:
   (a) Update properties/fields in sub-regions.
   (b) Fluid region:
      i. Calculate the interfacial momentum transfer coefficients.
      ii. Semi-discretizing the momentum transfer equation(s) and predicting velocities.
      iii. PISO loop:
         - Predict phase fluxes, with Eqs. 3.69 and 3.70.
         - Construct and solving the pressure equation, Eq. 3.72.
         - Correct phase fluxes, with Eqs. 3.73 and 3.74.
         - Reconstruct phase velocities from phase fluxes.
      iv. Solve phase saturation, with Eq. 3.36.
      v. Solve heat transfer.
      vi. Solve species transfers.
   (c) Electrolyte region:
      - Apply Butler-Volmer or Tafel relation for electrochemical reactions.
      - Solve current density distribution.
      - Calculate the dissolved water transfer.
      - Solve heat transfer.
3. Output: write out the simulation results.

3.5 Summary

In this chapter, the finite volume method application in discretizing governing equations is introduced. The computational domain, including space and time, is described at first. Afterwards, the FVM discretizations of transient, convection, diffusion, and source/sink terms on the computational domain are presented. The solution procedures in performing CFD simulations are also provided. At last, the solution sequences for the detail model and homogeneous model are shown.

Chapter 4

HT-PEFC detailed models

Abstract

In this chapter, a previous developed fuel cell model [32] was modified to consider the transport phenomena in HT-PEFCs (*model 1*). the comparisons of *model 1* with the detailed model (*model 2*) introduced in Chapter 2 were also conducted. The verification of *model 1* was performed by comparing the current density and oxygen concentration distributions with an analytical model in a one dimensional channel . The comparison between in-house experimentally gathered data and the numerical predictions of the two models presented minor deviations. Local variations of current density, and oxygen and water vapor mole fractions presented significant change from under-rib regions to under-channel regions. The serpentine type flow path resulted in higher pressure gradients, but contributed to better gas bypassing through the GDLs. This type of flow path was beneficial to the species redistribution and current density distribution. Never before had it been possible to construct such computational models that were able to predict fine-scale details in local current density variations. These details were not captured neither by previous models nor by the present-day experiments. It was also found that *model 1* and *model 2* in the present thesis presented similar results in predicting the overall cell performance and local current density distributions.

4.1 Introduction

In this chapter, two detailed models were introduced and applied on an in-house designed HT-PEFC prototype. In the following parts, *model 1* [97] represented the previously developed model, while *model 2* referred to the detailed model introduced in Chapter 2, Section 2.1. Both models considered all sub-components of HT-PEFC: the MEA, CLs, GDLs, gas channels, and BPPs.

In *model 1*, all transport phenomena, in terms of the numerical solution of the local Nernst equation for the open-circuit voltage, as well as the Kirchhoff-Ohm relationship for the local current density, allowed for local electrochemistry, fluid flow, species transport, and multi-region thermal analysis to be considered.

The difference between *model 1* and *model 2* was the way in treating the electrochemical reactions. In *model 1*, the electrochemical reactions was assumed to take place on an ultra-thin surface, while in *model 2*, the reactions happened in the catalyst (volumetric) regions. Considering the electrical potentials, *model 1* applied a Kirchhoff-Ohm relationship, while *model 2* solved the potential equations.

The flow path configuration of the HT-PEFC BPPs used in the present chapter was shown in Fig. 4.1, which was designed by Bendzulla [211] as part of a 5 kW HT-PEFC system. The fuel cell prototype considered was an in-house design [211–213], which allowed robust operating behaviors and reproducible high-level performance data to be achieved. It represented an ideal basis for the development of a 5 kW HT-PEFC system.

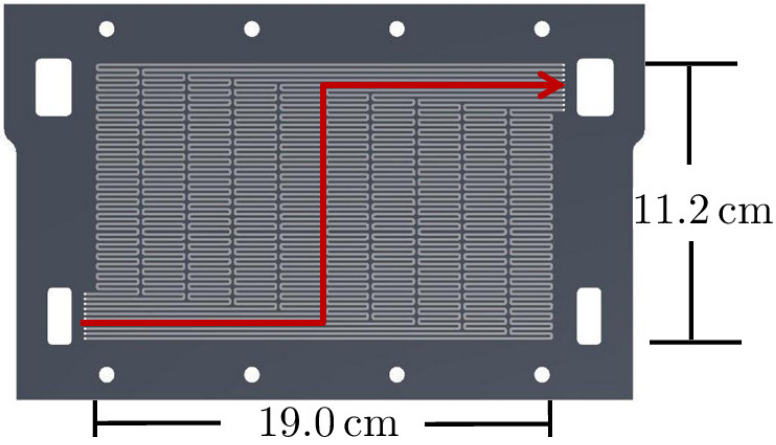

Figure 4.1: Bipolar plate used in the HT-PEFC stack. (Reproduced from [98])

On the anode side, the stack was supplied with dry hydrogen, and on the cathode side, dry air was fed. There were ten parallel flow paths, including straight paths and serpentine paths, with a nominally active area of 200 cm^2 (11.2cm $\times$ 19.0cm). The short stack contained 5 cells, therefore, the cell at the central location was selected as the reference cell to represent the overall performance of the entire stack.

4.2 Numerical analysis

4.2.1 Model 1

The governing equations of *model 1* in addressing the fluid flow, species transport, and multi-region heat transfers are similar to that in *model 2*. The Kirchhoff-Ohm relationship is applied for the cell voltage output,

$$V = E_{\text{Nernst}} - \eta_{\text{ca}} - \eta_{\text{an}} - \Omega_{\text{ASR}} i \tag{4.1}$$

where V represents the cell voltage, and Ω_{ASR} is the ohmic area specific resistance.

In HT-PEFCs, the activation overpotential at the anode side is negligibly small due to the fast HRR, $\eta_{\text{an}} \approx 0\text{V}$. In addition, a Tafel formulation is readily capable of representing the relation between activation overpotential and current density except for very low current densities,

$$i = \left(\frac{C_{\text{O}_2}}{C_{\text{ref}}}\right)^{\gamma} i_0 \exp\left(\frac{2\alpha F}{R_g T}\eta_{\text{ca}}\right) \tag{4.2}$$

Inverting Eq. 4.2,

$$\eta_{\text{ca}} = \frac{R_g T}{\alpha F} \ln \frac{i}{i_0} \left(\frac{C_{\text{ref}}}{C_{\text{O}_2}}\right)^{\gamma} \tag{4.3}$$

Subscribing Eq. 4.3 into Eq. 4.1, a formulation of current density, i, is obtained as,

$$f(i) = V - E_{\text{Nernst}} + \frac{R_g T}{\alpha F} \ln \frac{i}{i_0} \left(\frac{C_{\text{ref}}}{C_{\text{O}_2}}\right)^{\gamma} + \Omega_{\text{ASR}} i \tag{4.4}$$

The local current density, i, can be calculated via Newtons method:

$$i^{n+1} = i^n - \frac{f(i^n)}{f'(i^n)} \tag{4.5}$$

where n is iteration step.

4.2.2 Computational domain

The flow field geometry applied in the present chapter is displayed in Fig. 4.2, in which the flow channels and a sub-region are marked. The flow paths are numbered 1 - 10, with each flow channel containing 24 passes in the serpentine regions. The sub-region used in this chapter located at the center of the active area, with a size of $0.8\text{cm} \times 0.8\text{cm}$, where 5 points, namely A-E, are selected for following discussion. The master mesh is consisted of approximately 51.5×10^6 hexahedral elements. The mesh is created with a commercial program, ANSYS ICEM-CFD [37]. The total computational domain is decomposed manually by utilizing a contiguous multi-block mesh

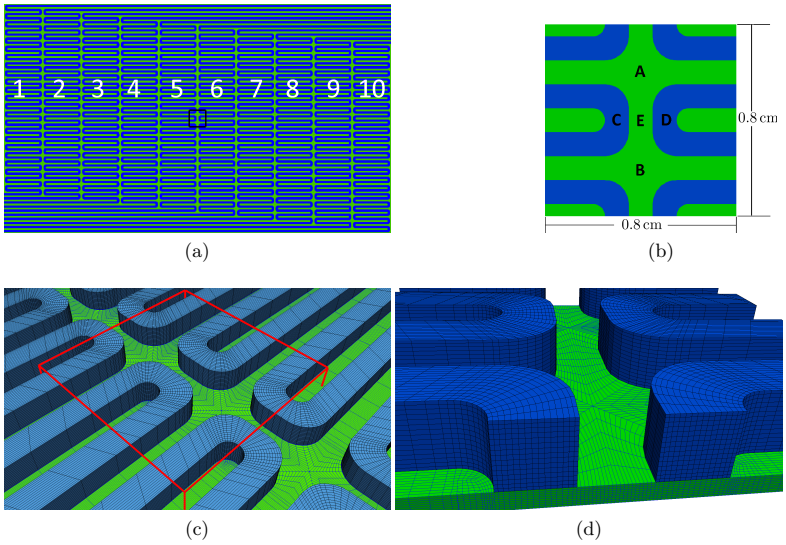

Figure 4.2: Flow channel configuration, with 10 channel-24 pass serpentine geometry: (a) active area and number of channels, from 1-10; (b) sub-region; (c) grid at local area; (d) sub-region mesh. (Reproduced from [98])

that is body-fitted to the serpentine passages and concentrated near the solid walls. The mesh is extruded through the MEA, BPPs and GDLs, as well as the gas channels.

4.2.3 Operating and boundary conditions

During operation, dry hydrogen is supplied at the anode side inlets, and dry air at the cathode side. The stoichiometric factor, λ, here is defined as the ratio of the maximum possible fuel/oxidant consumption to the actual consumption. The stoichiometric factors at anode and cathode sides are usually fixed under galvanostatic condition. The inlet velocities for hydrogen and air are calculated via Faraday's law,

$$u = \frac{M_{\mathrm{j}} A_{\mathrm{act}} \bar{i} \lambda}{\rho X_{\mathrm{j}} A_{\mathrm{in}} z F} \tag{4.6}$$

where u is velocity magnitude, M_{j} is the molar mass of each reactant (oxygen/hydrogen), A_{act} represents the active area, X_{j} is mole fraction of each reactant in the inlet gas and A_{in} represents the inlet area. Additionally, it is assumed that the fuel cell operated under isothermal boundary conditions with the temperature at the top and bottom of the BPPs maintained constant, while the side wall boundaries are treated to be adiabatic. Reactant gases enter the gas channels through the inlets at known temperatures.

Operating conditions and model parameters are summarized in Tables 4.1 and 4.2, respectively. All of these material properties, parameters and operating conditions are based on the work of Kvesić et al. [99], with the exception that the operating temperature is set as 439 K in the present chapter.

Table 4.1: Operating conditions and properties

Description	Value	Units
p_{an}	101325	Pa
p_{ca}	101325	Pa
λ_{an}	2.0(H_2)	-
λ_{ca}	2.0(air)	-
Flow-pattern	co-flow	-
T	439	K
Channel width	1.0	mm
Channel height	1.0	mm
Rib width	1.0	mm
GDL thickness	0.3	mm
Membrane thickness	0.05	mm

Table 4.2: Model parameters for *model 1* [99]

Parameters	Values
Transfer coefficient (α)	0.35
Exchange current density (i_0)	$5 \times 10^{-5}\,\mathrm{A\,cm^{-2}}$
Ohmic resistance (Ω)	$0.1\ \Omega\,\mathrm{cm^2}$
Porosity (ϵ)*	0.7
Permeability (κ_D)*	$1.0 \times 10^{-12}\ \mathrm{m^2}$
Thermal conductivity (k)*	(1.2^a, 0.95^b, 20^c) $\mathrm{W\,m^{-1}K^{-1}}$
Specific heat (c_p)*	(568^a, 1650^b, 1580^c) $\mathrm{J\,kg^{-1}K^{-1}}$

[a] GDL, [b] MEA, [c] BPP.

* Material properties are the same for the anode and cathode sides

While *model 1* assumes an ultra-thin catalyst layer, a thick catalyst layer is applied in *model 2*. Additional material properties and model parameters are shown in Table 4.3.

Table 4.3: Material properties and model parameters for *model 2* [98].

Description	value	Unit
GDL thickness	0.28	mm
CL thickness	0.02	mm
Exchange current density (i_0)	2.5×10^4 cathode 1.0×10^8 anode	$\mathrm{A\,m^{-3}}$
Transfer coefficient (α)	0.35 cathode 0.5 anode	–
Electric/protonic conductivity (σ)	20000 BPPs 5000 GDLs 2000 CLs 5 membrane	$\mathrm{S\,m^{-1}}$
Porosity (ε)	0.7 GDLs 0.2 CLs	–

The sub-regions in *model 2* include air, fuel, interconnect, membrane, and charged regions, where the former four sub-regions are the same with those in *model 1*. Charged regions (electron) represent the electron transfer fields at anode side and cathode side, respectively, including BPP, GDL, and CL. Charged regions (proton) represent the proton transfer field, including anode CL, cathode CL, and membrane.

4.2.4 Grid independence

In order to obtain a balance between the accuracy of the simulation results and the required computational effort, a computational mesh with suitable resolution needs to be selected. A fuel cell with one straight flow channel at anode and cathode sides are simulated to analyze the grid independence. Simulations are conducted for four cases with different number of mesh elements at a mean current density of 0.6 $\mathrm{A\,cm^{-2}}$. The fuel cell is separated into 20 segments from inlet to outlet. With successive mesh refinement, the segment-averaged parameters standard deviations from the case with the finest mesh are considered,

$$\sigma_\phi = \sqrt{\frac{\sum_{n=1}^{N}(\Delta\phi_n)^2}{N-1}} \tag{4.7}$$

where ϕ represents different variables, N is the number of observations in the sample ($N = 20$) and $\Delta\phi$ means the difference between the case with finest mesh and the considered mesh.

As shown in Table 4.4, the variables deviations decrease with the refinement of the grids. The predicted voltages are also provided. Considering the computational effort and precision of the results, the case with 150×10^3 elements is considered fine enough for numerical predictions. The equivalent mesh quality is then applied in the following numerical simulations.

Table 4.4: Grid dependence study

Number of points $\times 10^{-3}$	11	56	150	340
Voltage (V)	0.3934	0.3953	0.3957	0.3960
$\sigma(i) \times 10^3\,(\mathrm{A\,cm^{-2}})$	1.11	0.56	0.14	0
$\sigma(X_{\mathrm{O_2}}) \times 10^3$	2.05	0.4	0.2	0
$\sigma(X_{\mathrm{H_2O}}) \times 10^3$	3.09	0.67	0.39	0
$\sigma(p)\,(\mathrm{Pa})$	0.86	0.25	0.07	0

4.3 Results

4.3.1 Analytical verification for *model 1*

A comparison of *model 1* with the analytical solution derived by Kulikovsky et al. [214] for a 1-D idealized fuel cell operating under steady state conditions are provided. In calculating the analytical solution, the authors made several assumptions, including negligible transport limitations, perfect mixing, constant velocity, density and temperatures, no anodic losses, and no membrane hydration issues. The final expressions for oxygen concentration

and current density distributions along the channel were found as a function of cathode stoichiometric factor,

$$\frac{c\,(x)}{c_{\text{in}}} = \left(1 - \frac{1}{\lambda}\right)^{x/L} \tag{4.8}$$

$$\frac{i\,(x)}{\bar{i}} = \left(-\lambda \ln\left(1 - \frac{1}{\lambda}\right)\right)\left(1 - \frac{1}{\lambda}\right)^{x/L} \tag{4.9}$$

where $c\,(x)$ is local oxygen concentration, c_{in} is reference oxygen concentration, $i\,(x)$ is local current density, $\bar{i}$ is mean current density, λ is stoichiometry factor, and L is the cell length.

Assumptions are also made during the numerical simulations, including gas diffusion layers are eliminated at both anode and cathode sides, and diffusion coefficients are defined to be 100 times of that in normal condition. Three different cases are simulated by varying the stoichiometric factor, corresponding to 2, 4, and 10.

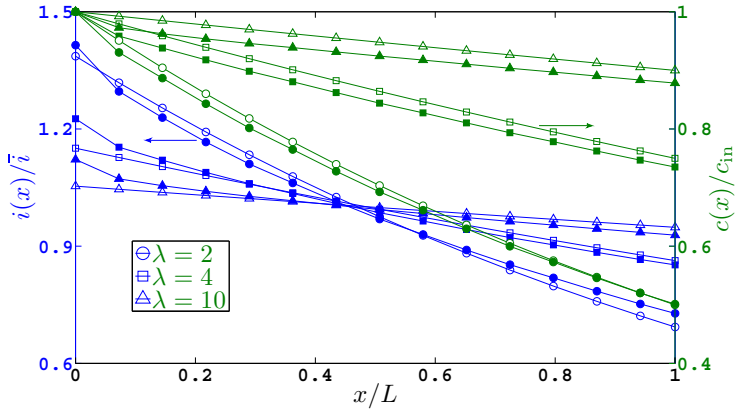

Figure 4.3: Analytical solution (void) and simulation results (solid), oxygen mole fraction (right) and current density (left) distributions along the channel, $\lambda = 2, 4, 10$. (Reproduced from [97])

It can be seen from Fig. 4.3 that the numerically simulated oxygen concentration and current density distributions are in good agreement with the analytical solution from the inlet to outlet for three different stoichiometric factors. For oxygen concentration distributions, a maximum deviation of 2.5% is found at $\lambda = 10$, while the largest deviation for current density distribution, 6.6%, is observed when $\lambda = 4$. Hence, slight difference exists between numerical simulations and analytical solutions. The simplifications

made for the numerical model are not sufficient to fulfill all of the assumptions in the analytical solution, while the densities are changing, streamwise velocities are also varying.

4.3.2 Experimental validation for *model 1*

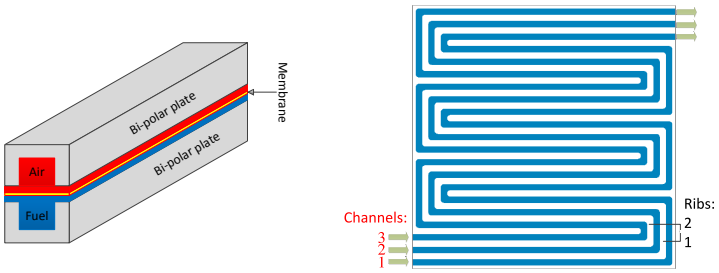

(a) (b)

Figure 4.4: Diagram of fuel cell composition and flow path used in the verification and validation. (a) Straight geometry; (b) Serpentine geometry. (Reproduced from [97])

A triple-channel serpentine fuel cell prototype designed in-house, shown in Fig. 4.4, is selected for the validation of the numerical model. The deassembled single cell is shown in Fig. 4.5, where the current collecting cables are directly connected to the endplates on both the anode and cathode sides. No additional heat removal system is implemented for this single cell. Heating of the cell is achieved via heating tubes inserted into the endplates. The gas inlets and outlets are placed in each endplate. In addition, special holes are placed for temperature measurement.

The operating conditions and physical properties for the numerical simulations are summarized in Tables 4.5 and 4.6. The single cell are assembled with components designed in-house except for the MEA, which is manufactured by BASF, Celtec P1100W. The total compression of the MEA in the fuel cell assembly is found to be 16 - 20 %. Stainless steel end-plates are employed and Sigraflex gaskets are applied for sealing. Graphite based composite BPPs with three serpentine flow paths are used to distribute gases over the active area of the MEA. The MEA is placed between two PerFluoroAlkoxy gaskets to guarantee proper sealing and compression.

The schematic diagram of the test station used to conduct the experimental measurement is presented in Fig. 4.6. The cell were operated for 72 hours at a constant current density of $0.2\,\mathrm{A\,cm^{-2}}$ with dry hydrogen at the anode side and dry air at the cathode side. The stoichiometric factors

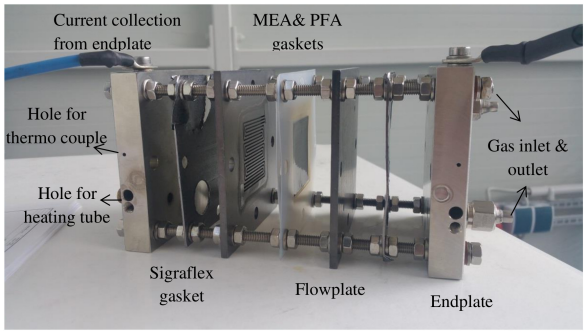

Figure 4.5: Deassembled view of the cell. (Reproduced from [97])

Table 4.5: Geometry and operating conditions in validations

Description	Value	Units
Anode/cathode outlet pressure	101325	Pa
λ_{an}(fuel)	2	-
λ_{ca}(air)	2/6	-
Flow-pattern	co-flow	-
Anode/cathode inlet temperature	433	K
Channel width	1	mm
Channel height	1	mm
Rib width	1	mm
GDL thickness	0.3	mm
Membrane thickness	0.02	mm

Table 4.6: Model parameters in validations, *model 1*

Description	Value	Ref.	Units
Transfer coefficient (α)	0.67	Fitted	-
Exchange current density (i_0)	0.14	Fitted	$\mathrm{A\,m^{-2}}$
Ohmic resistance (r)	0.2	Measured†	$\Omega\,\mathrm{cm^2}$
Porosity (ϵ)*	0.75	-	-
TP permeability of GDL (κ)*	1.0×10^{-12}	-	$\mathrm{m^2}$
IP permeability of GDL (κ)*	1.0×10^{-11}	-	$\mathrm{m^2}$
Thermal conductivity (k)*	1.2^{a}, 0.95^{b}, 20^{c}	[99]	$\mathrm{W\,m^{-1}K^{-1}}$
Specific heat (c_p)*	568^{a}, 1650^{b}, 1580^{c}	[99]	$\mathrm{J\,kg^{-1}K^{-1}}$

* Material properties are the same for anode and cathode sides.

† This is measured by electrochemical impedance spectroscopy in-house.

^{a,b,c} GDLs, membranes, bi-polar plates.

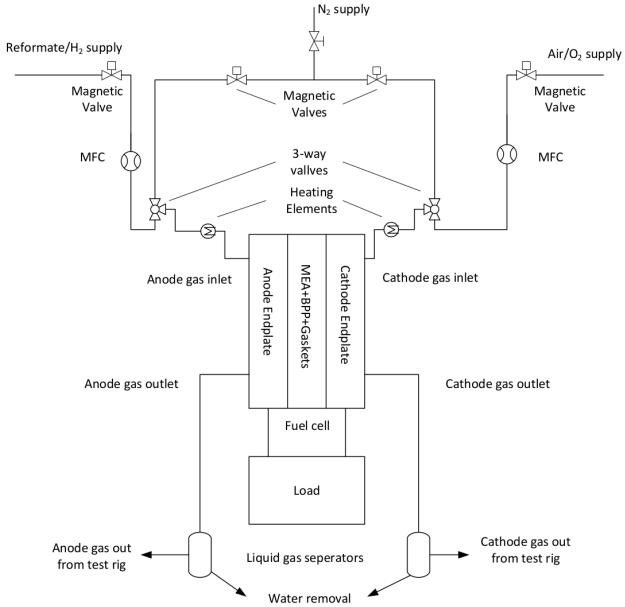

Figure 4.6: Schematic of the fuel cell test station used for the experiments. (Reproduced from [97])

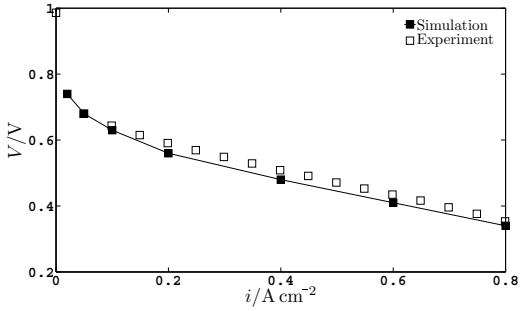

Figure 4.7: Comparisons of polarization curves from numerical and experimental results, $\lambda = 2/2$. (Reproduced from [97])

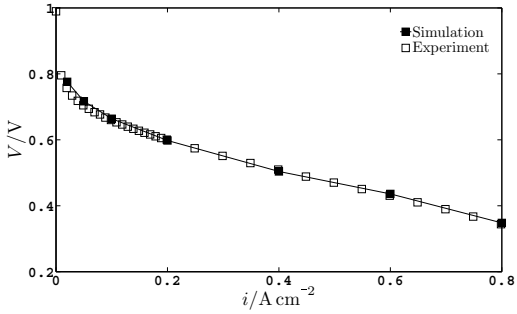

Figure 4.8: Comparisons of polarization curves from numerical and experimental results, $\lambda = 2/6$. (Reproduced from [97])

were fixed as 2 and 2 for anode and cathode sides, respectively, as a break-in (commissioning) procedure. After that, the polarization curves were measured with an anode/cathode stoichiometric factors of $\lambda = 2/2$ and $\lambda = 2/6$, respectively, at a cell temperature of 433K. During the injection of reactants, the stoichiometric factors were constant when the current density was larger than $0.2\,\mathrm{A\,cm^{-2}}$. Under lower current density loads, the injection flow rates were fixed corresponding to that at $i = 0.2\,\mathrm{A\,cm^{-2}}$.

Numerical simulations were performed on the corresponding fuel cell prototypes under the same operating conditions. The comparison of polarization curves are plotted in Figs. 4.7 and 4.8 for $\lambda = 2/2$ and $\lambda = 2/6$, respectively. It can be seen that the deviations between the numerical predictions and experimental measurements are minor at all measured current densities. The most significant differences for each case, are $25\,\mathrm{mV}, 5.7\%, i = 0.6\,\mathrm{A\,cm^{-2}}$ and $20\,\mathrm{mV}, 2.5\%, i = 0.02\,\mathrm{A\,cm^{-2}}$, respectively. Considering the uncertainty in the experimental measurements is about 5%, it is therefore suggested that the HT-PEFC model applied here is capable to predict the overall performance of fuel cells for this, and other designs.

4.3.3 Simulation results of *model 1*

Polarization curves

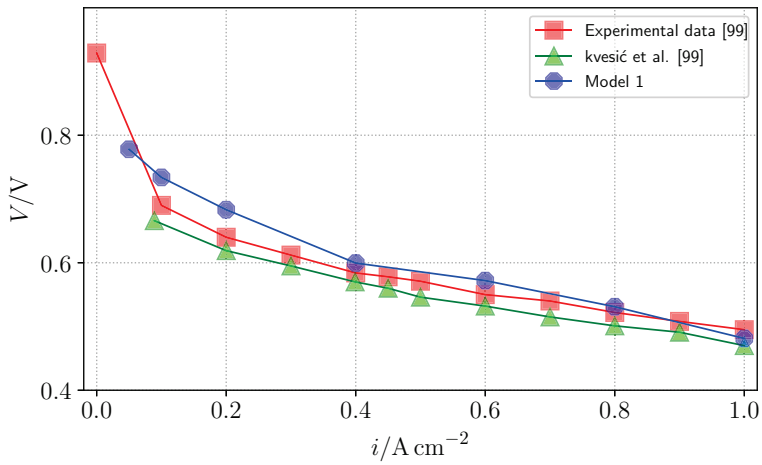

Figure 4.9: Polarization curves comparison between the present results [98], past numerical result [99] and experimental data [215]. (Reproduced from [98])

The polarization curves predicted by *model 1* [98], and the prior model

of Kvesić et al. [99], and data measured by Lüke [215], are shown in Fig. 4.9. The present simulations are for a detailed numerical method while the results of Kvesić et al. [99] are based on a volume average approach, see also Beale and Zhubrin [33]. Inspection of Fig. 4.9 reveals that the detailed calculations present slightly higher voltages at low current densities, while the averaged model provided slightly lower voltages under all current densities. These are due to the different polarization curve models. In the model of Kvesić et al. [99], a constant value for the Nernst voltage with the argument that the average concentrations does not vary significantly for constant stoichiometry is applied. This simplification works well for coarse engineering approaches. In *model 1*, the Nernst voltage is calculated locally. The calculated Nernst voltage is higher than the values measured under open circuit condition for the fuel cells. As discussed in Reimer et al. [41], a range of values of α, Ω_{ASR} and i_0 can provide essentially identical polarization curves. As the intention of the present work is to compare the coarse grained approach with the high resolution approach, the same model parameters as those in Kvesić et al. [99] are applied here. It is found that the deviation of the detail model from the experimental polarization curves is within a maximum of 6%. While the error in the experiment is about 5% [216], the deviation is minor.

Current density

The local current density distribution is an important attribute to assess the performance of fuel cells. It also serves as a measure to evaluate the fidelity of model predictions. The local current density distribution is shown in Fig. 4.10 at a mean current density of $i = 0.6\,\mathrm{A\,cm^{-2}}$. Figure 4.10(a) presents the results of the detailed model at a location between the cathodic GDL and membrane. Figure 4.10(b) shows the results of Kvesić et al. [99], whereas Fig. 4.10(c) exhibits the experimental measured data from Lüke [215]. While the experimental data and the numerical results of [99] are collected outside of the BPPs between the 3rd and 4th cells of the short stack, the numerical results predicted by the detailed model here are on a single cell. It can be observed that the local current density distributions of the three different data sets are qualitatively and quantitatively in good agreements. The current density is at a global maximum near the inlet and a minimum near the outlet due to the consumption of oxygen and hydrogen, and the production of water vapor. Hence, the detailed model compares favorably with both previous numerical and experimental results [99, 215] for a short stack under similar operating conditions.

The histogram shown in Fig. 4.11 represents the relative frequency density of current densities in the active area for numerical and experimental results. The relative frequency density is calculated as,

$$f_{\mathrm{j}} = \frac{\Delta N_{\mathrm{j}}}{N} \tag{4.10}$$

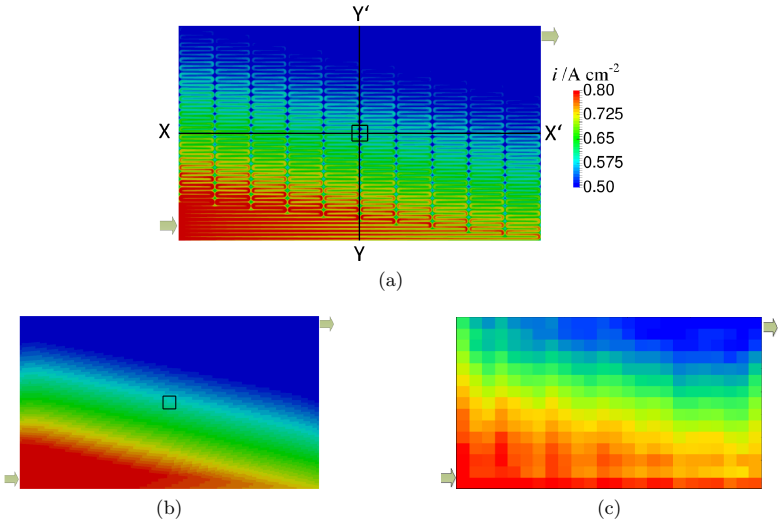

Figure 4.10: Local current density distribution, $i = 0.6\,\mathrm{A\,cm^{-2}}$: (a) results of present simulation [98]; (b) results from past simulation [99]; (c) experimental measured data [99], by S++ [63] current scan shunt. (Reproduced from [98])

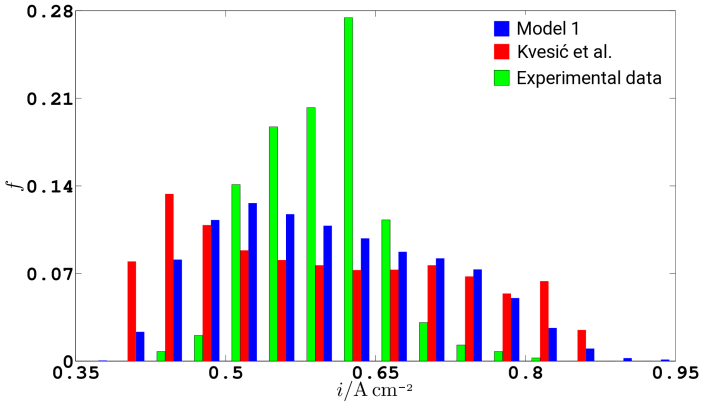

Figure 4.11: Current density relative frequency of present ($N = 727 \times 10^3$), previous ($N = 10 \times 10^3$) [99] numerical results and experimental ($N = 0.39 \times 10^3$) data [215], $i = 0.6\,\mathrm{A\,cm^{-2}}$. (Reprinted from [98])

where N represents the number of data points, and ΔN_{j} is the number of values between i and $i + \Delta i$.

These charts are important in evaluating the current density distributions, as they demonstrate that while there is a global agreement in the mean values, the variance of current density distribution is greatly higher than those indicated by the volume average approach and experimental measurements.

The differing statistical moments, including variance, skewness, curtosis etc., may provide possible explanations for the differences observed in Fig. 4.9. While it is true that the ohmic resistance, Ω_{ASR}, is assumed constant, and therefore the ohmic resistance is linear with i (i.e., not affected by higher moments). This is not true for activation overpotential, η_c, which is a logarithmic function of i. These would present effects on the polarization curve for any mean value of i, proportionately more so for lower mean/local current density conditions. This reinforces the importance of mesh independent analysis in CFD models.

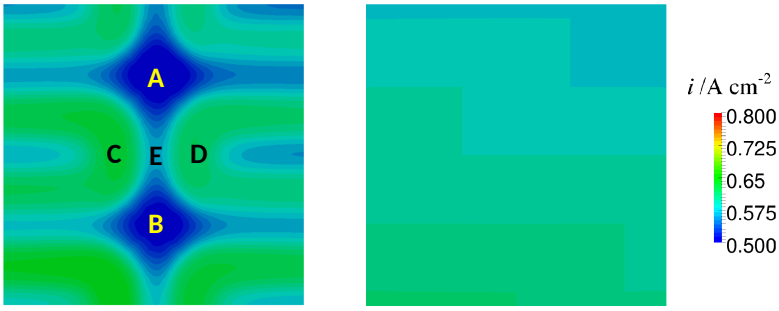

Figure 4.12: Current density distributions in sub-region, marked in Figure 4.2, of: (a) present and (b) previous [99] numerical results, $i = 0.6\,\mathrm{A\,cm^{-2}}$. (Reproduced from [98])

Additionally, differences between the volume average approach and the detailed model here are clear as shown in Fig. 4.12, which are enlargements of the sub-regions marked with rectangular boxes in Fig. 4.10. Local extrema in current density existing under the channel regions, points C and D, and rib regions, points A and B, are shown in Fig. 4.12 and are to be expected. It is clear that the local extrema cannot be captured by the previous work based on the volume averaging approach, as shown in Fig. 4.12(b). The local variations are smeared out due to the granularity of the methodology. That is to say, the detailed model here provided much superior spatial resolution over the previous work. The existence of local extrema can and

would present effects on the local performance of the cell and therefore the overall performance and long-term durability.

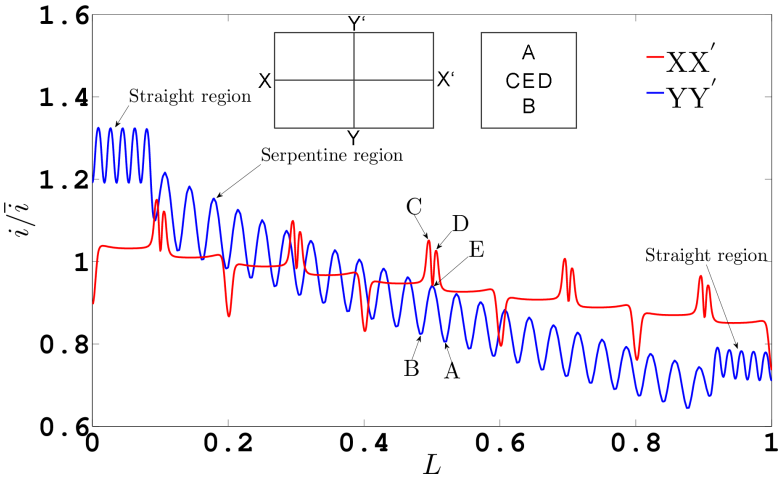

Figure 4.13: Current density distribution along sections XX′ and YY′, $i = 0.6\,\mathrm{A\,cm^{-2}}$. (Reproduced from [98])

In addition, the local current density distributions along the sections XX′ and YY′, shown in Fig. 4.10, and along the flow channels 1 and channel 10, shown in Fig. 4.2, are plotted in Fig. 4.13 and Fig. 4.14, respectively. In these figures, the current densities and distances are normalized.

Figure 4.13 shows the current density variations following the straight lines, XX′ and YY′. It can be clearly seen that the peaks and troughs appear periodically for both line XX′ and line YY′. These peaks and troughs are corresponding to the sites under the channel and under rib regions. Along line XX′, 10 local maximum can be found, each of which represented an under-channel locations as shown by regions C and D in Fig. 4.2. Similarly, regions A, E, and B appear periodically in serpentine region, which can be seen from the current density variations along line YY′. In the center, region E is a saddle point. It can be observed that large variations of current density in the under-channel regions and under-rib regions are significant. These local variations are completely damped-out in both the experimental and previous volume average approach results.

Current density variations along the flow paths are exhibited in Fig. 4.14. In this figure, only channel 1 and channel 10 are presented as the current density variation curves along the other channels are located between them. In addition, only 5% deviations are seen between the mean current densities that are averaged along each individual channel. The serrated shapes in the

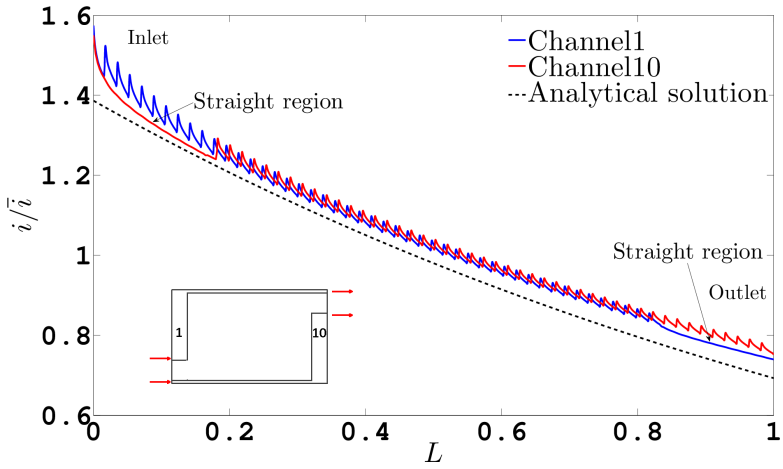

Figure 4.14: Current density distribution along channel 1 and channel 10, $i = 0.6\,\mathrm{A\,cm^{-2}}$. Analytical solution from Kulikovsky et al. [214] is also plotted. NB: $\bar{i}$ is for the whole cell, whereas i is located at the channel central line and therefore higher than at the rib location. (Reproduced from [98])

curves represent the serpentine parts of the flow channels, the maximum local variation of which is found to be 4.9%. The smooth parts of the curves represent the straight flow channels. It can be observed that the local current densities are higher for channel 1 near the inlet region and for channel 10 near the outlet region. It is revealed that the serpentine flow path contributes to higher current densities as compared to the straight flow path. Overall, the current density distribution along the flow channels approximately follows the analytical solution from Kulikovsky et al. [214], as shown in Fig. 4.14.

Oxygen and water mole fractions

The oxygen and water vapor mole fraction distributions on the reacting surface located at the base of the cathode GDL are shown in Fig. 4.15. As oxygen is consumed and water is produced during the electrochemical reaction, the oxygen mole fraction decreases from the cathode inlet to the outlet while the water vapor mole fraction increases. The local values of oxygen and water vapor mole fractions on the sub-region are also shown in Fig. 4.15. It can be seen that regions A and B, which are located under the innermost ribs, present the lowest oxygen mole fractions and highest water vapor mole fractions. When it comes to regions C and D, which are located

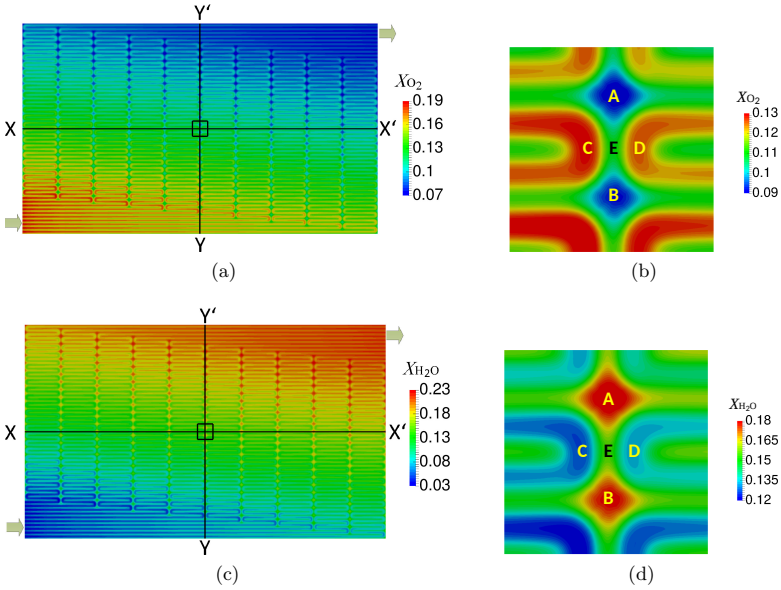

Figure 4.15: Global (a) oxygen (c) water vapor and local (b) oxygen (d) water vapor mole fractions distributions, $i = 0.6\,\mathrm{A\,cm^{-2}}$. NB: the distributions in sub-regions are relegend for better observation. (Reproduced from [98])

just under the channels, showed opposite situations. The center region E is also observed as a saddle point for both oxygen and water vapor mole fractions distributions. It is clear that regions near the gas channels provided higher current density and oxygen mole fraction but lower water mole fraction. As the GDLs are assumed to be homogeneous and isotropic, the further the distance that is traversed away from the gas channel, the larger the decrease of oxygen mole fraction due to the mass transfer phenomena. Conversely, the water vapor needed to transfer for the longest distance to enter the gas channels.

To account for the local values of oxygen and water vapor mole fractions, line XX′ and line YY′ are selected here to display the local variations in Fig. 4.16. Compared to the current density variation along line XX′ and line YY′, oxygen and water mole fractions exhibit similar and inverse distributions, respectively. It can be seen that the slope of oxygen and water vapor mole fractions variations in the straight regions is much smaller than that at the serpentine regions, as shown in Fig. 4.16.

The oxygen and water mole fractions along flow paths at the center of the channels and the values at the base of the cathode GDL are displayed in Fig. 4.17. The oxygen mole fractions are almost identical along channel 1 and channel 10, from cathode inlet to outlet, in the gas channels, which is also true for water vapor. The same situation can also be observed in channels $2-9$ (not shown here). With respect to the GDLs, the oxygen mole fraction is slightly higher under the serpentine channel regions than that under the straight channel regions; again, this is inverted for water vapor. Therefore, it is postulated that the serpentine flow path is beneficial for reactants and products redistribution, as the current density and oxygen mole fraction are found to be higher in serpentine regions, while the water vapor mole fraction is lower in serpentine region. The mole fraction of oxygen/water inside gas channels is higher/lower than that under channel (at the base of GDL), as is to be expected. In the meantime, the deviations of values between in-channel and under-channel vary slightly along the flow paths, ranging from 0.014 to 0.02, and 0.02 to 0.027, in Fig. 4.17 for oxygen and water, respectively.

Fluid flow and pressure distribution

The pressure coefficient was defined here as:

$$p_{\prime} = \frac{p - p_0}{1/2\rho {u_{\text{in}}}^2} \tag{4.11}$$

where p is the local pressure, ρ is the mixture density, p_0 is the outlet pressure and u_{in} represents the magnitude of the inlet velocity.

The pressure variation along 10 channels of the cathode side channel from the inlet to the outlet was shown in Fig. 4.18. It can be found that the

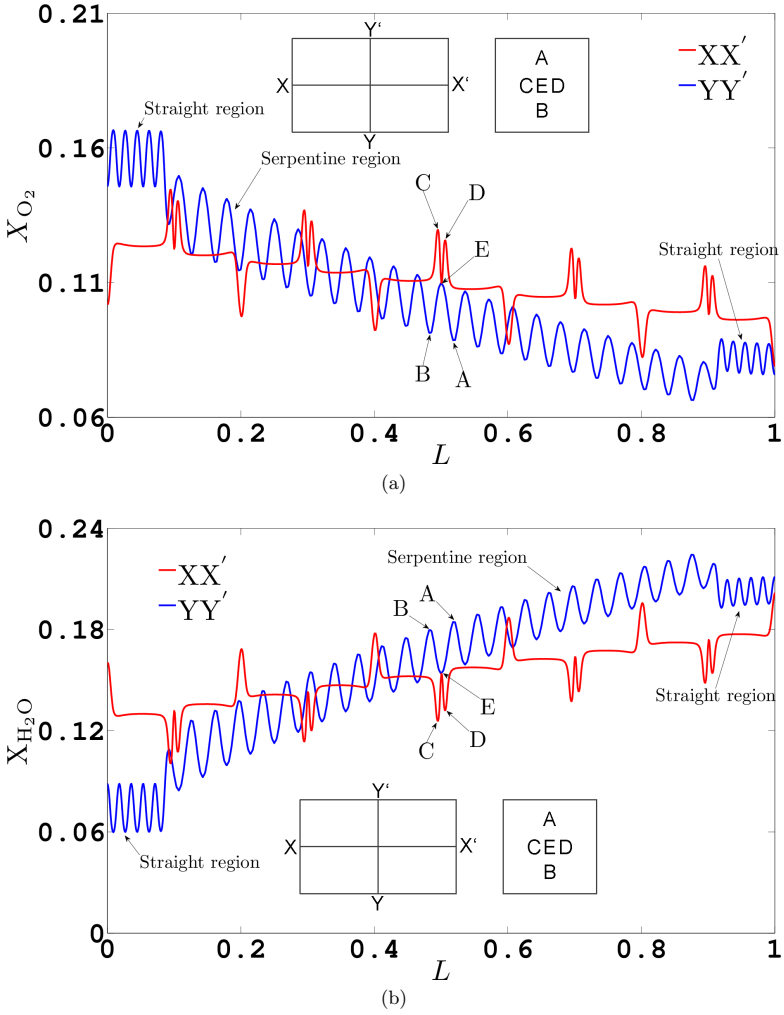

Figure 4.16: Oxygen (a) and water (b) mole fraction distribution along sections XX′ and YY′, $i = 0.6\,\mathrm{A\,cm^{-2}}$. (Reproduced from [98])

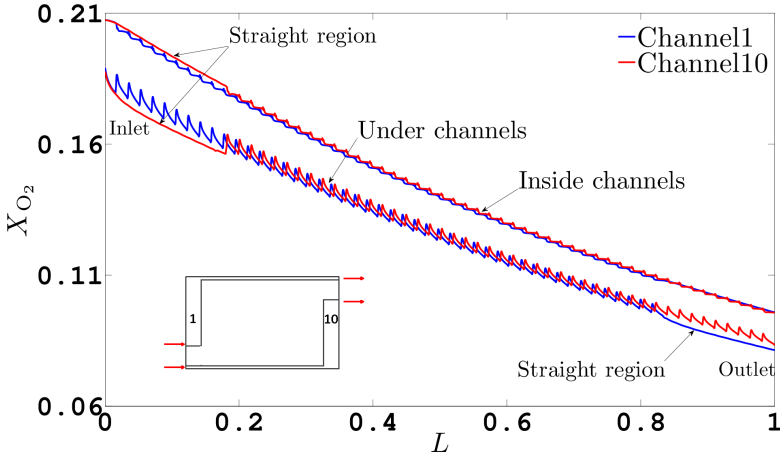

(a)

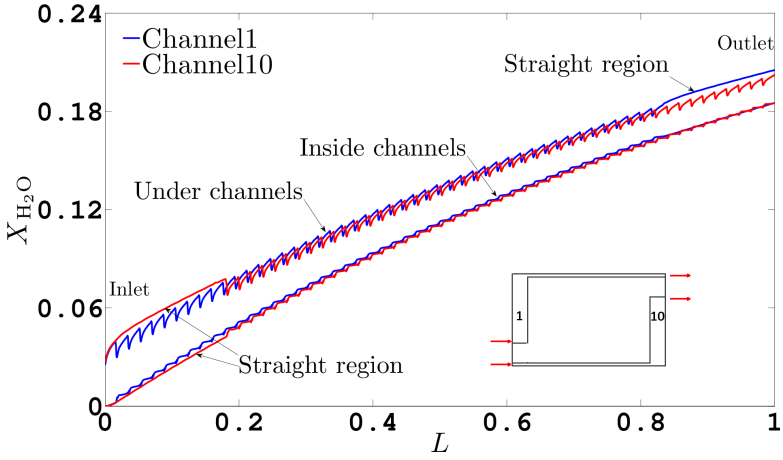

(b)

Figure 4.17: Oxygen (a) and water (b) mole fraction distribution along channel 1 and channel 10, $i = 0.6\,\mathrm{A\,cm^{-2}}$. (Reproduced from [98])

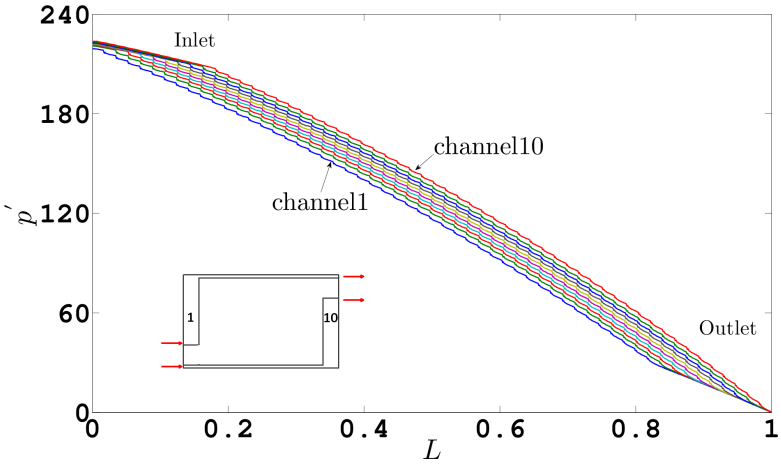

Figure 4.18: Pressure coefficient along the channels, $i = 0.6\,\mathrm{A\,cm^{-2}}$. (Reprinted from [98])

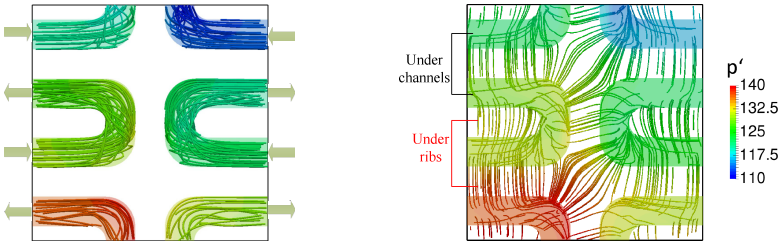

(a) (b)

Figure 4.19: Streak lines in the sub-region, colored by the pressure coefficient magnitude: (a) gas channels; (b) GDL, $i = 0.6\,\mathrm{A\,cm^{-2}}$. (Reprinted from [98])

pressure drop slopes were almost identical in the serpentine regions, as well as in the straight regions. The difference between the slopes in the serpentine and straight regions revealed that the pressure drop in the serpentine flow channels was larger than that in the straight channels. The magnitude of the slope of the pressure drop in the serpentine region was 1-2 times higher. The slope of the pressure was observed increasing in magnitude, with the total pressure decreasing and velocity increasing. To represent flow bypassing the gas channels through the GDLs, the streak lines in the channels and GDLs were displayed in Fig. 4.19. The gas flow in the channels was in the laminar regime, as the Reynolds number based on the inlet velocity and hydraulic diameter was only 379, which indicated that the convection was predominated in the gas channels and the main flow direction was perpendicular to the channel cross-section. The streak lines in the GDLs indicated the gas by-passing through the GDL between gas channels. Although the serpentine-type flow path resulted in higher parasitic losses, it contributed to reactant and product redistribution in the GDLs and between gas channels, as well as flow bypassing the channels through the GDLs.

4.3.4 Simulation results of *model 2*

Polarization curves

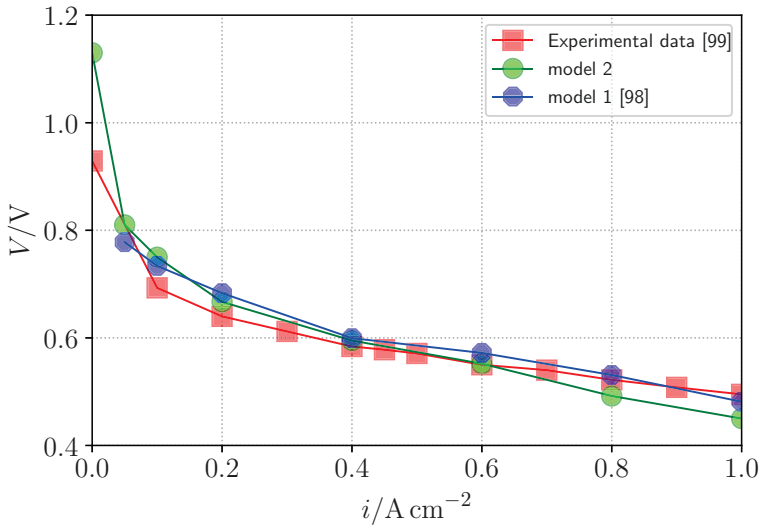

Figure 4.20: Polarization curves of experimental data [99] and numerical results [98].

The polarization curves from the experimental measurements, *model 1*, and *model 2* are shown in Fig. 4.20. It can be seen that all of the polarization curves are similar in terms of predicted voltages. There exist slight deviations between experimental measurements and numerical simulations. Concerning the error in experiment measurement of 5%, the numerical predictions deviations are within reasonable range. Therefore, both models present similar results, which agree well with the experiment data.

Global current density distributions

While the overall performance can be well predicted by *model 1* and *model 2*. The local properties are important to evaluate the performance of *model 2*. The current density distributions measured via S++ [63] device, as well as previous numerical predictions, were already shown in Fig. 4.10. Figure 4.21 exhibits the current density distributions predicted by *model 2*, in which the current density distributions in the membrane, as well as on the outer surface of BPPs, are shown. It can be seen that the general current density distributions predicted by *model 2* are in good agreement with the experimental measurement. Due to the consumption of oxygen and the production of water at cathode side, the oxygen concentration decreases while the water concentration increases, which results in higher electrochemical reaction rates near the inlet region and lower electrochemical reaction rates at the outlet region. Qualitatively and quantitatively speaking, *model 2* is capable of predicting the local current density variations for the fuel cell applied in the present study.

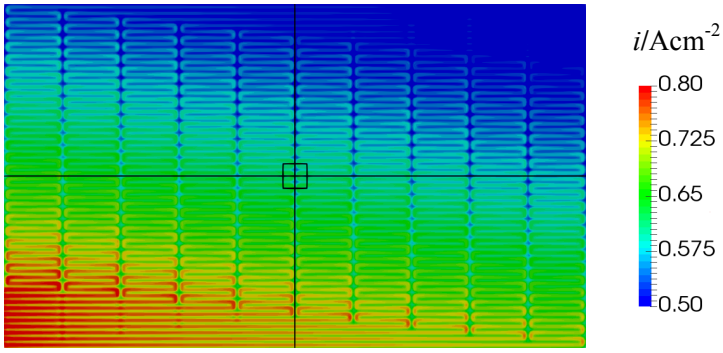

Figure 4.21: Global current density distributions, $i = 0.6\,\mathrm{A\,cm^{-2}}$.

In conducting the experimental measurements, the S++ device is placed outside of the BPPs to mitigate the influence on cell operation [215]. The numerical predictions presented in Figs. 4.10 and 4.21 were all taken from

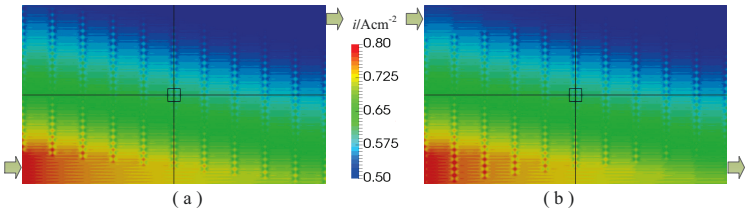

Figure 4.22: Current density distributions, $i = 0.6\,\mathrm{A\,cm^{-2}}$. (a) cathode side; (b) anode side.

inner surfaces of the cell. To represent the smear effects of BPPs, the current density distributions at the top (cathode) surface and the bottom (anode) surface are therefore shown in Fig. 4.22. Compared with the current density in the membrane (Fig. 4.21), it can be seen that the distributions at the top and bottom surfaces are more uniform. Nevertheless, the global tendencies of anodic and cathodic current density distributions exhibit reasonable agreements with the experimental data (see Fig. 4.10(d)).

Comparing the current density distributions at anodic and cathodic surfaces, it is observed that the local values differ from each other. In addition, the smearing effects are found not only acting on the global current density distributions, but also on the local values.

Local current density distributions

A sub-zone is selected to represent the smearing effects of BPPs and the MEA, where the sub-zones are marked in Figs. 4.2 and 4.22 with a dimension of $0.8 \times 0.8\,\mathrm{cm^2}$. The current density distributions in the sub-zone are compared between the present results, and the result obtained by *model 1* [98], which were shown in Fig. 4.23. It can be seen that current density distribution in the membrane for *model 2* is similar to that predicted by *model 1* [98]. The difference is observed when the local minimum values are considered. Model 1 showed slightly lower minimum value than that of *model 2*. The in-plane protonic conductivity in the CL, which is not taken into account by *model 1* [98], might result in a more uniform distributed current density, namely a slight higher minimum current density and lower maximum value. As the thickness of the MEA is very small, the effects are therefore minor.

The sub-zones at cathode and anode sides provide much more uniform current density distributions, which can be clearly seen from Fig. 4.23. The local maximum and minimum values can still be distinguished, while the local maximum values are observed above and below the land/rib regions, and the local minimum values are found above and below the channel regions,

for cathode side and anode side respectively. As presented in the previous work [98], also shown by the results of *model 1*, the current density distributions in the membrane show different situations. The local maximum current densities are observed at the locations that have the largest distance to the gas channels. Conversely, the local minimum values are detected at the locations that are closest to the gas channels. The reactant (oxygen) need to diffuse from the gas channels to the reaction sites. In other words, the local maximum values are located under the channel and the minimum values are found under the lands/ribs.

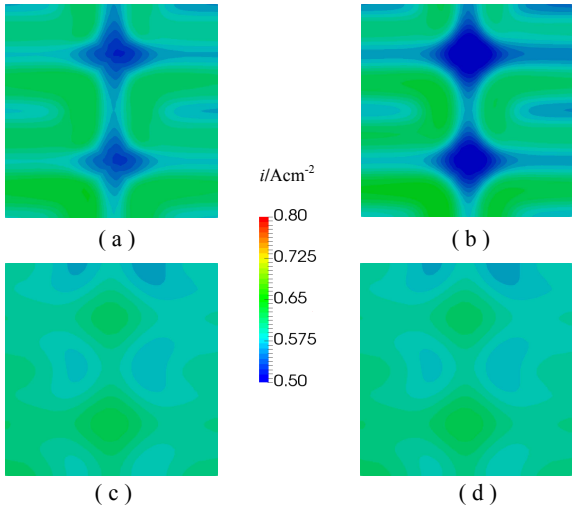

Figure 4.23: Local current density distributions on sub-zone, $i = 0.6\,\mathrm{A\,cm^{-2}}$. (a) Model 2, membrane; (b) Model 1 results, membrane [98]; (c) Model 2, cathode side; (d) Model 2, anode side.

Additional comparisons are conducted by choosing two lines, by means of a horizontal and a vertical lines, which are shown in Figs. 4.10 and 4.22. The current density values along the lines, are displayed in Fig. 4.24 and Fig. 4.25, respectively. It can be observed that the local variations are similar for the results presented in the MEA for both models. Model 1 provided slightly larger local variations compared to that predicted by *model 2*. Nevertheless, both models presented similar current density distributions locally and globally. From Fig. 4.24, it can be seen that the current density decreased from left side to right side, which is true for the distributions at either membrane or the BPP surfaces. It can be seen that the current densities at anodic and cathodic surfaces are almost identical along the horizontal

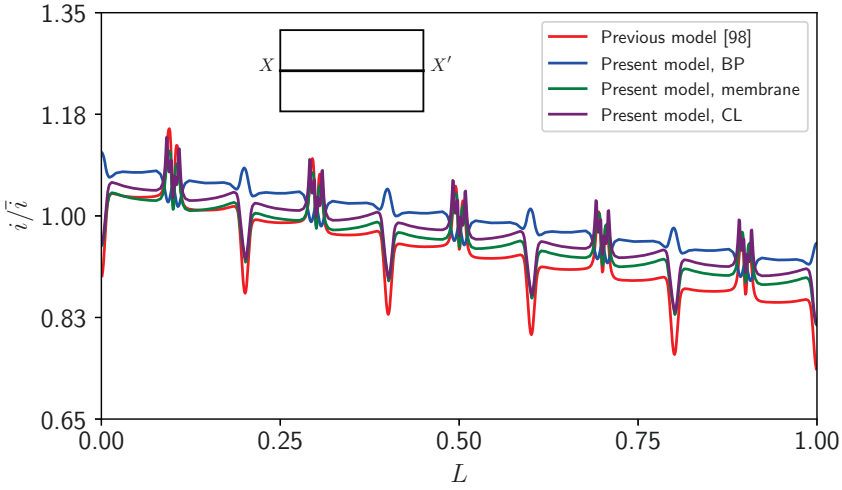

Figure 4.24: Current density along the horizontal (left to right) line, $i = 0.6\,\mathrm{A\,cm^{-2}}$. (Note: the current density and the distance are normalized).

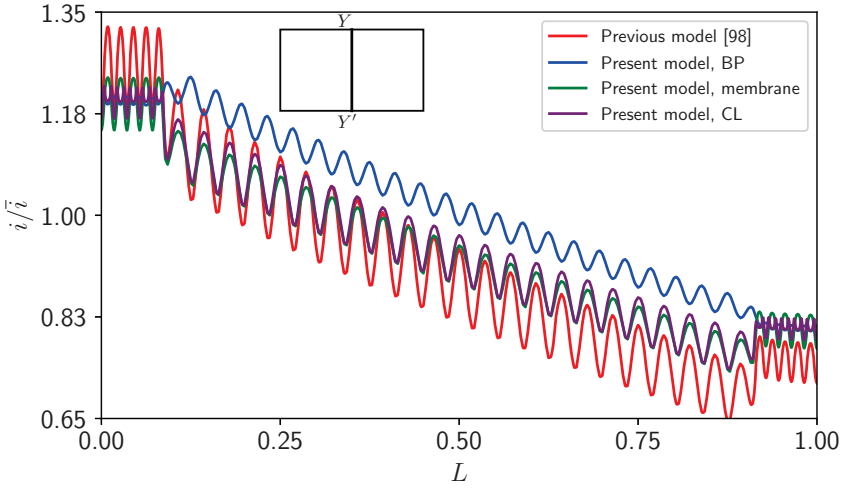

Figure 4.25: Current density along the vertical (bottom to top) line, $i = 0.6\,\mathrm{A\,cm^{-2}}$. (Note: the current density and the distance are normalized).

line, while those in the membrane presented deviations. The distributions of the local maximum and minimum values are reversed for the current density at the BPP surfaces and in the membrane. The ranges of local maximum to minimum values decrease at the BPP surfaces due to the smearing effects of BPPs. Figure 4.25 exhibited the current density along a vertical line presented similar scenario.

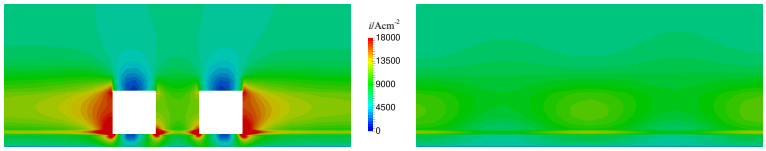

Figure 4.26: Current density distributions in through-plane direction, $i = 0.6\,\mathrm{A\,cm^{-2}}$. (a) slice CD; (b) slice AB. (Shown in Fig. 4.2(b))

To account for the smearing effects of BPPs, two slices, namely AB and CD, are selected from the potential field at the cathode side, which are marked in Fig. 4.2(b). The current density distributions in through-plane direction are shown in Fig. 4.26. It is easy to find the significant influence on the current density distribution due to the existence of gas channels. The gas channels are filled with insulated air/fuel, therefore, the electrical current cannot pass through these regions. In such case, the electrical current flows around the gas channels, which leads to very high current at the outside surfaces and bottom corners. The current density in the regions above the gas channels are smaller compared to that above the lands/ribs. Figure 4.26(b) presents the current density in the land/rib region, where the distribution is more uniform. The electrical conductivity of the porous GDLs and the BPPs are very high, which results in more uniform current density distributions on the outer surfaces. The presence of gas channels alters the local properties of current density distributions.

The local current density variations in through-plane direction are presented by picking up a point E (see Fig. 4.2(b)). The electronic and protonic current density variations in the MEA are shown in Fig. 4.27. It can be seen that the current density increases and decreases almost linearly at cathode side from the CL to membrane for electron and proton, respectively. Those at anode side the current density increased and decreased quickly at first then with flatter slop, respectively. Pure hydrogen is supplied at anode side, therefore, the hydrogen molar concentration variation is minor at anode side. Considering that the curves are not symmetric at both sides, it reveals that the oxygen concentration variation in the CL of cathode side is significant.

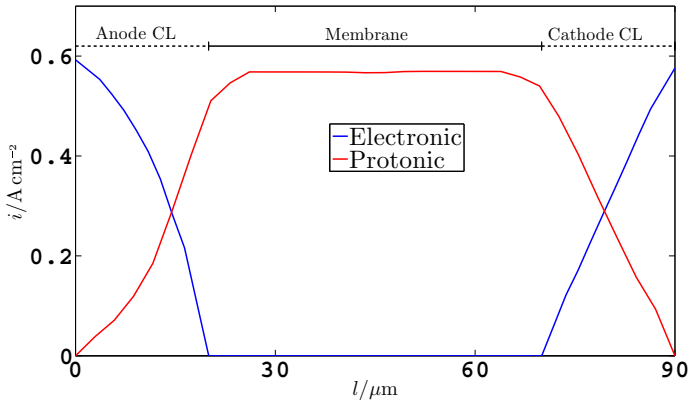

Figure 4.27: Current density in the MEA, $i = 0.6\,\mathrm{A\,cm^{-2}}$.

4.4 Discussion

Two detailed models are introduced and applied to a single HT-PEFC. The overall cell performance and current density distributions can be readily predicted with minor deviations. Although the grids with approximately 50×10^6 cells consumed significantly computational effort, the cost is justified by the level of detail in the spatial resolution of important parameters, including current density, species mole fraction, pressure, etc.

While previous experimental measurements and coarse numerical predictions present fairly good agreement on the overall behavior, the detailed local variations cannot be captured. The models applied in this thesis allows for local analysis of the finest level of resolution in macroscopic scale to be undertaken. Generally speaking, an even current density distribution means a fuel cell with better design. The work of Kvesić et al. [99] provided current density distributions with relative uniformity, whereas the results predicted by the present models reveals that the local current density varies substantially.

The gas convective transport in the GDLs was analyzed in the work of Pharoah [217], Park and Li [178], Niu et al. [218], and Bachman et al. [219]. The results in the present study fit well with previous studies by means of reactant bypassing through the GDLs and performance enhancement in the serpentine flow path region. As shown, the serpentine flow path leads to a higher pressure drop compared to that in the straight flow path, which results from the form drag in addition to skin friction. Notwithstanding the fact that the serpentine flow path is beneficial for better reactant redistribution, the local points still exhibit poorly distributed reactants. Therefore,

under very low stoichiometric operating conditions, starvation will be a key factor that contributes to the deterioration of cell performance.

It is estimated that the mechanical compression of the GDLs in the cell applied in the present study may be as much as 16-20%. The heterogeneity of the GDLs due to the compression during cell assembly is not taken into account in the present simulations. As shown in the work of Randrianarizafy et al. [220], the heterogeneity of the distributions of current density and reactants varied due to the GDL compression. The impact of compression on non-woven GDLs is studied numerically by Froning et al. [118]; for a fixed channel/rib case, different level of compression were studied. It is found that the effect of uneven compression is a function of channel to rib width ratio. In addition, non-uniform compression during cell assembly may deteriorate the cell/stack performance. These aspects need to be considered in future work.

In conducting numerical simulations, *model 2* consumes approximately triple of the computational power of *model 1* and in the previous work [98]. While *model 2* provides additional electric current fields in the computational domain, *model 1* only shows the current density in the electrode-membrane surface. In addition, as the electrodes are in fact regions with finite thickness, the local reactant depletion in through-plane direction can only be accounted for by *model 2* when the current density load is high. Under normal operating conditions, both models can readily predict the overall performance and internal current density distributions, as shown in this chapter. Therefore, a choice can be made depending on the computational capacity, operating conditions, and the additional requirement of electric current information.

4.5 Conclusion

Both models in this chapter are capable to predict the overall performance and local current density distribution within a representative single-cell in a short stack with fairly good agreements with experimental data and previous numerical results. The deviations of cell voltages predicted by the present models, previous volume-averaged model, and experimental data are with 6%, which is relatively minor, given the model assumptions and the fact that only a single cell was considered rather than an entire stack.

It is found that the current density distribution in a fuel cell is not uniform, neither locally nor globally. The general tendency is seen as a global maximum near the inlet region and a global minimum at the outlet region. However, the present simulation results reveal that significant local variations exists that are not previously captured. The finite mass transfer conductance results in a situation in which the current density is higher under the gas channels and lower under the ribs. The distributions of water

vapor in the GDLs is in a opposite sense, i.e., higher under the ribs and lower under the channels.

The serpentine-type flow path contributes to higher pressure losses, namely 1–2 times that in straight channels. However, this is beneficial for a better distribution of the current density, oxygen and water vapor, by means of gas bypassing between the channels in the GDLs.

Local current density distribution, oxygen and water mole fraction variation, along with pressure drop are among the most important parameters in fuel cell operation, especially when it comes to extreme operating conditions. The level of modeling detail exceeds both previous modeling and present-day experimental capabilities. Fuel cell and stack designs can be improved through the identification and elimination of local hot spots in current density.

The current density variation through the MEA is plotted. It is revealed that the species concentration gradient exists in the cathode CL, which cannot be predicted by *model 1* where the CL is treated to be infinite thin. The effects may be minor if the mean current density is low. However, the influence increases with the current density loads. It is suggested that *model 2* should be applied if the mean current density is high, whereas, both models may be applied for lower current density loads.

It is also found that the current density distributions on the outer surfaces are much more uniform compared to that in the membrane. The local current density distributions on the outer surfaces show reversed situations from that in the membrane. The deviations between membrane and outer surfaces on local current density distributions are mainly due to the presence of gas channels.

Chapter 5

HT-PEFC homogeneous model

Abstract

In this chapter, two distinct HT-PEFC models are introduced and constructed, in terms of a detailed numerical model (DNM), as shown in Chapter 4, *model 1*, which applies a fine-scale computational mesh, and a distributed resistance analogy (DRA) based homogeneous model (Section 2.2), *model 3*, which replaces the transport equations with rate terms to allow the utilization of coarse grids. Both models are applied to an in-house designed five-cell, HT-PEFC stack with an active area of 200 cm^2 per cell. The polarization curves and local current density distributions, which are calculated via DNM and DRA, are compared with experimental data, where preferable agreements are observed. The distributions of local temperature, Nernst potential, and species concentrations are displayed. It is found that the DNM shows details of fine-scale local extrema that are not predicted and captured by the DRA. However, the DNM requires orders of magnitude higher computational power for numerical simulations than that consumed by the DRA. Nevertheless, both models provide much finer-scale results than the experimental measurements.

5.1 Introduction

Beief introductions concerning the applications were given,

1. The DNM is used for the numerical simulations on the computational mesh of a five-cell stack, where a set of conformal meshes are body-fitted to the different components of the stack. Calculations are performed in parallel, on around 900 computer cores.

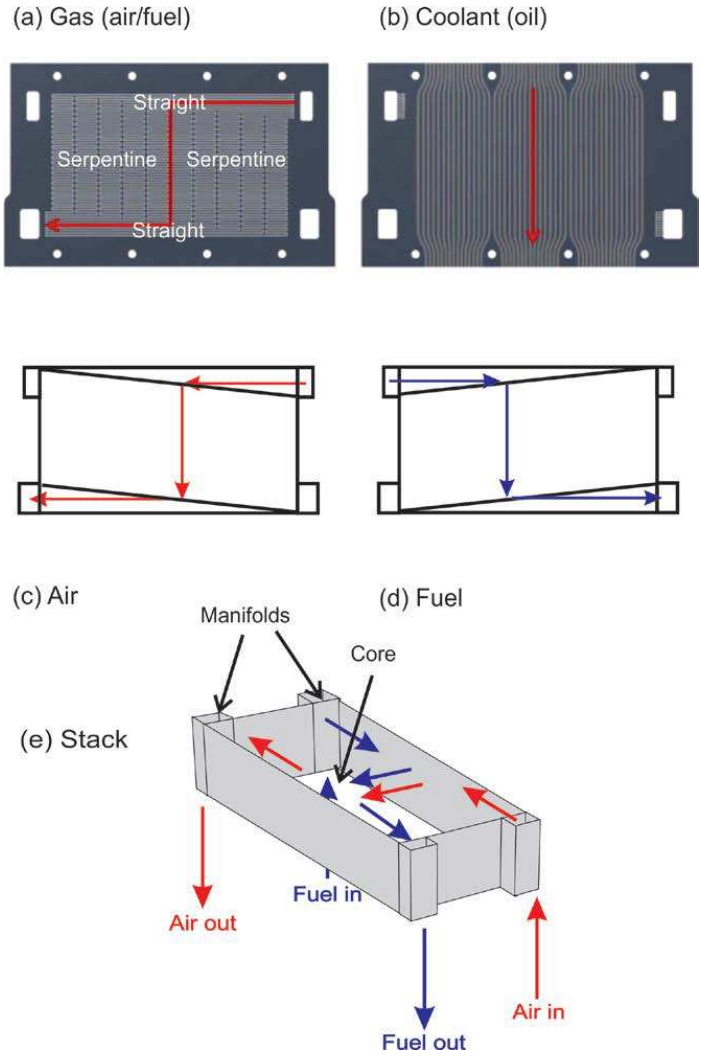

Figure 5.1: Jülich HT-PEFC stack showing (Reproduced from [103]). (a) Gas flow channels; (b) Oil cooling passages machined in BPPs; (c) Schematic of air flow; (d) Schematic of fuel flow; (e) Entire stack/manifold assembly.

2. The DRA is applied on the computational mesh of the stack, where the mesh is much coarser than that used in the DNM simulations. The calculations are executable on a local personal computer within several hours.

Both models are implemented by instantiating 5 distinct meshes, by means of fluid parts: air, fuel, oil, and solid parts: MEAs and BPPs. The governing equations are discretized in each of these meshes. In both models, the electric potentials, or cell voltages, are obtained from the Nernst potential, activation overpotential loss, and ohmic loss.

A sketch of HT-PEFC stack is presented in Fig. 5.1, which is an in-house design at Forschungszentrum Jülich. The gas channels are in the form of a complex pattern with both straight and serpentine flow passages, which acts as conduits for air and fuel. The flow paths were machined out in the BPPs, as shown in Fig.5.1(a). On each side, there are a total of ten gas flow channels. On the other side of the BPPs, cooling channels, see Fig. 5.1(b), are machined to actively control the temperature inside of the stack. In this chapter, the stack is cooled with UCOTHERM S-15-A heat transfer oil. Anode and cathode gases flows are in a co-flow pattern as shown in Fig. 5.1(c, d). The gases are supplied and exhausted through manifolds (uprisers and downcomers, respectively), as displayed schematically in Fig. 5.1(e).

5.2 Numerical

The computational meshes applied by the DRA are shown in Fig. 5.2. The green regions were utilized by 'air', 'fuel', 'MEA', and 'BPPs'. In addition, the detailed computational meshes for the DNM simulations are displayed in Fig. 5.3. The meshes for the BPPs and MEAs are not shown here.

The experimental measurements and numerical simulations are conducted under the ambient pressure, with fixed stoichiometric factors, $\lambda = 2/2$, for both anode and cathode sides. The cooling oil is supplied with a constant flow rate of 1.5 $\mathrm{L\,min^{-1}}$. The inlets temperature for air, fuel, and oil are also fixed, with a degree of 160 ^oC. The parameters applied in the present study are listed in Table 5.1.

5.3 Model validation

Before conducting the numerical simulations, the accuracy of the present DRA method is evaluated via comparison between experimental measurements and numerical predictions of temperature and pressure distributions.

The temperature comparison between experimental data and numerical results are exhibited in Fig. 5.4. (The DNM results are not shown here.) Figure 5.4(a) represents the temperature distribution in the BPPs within

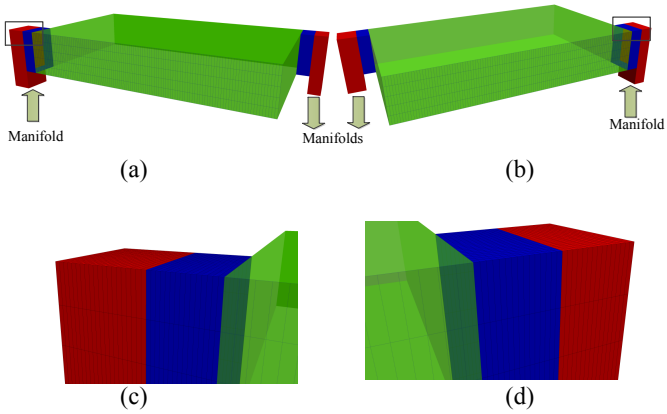

Figure 5.2: The computational mesh in DRA simulations. (a) Cathode side; (b) Anode side; (c) Local grid marked in (a); (d) Local grid marked in (b). (The green regions represent the 'core' region, and the red regions is the manifolds.)

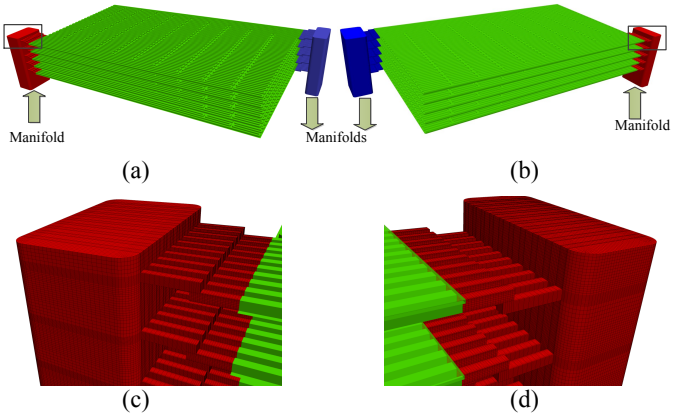

Figure 5.3: The computational mesh in DNM simulations. (a) Cathode side; (b) Anode side; (c) Local grid marked in (a); (d) Local grid marked in (b).

Table 5.1: Model parameters

Description	Value		Unit
Pressure p	101325		Pa
Reference potential E^0	1.15		V
Transfer coefficient α	0.35		-
Exchange current density i_0	0.5		$\mathrm{A\,cm^{-2}}$
Thermal conductivity k	MEA	0.95	$\mathrm{W\,m^{-1}\,K^{-1}}$
	BPP	20	
Volume fraction r	Air	0.075	-
	Fuel	0.075	
	BPP	0.67	
	Oil	0.08	
	MEA	0.0075	
Shape factor S_f	Straight	0.42	-
	Serpentine	0.51	
Sherwood number Sh	2.78		-
Nusselt number Nu	3.5		-

Figure 5.4: Temperature distribution, $i = 0.6\,\mathrm{A\,cm^{-2}}$. (a) Numerical prediction by the DRA method; (b) Experimental measurements [99]. (Reproduced from [103])

the electrochemically active region. It is observed that the overall temperature distributions for experimental and numerical data are similar, although the DRA predicts slightly higher temperature, approximately 2-3 ^oC, than that measured in experiments. In the present model, the contact resistance between each components is not taken into account, in addition, the heat losses through the insulated solid surface is not accounted for, the slight deviations were reasonable.

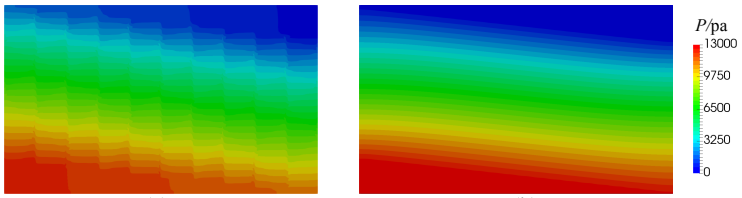

Figure 5.5: Pressure distribution, $i = 0.6\,\mathrm{A\,cm^{-2}}$. (a) Numerical prediction by the DRA method; (b) Numerical prediction by the DNM method. (Reproduced from [103])

The pressure distributions predicted by both DRA and DNM are presented in Fig. 5.5. (The local pressure measurements in the gas passages were not conducted as part of the experimental research.) It can be seen that the overall pressure drops from inlet to the outlet are almost identical for both approaches. However, the local pressure distributions exhibits slight difference. While the DNM captures the detailed tangential losses in the serpentine passages, the DRA only provides the averaged values. It should be noted that, in the present chapter, the distributed resistance coefficient is considered as a constant in the whole serpentine region, whereas it varied between the straights and bends. Considering the very slight deviations between the predictions of the DNM and the DRA, the constant distributed resistance utilized in the core of the stack is a reasonable engineering approximation.

5.4 Results

5.4.1 Polarization curves

The overall stack performance, in terms of polarization curves measurements from the experiments, is compared with the numerical predictions of both the DRA and DNM approaches. As shown in Fig. 5.6, the cell voltages predicted by the numerical models, DNM and DRA, are almost identical, within a maximum deviation of less than 10 mV. The maximum difference between the experimental data and the DRA predictions is 36 mV, $i = 0.2\,\mathrm{A\,cm^{-2}}$.

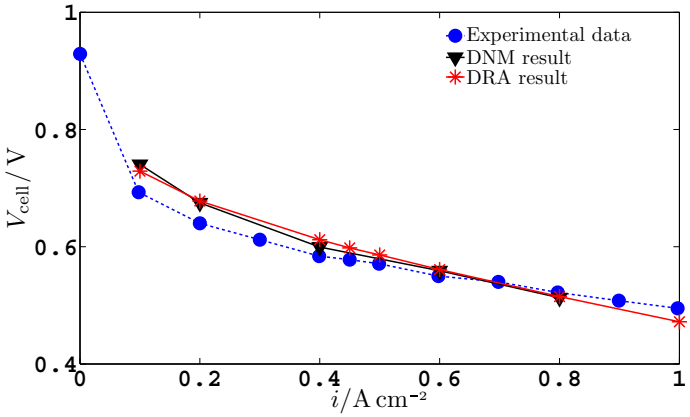

Figure 5.6: Polarization curves from experimental data, the DNM and DRA. (Reproduced from [103])

Under the typical current load, e.g. $i = 0.6\,\text{A}\,\text{cm}^{-2}$, the experimental and numerical results are in good agreements, with less than 5% deviation.

5.4.2 Local current density distribution

In addition to the polarization curves, which represents the overall behavior of a stack, the internal current density distribution is critical to evaluate the design of stacks. A S++ [63] current scan shunt is applied to measure the current density distributions. The S++ device is placed between the third and forth cells in the short stack. The comparison are performed between experimental data and numerical simulations, as shown in Fig. 5.7. It can be observed that the global highest current density locates at cathode inlet region, while the minima is found in the cathode outlet region. The current density distributions calculated via the DNM, in Fig. 5.7(a) and the DRA, in Fig. 5.7(b) are comparable to the experimental measurements, as shown in Fig. 5.7(c). Hence, the numerical and experimental results quantitatively and qualitatively agree with each other.

The current density distributions in the active area of the whole stack predicted by the DNM and the DRA are exhibited in Fig. 5.8. It can be found that the total current density distributions in the stack from both models are similar locally and globally. Additionally, the current density distributions in each cell (except the third one that is shown in Fig. 5.7) are displayed in Fig. 5.9. The current density distributions in each cell are almost identical. In this 5-cell short stack, the temperature variation in the through-plane direction is very small, and the gases temperature supplied

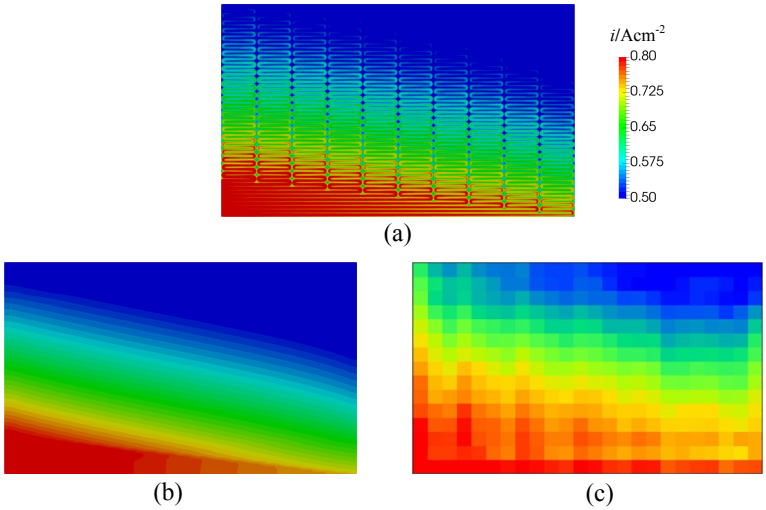

Figure 5.7: Current density distribution, $i = 0.6\,\mathrm{A\,cm^{-2}}$. (a) DNM, the third cell; (b) DRA; (c) Experimental data [99]. (Reproduced from [103])

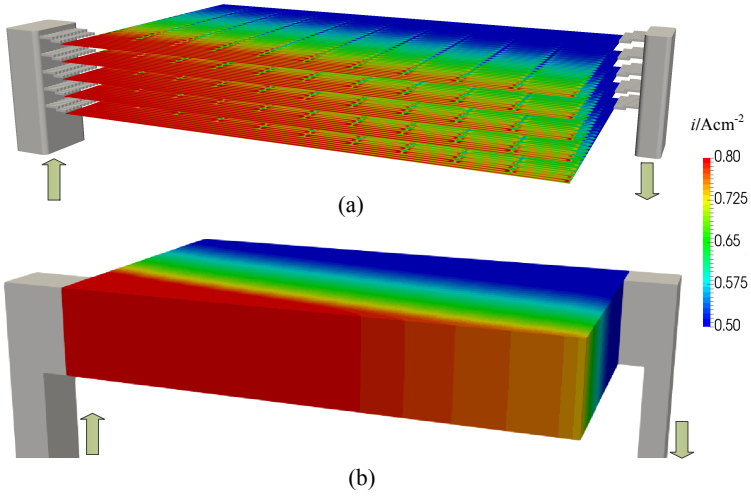

Figure 5.8: Current density distribution from (a) the DNM and (b) the DRA, $i = 0.6\,\mathrm{A\,cm^{-2}}$. (Reprinted from [103])

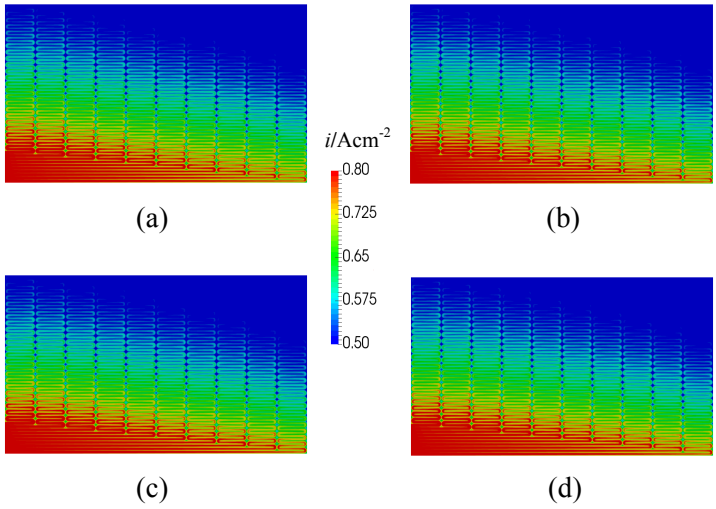

Figure 5.9: Current density distribution in each cell, $i = 0.6\,\mathrm{A\,cm^{-2}}$. (a) Cell 1; (b) Cell 2; (c) Cell 4; (d) Cell 5.

from the manifold is uniform, therefore, the electrochemical reaction rates similar close for each cell.

5.4.3 Reaction mole fractions

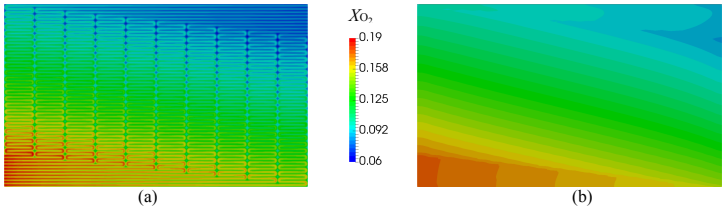

Figure 5.10: Oxygen mole fraction distributions from (a) the DNM (cell 3) and (b) the DRA, $i = 0.6\,\mathrm{A\,cm^{-2}}$. (Reprinted from [103])

During the operation, the stack was supplied with pure hydrogen at anode side. The gas cross-over through the membrane does not contribute in this chapter, therefore, the hydrogen mole-fraction is always unity in the anode side. The oxygen and water vapor mole fractions are shown in Figs. 5.10 and 5.11, respectively. Due to the electrochemical reaction, the

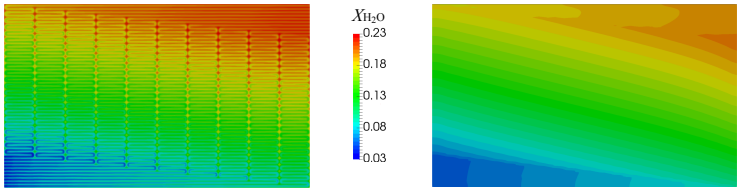

Figure 5.11: Water vapor mole fraction distributions from (a) the DNM (cell 3) and (b) the DRA, $i = 0.6\,\mathrm{A\,cm^{-2}}$. (Reproduced from [103])

oxygen is consumed and the water is produced. The oxygen mole fraction decreases from inlet to outlet, while the water vapor mole fraction increases correspondingly. The overall distributions predicted by the DNM and DRA are similar for both oxygen and water vapor.

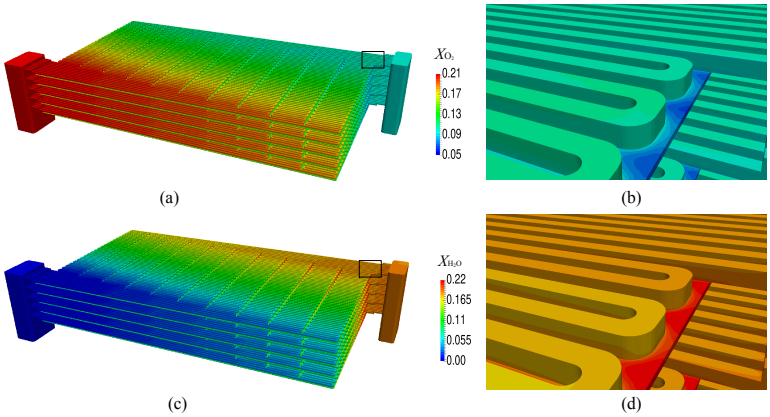

Figure 5.12: Mole fraction distributions for oxygen in (a) the whole stack and (b) in local region, and water vapor in (c) the whole stack (d) in local region, predicted by the DNM, $i = 0.6\,\mathrm{A\,cm^{-2}}$.

In addition, the local properties of the oxygen and water vapor mole fraction are not captured by the DRA. As discussed in Chapter 4, the local minima and maxima are observed in the single cell. The oxygen and water vapor mole fractions in the whole stack, as well as the local distributions, are displayed in Fig. 5.12. It can also be seen that the oxygen mole fraction predicts higher values in the channels and lower in the porous GDL, while the water vapor mole fraction shows in a reversed situation.

5.4.4 Nernst potential

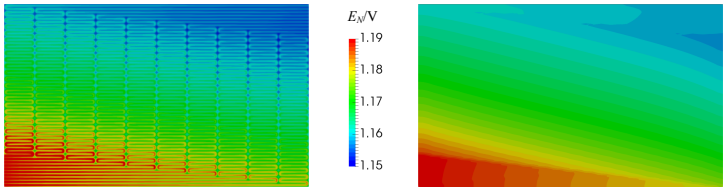

Figure 5.13: Nernst potentials distribution from (a) the DNM and (b) the DRA, $i = 0.6\,\mathrm{A\,cm^{-2}}$. (Reproduced from [103])

The Nernst potential is a function of temperature and reactants partial pressures, which is in positive relation to the oxygen partial pressure and negative to the water vapor partial pressure. Figure 5.13 exhibits the Nernst potential distributions obtained from the DNM and the DRA. As the total pressure and oxygen mole fraction are higher at the cathode inlet region, as well as lower water vapor mole fraction, the maximum Nernst potentials are observed near the inlet. The maximum variation of Nernst potential in the active area is approximately 40 mV, which is minor concerning the overall Nernst potential. Therefore, it is reasonable to treat the Nernst potential as a constant.

5.5 Discussion

The two numerical models, the DRA (homogeneous) and DNM, applied in the present study were implemented into the open source library, OpenFOAM [208]. The DRA (homogeneous) approach provided a fast and easy tool for fuel cells with relatively large active areas and tall fuel cell stacks. It was able to conduct the numerical simulations with less computational power requirement. However, the fine geometrical details were not resolved, hence, the local extrema can not be captured. Conversely, the DNM approach considered the fine-scale resolution of geometrical details, where the local variations of various parameters were resolved. Therefore, it consumed large amounts of computational resources, in terms of processors(cores), memory and computational time, in order to obtain convergent results. Mathematically, the DRA (homogeneous) was more complex in code design and development, whereas the DNM was based on the conventional CFD governing equations and electrochemistry.

The presence of thermal contact resistances between the different components will, generally speaking, hinder heat transfer. The heat source in the stack includes both Joule heating and electrochemical heating compo-

nents. This heat is mainly generated at the catalyst layer(s) and also inside the membrane. The thermal contact resistance between the MEA and gas diffusion layers, as well as that between the gas diffusion layers and bipolar plate ribs, reduces heat transfer to the bi-polar plates. Therefore, due to the assumption of perfect contact resistance made in this study, the temperature in the bipolar plates may be over-predicted, a little.

5.6 Conclusion

In this chapter, numerical simulations regarding a short HT-PEFC stack were conducted. These were achieved from a conventional detail numerical model and a novel distributed resistance analogy scheme. Both models were validated with pre-existing experimental data. The overall performance of the stack is readily predicted by both numerical schemes. The maximum deviations between the polarization curves are minor. The simulated local current density distributions are in good agreement with the experimental measurement.

Oxygen and water mole fraction distributions obtained by both models are compared. The DRA (homogeneous) method may readily be applied to perform simulations of large HT-PEFC stack, whereas the conventional DNM method is limited by the computational requirement that it is only applicable for relatively small stacks. However, parameters local variations cannot be captured by the DRA (homogeneous) model. Thus, the level of model applied can be considered a tradeoff between fidelity/granularity and processor size/speed.

Both the DNM and DRA (homogeneous) models provide substantially more detailed results than existing measurement techniques for local parameters, namely distributions of temperature and current density. In addition, both models are implemented into a modular, object-oriented library and, as such, can readily be applied to future generic electrochemical applications, such as fuel cells, electrolyzer, over and above the HT-PEFC stack considered in this chapter.

Chapter 6

LT-PEFC detailed model

Abstract

In this chapter, a detailed model (*model 4*) is applied to LT-PEFCs. This model is verified by an analytical solution and validated via an in-house designed LT-PEFC. Simulations are performed to represent the effects of cracks in the catalyst region and the causes of MEA failure during operation. These cracks may result in reduced active area and therefore lower cell performance. It is found that cracks show slight influence on the overall performance, whereas the local liquid water saturation and the current density are altered significantly. The liquid water accumulate in the crack regions and the water content in the catalyst region increases due to these cracks. The present study is among the first to consider the crack effects in both local and global aspects. The MEA failure is found resulting from the high local temperature, which may deteriorate membrane mechanical properties. The simulations are performed on simple fuel cell designs, which can serve as representative studies, while prototypes with complex designs may be taken into account in further studies.

6.1 Introduction

In the ex-situ measurements, it is found that the cracks are common in catalyst regions, even for the fresh MEAs. The cracks detected in the experiments are shown in Fig. 6.1. As suggested by Berg and Kulikovsky [221], the crack size in PEFCs can range from 10 to 30 μm, which may vary in the aged MEAs. The work of Kundu et al. [222] revealed several possible impacts resulting from cracks in the catalyst layers, including defect propagation from a pinhole, increased resistance, flooding, increased area for catalyst erosion, and the existence of areas with higher radical concentration. Guo and Qi [223] investigated the freeze-thaw cycles effects on the freestanding piece of MEA and the MEA assembled into cells. They

found that lowering the water content in the MEA may mitigate the damage incurred during freeze-thaw cycles. Kusoglu et al. [224] found that the catalyst layer presented an appreciable hydrophilicity that was a strong function of the existence of cracks. In the numerical work performed by Berg and Kulikovsky [221], an analytical model was developed to represent the crack effects at the anode side.

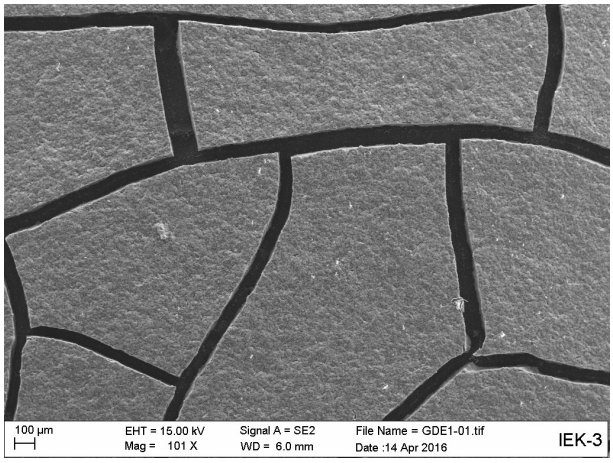

Figure 6.1: The cracks in catalyst region.

In conducting the experimental tests of LT-PEFCs, it is also found that the MEA failure is also a common issue. Figure 6.2 shows one type of MEA failure after the experimental measurements. As it is shown, the whole active area of the catalyst coated membrane (CCM) was larger than the area covered by the GDLs at one/both sides. While the uncovered regions are electrochemically active, the reactions take place in these regions. It can be seen that the MEA in these regions are broken and continuous gaps are formed between the MEA and gaskets. Numerical calculations are therefore performed to analyze the performance when the MEA is partially covered by the GDLs.

6.2 Numerical analysis

The transport phenomena and solution procedure are introduced in Chapter 2, section 2.1. In LT-PEFC simulations, water is assumed to be produced as liquid phase at the cathode side. Two phase flow is therefore considered

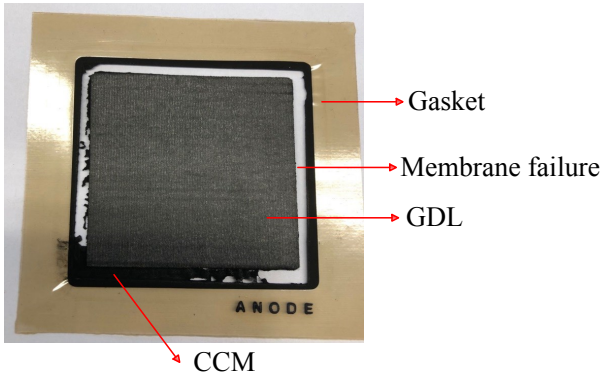

Figure 6.2: One type of MEA broken in the experiment. (CCM: catalyst coated membrane)

at the cathode side, and the governing equations are solved accordingly. At the anode side, water is assumed to exist only in vapor phase and the single phase solver is selected.

6.2.1 Verification

The two phase flow is one of the most important issue that needs to be addressed in LT-PEFC simulations. The numerical calculation is conducted on a simple geometry to predict the liquid water transport in the porous regions. The geometry is shown in Fig. 6.3, where the flow channel, GDL, and CL are marked. The velocities of both air and water in the channel are set as 0.1 $\mathrm{m\,s^{-1}}$ to make sure that the liquid water is blew away as soon as it reaches the channel. Liquid water is produced in the CL region. Condensation and evaporation are not taken into account. Although a 2-D geometry is presented, the boundary conditions of both left and right sides are set as 'empty'. The simulated case is 1-D by taking the dimension in thickness direction into account. In such a case, the 1-D analytical model in the work of Pasaogullari and Wang [137] can be applied to consider the same problem.

Table 6.1 gives the necessary material properties and model parameters in the numerical simulations and analytical solutions. The GDLs are treated to be hydrophilic and hydrophobic, where the contact angles are 80°and 100°, respectively.

The comparisons of liquid water saturation in the GDLs are shown in Fig.

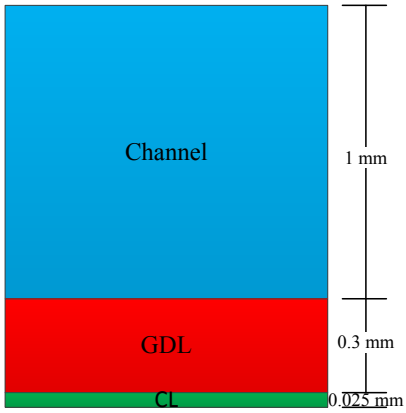

Figure 6.3: Geometry in model verification (1-D).

Table 6.1: Parameters

	hydrophilic	hydrophobic
Current density	1.4 A cm^{-2}	1.4 A cm^{-2}
contact angle	80^o	100^o
permeability	6.875×10^{-13}	6.875×10^{-13}
porosity	0.5	0.5

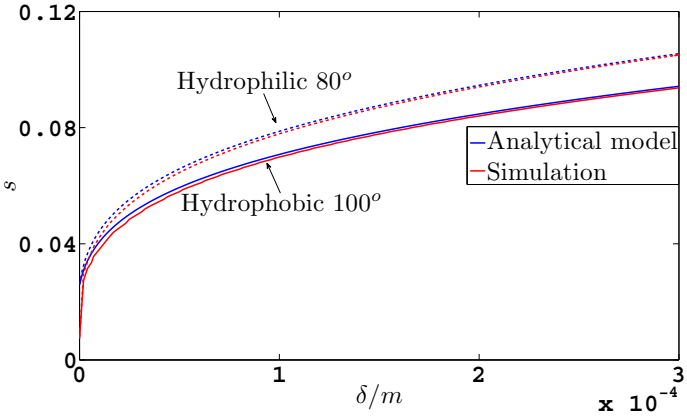

Figure 6.4: The comparison of liquid water saturation variations between the present numerical simulation and analytical model [137] results.

6.4. The liquid water saturation is almost 0 when $\delta = 0$, which corresponds to the interface between the GDL and gas channel. It can be seen that the simulation results are almost identical with analytical solution with two different types of GDLs.

6.2.2 Validation

In order to conduct the experimental validation, the polarization curves are measured from an in-house-designed LT-PEFC prototype. This design is also used in HT-PEFC applications, as shown in Chapter 4. The detail of the geometry and components information can be found in the work of Shi et al. [225]. Experimental measurements were conducted under an operating condition as shown in Table 6.2.

Table 6.2: Operating condition in validations

Description	Value	Units
Pressure: a, c	101325, 101325	Pa
Temperature:	343.15	K
Stoichiometric factor: a, c	2, 2	-
Relative humidity: a, c	90%, 90%	-

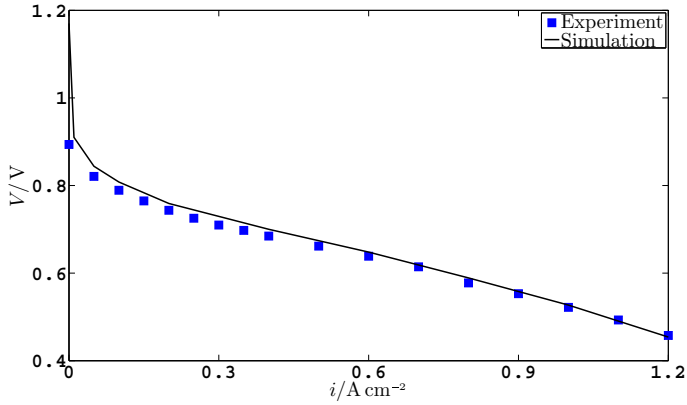

Figure 6.5: The comparison of polarization curves for numerical prediction and experimental measurement.

Under galvanostatic operating mode, the polarization curves are experimentally measured and numerically predicted. Figure 6.5 displays the comparison of both curves. Slight deviations are observed under various current

density loads, except for the open circuit operating condition, in which case the numerical results predict much higher voltage. As the Nernst potentials in the present model are calculated from reactants/products concentration in the gas phase, while the reactant/product are dissolved in the solution during reactions, the obtained values are higher. It can be seen that the present model is capable of predicting the cell voltages that vary slightly from the experimental measurements under various operating conditions, except the open-circuit-voltage. It is well-known that the actual open circuit potential is lower than the Nernst potential in PEFCs. A detailed discussion is considered in the study of Reimer et al. [41]. Nevertheless, the reasonable agreement between the numerical simulations and the experimental results illustrate the capability of the present model to predict the overall cell performance.

In addition to the polarization curves measured in-house, which represents the overall cell behavior, the local current density variation is also important. Therefore a PEFC prototype is selected from the work of [226]. The dimension of the fuel cell is 0.7×0.8 cm^2. Fully humidified hydrogen and air are supplied with a temperature of 70 ℃ under ambient pressure. The fuel cell is working under potentiostatic mode. The stoichiometric factors are 20 and 24 for the cathode and cathode sides, respectively, which are corresponding to a mean current density of 1.0 A cm^{-2}. Figure 6.6 shows the flow configuration applied in the simulations.

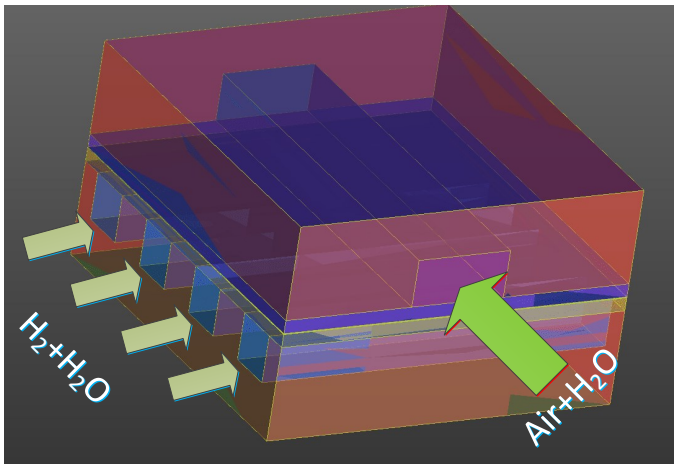

Figure 6.6: The flow configuration for numerical validation.

The current density variation in air flow direction is almost constant pro-

vided the stoichiometric factors are so large at both sides. The local current density variations in under channel/land regions are considered by choosing a straight line in the center of membrane normal to air flow direction. Figure 6.7 exhibits the comparison of local current density values. It can be seen that the local current densities are captured by the present numerical simulations under various cell voltages. The slightly decreasing current densities in the channel zone result from lower water content in the membrane considering less liquid water accumulation in this region. There exist deviations between both results, e.g. the peak values and their locations, etc. The GDL compression and the contact resistance are not considered in the simulations, which may lead to local deviations.

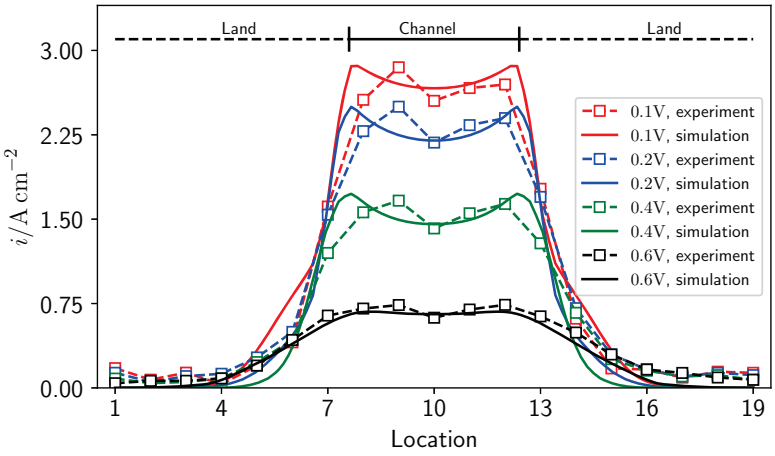

Figure 6.7: Comparison of local current density variation under different cell voltages [226].

6.2.3 Geometry and model parameters

In this chapter, a LT-PEFC prototype, as shown in Fig. 6.8, is applied to analyze the effects of catalyst cracks and the MEA failure problems. The model parameters in the following parts of this chapter are summarized in Table 6.3.

Table 6.3: Model parameters and operating conditions

Description	Values
Channel height: (mm)	1.0
Channel width: (mm)	1.0
Channel length: (mm)	24
Rib height: (mm)	3.0
Rib width: (mm)	0.5
GDL thickness: (mm)	0.28
MPL thickness: (mm)	0.02
CL thickness: (mm)	0.0129
Membrane thickness: (mm)	0.025
Porosity: GDL, MPL, CL (-)	0.7, 0.4, 0.3
Permeability: GDL, MPL, CL (μm^2)	10, 1.0, 0.1
Contact angle: GDL, MPL, CL (^{o})	120, 120, 100
Surface tension: GDL, MPL, CL ($N\,m^{-1}$)	0.0625, 0.0625, 0.0625
Thermal conductivity	
BPP, GDL, MPL, CL, mem: ($W\,m^{-1}\,K^{-1}$)	20, 1.0, 1.0, 1.0, 0.95 [166]
Electric conductivity	
BPP, GDL, MPL, CL: ($S\,m^{-1}$)	20000, 8000, 8000, 5000 [166]
Membrane water	
desorption, adsorption rate: (s^{-1})	1.3, 1.3 [166]
Droplet diameter: (mm)	0.15 [58]
Exchange current density: a, c ($A\,m^{-3}$)	1.0×10^8, 120 [166]
Transfer coefficient: a, c (-)	0.5, 0.5
Pressure: a, c (Pa)	101325, 101325
Temperature: (K)	353.15
Stoichiometric factor: a, c (-)	2, 2
Relative humidity: a, c (-)	50%, 50%

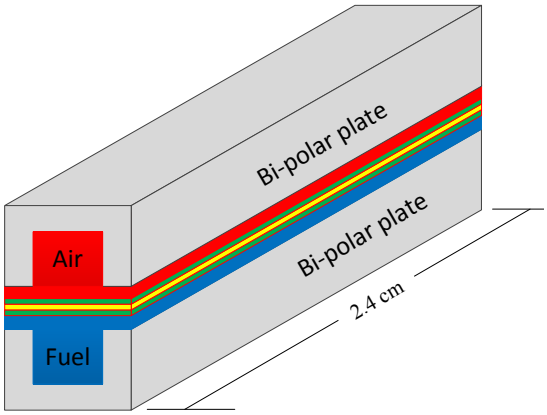

Figure 6.8: The prototype of a LT-PEFC.

6.3 Results

6.3.1 Catalyst cracks

As it was indicated that the width of cracks in PEFCs ranged from 10 - 30 μm [221], the initial size of cracks in this chapter is assumed to be uniform with a width of 20 μm. During the cell operation, the crack size may increase, e.g. aged MEAs. The schematic of the positions for cracks are shown in Fig. 6.9. Two types of cracks are considered, namely horizontal and vertical orientations. The horizontal cracks are placed horizontally from inlet to outlet, while the vertical cracks are distributed uniformly.

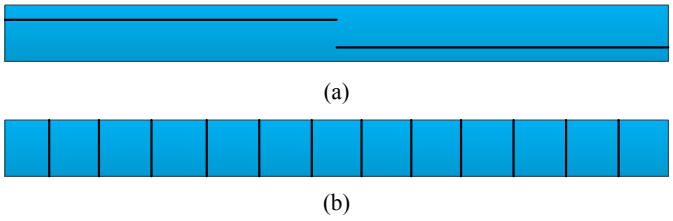

Figure 6.9: Locations and orientations of cracks in the MEAs.

Normal crack size

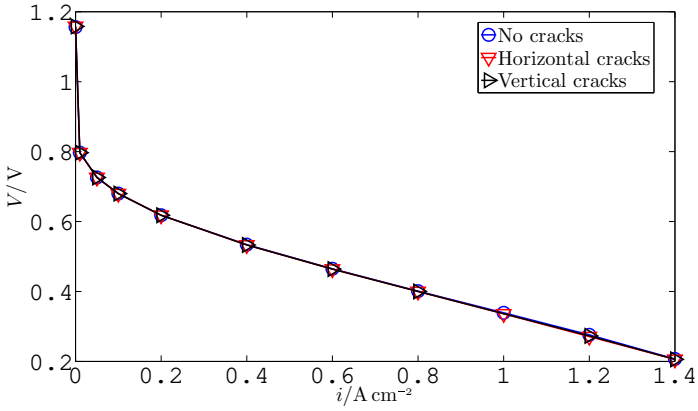

Figure 6.10: Polarization curves comparison of the cases with cracks and without cracks.

The initial crack size is set as 20 μm. The overall performance of the fuel cell with and without cracks are compared, as displayed in Fig. 6.10. It can be seen that the cracks present negligible effects on the cell voltages. Considering the fact that the cracks only occupy 1% of the total electrochemically active region, the effects on electrochemical reactions are minor.

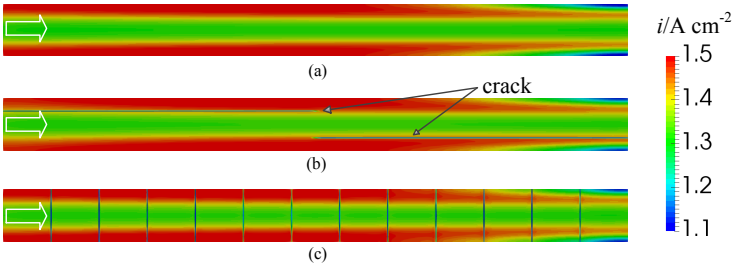

Figure 6.11: Current density distributions at the center of membrane, $i = 1.4\,\mathrm{A\,cm^{-2}}$. (left: inlet; right: outlet) (a) Case without crack; (b) Case with horizontal cracks; (c) Case with vertical cracks.

The through-plane current density distributions on the center plane of the membrane are displayed in Fig. 6.11. Considering the assumption that no electrochemical reaction takes place in cracks, as well as the application

of a thin membrane (25 μm), current densities in the crack regions are lower than in nearby regions. This results in very large nonuniformity of current density distribution, where local extrema can be observed in the crack and neighbor regions. The overall current density distributions for three cases exhibit similar situations that the current densities decrease from the inlet region to the outlet region. It can be revealed that the cracks present negligible effects on the overall cell performance and current density distributions provided crack width and length are relatively small.

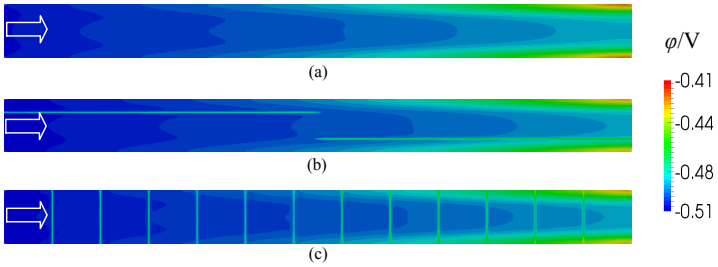

Figure 6.12: Potential distributions at the center of membrane, $i = 1.4\,\mathrm{A\,cm^{-2}}$. (left: inlet; right: outlet) (a) Without crack; (b) With horizontal cracks; (c) With vertical cracks.

Figure 6.12 presents the potential fields on the center of membrane. Corresponding to the current density distribution, it can be found that the cracks mainly affect locally. While the overall potential distributions are similar for difference cases, local potential values in the cracks regions shows significant variations.

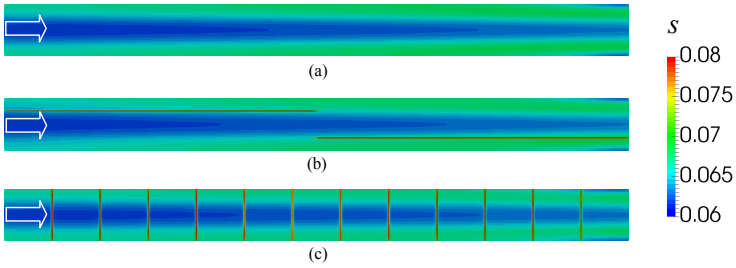

Figure 6.13: Liquid water saturation at the cathodic surface of membrane, $i = 1.4\,\mathrm{A\,cm^{-2}}$. (left: inlet; right: outlet) (a) Without crack; (b) With horizontal cracks; (c) With vertical cracks.

The liquid water saturation at the cathodic surface of the membrane is

shown in Fig. 6.13. It is easy to find that the liquid water saturation in the cracks is much higher than that in the nearby regions. Though no liquid water is produced from electrochemical reactions in the cracks, the liquid water may be imported from neighbors. The CLs are hydrophobic with a contact angle of 100 °, hence, water produced due to electrochemical reaction and water desorption of the MEA can transfer to the hydrophobic GDLs and finally reach the gas channels or the cracks. The cracks are, in fact, dead-end mini flow channels, where the extra liquid water can only flow out through the GDL/CL or evaporate into water vapor. Therefore, much more liquid water is accumulated. The overall distributions agree with each other. The existence of crack alters the local liquid water distribution, which is more obvious for the vertical cracks. In the catalyst layer, the vertical cracks may block the flow paths of gas phase and liquid phase flow. Therefore, higher liquid water saturation can be observed in these regions. The horizontal cracks are in the same direction with the flow in porous media, hence, its influence on liquid water distribution is not so significant.

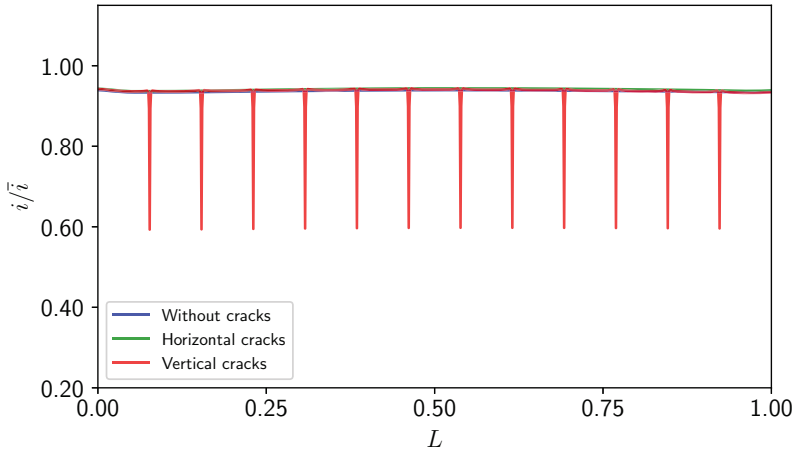

Figure 6.14: Current density on the cross-line from inlet to outlet, $i = 1.4\,\mathrm{A\,cm^{-2}}$.

Cross lines, located at the middle of the cross sections in Figs. 6.11, 6.12 and 6.13 from inlet to outlet, are selected to represent the local variations. As shown in Fig. 6.14, the overall current density variations on the selected lines are almost identical. The most significant difference can be clearly seen for the case with vertical cracks. The local minimum current densities are only 63% of the values in nearby points. Meanwhile, the local peak values of potentials are $\tilde{0}.03$ V higher. The liquid water saturation variations are

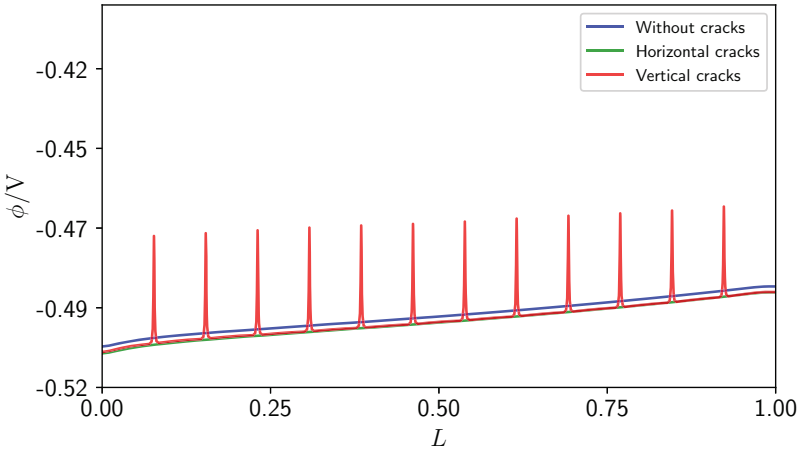

Figure 6.15: Potential on the cross-line from inlet to outlet, $i = 1.4\,\mathrm{A\,cm^{-2}}$.

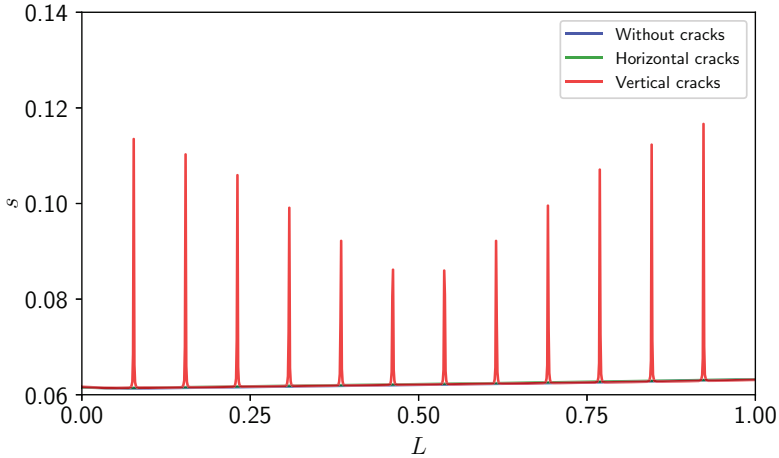

Figure 6.16: Liquid water saturation on the cross-line from inlet to outlet, $i = 1.4\,\mathrm{A\,cm^{-2}}$.

plotted in Fig. 6.13. The cases with and without cracks show fairly similar overall distributions, while the local values of the case with vertical cracks reveal significant deviations. It can be seen that liquid water saturation is much higher in the cracks. The existence of cracks can increase overall water content in the catalyst regions.

Multiple horizontal cracks

Table 6.4: Cell performance variation with number of cracks, $i = 1.4\,\mathrm{A\,cm^{-2}}$

	0	1	2	3	4
Voltage (V)	0.209	0.206	0.203	0.205	0.203

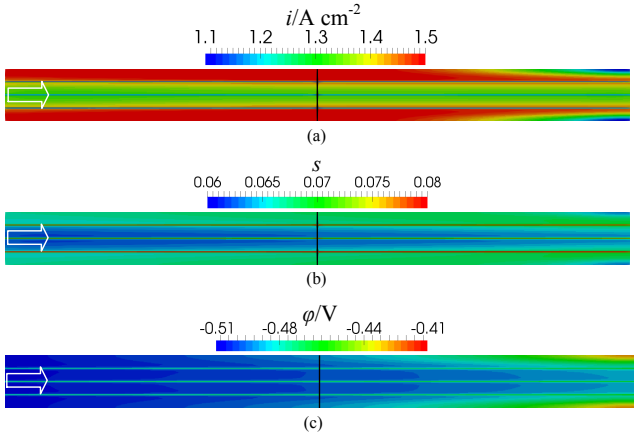

Figure 6.17: (a) Current density, (b) Liquid water saturation, and (c) Potential distributions for case with 3 horizontal cracks, $i = 1.4\,\mathrm{A\,cm^{-2}}$.

Cells performed with multiple horizontally orientated cracks are also taken into account. The cracks are uniformly placed from one side to the other. The cell performance variations with the number of cracks are listed in Table 6.4. The results indicate that cell performance decreases if more cracks exist. However, the effects are also slight, with a maximum of 3%. Current density and liquid water saturation distributions are displayed in Fig. 6.17. Comparing with the case without cracks, it is easy to find that the overall current density/liquid water saturation are both similar, respectively.

Current density and liquid water saturation along the cross-lines, as marked in Fig. 6.17, are displayed in Figs. 6.18, 6.19, and 6.20, respectively. Similar to the vertical cracks, horizontal cracks contribute to lower current density, higher potentials and higher liquid water saturation. However, the

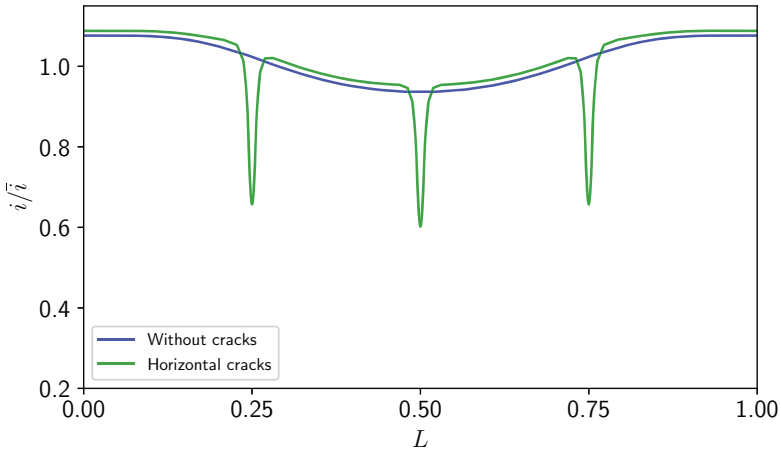

Figure 6.18: Current density along the cross-line as marked in Fig. 6.17, $i = 1.4\,\mathrm{A\,cm^{-2}}$.

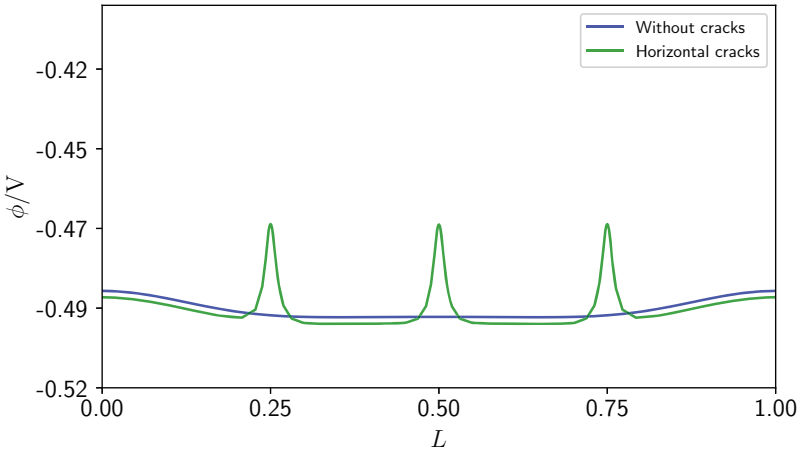

Figure 6.19: Potential along the cross-line as marked in Fig. 6.17, $i = 1.4\,\mathrm{A\,cm^{-2}}$.

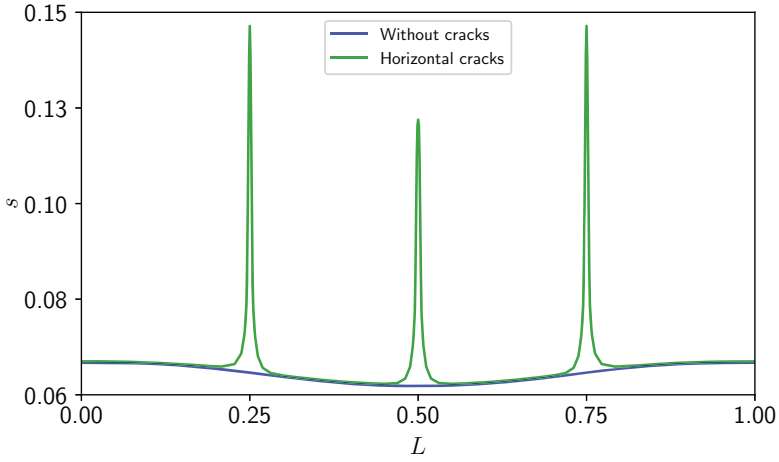

Figure 6.20: Liquid water saturation along the cross-line as marked in Fig. 6.17, $i = 1.4\,\mathrm{A\,cm^{-2}}$.

current densities in the nearby regions of cracks are slightly higher, which is also true for potentials, whereas those of liquid water saturation are not affected.

Larger crack size

Cracks with widths of 0.04 mm, 0.06 mm, and 0.08 mm are selected to represent the cracks in the aged MEAs. Accordingly, the ratios of cracks volume to the catalyst region volume are 2%, 3%, and 4%. With the increasing of the crack size, the voltage variations are exhibited in Fig. 6.21 when $i = 1.4\,\mathrm{A\,cm^{-2}}$. It can be seen that the voltages drop with the increasing of crack size. However, the maximum voltage losses due to cracks are only 3.4%. Figure 6.23 presents the current density distribution when the crack width is 0.06 mm. While the overall current density distributions are generally similar to the case without cracks, the local variations are much more apparent compared to the cases with smaller crack sizes. In Fig. 6.22, it can also be seen that while the overall potential variations are similar, the presence of cracks result in significant local nonuniformity.

Liquid water saturation on the cathodic surface of membranes is exhibited in Fig. 6.24. Comparing with those for smaller crack size, as shown in Fig. 6.13, it can be found that the distributions are generally the same except for values in the crack regions. With larger crack sizes, more liquid water can be observed in the cracks.

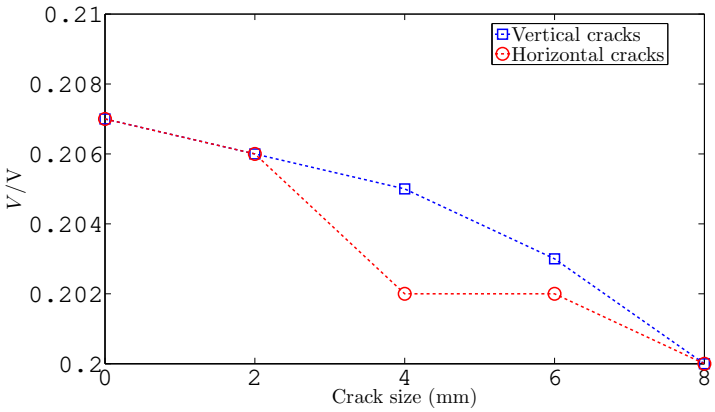

Figure 6.21: The voltage variations for different crack sizes, $i = 1.4\,\mathrm{A\,cm^{-2}}$.

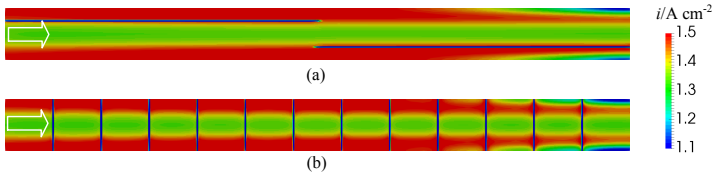

Figure 6.22: Current density distributions, crack size = 0.06 mm, $i = 1.4\,\mathrm{A\,cm^{-2}}$.

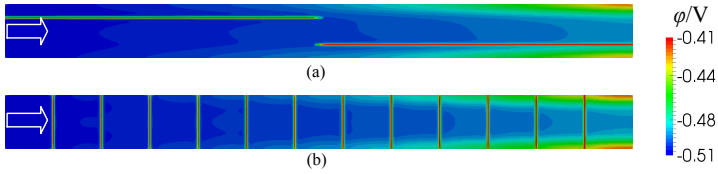

Figure 6.23: Potential distributions, crack size = 0.06 mm, $i = 1.4\,\mathrm{A\,cm^{-2}}$.

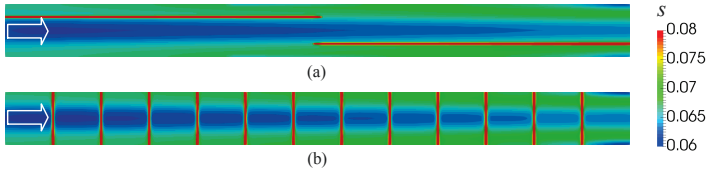

Figure 6.24: The liquid water saturation distributions, crack size = 0.06 mm, $i = 1.4\,\mathrm{A\,cm^{-2}}$.

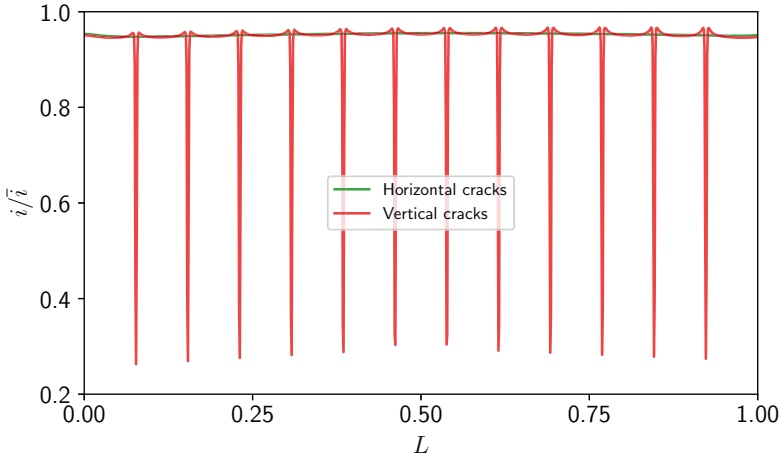

Figure 6.25: Current density distributions on the cross-line from inlet to outlet, crack size = 0.06 mm.

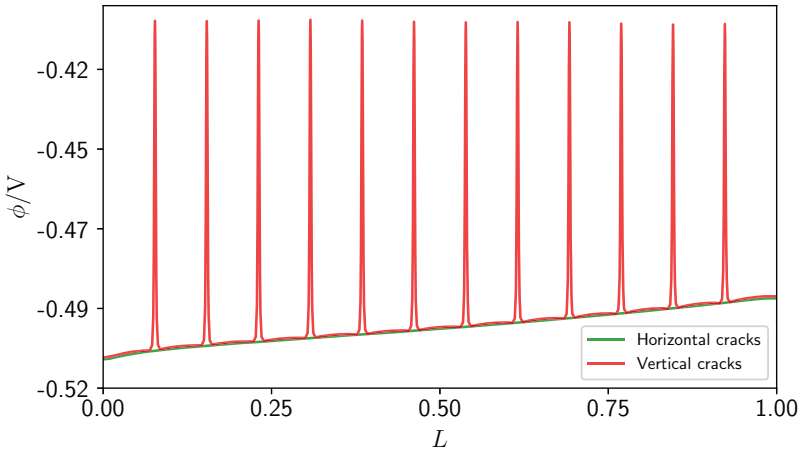

Figure 6.26: Current density distributions on the cross-line from inlet to outlet, crack size = 0.06 mm.

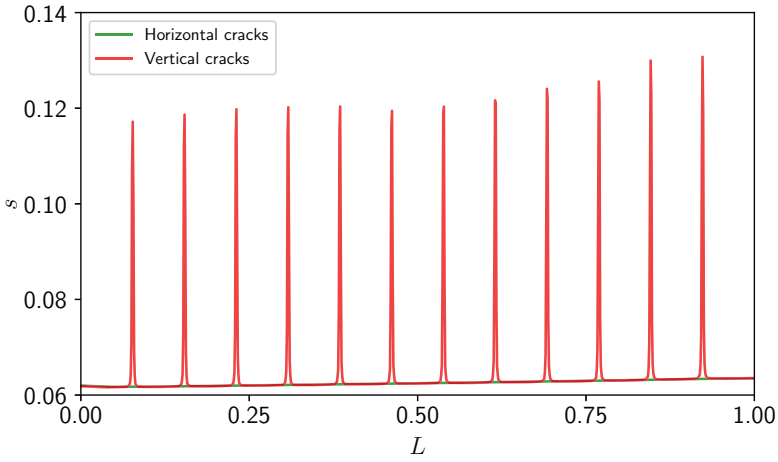

Figure 6.27: Liquid water saturation distributions on the cross-line from inlet to outlet, crack size = 0.06 mm.

The current density, potential, and water saturation distributions along the center cross-line from the inlet to the outlet are shown in Figs. 6.25, 6.26, and 6.27, respectively. It is clear that local variations of these parameters are more significant with a crack size of 0.06 mm than that with 0.02 mm. Especially for the current density distribution, local minima are decreased to approximately 31% of the mean values. The local potential extrema are also higher with larger crack width, with a range of 0.085 – 0.1 V. The liquid water saturation inside the cracks is also higher, where liquid water is more preferable to be formed. However, the overall distributions from inlet to outlet keep nearly the same for the crack widths in the present study. The cracks mainly contribute to the local nonuniformity.

6.3.2 MEA failure

In order to analyze the effects of GDL shortage on the overall performance of the fuel cell and the possible reasons for MEA failure, simulations are conducted on a single LT-PEFC. The standard geometry was shown in Fig. 6.8. Figure 6.28 displays the case when the MEA is not fully covered by the GDL. In this section, the distance, d, between edges of GDL and those of MEA are assumed uniform. It should be noted that the active area accounts for the total MEA area.

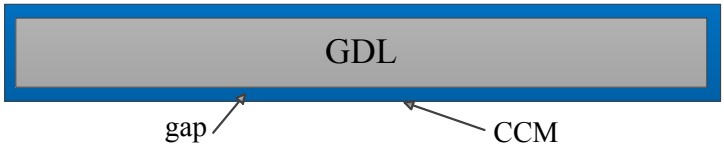

Figure 6.28: The sketch of fuel cells in which the CCM (MEA) is partially covered by the GDL (not to scale).

Cathode side

All of simulations are conducted under half humidified conditions at both sides. The distance is set as 0.04 mm, 0.08 mm, 0.12 mm, and 0.16 mm. In the real fuel cell applications, the distance might be larger, e.g. 1 – 2 mm. In the meantime, the active area of these fuel cells are also bigger. The single cell applied in this study is relatively small in size, therefore, as representative studies, the distance is also smaller. The effects may be more obvious in large industrial applications.

The cross section of the geometry is shown in Fig. 6.29. It can be seen that the GDL is in contact with the CL in the middle region, while in the

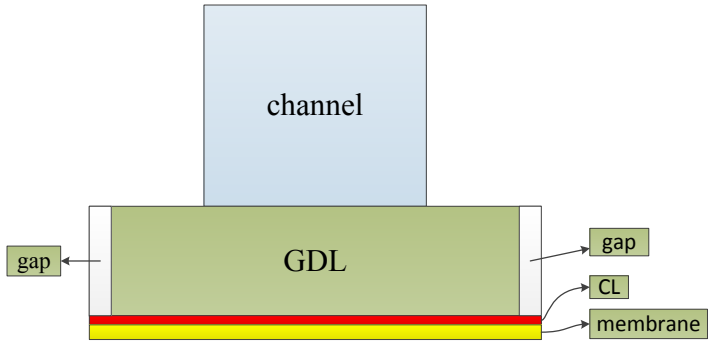

Figure 6.29: The cross section of the geometry (not to scale).

marginal regions, the CL is untouched/uncovered. A duct is formed between the GDL, CL, and the lands. This duct is not a dead-end channel, as it is connected with the gas channel at the inlet and outlet regions. It provides an additional path for gas/liquid flow from the inlet to the outlet.

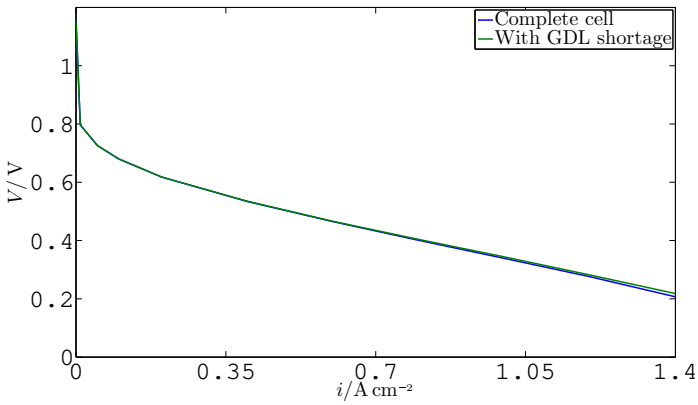

Figure 6.30: The comparison of polarization curves for normal cell and cell with GDL shortage.

As the two-phase flow phenomena usually happen at the cathode side, severe flooding problem appears if the liquid water cannot be removed in time. The fuel cell with GDL shortage at cathode side may encounter more critical flooding issue. The distance is set as 0.08 mm to obtain the cell per-

formance, in terms of polarization curves, under half-humidified conditions. As it is shown in Fig. 6.30, it can be found that the voltages generated by the fuel cell with GDL shortage are identical with the normal cell when the mean current density is below $i = 1.4\,\mathrm{A\,cm^{-2}}$. Under normal working load, the overall cell performance is not affected due to the existence of GDL shortage. When the current density is relatively high, e.g. $i = 1.4\,\mathrm{A\,cm^{-2}}$, the fuel cell with GDL shortage provides higher voltage, 0.011 V, 5.3%. Under higher current density loads, the concentration losses become more obvious for the normal cell, in which the regions under lands may be starved due to oxygen depletion or liquid water flooding. While for the fuel cell with GDL shortage, the regions that are not covered by the GDLs act as alternative paths for reactants. In such a case, the concentration losses may be mitigated.

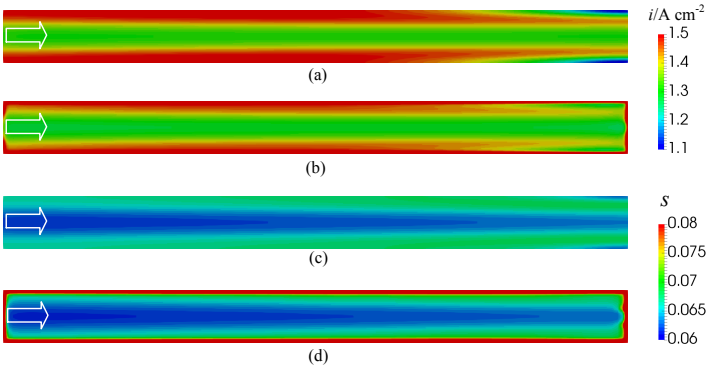

Figure 6.31: The current density and liquid water saturation distributions, $i = 1.4\,\mathrm{A\,cm^{-2}}$. (a) Current density for normal cell. (b) Current density for cell with GDL shortage. (c) Liquid water saturation for normal cell. (d) Liquid water saturation for cell with GDL shortage.

The current density distributions, in the middle of the membrane, and liquid water saturation on the cathode CL-membrane interface, are shown in Fig. 6.31. It is clear to see that the overall current density and water saturation distributions for both cases are generally similar, respectively. The current density decreases from the inlet to the outlet, whereas the water saturation increases. The significant difference between the cells with GDL shortage and normal cell are found in the uncovered regions. Due to the gravity force and the electrochemical reaction, as well as the slow water evaporation process, much more liquid water accumulates in these regions. However, the local current densities are still very high, which means that the

flooding may not happen. Especially, the local maxima of current densities can be found in regions uncovered by the GDL.

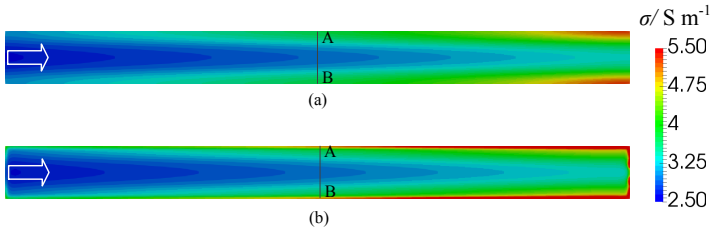

Figure 6.32: The in-plane protonic conductivity distributions, $i = 1.4\,\mathrm{A\,cm^{-2}}$. (a) Normal cell. (b) Cell with GDL shortage.

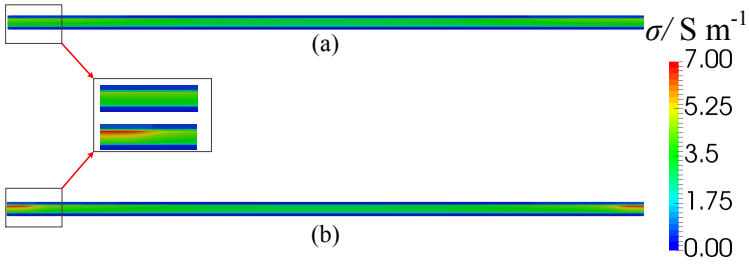

Figure 6.33: The through-plane protonic conductivity distributions, A – B, $i = 1.4\,\mathrm{A\,cm^{-2}}$. (a) Normal cell. (b) Cell with GDL shortage.

In LT-PEFCs, the protonic conductivity is sensitive to the water content. Figure 6.32 presents the in-plane protonic conductivity distributions in the center of the membrane for the normal cell and the cell with GDL shortage. Comparing Fig. 6.32(a) and Fig. 6.32(b), it can be seen that the protonic conductivity in the uncovered regions is higher. Extra liquid water saturation in the uncovered regions contributes to a larger water content in the membrane. The protonic conductivity is also higher. A more obvious comparison can be observed in Fig. 6.33, in which the through-plane protonic conductivity is plotted on a cross-plane (A–B).

In order to represent the concentration effects on the cell performance, the oxygen mole fraction distributions are exhibited, as shown in Fig. 6.34. It is found that catalyst layer under the land may be partially starved near the outlet. Under such a high current density load, the concentration losses

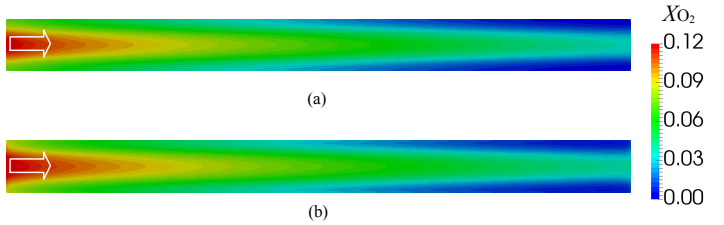

Figure 6.34: The oxygen mole fraction distributions, $i = 1.4\,\mathrm{A\,cm^{-2}}$. (a) Complete cell. (b) Cell with GDL shortage.

need to be accounted for to consider the cell performance. The mole fraction distributions shown in Fig. 6.34 reveal that oxygen mole fraction in cell with GDL shortage is slightly higher, and the concentration losses in both cases are almost identical. Under higher current density loads, e.g. $i > 1.4\,\mathrm{A\,cm^{-2}}$, the local oxygen starvation becomes more severe. The concentration losses in the normal cell should be higher than the cell with GDL shortage, as the additional paths are formed for gas to flow by. In addition, the protonic conductivity gain from the higher water saturation in the uncovered regions contributes to the improvement of cell performance. This might not be true if full-humidified gases are supplied and much more liquid water accumulates, where water flooding is a critical problem in deteriorating the cell performance.

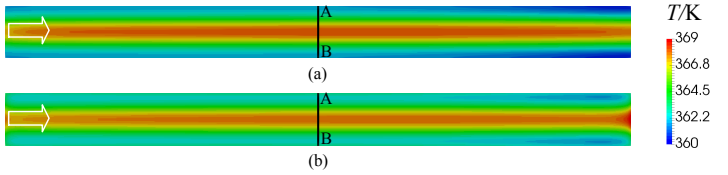

Figure 6.35: The temperature distributions on the center plane of membrane, $i = 1.4\,\mathrm{A\,cm^{-2}}$. (A cross line, AB, was marked in the middle). (a) Normal cell. (b) Cell with GDL shortage.

The temperature distributions in the center plane of the membrane for both cases are shown in Fig. 6.35. It is noted that while the overall temperature range is similar for cases with and without GDL shortage, the former of which presents a higher temperature near the central line and lower near points 'A' and 'B' compared to the latter one. As the thermal conductivity of GDLs is higher than that of gases, less heat is removed if GDL shortage

exists. It is also found that when the distance was 0.08 mm, the temperature deviations at points 'A' and 'B', on the line as marked in Fig. 6.35, is approximately 0.5 K.

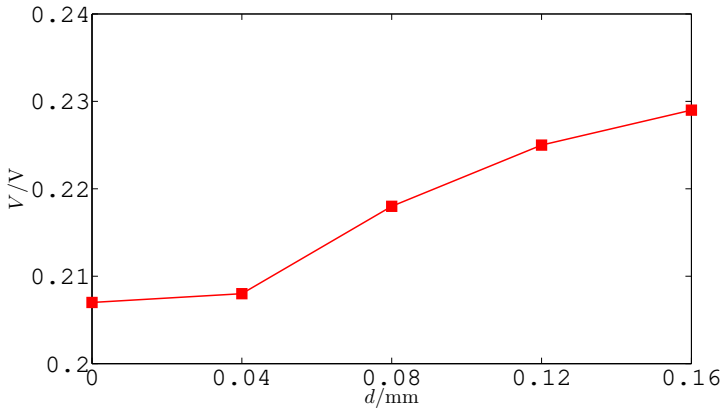

Figure 6.36: Voltage variations for various distances, $i = 1.4\,\mathrm{A\,cm^{-2}}$.

Cases with various distances, namely 0.04 mm, 0.12 mm, and 0.16 mm, were numerically simulated under $i = 1.4\,\mathrm{A\,cm^{-2}}$, in addition to the case with a distance of 0.08 mm. The voltage variations for various d are exhibited in Fig. 6.36. It can be found that the predicted voltages increases with distances. A larger d contributes to less concentration loss and more water content benefit.

The water content in the membrane along the cross line (AB) is shown in Fig. 6.37. It can be seen that water content for cells with GDL shortage is higher compared to the normal cell near the boundaries, whereas the water content in the central region is negligibly affected. The water content in the uncovered regions increase significantly with the distance if d is small. Under larger distances, e.g. $d = 0.16$ mm, the water content enhancement due to distance becomes minor. The protonic conductivity is enhanced in the region that is not covered by the GDL. The overall performance, in terms of cell voltage, increases with d, as shown in Fig. 6.36. In addition, more and more heat remains in the MEA and higher temperatures are expected.

The temperature variations along the cross line, AB, are plotted in Fig. 6.38. It can be seen that temperatures at the boundary increases with the distance. For cells with GDL shortage, the highest temperatures are found in the middle, whereas the lowest temperatures varies with distances. It can be seen that temperature firstly decreases from the middle of the cell, then increases. The maximum temperatures for various cases are insensitive to the distance. The largest temperature deviations between the cells with and

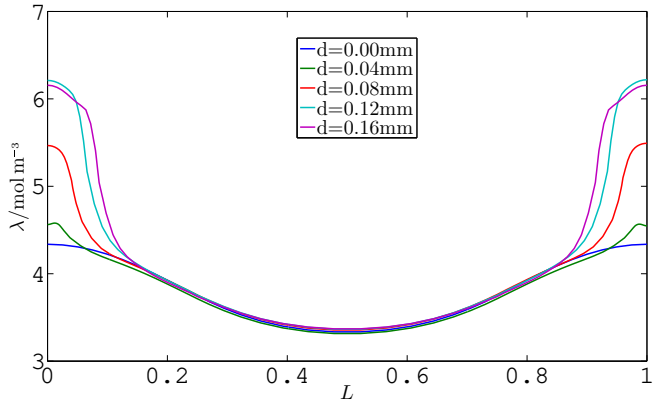

Figure 6.37: Water content variations along AB for various distances, $i = 1.4\,\mathrm{A\,cm^{-2}}$.

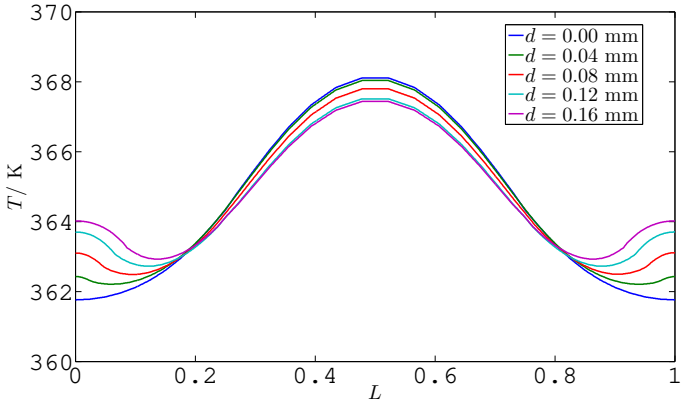

Figure 6.38: Temperature variations along AB for various distances, $i = 1.4\,\mathrm{A\,cm^{-2}}$.

without GDL shortage are found at the boundaries (points A and B). The values are depicted in Fig. 6.39. The temperature deviations do not increase significantly, as the GDL at anode side still contributes to heat removal.

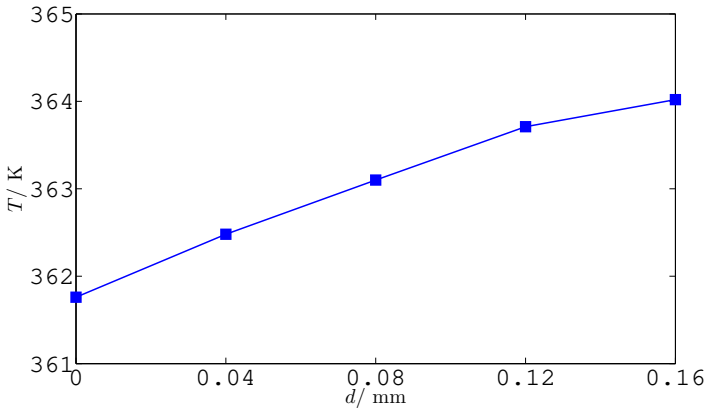

Figure 6.39: Temperature deviations at point A or B under various distances, $i = 1.4\,\mathrm{A\,cm^{-2}}$.

Both sides

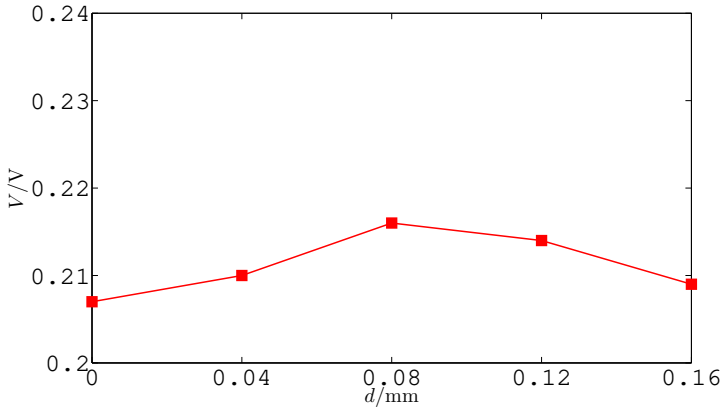

Figure 6.40: Voltage variations under various distances for cases with GDL shortage at both anode and cathode sides, $i = 1.4\,\mathrm{A\,cm^{-2}}$.

The GDL shortage may exist at both the anode and cathode sides. Similarly, cases with various distances are simulated under a mean current density of $i = 1.4\,\mathrm{A\,cm^{-2}}$. It is assumed that the distances are the same at both sides. Cell voltage variations with different distances are shown in Fig. 6.40. Unlike the cases with GDL shortage at cathode side, the cell voltage firstly increases with distances when d is small, e.g. $d \leq 0.08$ mm, then decreases.

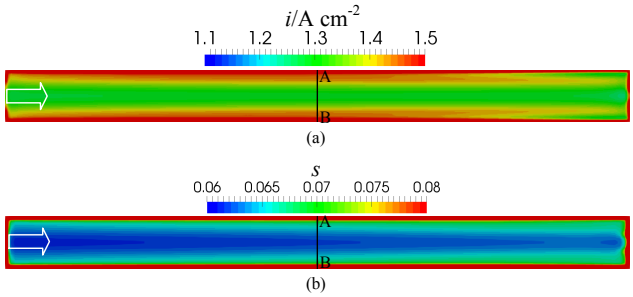

Figure 6.41: (a) Current density and (b) liquid water saturation distributions, $d = 0.08$ mm and $i = 1.4\,\mathrm{A\,cm^{-2}}$.

The current density and liquid water saturation distributions are exhibited in Fig. 6.41 for $d = 0.08$ mm. Both current density and liquid water saturation present comparable distributions for cases with GDL shortage at only cathode side and both sides. With smaller distances, uncovered regions at both sides present negligible effects, as well as internal current density and liquid water saturation distributions. This is not true for cases with larger distances.

As shown in Fig. 6.38, the temperature at the boundaries increase with the distance. If the GDL shortage exists at both sides, heat generated due to electrochemical reaction and Joule heat in the uncovered regions can only be removed via gases, liquid water evaporation, and MEA itself. All of these transport processes are slow due to the low thermal conductivity and evaporation rate. The temperature variations along the cross-line AB, as marked in Fig. 6.41, are presented in Fig. 6.42 for various distances. It can be seen that the temperature in the uncovered regions increased significantly, especially for cases with larger distances. The temperature at boundaries (points A and B) are also plotted versus distance d in Fig. 6.43. It is indicated that the temperature increases almost linearly with distances . The slope of the linear regression is large, $47\,\mathrm{K\,mm^{-1}}$. The local temperature in the uncovered regions are high, which can result in local thermal stress. In addition, the temperature enhancement due to the GDL shortage may cause severe damage to the Nafion membranes.

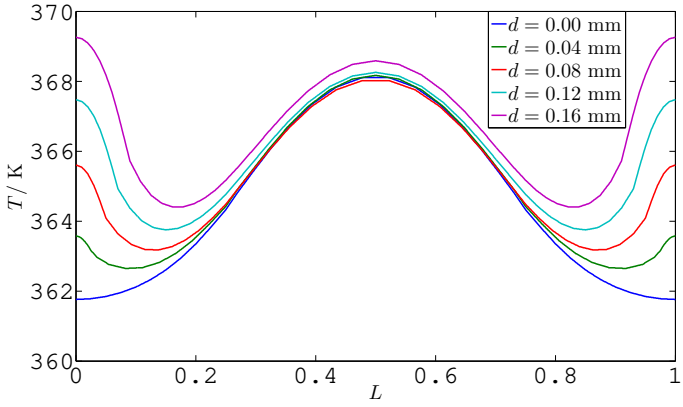

Figure 6.42: Temperature variations along AB under various distances, $i = 1.4\,\mathrm{A\,cm^{-2}}$.

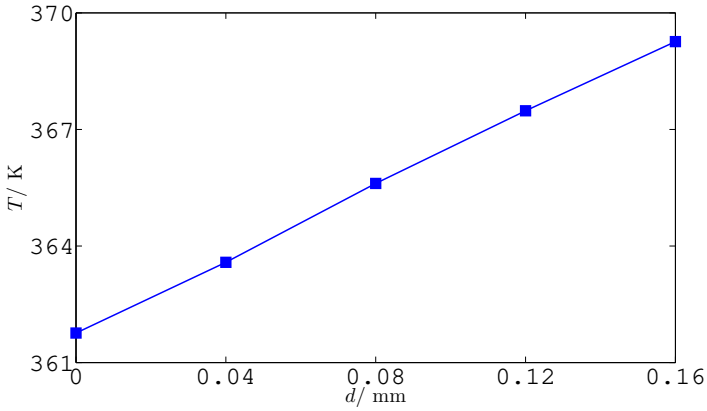

Figure 6.43: Temperature deviation at point A/B under various distances, $i = 1.4\,\mathrm{A\,cm^{-2}}$.

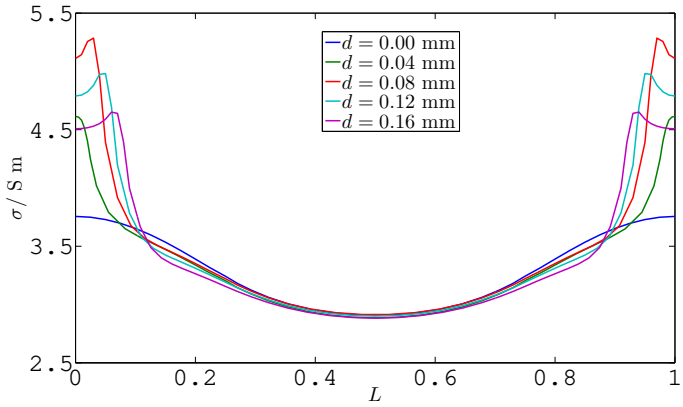

Figure 6.44: Electric conductivity along AB under various distances, $i = 1.4\,\mathrm{A\,cm^{-2}}$.

A large distance also results in worse cell performance, as shown in Fig. 6.40. The electric conductivity in the center of membrane is shown in Fig. 6.44 for various d. It can be found that electric conductivity increases; otherwise under smaller distances, i.e. $d < 0.08$; otherwise it decreases. This contributes directly to the cell voltage drop. The high temperature in the uncovered regions leads to higher saturation pressure, and therefore lower water content.

6.4 Discussion

The detailed model is numerically verified and experimentally validated. Both comparisons show very slight deviations. The applications of the model are performed to investigate two common issues in LT-PEFC components and assembly, namely the cracks in catalyst region and the GDL shortage due to smaller GDLs size. It is found that the cell performance deterioration due to catalyst layer cracks mainly results from the reaction sites missing. The liquid water accumulates in the cracks, where higher water content is observed in these regions. The GDL shortage at the cathode side may contribute to better cell performance due to the higher water content and protonic conductivity in the uncovered regions. However, the GDL shortage at both anode and cathode sides may lead to local temperature maxima, which can cause MEA damage; in addition, cell performance is only slightly enhanced or even decreased for various distances.

It is found the cracks present slight effects on the overall cell performance

under RHs of 50% for both anode and cathode sides. It is indicated that liquid water does not filled up the cracks. Under high RHs, e.g. 90% for both sides, the situation may change: the flooding problem may happen locally in and near the cracks, which is more complicated than the cases in this study. The present model is a macroscopic model, in which the water droplet dynamics is not captured like the VOF method and the LBM approach. Therefore, for high RHs, the local transport phenomena may not be readily simulated by this model. Nevertheless, further analysis under high RHs are important and should be conducted in the future studies.

Membrane swelling is an important aspect that needs to be considered in fuel cell design and optimization [227]. In the present model, this is not taken into account. The membrane swelling in the crack regions is complex and additional models are needed. The membrane may intrude into the cracks. It is more significant for MEAs with larger crack width. Additionally, membrane swelling varies for different membrane thickness and properties, e.g. the swelling effect may be larger for a thinner membrane. The membrane deformation due to swelling also needs to be accounted for. In the detailed simulations, these should be described more accurately.

Some of previous studies have shown that the catalyst cracks impact PEFC performance, including buckling deformation of MEAs [228], formation of pin-holes in the membrane [229], hindering multi-phase transport [230], and affecting the triple-phase boundaries, etc. These lead to performance deterioration. On the other hand, the cracks may be beneficial for the reactants access to reaction sites and contribute better water management [231]. The effects of catalyst cracks on fuel cell operation might not be straightforward. Previous studies mainly focused on experimental measurements, while modeling and simulation investigations of the cracks are still challenges [232]. The formation of catalyst cracks results from either manufacturing processes or operating processes, or both. Therefore, it is accompany by other physical and chemical processes. This study only consider the influence from the geometrical point of view. As a macroscopic CFD model, this study provide one of the first simulations on the crack effects locally and globally. Future studies will take the related physical and chemical processes into account.

The aforementioned issues, higher RHs and membrane swelling, are also critical to be considered in the GDL shortage problems. Under high RHs, additional liquid water accumulates in the uncovered regions, which may cause severe flooding problem. It seems that the GDL shortage at cathode side is beneficial for cell performance in the present study. However, under high RHs, it is probably not the case. More importantly, the mechanical assembly pressure acts directly on the through-plane direction of the membrane, in which a larger shear stress is formed and the membrane may be tore up. If the GDL shortage appears at both sides, the shear stress also exists. While the great temperature enhancement is observed, the mechan-

ical properties of Nafion membrane may deteriorate. The membrane failure is also prone to appear. Therefore, it is not suggested to have the GDL shortage at either one side or both sides.

The current densities, normal to the flow direction, vary with different operating conditions, as presented in the work of Schneider et al. [226]. It was revealed that the current density peaks appeared in the under-channel and under-land regions for fully-humidified gas and dry gases, respectively. The numerical simulations in this chapter consider cases with fully humidified gases, which presents higher current densities in the channel regions. The predictions agree with the data measured by Schneider et al. [226], considering the simulations account for geometries with straight channels. In these cases, the current density variations are straightforward, which are mainly determined by the relative humidities. However, the situations might be different for PEFCs with complex flow path configurations and/or operating under critical conditions, e.g. starvation, dehydration, flooding, etc.

6.5 Conclusion

In this chapter, the detailed model is verified via an analytical model and validated experimentally with an in-house designed LT-PEFC. Two phenomena that are common in LT-PEFCs are numerically simulated via the detailed model: the catalyst layer cracks and the MEA failure due to the GDL shortage. From the numerical results in this study, it can be concluded as following:

The catalyst cracks present limit effects on the overall cell performance. With the increasing of catalyst layer crack size, cell performance drops. The cracks play roles locally in and near the crack regions. Liquid water saturation is much higher in the cracks. With larger cracks, water content is also higher in the catalyst layer. Meanwhile, the nonuniformity of current density increases.

If the GDL shortage exists only at the cathode side, the cell performance increases due to high water content and protonic conductivity in the MEA. If it exists at both anode and cathode sides, cell performance firstly increases and then decreases with the distance. The membrane temperature at the boundaries increases linearly with the distance. A larger distance may result in severe membrane damage. Considering the mechanical pressure during cell assembly, it is not recommended to have GDL shortage either at one side or both sides. The MEA failure may be mainly caused by the high local temperature and/or the mechanical pressure.

Future studies should consider cells operating under high relative humidity and with more complex fuel cell designs. It is also important to more accurately describe major transport phenomena by implementing and

applying additional models.

Chapter 7

LT-PEFC homogeneous model

Abstract

In this chapter, a homogeneous model (*model 5*) is introduced and built for LT-PEFC cell and stack level simulations. The model accounts for all of the major transport phenomena, including heat and mass transfer, two-phase flow, condensation, and evaporation, electrochemical reactions, water transport, etc. Based on the distributed resistance analogy (DRA) approach, the model allows utilization of very coarse grid. The verification of the present model is conducted by comparing numerical simulations with the detailed model (*model 4*) in this thesis. As both models are based on slightly different assumptions, there existed deviations in the numerical predictions. The validation is conducted on an in-house designed LT-PEFC. The model is able to predict the overall cell performance with slight deviations from the experimental results. Parameters distributions are also presented.

7.1 Introduction

Water management in PEFCs is a critical issue that needs to be addressed, especially when it comes to the two-phase phenomena. Detailed simulations, like VOF method, can only be applied on one/several channels due to the heavy computational requirement. The applications of M2 [119, 120] or multi-fluid models are also limited by computational power. In order to consider the two-phase issue in PEFCs (with the relative large active area) and in PEFC stacks, homogeneous models are more desirable. Previous homogeneous models mainly neglected the two-phase flow or applied an equilibrium phase change model where liquid water transfer was not taken into account. The present model utilizes a non-equilibrium phase change model and allows the solution of two-phase transport phenomena. In addition, the major

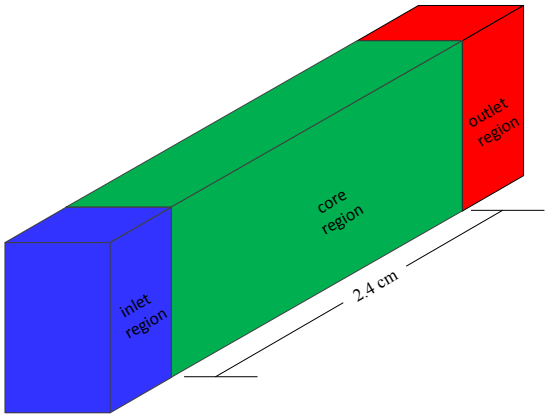

Figure 7.1: The geometry applied in the calculation of the homogeneous model.

transport phenomena are considered simultaneously.

The transport phenomena and corresponding governing equations were described in Chapter 2, Section 2.2. Considering the liquid water production at the cathode side, two phase flow needs to be simulated; single phase flow is calculated at the anode side due to the low RH.

7.2 Verification

The geometry applied in numerical verification for the detailed model was the same as shown in Chapter 6. In the homogeneous model, a much simpler geometry and the computational domain is considered and applied. The whole cell is consisted with an inlet region, an outlet region, and a core region, as shown in Fig. 7.1. The inlet and outlet regions are presented only for 'air' and 'fuel'. The core region is shared by 'air', 'fuel', 'interconnect', and 'electrolyte/membrane'. All of the major transport phenomena are coupled in the 'core' region. In constructing the computational mesh, only one layer is used in the through-cell direction. For single cell simulations, the 3-D problem is simplified to be 2-D or 1-D, while the transport phenomena in the through-plane direction are assumed homogeneous and can be described by simple models. For multi-cell stacks, the 3-D transport equations are reduced into pseudo-3-D, in which the heat transfer needs to be accounted for in the through-stack direction. In addition, the fluid flow, species, and heat transfer are 3-D in the manifolds.

As a comparison study, the operating conditions and material properties

Table 7.1: Model parameters in verification

Description	Value	Unit
Reference potential: E^0	1.18	V
Condensation rate: Υ_{co}	100	s^{-1}
Evaporation rate: Υ_{ev}	100	s^{-1}
Total thickness: l	0.004625	mm
Volume fraction r	Air 0.1075 Fuel 0.1075 BPP 0.6452 MEA 0.0054	-
Fitting parameter ζ	CLs 4.7 membrane 1.0	-
Tortuosity: τ	1	-
Shape factor S_f	0.5	-
Sherwood number Sh^*	2.78	-
Nusselt number Nu^*	3.5	-
Permeability K: gas	$(4.76 \times 10^{-7}\, 4.76 \times 10^{-10}\, 4.76 \times 10^{-10})$	m^{-2}
Permeability K: liquid	$(1.0 \times 10^{6}\, 1.0 \times 10^{-14}\, 1.0 \times 10^{-14})$	m^{-2}

are the same as shown in Chapter 6. Additional parameters and values are summarized in Table 7.1.

7.2.1 Results

The comparison of polarization curves obtained from both the detailed and homogeneous models is shown in Fig. 7.2. It can be found that the voltages predicted by both models showed fairly good agreement. The largest deviations was found at $i = 1.2\,\mathrm{A\,m^{-2}}$ with an amount of 6%. Therefore, the homogeneous model can provide the overall cell behavior with reasonable difference under various current density loads.

Current density distribution

The internal current density distribution is then exhibited in this section at a mean current density load of $i = 0.8\,\mathrm{A\,m^{-2}}$. As shown in Fig. 7.3, the current density distributions are compared. It can be seen that deviations exist between both results. The detailed model represents 3-D transport phenomena, while the homogeneous model simulated 1-D ones. In addition, different phase change models are applied in both models, which contributes to further deviations.

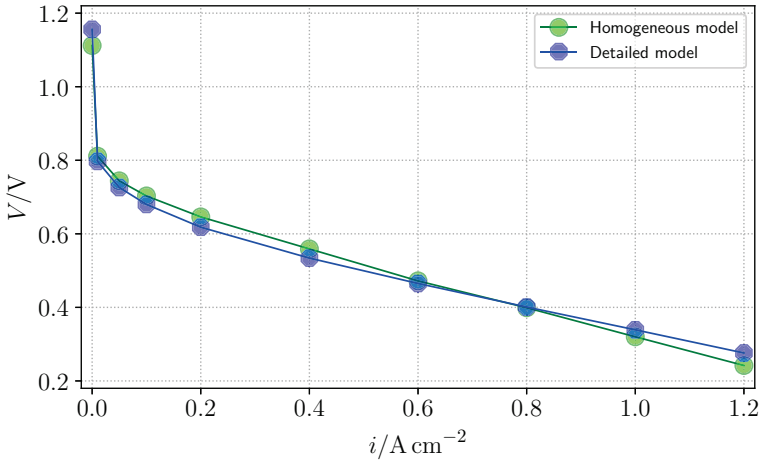

Figure 7.2: The comparison of polarization curves predicted by the detailed and homogeneous models.

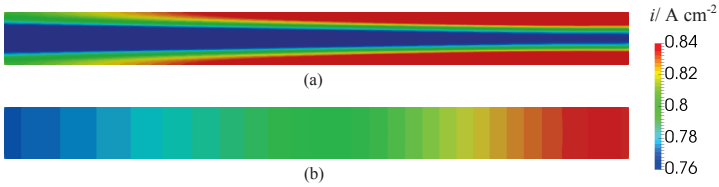

Figure 7.3: The current density distribution in the membrane. (a) Detailed model. (b) Homogeneous model.

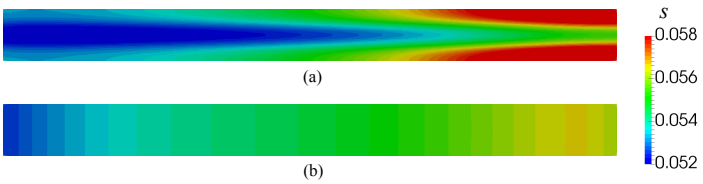

Figure 7.4: Liquid water saturation distribution at interface of membrane and catalyst electrode. (a) Detailed model. (b) Homogeneous model.

Liquid water saturation

In both models, liquid water transport is taken into account at the cathode side. The liquid water mainly exists in the porous GDL. Under very high current density load and/or under high relative humidifies conditions, liquid water may enter the channel, stay on the interface between the GDLs and flow channels, and even fill the channel. For a mean current density load of $i = 0.8\,\mathrm{A\,m^{-2}}$, the amount of liquid water in the gas channel is negligibly minor. The liquid water saturation on the interface between the membrane and catalyst electrode is compared between both models.

As shown in Fig. 7.4, the liquid water saturation is lower near the inlet and higher near the outlet. The detailed model gives lower values than that of the homogeneous model near the inlet region. As aforementioned, the deviations mainly results from the volume-averaging approach for the transport fields and the simplification for phase change model. In addition, the liquid water transport phenomena in GDLs are described by an analytical expression, which is also a 1-D model. It is revealed that the homogeneous model is capable of providing the liquid water distribution in reasonable agreement with the detailed model.

7.3 Validation

In conducting the experimental validation, a geometry [225] with the design of three-serpentine flow paths, as shown in Fig. 7.5(a), is selected. Assuming that the flow enters the flow path via the left-bottom inlet and leaves from the right-top outlet, the flow directions in the flow paths can be clearly marked as shown in Fig. 7.5(b). To make the fluid flow in the serpentine flow paths simpler, the DRA algorithm is applied. The computational domains for air and fuel can be categorized into two types of regions, namely x-region and y-region. x-region is the zone where fluid flows only in horizontal (x) direction, and y-region represented the zone where flow direction is only in vertical (y) direction. The stoichiometric factors for cathode and anode

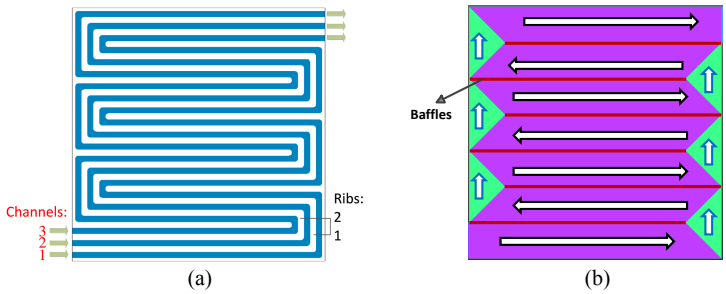

Figure 7.5: The geometry and the computational domains. (a) The flow path design [97]. (b) The present simplification (Baffles are marked with red lines).

sides are 2.5 and 1.2, respectively. The relative humidity (RH) at both sides are set as 50%. While some parameters were listed in Chapter 6, Table 6.2, additional ones are summarized in Table 7.2.

7.3.1 Results

The overall cell performance, namely polarization curves, is compared between the experimental data and numerical predictions in Fig. 7.6. The predicted voltages and experimentally measured values presented very slight difference under various current density loads, except the open circuit operating condition.

Current density distribution

Figure 7.7 displays the current density distribution in the membrane for a mean current density of $i = 0.8\,\mathrm{A\,m^{-2}}$. It can be found that the current density increases from the inlet region to the outlet region. Considering the decrease of oxygen molar concentration from the inlet to the outlet, the electric conductivity of the membrane increases accordingly, as presented in Fig. 7.8. The minima are observed near the inlet and the maxima locate at near the outlet. As half-humidified gases are supplied from the inlets for both anode and cathode sides, the membrane is not sufficiently humidified firstly. With the production of water, the water content in the membrane increases. The electric conductivity of membrane therefore increases from $2.5\ \mathrm{S\,m^{-1}}$ (inlet region) to $8.9\ \mathrm{S\,m^{-1}}$ (outlet region).

The activation overpotential for both sides is displayed in Fig. 7.9. It can be seen that the cathodic activation overpotential is much higher than

Table 7.2: Model parameters in validation

Description	Value	Unit
Reference potential E^0:	1.18	V
Condensation rate: Υ_{co}	100	s^{-1}
Evaporation rate: Υ_{ev}	100	s^{-1}
Total thickness l:	0.00665	mm
Volume fraction r:	Air 0.075 Fuel 0.075 BPP 0.75 MEA 0.00376	-
Fitting parameter ζ	CLs 2.5 membrane 1.0	-
Tortuosity: τ:	1	-
Shape factor S_f:	0.5	-
Sherwood number Sh*:	2.78	-
Nusselt number Nu*:	3.5	-
Permeability K: gas	x $(4.76 \times 10^{-7}\ 4.76 \times 10^{-10}\ 4.76 \times 10^{-10})$ y $(4.76 \times 10^{-9}\ 4.76 \times 10^{-7}\ 4.76 \times 10^{-9})$	m^{-2}
Permeability K: liquid	x $(1.0 \times 10^{6}\ 1.0 \times 10^{-14}\ 1.0 \times 10^{-14})$ y $(1.0 \times 10^{-14}\ 1.0 \times 10^{6}\ 1.0 \times 10^{-14})$	m^{-2}

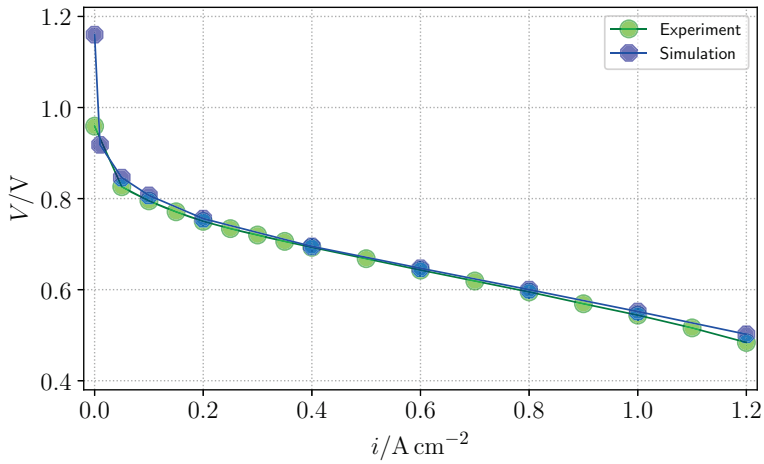

Figure 7.6: The comparison of polarization curves between experimental measurement and numerical simulation.

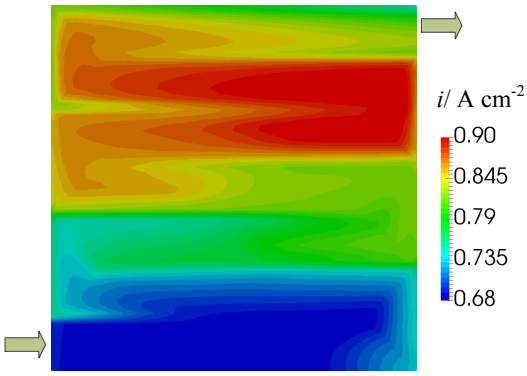

Figure 7.7: The current density distribution, $i = 0.8\,\mathrm{A\,m^{-2}}$.

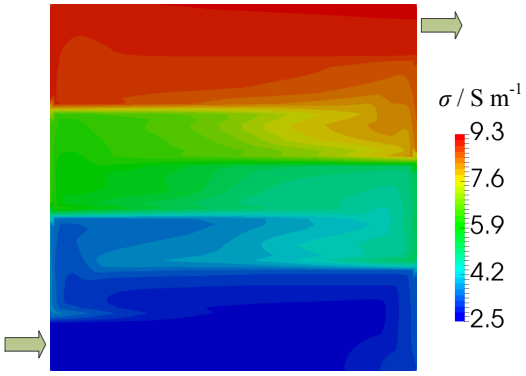

Figure 7.8: The protonic conductivity distribution in the membrane, $i = 0.8\,\mathrm{A\,m^{-2}}$.

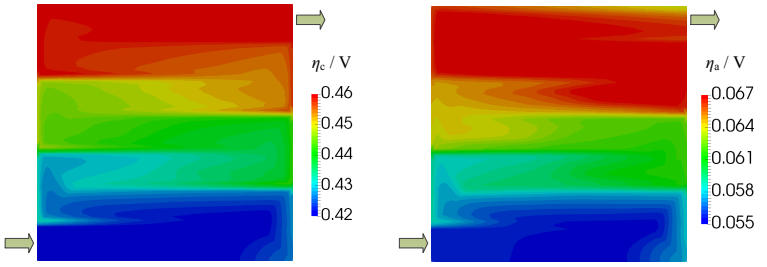

(a) (b)

Figure 7.9: Activation overpotential distributions, $i = 0.8\,\mathrm{A\,cm^{-2}}$. (a) Cathode side. (b) Anode side.

that at the anode side. The HOR is much faster than the ORR in a PEFC. This can be seen from the exchange current density at each side, which are $1.6{\times}10^4$ and $1.0{\times}10^8$ $\mathrm{A\,m^{-3}}$ for the cathode and the anode sides, respectively. Nevertheless, the activation overpotential at the anode side cannot be readily neglected. It can be found that the activation overpotential varies slightly with current density at both sides. These variations mainly result from the reactant consumption and water production.

Liquid water saturation

Figure 7.10 exhibits the liquid water saturation at the interface between the membrane and cathode catalyst electrode. It can be seen that the maximum values appear at the outlet region, while the minima are observed near the inlet region. As shown in Fig. 7.7 for current density distribution, higher current density leads to more liquid water production. In addition, with the liquid water evaporation, water vapor partial pressure is closer to the saturation pressure from the inlet to the outlet. Therefore, liquid water accumulates. In the regions where local minima are observed, more water may transfer to the anode side or less water transfers from the anode side through the membrane, depending on the water content difference between both sides. The overall liquid water saturation is not very high, with a maximum value of 0.06, as the supplied fuel and air are half-humidified.

Species mole fraction

It is important to account for the reactant/product distributions in order to consider the fuel cell design and optimization. The electrochemical reaction is directly related to the mole fraction/concentration of the reactant/product, vice versa. In a LT-PEFC, humidified hydrogen and air are

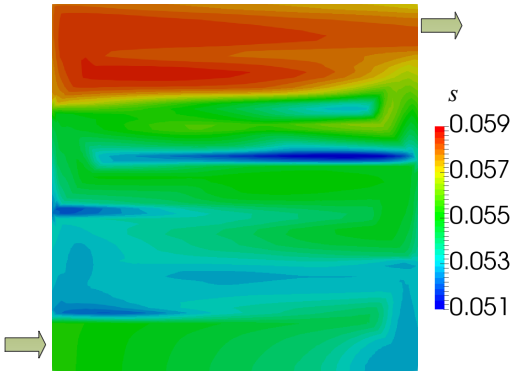

Figure 7.10: Liquid water saturation distribution at interface of membrane and catalyst electrode, $i = 0.8\,\mathrm{A\,cm^{-2}}$.

supplied from the inlet. During the reaction, oxygen and hydrogen are consumed; in the meantime, liquid water is produced at the cathode side. Considering the water transfer through the membrane and liquid water evaporation, water vapor may be produced or consumed at both sides. Figure 7.11 shows the oxygen and water vapor mole fraction distributions on the interface between the membrane and cathode catalyst electrode. It can be found that the oxygen and water vapor mole fraction decreases and increases from the inlet region to the outlet region, respectively. It is clear that the oxygen is continuously consumed due to electrochemical reaction and water vapor produced depending on the saturation pressure.

Oxygen and water vapor mole fraction distributions in gas channels are exhibited in Fig. 7.12. Taking the reactant diffusion process into account, the oxygen mole fraction at the reaction sites is smaller compared to that in the gas channels. However, the molar fraction for water vapor varies slightly from the electrode region to the gas channel. In both regions, water vapor is only produced from the evaporation, which is relatively slow. Gas transport in the porous GDLs is dominated by the diffusion, where the convection is usually readily neglected. Therefore, the species diffusion in gas channels is similar to that at the interface between the membrane and cathode catalyst electrode.

Figure 7.13 exhibits the hydrogen molar fraction distributions in the anode electrode and gas channel, respectively. From the inlet to the outlet, the molar fraction varies due to the electrochemical reaction and water transfer through the membrane. The molar fraction of hydrogen firstly increases as more water transfers from the anode side to the cathode side due to the

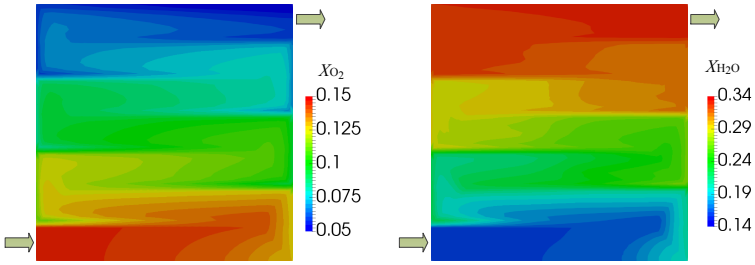

(a) (b)

Figure 7.11: (a) Oxygen and (b) water vapor mole fraction distributions at the interface between membrane and cathode catalyst electrode, $i = 0.8\,\mathrm{A\,cm^{-2}}$.

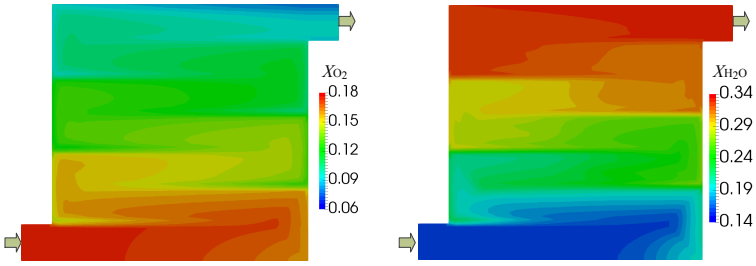

(a) (b)

Figure 7.12: (a) Oxygen and (b) water vapor mole fraction distributions in cathode gas channels, $i = 0.8\,\mathrm{A\,cm^{-2}}$.

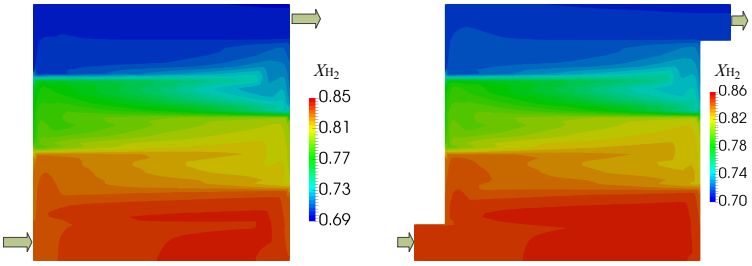

(a) (b)

Figure 7.13: Hydrogen mole fraction at (a) the interface between membrane and anode catalyst electrode and (b) gas channels, $i = 0.8\,\mathrm{A\,cm^{-2}}$.

strong EOD. It decreases subsequently considering that more hydrogen is consumed compared to the water vapor at the anode side.

Pressure

Figure 7.14 presents the pressure distribution in cathode side gas channels under a current density load of $i = 0.8\,\mathrm{A\,cm^{-2}}$. The total pressure drop from the inlet to the outlet is approximately 675 Pa, which is close to the experimental measurement of 636 Pa. In the present model, the friction drag force is only applied for the gas phase. Under the assumption that the liquid phase was in mist state in gas channels, the friction drag force applied on the liquid phase can be neglected. However, the water droplets formed on the interface between gas channels and GDLs due to gravity force and gas bypassing through the GDLs are not taken into consideration. The formation of water droplets can increase the pressure drop, on the other hand, the gas bypassing mitigated pressure drop. In the present case, it is reasonably assumed that liquid water saturation is low in the gas channel as half-humidified gases are supplied.

Temperature

Temperature distribution in the membrane is presented in Fig. 7.15. It can be seen that the temperature distribution generally follows the current density distribution in the membrane. However, the temperature variation in the membrane is relatively small, within 1 K. In the simulation, the fuel cell is operated under isothermal boundary condition, which was also true during the experimental measurements. Considering the high thermal conductivity of BPPs, the temperature variation in the fuel cell is slight. In

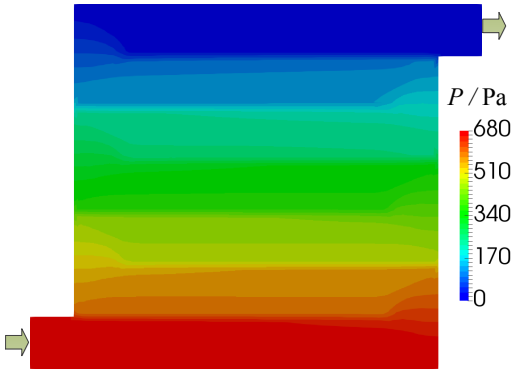

Figure 7.14: Pressure distribution in cathode side gas channels, $i = 0.8\,\mathrm{A\,cm^{-2}}$.

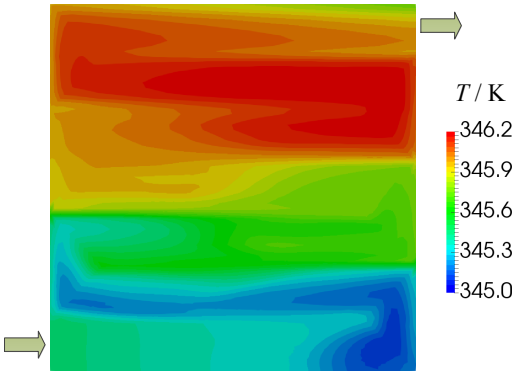

Figure 7.15: Temperature distribution in cathode side gas channels, $i = 0.8\,\mathrm{A\,cm^{-2}}$.

addition, the present model is based on the volume-averaging method, the local values of temperature are not resolved.

7.4 Discussion

The homogeneous model is verified and validated in this chapter. The overall cell performance predicted by the detailed and homogeneous models are compared and reasonable agreement can be achieved. The deviations of current density and liquid water saturation distributions between both models exist. In the detailed model, 3-D transport phenomena are taken into consideration. In the homogeneous model, a series of 1-D and 2-D models are applied to represent the transport phenomena in the fuel cell by averaging the local properties to make the computational domain simple. However, some physical processes, for example, the condensation and evaporation, are sensitive to the local values. The volume averaging approach may neglect the local sensitivity and finally contributes to the deviations between the detailed model and the homogeneous model.

The flow by-passing through the GDL between adjacent gas channels is important in PEFCs. It has been studied in Chapter 4, as well as in the work of Pharoah [217], Park and Li [178], Bachman et al. [219], etc. As baffles are applied in the case with serpentine flow paths, the flow by-passing between adjacent regions is hindered. It was also indicated that flow by-passing is dominated by both diffusion and convection, which contributes to better species redistribution when serpentine flow path is used. The presence of baffles may lead to more non-uniformal species distribution, which also results in worse cell performance. In the present study, it can be seen that the pressure drop is relative minor, the effect due to flow by-passing is therefore slight. However, flow by-passing is significant in larger stacks with higher pressure drops.

In addition, due to the existence of gravity force, the liquid water distribution in the gas channel cross-section is not uniform. The liquid water droplets can be generated on the interface between GDLs and gas channels, which can partially block the reactants diffusion from gas channel to reaction sites. In such a case, the flooding issue cannot be resolved in the homogeneous model. In order to account for this, additional models are necessary to address the liquid water variation in the through-plane direction and/or in in-plane directions. The cases applied in this chapter is supplied with half-humidified gases at both anode and cathode inlets, in which cases, the liquid water saturation in gas channels can be assumed to be minor. The effect of liquid phase coverage on the GDL on cell performance is also insignificant. However, for more humidified gases and larger current density loads, the present model may not be able to provide correct results. Corresponding models should be implemented in the future.

In the present model, transport phenomena in the GDLs are described by several 1-D models. The heterogeneity and compression of GDLs are not taken into account. Additionally, the gas/liquid convective transport in the GDLs are also important [218]. By removing the GDLs from computational domains, the computational effort can be mitigated; however, sane models should be implemented to consider various transport phenomena. These should be addressed in future studies.

The present model is based on the DRA method. As a much simpler geometry can be applied and the much coarser grid can be utilized, the computational effort in conducting the simulations is greatly decreased. The model may be applied in LT-PEFC stacks. However, the deviations by using volume averaged approach should be considered. It is known that the detailed two-phase simulations in fuel cells consume great computational resource. Therefore, a balance should be reached between computational power and prediction accuracy.

7.5 Conclusion

In the present chapter, a 3-D homogeneous LT-PEFC model is introduced. All of the major transport phenomena are considered. This model is verified by comparing the results between the present model and a detailed model. A LT-PEFC with a design of triple-serpentine flow path at both anode and cathode sides were numerically simulated and experimentally measured. It is found that the cell voltages are readily predicted by the present model with minor deviations.

The current density, liquid water saturation, temperature, and species mole fraction distributions predicted by the homogeneous model are presented. It can be seen that the current density, liquid water saturation, and temperature distributions are relatively uniform. The oxygen and water vapor mole fractions in gas channels decreases and increases from the inlet region to the outlet region, respectively. This is also true for oxygen and water at the interface between the membrane and cathode catalyst electrode. The hydrogen mole fraction presents a tendency that it increases firstly and decreases subsequently from the inlet region to the outlet region.

Though the overall cell behavior is readily predicted by the present model, model parameters still need to be adjusted to provide more reasonable internal variables distributions. The pressure drop between the gas inlet and outlet can be measured. The S++ device can be applied to measure the current density distribution in a fuel cell. Several fitting parameters are used in the present model, hence additional experimental data offer more accurate values.

Chapter 8

Discussion

In this thesis, two types of fuel cell models were introduced, namely the detailed model and the homogeneous model, in Chapter 2. Both models considers the major transport phenomena in PEFCs, including fluid flow, species transfer, charge transfer, heat transfer, and electrochemical reactions. While the detailed model shows the ability to capture the fine-scale information, the homogeneous model provided an easy tool for fast predictions. In the homogeneous model, the volume averaging approach is applied to simplify the computational domain and transport equations. In the meantime, supplementary relations are introduced to address the physical gaps from the detailed computational domain and transport equations to the simplified domain and homogeneous transport equations, respectively. Mathematically speaking, the homogeneous model is more complex than the detailed model that utilizes the general governing equations in CFD. It is worthy as the computational requirement decreases significantly for the homogeneous model applications.

The present models enable the cell and stack levels simulations. The application of the detailed model is limited by computational power, whereas fine-scale results can be provided. The application of the homogeneous model is hindered by the accuracy of simulated results, whereas the computational requirement is very low. Therefore, the cell level fuel cell design and optimization can be obtained with the detailed model, while the stack level fuel cell design and optimization should be achieved from the homogeneous model. The application of the detailed model on the stack level simulations is greatly limited by the stack active area and number of stacks. As shown in this study, the simulations on a 5-cell HT-PEFC stack, with each of which an active area of 200 cm^2, is possible. However, simulation of a stack with more cells, e.g. 7, is fairly difficult even in constructing the computational grid.

As the detailed model may act as an alternative method other than the detailed model, it can provide an easy tool for larger scale simulations. In

this thesis, the homogeneous model is applied on a HT-PEFC short stack and a LT-PEFC single cell. The industrial applications of PEFCs, e.g. electrical vehicles, stationary power station, etc., utilize relative large stacks. The simulations on larger HT-PEFC and LT-PEFC stacks, with more cells, should be performed. In these stacks, the water management, and heat and mass transfer are more critical than those in the short stacks and single cells. In addition, the Reynolds number is also high in a large stack. In such a case, turbulent flow occurs in the stack, especially in the manifolds, where turbulent models are needed to accurately describe this phenomena. It may greatly increase the computational requirement during the simulations. Fortunately, the fluid flow in gas channels of both anode and cathode side is laminar. The volume averaging method is still applicable in these regions. The utilization of the homogeneous model in larger stacks is promising.

In the cases shown in this study, the material properties are always assumed to be homogeneous and isotropic. For the real fuel cell applications, the material properties are usually not the case, especially for the porous GDLs. The effective properties, including diffusion coefficients, thermal conductivity, electrical conductivity, permeability, etc, and their inhomogeneity and anisotropicity are critical in fuel cell designs, especially for LT-PEFCs. The characterizations of GDLs have been investigated [50, 233, 234]. It is important to take these parameters into consideration in following studies.

During the long-term test [235], e.g. freeze/thaw cycling, start-up/shut-down, etc., the catalyst layer cracks and delamination appear in the PEFCs. As shown in Chapter 6, the effects due to the presence of cracks in the catalyst layer are insignificant on the overall cell performance. However, the crack grows during long-term operation [236], accompanying with the membrane and catalyst degradation. The catalyst layer delamination [235, 237] in PEFCs is important. The combination effects due to cracks and delamination may be investigated in following work.

The electrochemical reaction on the catalyst surface is very complicated. The distribution of catalyst in the catalyst layer might be fairly nonuniform. In the present study, the electrochemical reaction is described by the Butler-Volmer and Tafel relations for simplicity. Meanwhile, the catalyst is assumed to distribute uniformly. As shown in previous studies [238–243], agglomerate models are usually applied to represent the electrochemical reaction on surfaces of catalyst agglomerates, in which catalyst distribution nonuniformity may also be taken into account. In addition, the transport resistance can be more accurately captured by considering the local partial flooding and starvation issues. Meanwhile, the catalyst nonuniformity appeared in the cases of cracks and GDL shortage, see Chapter 6, may contributed alternatively to the overall behavior and local variable variations. The agglomerate models or equivalent models should be applied for electrochemical reaction on the catalyst for further studies.

The membrane is usually assumed to be nonpermeable to gases, with an

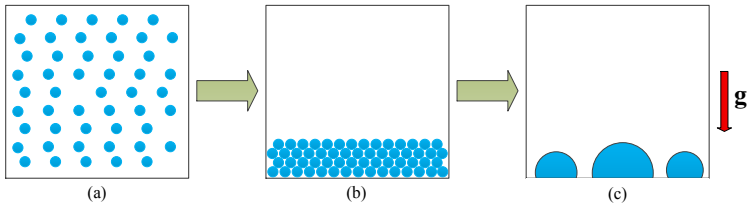

Figure 8.1: Skematic of liquid water distribution in a channel cross section. (a) Homogeneous. (b) Condensed. (c) Merged.

exception for the water. Water transfers through the membrane in dissolved phase, with diffusion, electro-osmotic drag, and permeation. In reality, hydrogen and oxygen may also diffuse through the membrane, which results in accelerated membrane degradation [244] and lower cell performance [245]. The crossover of reactants through the membrane is much significant for the aged membranes. The diffusion of the reactant/product through the membrane depends on the concentration difference between both sides. Much more significant gas crossover may occur if pinholes are formed in the membranes, in which case, the gas can flow directly through the pinholes [93]. In the present study, the fuel cells are assumed to operate with fresh MEAs, therefore, the gas crossover may be neglected. Nevertheless, a model capable of capturing gas crossover processes should be considered.

Figure 8.1 presents the liquid water distribution in a cross-section of flow channels for three different scenarios. To describe two-phase flow phenomena, the liquid phase is assumed existing in the mist state, as shown in Fig. 8.1(a). Due to the gravity force, liquid water droplets may accumulate near the bottom of the channel, as shown in Fig. 8.1(b). However, the liquid water may merge with each other and larger droplets are formed on the bottom surface as shown in Fig. 8.1(c). In the present study, Fig. 8.1(a) represents the liquid water distribution in the homogeneous model, in which the gravity effects on liquid water distribution in channel cross-section directions cannot be captured. Figure 8.1(b) exhibits the liquid water distribution in the detailed model, in which the coverage of liquid water on the bottom surface cannot be fully captured. In the present study, liquid water saturation in gas channels is relatively low considering the humidity of inlet gases. Therefore, the deviations of liquid water distributions for Figs. 8.1(a) and 8.1(b) from Fig. 8.1(c) are also small. However, for further application, e.g. flooding, additional correlations are necessary to address the deviations. A face coverage model [128] may be applied in the detailed model in case of a large amount of liquid water appears in the channels. For the homogeneous model, the liquid water droplets may be treated as 'solid

particles', and they can settling down from the case Fig. 8.1(a) to case Fig. 8.1(b). A settling theory may be applied. These are important in LT-PEFC and/or stack applications.

The orientation of fuel cells and stacks is important for the performance due to the gravity force. The effects are insignificant for single phase simulations. In the two phase flow, the density difference between liquid phase and gas phase is large. By varying the orientation of cell and stack, the liquid water accumulates on different locations, including the side walls of the channel and the surface of the GDL. In addition, the two phase flow may exist at both sides. In this thesis, the gravity is only in one direction as shown by Fig. 8.1 if the bottom represents the GDL surface. It is obvious that the liquid water distribution exhibited in Figs. 8.1(b) leads to higher liquid water saturation in the cathode electrode. The flooding problem is prone to happen at the cathode side. Cases with different orientations will be studied in the following studies.

The liquid phase are assumed to exist in perfect spherical droplets. However, the droplets may deform depending on the flow regimes. In addition, if the droplets are formed on the side walls or the GDL surface, the morphology exists due to the wall adhesion and the interfacial forces from the gas phase. The heat and mass transfer coefficients in this thesis are derived based on the spherical droplet assumption. If the morphology is taken into account, the heat and mass transfer may be different. In the meantime, for the interfacial forces, only the drag force acts on both phases, while the lift force, virtual mass, etc., are also important in two phase simulations. In this study, liquid water saturation in the gas channels is not so large, therefore, the effects may be slight. Nevertheless, the droplet morphology and additional interfacial momentum transfer terms will be considered.

For the present two-phase Eulerian-Eulerian model, there should be a continuous phase and a dispersed phase. However, it is not always true in LT-PEFC and/or stack simulations. As shown in Fig. 8.1(b), liquid phase near the bottom surface can be considered as the continuous phase and gas phase as the dispersed phase. However, the gas phase is continuous and the liquid phase is dispersed in the top region. If the liquid water saturation is not very high, e.g. < 0.7, a blending function can be used to switch the dispersed and continuous phases. However, more liquid water may be produced and accumulate, and a new flow regime is formed, segregated two-phase flow [196]. The present model cannot describe this kind of two-phase flow accurately. Therefore, a segregated two-phase flow model, as proposed by Marschall [196], should be implemented into the present model.

The convergence issue is still a critical problem for the present detailed model to consider two phase flow. Although the LTS method is applied to promote convergence, it is still time-consuming to obtain 'steady state' solutions. A proper solution scheme is needed to enable faster convergence.

Chapter 9

Conclusion

In this thesis, a detailed model and a homogeneous model were developed, introduced, and applied on the simulations of PEFCs. Both models enabled the simulations of HT-PEFC/LT-PEFCs with single-phase/two-phase flow phenomena for single-component/multi-component species under isothermal/nonisothermal conditions. The models are based on the multiple-region technique, in each of which corresponding transport phenomena are accounted for and solved. The detailed model considers the transport phenomena with fine-scale information, based on the conventional CFD, whereas, the homogeneous model serves as a tool for fast and easy predictions, based on the DRA method. The two phase Eulerian-Eulerian model is applied to address two phase flow in the LT-PEFCs.

The applications of the detail modeled and homogeneous model on HT-PEFC/LT-PEFC are presented separately. Both models are numerically verified and experimentally validated. With slight deviations being observed in comparisons, both models show the capability of predicting the cell performance with minor errors from the experimental results. The discussions and conclusions are given in each application, and summarized as following:

1. HT-PEFC detailed models, Chapter 4:

    - It is revealed that significant local variations exist, which are not previous captured. The current density is higher under the gas channels and lower under the lands due to the finite mass transfer conductance. The serpentine flow path contributes to the higher pressure losses, however, it is beneficial for better distributions of current density, oxygen and water vapor, in terms of gas bypassing through the GDLs.
    - It is also revealed that the oxygen and water concentration gradients existe in the cathode CL. This is neglected by *model 1* where the CL is treated to be infinite thin. The influence increases with the thickness of catalyst electrode, especially when

the current density is larger. Therefore, the present model should be preferably applied if the catalyst electrode is relatively thick.

2. HT-PEFC homogeneous model, Chapter 5:

   - The distributions of oxygen and water vapor mole fraction are compared between the homogeneous model and a detailed model. The application of the detailed model is limited by the computational requirement, whereas, the homogeneous model is readily applied to large HT-PEFC stacks. However, the local variations for the involved parameters cannot be resolved by the homogeneous model.
   - A tradeoff of the detailed model and the homogeneous model should be reached between fidelity/granularity and processor size/speed.

3. LT-PEFC detailed model, Chapter 6:

   - The cracks in the catalyst layer exhibit slight effects on the overall cell performance. The cracks contribute to reaction area missing, which deteriorates the performance. The effects of cracks are much more significant in and near the cracks regions, with much higher liquid water saturation and much lower current density. The nonuniformity of current density is also more obvious due to the cracks.
   - If the GDL shortage occurs only at the cathode side, the uncovered membrane is exposed with high water content and protonic conductivity, which results in better cell performance. If it appears at both sides, cell performance firstly increases, then decreases with the increasing of GDL shortage size. The GDL shortage leads to high local temperature in the membrane, which can cause severe damage. In such a case, the MEA failure may be mainly caused by the high local temperature and/or the mechanical pressure.

4. LT-PEFC homogeneous model, Chapter 7:

   - The distributions of current density, liquid water saturation, and temperature predicted by the homogeneous model are relatively uniform. The molar fraction distributions of oxygen and water vapor at the cathode side, and hydrogen at the anode side are presented. The oxygen molar fraction decreases from the inlet to the outlet due to the electrochemical reaction. The water and hydrogen molar fractions are complex considering the water transfer in the membrane and phase change issues.

- These still exist deviations between the simulation results predicted by the detailed model and the homogeneous model. As slightly different physical models are applied, additional experimental data are necessary. They may provide information and adjust the model parameters for the homogeneous model.

To promote further applications for the present models, several issues still needed to be addressed. Especially, more experimental data are critical for more comprehensive model validations. Material properties, electrochemical reactions, and two phase flow are the most challenging aspects that deserved more attention.

Chapter 10

Outlook

The detailed and homogeneous models introduced in the present thesis have already been implemented into the source code by the present author under the open source environment, OpenFOAM ®. The applications on HT-PEFCs and LT-PEFCs are validated by the corresponding experimental measurements. The aim of the present study is to offer two frameworks for the detailed model and the homogeneous model. Since both models are developed to consider 3-D, nonisothermal, multi-region, multi-physics, multi-scale, and multi-phase transport phenomena that are coupled with each other, the applicability of both models are not limited to PEFCs. A generic form for electrochemical reaction is taken into account, hence, simulations on fuel cells, including DMFC, SOFC, etc., electrolyzer, like proton exchange membrane (PEM) water electrolyzer, (solid oxide electrolyzer cell) SOEC, etc., and/or battery, should be possible. In addition, the simulations are not limited to cell level, whereas, the homogeneous model offers an easy tool for stack level simulations.

The author would firstly like to address some issues concerned in the discussion, (see Chapter 8). They are important in future applications of the models. Some of them are presently beyond the scope of the thesis. Contribution from others will be much more helpful for further development of the present codes. Therefore, the source code will be made open source in the near future.

Nomenclature

Abbreviation

ASR	Area specific resistance
BD	Blending differencing
BPP	Bipolar plate
CFD	Computational fluid dynamics
CCM	Catalyst coated membrane
CO	Carbon monoxide
CO_2	Carbon dioxide
CD	Central differencing
CL	Catalyst layer
DRA	Distributed resistance analogy
EOD	Electro-osmotic drag
EW	Equivalent weight, $\mathrm{kg\,mol^{-1}}$
FVM	Finite volume method
GDL	Gas diffusion layer
H_3PO_4	Phosphoric acid
H_3O^+	Hydronium complexes
HOR	Hydrogen oxidation reaction
HT	High temperature
LBM	Lattic boltzmann method
LT	Low temperature

LTS Local time-stepping

M2 Multiphase mixture

MEA Membrane electrode assembly

MUSES Multi-shared space

ORR Oxygen reduction raction

PBI polybenzimidazole

PEFC Polymer electrolyte fuel cell

PISO Pressure Implicit with Splitting of Operators

PDE Partial differential equation

PTFE Polytetrafluoroethylene

RH Relative humidity

UD Upwind differencing

VOF Volume of fluid

English

$\mathbf{A}$ Coefficients matrix

A Area, m^2

a Water activity, -

c Concentration, $\mathrm{mol\,s}^{-3}$

C Coefficient, -

C_K Mass transfer coefficient, $\mathrm{m\,s}^{-1}$

Cp Specific heat, $\mathrm{J\,K}^{-1}$

$\mathbf{D}$ Diagonal matrix

D Diffusion coefficient, $\mathrm{m}^2\,\mathrm{s}^{-1}$

D_h Hydraulic diameter, m

E Potential, V

$\mathbf{F}$ Force, $\mathrm{N\,m}^{-3}$

F Faraday's constant, $\mathrm{C\,mol}^{-1}$

f	Relative frequency density
G	Gibbs free energy, J
g	Gravity, $\mathrm{m\,s^{-2}}$
H	Enthalpy, J
$h*$	Convective heat transfer coefficient, $\mathrm{W\,m^{-2}, K^{-1}}$
h	Enthalpy, $\mathrm{J\,kg^{-1}}$
$\mathbf{I}$	Protonic current density, $\mathrm{A\,cm^{-2}}$
$\mathbf{i}$	Current density vector, $\mathrm{A\,cm^{-2}}$
i_0	Exchange current density, $\mathrm{A\,m^{-3}}$
$\mathbf{J}$	Diffusion flux, $\mathrm{mol\,s^{-1}}$
J	Charger source, $\mathrm{A\,m^{-3}}$
K	Permeability, $\mathrm{m^{-2}}$
k	Thermal conductivity, $\mathrm{W\,m^{-1}\,K^{-1}}$
L	Characteristic length, m
$\mathbf{M}$	Interfacial momentum transfer, $\mathrm{N\,m^{-3}}$
M	Mole Mass, $\mathrm{kg\,mol^{-1}}$
m	Mass flux, $\mathrm{kg\,m^{-2}\,s^{-1}}$
$\mathbf{N}$	Off-diagonal matrix
n_d	EOD coefficient, -
p	Pressure, Pa
p_{Sat}	Saturation pressure, Pa
Q	Heat source, $\mathrm{J\,kg^{-3}\,s^{-1}}$
Q	Heat source, $\mathrm{J\,m^{-3}\,s^{-1}}$
q	Heat flux, $\mathrm{J\,m^{-2}\,s^{-1}}$
R	Mass source, $\mathrm{kg\,m^{-3}\,s^{-1}}$
R	Radius, m
R_g	Universal gas constant, $\mathrm{J\,mol^{-1}\,K^{-1}}$

r	Porosity, -
S	Entrolpy, $\mathrm{J\,K^{-1}}$
S	Momentum source term, $\mathrm{N\,m^{-3}}$
s	Saturation, -
S_f	Shape factor, -
T	Temperature, K
t	Time, s
$\mathbf{U}$	Phase velocity, $\mathrm{m\,s^{-1}}$
U	Overall heat transfer coefficient, $\mathrm{W\,m^{-2}, K^{-1}}$
U	Velocity magnitude, $\mathrm{m\,s^{-1}}$
V	Cell voltage, V
V	Volume, $\mathrm{m^3}$
X	Mole fraction, -
Y	Mass fraction, -
z	Number of electrons transfer

Greek

α	Contact angle, -
α	Transfer coefficient
β	Power exponent
χ	Thermal diffusivity, $\mathrm{m^2\,s^{-1}}$
δ	Distance, m
ϵ	Porosity, -
η	Activation overpotential, V
Γ	Diffusion coefficient, $\mathrm{kg\,m^{-1}\,s^{-1}}$
γ	Power exponent
κ	Inter-phase heat transfer coefficient, $\mathrm{W\,m^{-3}, K^{-1}}$
λ	Stoichiometric factor

λ	Water content, -
λ	Water content, -
μ	Dynamic viscosity, $\mathrm{kg\,m^{-1}\,s^{-1}}$
ν	Kinematic viscosity, $\mathrm{m^2\,s^{-1}}$
ω	Consumption/production index
Ω	Ohmic resistance, $\Omega\,\mathrm{cm^2}$
ψ	Desorption/adsorption rate, s^{-1}
ρ	Density, $\mathrm{kg\,m^{-3}}$
σ	Electric conductivity, $\mathrm{S\,m}$
σ	Surface tension, $\mathrm{N\,m}$
τ	tortuosity, -
Υ	Phase change rate, $\mathrm{s^{-1}}$
φ	Potential, V
ζ	Fitting parameter, -

Superscripts

b	Bulk value
c	Capillary
an	Anode side
ca	Cathode side
d	Drag
diff	Diffusion process
e	Equivalent
E	Electron
i	Species index
in	Inlet
int	Interfacial
j	Species index

kn	Kundsen
l	Lift
mix	Mixture
m	Membrane
NB	Neighbor regions
ϕ	Phase index
P	Proton
r	Relative
vm	Virtual mass
w	Wall value or values on the membrane surfaces

Subscripts

$''$	Per area
eff	Effective

Bibliography

[1] *fuelCell*. `http://americanhistory.si.edu/fuelcells/origins/origins.htm`. Accessed date: 04-06-2019.

[2] M. Carmo, D. L. Fritz, J. Mergel, and D. Stolten. "A comprehensive review on PEM water electrolysis". In: *International Journal of Hydrogen Energy* 38.12 (2013), pp. 4901 –4934.

[3] A. M. Abdalla, S. Hossain, O. B. Nisfindy, A. T. Azad, M. Dawood, and A. K. Azad. "Hydrogen production, storage, transportation and key challenges with applications: A review". In: *Energy Conversion and Management* 165 (2018), pp. 602 –627.

[4] C. Siegel. "Review of computational heat and mass transfer modeling in polymer-electrolyte-membrane (PEM) fuel cells". In: *Energy* 33.9 (2008), pp. 1331 –1352.

[5] Y. Wang, K. S. Chen, J. Mishler, S. C. Cho, and X. C. Adroher. "A review of polymer electrolyte membrane fuel cells: Technology, applications, and needs on fundamental research". In: *Applied Energy* 88 (2011), pp. 981 –1007.

[6] A. Z. Weber, R. L. Borup, R. M. Darling, P. K. Das, T. J. Dursch, W. Gu, D. Harvey, A. Kusoglu, S. Litster, M. M. Mench, R. Mukundan, J. P. Owejan, J. G. Pharoah, M. Secanell, and I. V. Zenyuk. "A Critical Review of Modeling Transport Phenomena in Polymer-Electrolyte Fuel Cells". In: *Journal of The Electrochemical Society* 161 (2014), F1254–F1299.

[7] J. Park, H. Oh, T. Ha, Y. I. Lee, and K. Min. "A review of the gas diffusion layer in proton exchange membrane fuel cells: Durability and degradation". In: *Applied Energy* 155 (2015), pp. 866 –880.

[8] S. S. Araya, F. Zhou, V. Liso, S. L. Sahlin, J. R. Vang, S. Thomas, X. Gao, C. Jeppesen, and S. K. Kr. "A comprehensive review of PBI-based high temperature PEM fuel cells". In: *International Journal of Hydrogen Energy* 41 (2016), pp. 21310 –21344.

[9] R. Taherian. “A review of composite and metallic bipolar plates in proton exchange membrane fuel cell: Materials, fabrication, and material selection”. In: *Journal of Power Sources* 265 (2014), pp. 370 –390.

[10] A. Chandan, M. Hattenberger, A. El-kharouf, S. Du, A. Dhir, V. Self, B. G. Pollet, A. Ingram, and W. Bujalski. “High temperature (HT) polymer electrolyte membrane fuel cells (PEMFC) A review”. In: *Journal of Power Sources* 231 (2013), pp. 264 –278.

[11] V. Weissbecker, K. Wippermann, and W. Lehnert. “Electrochemical Corrosion Study of Metallic Materials in Phosphoric Acid as Bipolar Plates for HT-PEFCs”. In: *Journal of The Electrochemical Society* 161.14 (2014), F1437–F1447.

[12] L. Cindrella, A. Kannan, J. Lin, K. Saminathan, Y. Ho, C. Lin, and J. Wertz. “Gas diffusion layer for proton exchange membrane fuel cells - A review”. In: *Journal of Power Sources* 194.1 (2009). XIth Polish Conference on Fast Ionic Conductors 2008, pp. 146 –160.

[13] G. Lin and T. V. Nguyen. “Effect of Thickness and Hydrophobic Polymer Content of the Gas Diffusion Layer on Electrode Flooding Level in a PEMFC”. In: *Journal of The Electrochemical Society* 152.10 (2005), A1942–A1948.

[14] R. B. Ferreira, D. Falco, V. Oliveira, and A. Pinto. “Experimental study on the membrane electrode assembly of a proton exchange membrane fuel cell: effects of microporous layer, membrane thickness and gas diffusion layer hydrophobic treatment”. In: *Electrochimica Acta* 224 (2017), pp. 337 –345.

[15] C.-H. Liu, T.-H. Ko, J.-W. Shen, S.-I. Chang, S.-I. Chang, and Y.-K. Liao. “Effect of hydrophobic gas diffusion layers on the performance of the polymer exchange membrane fuel cell”. In: *Journal of Power Sources* 191.2 (2009), pp. 489 –494.

[16] C. Lim and C. Wang. “Effects of hydrophobic polymer content in GDL on power performance of a PEM fuel cell”. In: *Electrochimica Acta* 49.24 (2004), pp. 4149 –4156.

[17] E. M. Khetabi, K. Bouziane, N. Zamel, X. Franois, Y. Meyer, and D. Candusso. “Effects of mechanical compression on the performance of polymer electrolyte fuel cells and analysis through in-situ characterisation techniques - A review”. In: *Journal of Power Sources* 424 (2019), pp. 8 –26.

[18] F. Liu, S. Mohajeri, Y. Di, K. Wippermann, and W. Lehnert. “Influence of the Interaction Between Phosphoric Acid and Catalyst Layers on the Properties of HTPEFCs”. In: *Fuel Cells* 14.5 (Oct. 2014), pp. 750–757.

[19] N. Zamel. "The catalyst layer and its dimensionality A look into its ingredients and how to characterize their effects". In: *Journal of Power Sources* 309 (2016), pp. 141 –159.

[20] K. Karan. "PEFC catalyst layer: Recent advances in materials, microstructural characterization, and modeling". In: *Current Opinion in Electrochemistry* 5.1 (2017), pp. 27 –35.

[21] E. Majlan, D. Rohendi, W. Daud, T. Husaini, and M. Haque. "Electrode for proton exchange membrane fuel cells: A review". In: *Renewable and Sustainable Energy Reviews* 89 (2018), pp. 117 –134.

[22] F. Barbir. *PEM fuel cells: theory and practice*. Academic Press, 2012.

[23] Y. Garsany, B. D. Gould, O. A. Baturina, and K. E. Swider-Lyons. "Comparison of the Sulfur Poisoning of PBI and Nafion PEMFC Cathodes". In: *Electrochemical and Solid-State Letters* 12 (2009), B138–B140.

[24] J. S. Wainright, J.. Wang, D. Weng, R. F. Savinell, and M. Litt. "AcidDoped Polybenzimidazoles: A New Polymer Electrolyte". In: *Journal of The Electrochemical Society* 142.7 (1995), pp. L121–L123.

[25] L. Qingfeng, H. Hjuler, and N. Bjerrum. "Phosphoric acid doped polybenzimidazole membranes: Physiochemical characterization and fuel cell applications". In: *Journal of Applied Electrochemistry* 31 (2001), pp. 773–779.

[26] C. Wannek, W. Lehnert, and J. Mergel. "Membrane electrode assemblies for high-temperature polymer electrolyte fuel cells based on poly(2,5-benzimidazole) membranes with phosphoric acid impregnation via the catalyst layers". In: *Journal of Power Sources* 192.2 (2009), pp. 258 –266.

[27] K. Wippermann, C. Wannek, H.-F. Oetjen, J. Mergel, and W. Lehnert. "Cell resistances of poly(2,5-benzimidazole)-based high temperature polymer membrane fuel cell membrane electrode assemblies: Time dependence and influence of operating parameters". In: *Journal of Power Sources* 195 (2010), pp. 2806 –2809.

[28] T. Arlt, W. Lke, N. Kardjilov, J. Banhart, W. Lehnert, and I. Manke. "Monitoring the hydrogen distribution in poly(2,5-benzimidazole)-based (ABPBI) membranes in operating high-temperature polymer electrolyte fuel cells by using H-D contrast neutron imaging". In: *Journal of Power Sources* 299 (2015), pp. 125 –129.

[29] M. Andersson, S. B. Beale, M. Espinoza, Z. Wu, and W. Lehnert. "A review of cell-scale multiphase flow modeling, including water management, in polymer electrolyte fuel cells". In: *Applied Energy* 180 (2016), pp. 757 –778.

[30] Y.-L. He and W.-Q. Tao. "Multiscale simulations of heat transfer and fluid flow problems". In: *Journal of heat transfer* 134.3 (2012), p. 031018.

[31] J. Wang. "Theory and practice of flow field designs for fuel cell scaling-up: A critical review". In: *Applied Energy* 157 (2015), pp. 640 –663.

[32] S. B. Beale, H.-W. Choi, J. G. Pharoah, H. K. Roth, H. Jasak, and D. H. Jeon. "Open-source computational model of a solid oxide fuel cell". In: *Computer Physics Communications* 200 (2016), pp. 15 –26.

[33] S. B. Beale and S. V. Zhubrin. "A Distributed Resistance Analogy for Solid Oxide Fuel Cells". In: *Numerical Heat Transfer, Part B: Fundamentals* 47 (2005), pp. 573–591.

[34] R. T. Nishida, S. B. Beale, and J. G. Pharoah. "Comprehensive computational fluid dynamics model of solid oxide fuel cell stacks". In: *Int. J. Hydrogen Energy* 41 (2016), pp. 20592 –20605.

[35] *OpenFOAM*. `https://openfoam.org/`. Accessed date: 04-06-2019.

[36] *OpenFuelCell*. `http://openfuelcell.sourceforge.net/`. Accessed date: 04-06-2019.

[37] *ANSYS*. `https://www.ansys.com/`. Accessed date: 04-06-2019.

[38] *matplotlib*. `https://https://matplotlib.org//`. Accessed date: 01-01-2020.

[39] *ParaView*. `https://www.paraview.org/`. Accessed date: 04-06-2019.

[40] R. C. Weast, M. J. Astle, W. H. Beyer, et al. *CRC handbook of chemistry and physics*. Vol. 69. CRC press Boca Raton, FL, 1988.

[41] U. Reimer, W. Lehnert, Y. Holade, and B. Kokoh. "Irreversible losses in fuel cells". In: *Fuel Cells and Hydrogen - From Fundamentals to Applied Research*. Ed. by V. Hacker and S. Mitsushima. Elsevier, 2018, pp. 15–40.

[42] K. Jiao and X. Li. "Water transport in polymer electrolyte membrane fuel cells". In: *Progress in Energy and Combustion Science* 37 (2011), pp. 221 –291.

[43] T. A. Zawodzinski Jr, M. Neeman, L. O. Sillerud, and S. Gottesfeld. "Determination of water diffusion coefficients in perfluorosulfonate ionomeric membranes". In: *The Journal of Physical Chemistry* 95.15 (1991), pp. 6040–6044.

[44] T. E. Springer, T. A. Zawodzinski, and S. Gottesfeld. "Polymer Electrolyte Fuel Cell Model". In: *Journal of The Electrochemical Society* 138.8 (1991), pp. 2334–2342.

[45] T. F. Fuller and J. Newman. "Experimental Determination of the Transport Number of Water in Nafion 117 Membrane". In: *Journal of The Electrochemical Society* 139.5 (1992), pp. 1332–1337.

[46] U. Reimer, J. Ehlert, H. Janßen, and W. Lehnert. "Water distribution in high temperature polymer electrolyte fuel cells". In: *International Journal of Hydrogen Energy* 41 (2016), pp. 1837 –1845.

[47] T. A. Zawodzinski, T. E. Springer, J. Davey, R. Jestel, C. Lopez, J. Valerio, and S. Gottesfeld. "A Comparative Study of Water Uptake By and Transport Through Ionomeric Fuel Cell Membranes". In: *Journal of The Electrochemical Society* 140.7 (1993), pp. 1981–1985.

[48] T. A. Zawodzinski, J. Davey, J. Valerio, and S. Gottesfeld. "The water content dependence of electro-osmotic drag in proton-conducting polymer electrolytes". In: *Electrochimica Acta* 40.3 (1995). Polymer electrolyte fuel cells, pp. 297 –302.

[49] D. M. Bernardi and M. W. Verbrugge. "A Mathematical Model of the SolidPolymerElectrolyte Fuel Cell". In: *Journal of The Electrochemical Society* 139.9 (1992), pp. 2477–2491.

[50] D. Fadzillah, M. Rosli, M. Talib, S. Kamarudin, and W. Daud. "Review on microstructure modelling of a gas diffusion layer for proton exchange membrane fuel cells". In: *Renewable and Sustainable Energy Reviews* 77 (2017), pp. 1001 –1009.

[51] J. Brackbill, D. Kothe, and C Zemach. "A continuum method for modeling surface tension". In: *Journal of Computational Physics* 100 (1992), pp. 335 –354.

[52] X. Liu, F. Peng, G. Lou, and Z. Wen. "Liquid water transport characteristics of porous diffusion media in polymer electrolyte membrane fuel cells: A review". In: *Journal of Power Sources* 299 (2015), pp. 85 –96.

[53] K. S. Udell. "Heat transfer in porous media considering phase change and capillarythe heat pipe effect". In: *International Journal of Heat and Mass Transfer* 28.2 (1985), pp. 485 –495.

[54] X.-D. Wang, Y.-L. Wang, Y. Chen, C. Si, A. Su, and D.-J. Lee. "Proton exchange membrane fuel cell modeling with diffusion layer-based and sands-based capillary pressure correlations: Comparative study". In: *Journal of the Taiwan Institute of Chemical Engineers* 45.4 (2014), pp. 1532 –1541.

[55] R. B. Ferreira, D. Falco, V. Oliveira, and A. Pinto. "1D+3D two-phase flow numerical model of a proton exchange membrane fuel cell". In: *Applied Energy* 203 (2017), pp. 474 –495.

[56] M. Andersson, S. B. Beale, U. Reimer, W. Lehnert, and D. Stolten. "Interface resolving two-phase flow simulations in gas channels relevant for polymer electrolyte fuel cells using the volume of fluid approach". In: *International Journal of Hydrogen Energy* 43.5 (2018), pp. 2961 –2976.

[57] M. Andersson, A. Mularczyk, A. Lamibrac, S. B. Beale, J. Eller, W. Lehnert, and F. N. Büchi. "Modeling and synchrotron imaging of droplet detachment in gas channels of polymer electrolyte fuel cells". In: *Journal of Power Sources* 404 (2018), pp. 159 –171.

[58] J. Yu, D. Froning, U. Reimer, and W. Lehnert. "Apparent contact angles of liquid water droplet breaking through a gas diffusion layer of polymer electrolyte membrane fuel cell". In: *International Journal of Hydrogen Energy* 43.12 (2018), pp. 6318 –6330.

[59] G. Molaeimanesh and M. Akbari. "Role of wettability and water droplet size during water removal from a PEMFC GDL by lattice Boltzmann method". In: *International Journal of Hydrogen Energy* 41.33 (2016), pp. 14872 –14884.

[60] J. Yu, D. Froning, U. Reimer, and W. Lehnert. "Liquid water breakthrough location distances on a gas diffusion layer of polymer electrolyte membrane fuel cells". In: *Journal of Power Sources* 389 (2018), pp. 56 –60.

[61] K. R. Minard, V. V. Viswanathan, P. D. Majors, L.-Q. Wang, and P. C. Rieke. "Magnetic resonance imaging (MRI) of PEM dehydration and gas manifold flooding during continuous fuel cell operation". In: *Journal of Power Sources* 161.2 (2006), pp. 856 –863.

[62] D. S. Hussey, D. Spernjak, A. Z. Weber, R. Mukundan, J. Fairweather, E. L. Brosha, J. Davey, J. S. Spendelow, D. L. Jacobson, and R. L. Borup. "Accurate measurement of the through-plane water content of proton-exchange membranes using neutron radiography". In: *Journal of Applied Physics* 112.10 (2012), p. 104906.

[63] *S++ scan shunt*. `www.splusplus.com`. Accessed date: 04-06-2019.

[64] L. Jabbour, C. Robin, F. Nandjou, R. Vincent, F. Micoud, J.-P. Poirot-Crouvezier, J. d'Arbigny, and M. Gerard. "Feasibility of in-plane GDL structuration: Impact on current density distribution in large-area Proton Exchange Membrane Fuel Cells". In: *Journal of Power Sources* 299 (2015), pp. 380 –390.

[65] I. V. Zenyuk, D. Y. Parkinson, G. Hwang, and A. Z. Weber. "Probing water distribution in compressed fuel-cell gas-diffusion layers using X-ray computed tomography". In: *Electrochemistry Communications* 53 (2015), pp. 24 –28.

[66] T. V. Nguyen and R. E. White. "A Water and Heat Management Model for ProtonExchangeMembrane Fuel Cells". In: *Journal of The Electrochemical Society* 140.8 (1993), pp. 2178–2186.

[67] T. F. Fuller and J. Newman. "Water and Thermal Management in Solid Polymer Electrolyte Fuel Cells". In: *Journal of The Electrochemical Society* 140.5 (1993), pp. 1218–1225.

[68] J. S. Yi and T. Van Nguyen. "Multicomponent Transport in Porous Electrodes of Proton Exchange Membrane Fuel Cells Using the Interdigitated Gas Distributors". In: *Journal of The Electrochemical Society* 146.1 (1999), pp. 38–45.

[69] J. S. Yi and T. V. Nguyen. "An Along–the–Channel Model for Proton Exchange Membrane Fuel Cells". In: *Journal of The Electrochemical Society* 145.4 (1998), pp. 1149–1159.

[70] V. Gurau, H. Liu, and S. Kaka. "Two-dimensional model for proton exchange membrane fuel cells". In: *AIChE Journal* 44.11 (1998), pp. 2410–2422.

[71] B. Sivertsen and N. Djilali. "CFD-based modelling of proton exchange membrane fuel cells". In: *Journal of Power Sources* 141 (2005), pp. 65 –78.

[72] T. Berning and N. Djilali. "A 3D, Multiphase, Multicomponent Model of the Cathode and Anode of a PEM Fuel Cell". In: *Journal of The Electrochemical Society* 150 (2003), A1589–A1598.

[73] T. Berning, D. Lu, and N. Djilali. "Three-dimensional computational analysis of transport phenomena in a PEM fuel cell". In: *Journal of Power Sources* 106 (2002), pp. 284 –294.

[74] J. Fimrite, H. Struchtrup, and N. Djilali. "Transport Phenomena in Polymer Electrolyte Membranes: I. Modeling Framework". In: *Journal of The Electrochemical Society* 152.9 (2005), A1804–A1814.

[75] A. Kulikovsky. "Gas dynamics in channels of a gas-feed direct methanol fuel cell: exact solutions". In: *Electrochemistry Communications* 3.10 (2001), pp. 572 –579.

[76] A. Kornyshev and A. Kulikovsky. "Characteristic length of fuel and oxygen consumption in feed channels of polymer electrolyte fuel cells". In: *Electrochimica Acta* 46 (2001), pp. 4389 –4395.

[77] A. A. Kulikovsky, J. Divisek, and A. A. Kornyshev. "Two–Dimensional Simulation of Direct Methanol Fuel Cell. A New (Embedded) Type of Current Collector". In: *Journal of The Electrochemical Society* 147 (2000), pp. 953–959.

[78] A. A. Kulikovsky. “Quasi-3D Modeling of Water Transport in Polymer Electrolyte Fuel Cells”. In: *Journal of The Electrochemical Society* 150 (2003), A1432–A1439.

[79] W. Lehnert, C. Wannek, and R. Zeis. “Chapter 3 Trends in High-Temperature Polymer Electrolyte Fuel Cells”. In: *Innovations in Fuel Cell Technologies*. The Royal Society of Chemistry, 2010, pp. 41–75.

[80] F. Conti, A. Majerus, V. Di Noto, C. Korte, W. Lehnert, and D. Stolten. “Raman study of the polybenzimidazolephosphoric acid interactions in membranes for fuel cells”. In: *Phys. Chem. Chem. Phys.* 14 (28 2012), pp. 10022–10026.

[81] A. R. Korsgaard, R. Refshauge, M. P. Nielsen, M. Bang, and S. K. Kr. “Experimental characterization and modeling of commercial polybenzimidazole-based MEA performance”. In: *Journal of Power Sources* 162 (2006), pp. 239 –245.

[82] D. F. Cheddie and N. D. Munroe. “Parametric model of an intermediate temperature PEMFC”. In: *Journal of Power Sources* 156 (2006), pp. 414 –423.

[83] D. F. Cheddie and N. D. Munroe. “Mathematical model of a PEMFC using a PBI membrane”. In: *Energy Conversion and Management* 47 (2006), pp. 1490 –1504.

[84] D. F. Cheddie and N. D. Munroe. “Three dimensional modeling of high temperature PEM fuel cells”. In: *Journal of Power Sources* 160 (2006), pp. 215 –223.

[85] K. Jiao and X. Li. “A Three-Dimensional Non-isothermal Model of High Temperature Proton Exchange Membrane Fuel Cells with Phosphoric Acid Doped Polybenzimidazole Membranes”. In: *Fuel Cells* 10 (2010), pp. 351–362.

[86] K. Jiao, I. E. Alaefour, and X. Li. “Three-dimensional non-isothermal modeling of carbon monoxide poisoning in high temperature proton exchange membrane fuel cells with phosphoric acid doped polybenzimidazole membranes”. In: *Fuel* 90 (2011), pp. 568 –582.

[87] K. Jiao, Y. Zhou, Q. Du, Y. Yin, S. Yu, and X. Li. “Numerical simulations of carbon monoxide poisoning in high temperature proton exchange membrane fuel cells with various flow channel designs”. In: *Applied Energy* 104 (2013), pp. 21 –41.

[88] J. Lobato, P. Cañizares, M. A. Rodrigo, F. J. Pinar, E. Mena, and D. Úbeda. “Three-dimensional model of a 50cm2 high temperature PEM fuel cell. Study of the flow channel geometry influence”. In: *International Journal of Hydrogen Energy* 35 (2010), pp. 5510 –5520.

[89] D. Úbeda, F. J. Pinar, P. Cañizares, M. A. Rodrigo, and J. Lobato. "An easy parameter estimation procedure for modeling a HT-PEMFC". In: *International Journal of Hydrogen Energy* 37 (2012), pp. 11308 –11320.

[90] T. Sousa, M. Mamlouk, and K. Scott. "An isothermal model of a laboratory intermediate temperature fuel cell using PBI doped phosphoric acid membranes". In: *Chemical Engineering Science* 65 (2010), pp. 2513 –2530.

[91] T. Sousa, M. Mamlouk, K. Scott, and C. M. Rangel. "Three Dimensional Model of a High Temperature PEMFC. Study of the Flow Field Effect on Performance". In: *Fuel Cells* 12 (2012), pp. 566–576.

[92] P. Chippar, K. Oh, D. Kim, T.-W. Hong, W. Kim, and H. Ju. "Coupled mechanical stress and multi-dimensional CFD analysis for high temperature proton exchange membrane fuel cells (HT-PEMFCs)". In: *International Journal of Hydrogen Energy* 38 (2013), pp. 7715 –7724.

[93] P. Chippar, K. Oh, W.-G. Kim, and H. Ju. "Numerical analysis of effects of gas crossover through membrane pinholes in high-temperature proton exchange membrane fuel cells". In: *International Journal of Hydrogen Energy* 39 (2014), pp. 2863 –2871.

[94] K. Oh, P. Chippar, and H. Ju. "Numerical study of thermal stresses in high-temperature proton exchange membrane fuel cell (HT-PEMFC)". In: *International Journal of Hydrogen Energy* 39 (2014), pp. 2785 – 2794.

[95] H. Sun, C. Xie, H. Chen, and S. Almheiri. "A numerical study on the effects of temperature and mass transfer in high temperature PEM fuel cells with ab-PBI membrane". In: *Applied Energy* 160 (2015), pp. 937 –944.

[96] D. Singdeo, T. Dey, S. Gaikwad, S. J. Andreasen, and P. C. Ghosh. "A new modified-serpentine flow field for application in high temperature polymer electrolyte fuel cell". In: *Applied Energy* 195 (2017), pp. 13 –22.

[97] S. Zhang, U. Reimer, Y. Rahim, S. B. Beale, and W. Lehnert. "Numerical modeling of polymer electrolyte fuel cells with analytical and experimental validation". In: *Journal of Electrochemical Energy Conversion and Storage* 16.3 (2019), p. 031002.

[98] S. Zhang, U. Reimer, S. B. Beale, W. Lehnert, and D. Stolten. "Modeling polymer electrolyte fuel cells: A high precision analysis". In: *Applied Energy* 233-234 (2019), pp. 1094 –1103.

[99] M. Kvesić, U. Reimer, D. Froning, L. Lüke, W. Lehnert, and D. Stolten. "3D modeling of a 200cm2 HT-PEFC short stack". In: *International Journal of Hydrogen Energy* 37 (2012), pp. 2430 –2439.

[100] M. Kvesić, U. Reimer, D. Froning, L. Lüke, W. Lehnert, and D. Stolten. "3D modeling of an HT-PEFC stack using reformate gas". In: *International Journal of Hydrogen Energy* 37 (2012), pp. 12438 –12450.

[101] D. Bezmalinovi, S. Strahl, V. Roda, and A. Husar. "Water transport study in a high temperature proton exchange membrane fuel cell stack". In: *International Journal of Hydrogen Energy* 39.20 (2014), pp. 10627 –10640.

[102] M. Drakselov, R. Kodm, D. nita, F. Beckmann, and K. Bouzek. "Three-dimensional macrohomogeneous mathematical model of an industrial-scale high-temperature PEM fuel cell stack". In: *Electrochimica Acta* 273 (2018), pp. 432 –446.

[103] S. Zhang, S. B. Beale, U. Reimer, R. T. Nishida, M. Andersson, J. G. Pharoah, and W. Lehnert. "Simple and Complex Polymer Electrolyte Fuel Cell Stack Models: A Comparison". In: *ECS Transactions* 86.13 (2018), pp. 287–300.

[104] A. Z. Weber and J. Newman. "Modeling Transport in Polymer-Electrolyte Fuel Cells". In: *Chemical Reviews* 104.10 (2004), 46794726.

[105] J. R. Lile and S. Zhou. "Theoretical modeling of the PEMFC catalyst layer: A review of atomistic methods". In: *Electrochimica Acta* 177 (2015), pp. 4 –20.

[106] V. Gurau and J. J. Adin Mann. "A Critical Overview of Computational Fluid Dynamics Multiphase Models for Proton Exchange Membrane Fuel Cells". In: *SIAM Journal on Applied Mathematics* 70 (2009), pp. 410–454.

[107] R. Anderson, L. Zhang, Y. Ding, M. Blanco, X. Bi, and D. P. Wilkinson. "A critical review of two-phase flow in gas flow channels of proton exchange membrane fuel cells". In: *Journal of Power Sources* 195 (2010), pp. 4531 –4553.

[108] R. B. Ferreira, D. Falco, V. Oliveira, and A. Pinto. "Numerical simulations of two-phase flow in proton exchange membrane fuel cells using the volume of fluid method A review". In: *Journal of Power Sources* 277 (2015), pp. 329 –342.

[109] G. Zhang and K. Jiao. "Multi-phase models for water and thermal management of proton exchange membrane fuel cell: A review". In: *Journal of Power Sources* 391 (2018), pp. 120 –133.

[110] A. Verma and R. Pitchumani. "Influence of membrane properties on the transient behavior of polymer electrolyte fuel cells". In: *Journal of Power Sources* 268 (2014), pp. 733 –743.

[111] S. Chaudhary, V. K. Sachan, and P. K. Bhattacharya. "Two dimensional modelling of water uptake in proton exchange membrane fuel cell". In: *International Journal of Hydrogen Energy* 39.31 (2014), pp. 17802 –17818.

[112] L. Karpenko-Jereb, P. Innerwinkler, A.-M. Kelterer, C. Sternig, C. Fink, P. Prenninger, and R. Tatschl. "A novel membrane transport model for polymer electrolyte fuel cell simulations". In: *International Journal of Hydrogen Energy* 39.13 (2014), pp. 7077 –7088.

[113] K. Jiao and B. Zhou. "Innovative gas diffusion layers and their water removal characteristics in PEM fuel cell cathode". In: *Journal of Power Sources* 169.2 (2007), pp. 296 –314.

[114] J. W. Park, K. Jiao, and X. Li. "Numerical investigations on liquid water removal from the porous gas diffusion layer by reactant flow". In: *Applied Energy* 87.7 (2010), pp. 2180 –2186.

[115] Z. Niu, Z. Bao, J. Wu, Y. Wang, and K. Jiao. "Two-phase flow in the mixed-wettability gas diffusion layer of proton exchange membrane fuel cells". In: *Applied Energy* 232 (2018), pp. 443 –450.

[116] M. A. Khan, B. Sundén, and J. Yuan. "Analysis of multi-phase transport phenomena with catalyst reactions in polymer electrolyte membrane fuel cells A review". In: *Journal of Power Sources* 196 (2011), pp. 7899 –7916.

[117] D. Froning, J. Brinkmann, U. Reimer, V. Schmidt, W. Lehnert, and D. Stolten. "3D analysis, modeling and simulation of transport processes in compressed fibrous microstructures, using the Lattice Boltzmann method". In: *Electrochimica Acta* 110 (2013), pp. 325 –334.

[118] D. Froning, J. Yu, G. Gaiselmann, U. Reimer, I. Manke, V. Schmidt, and W. Lehnert. "Impact of compression on gas transport in nonwoven gas diffusion layers of high temperature polymer electrolyte fuel cells". In: *Journal of Power Sources* 318 (2016), pp. 26 –34.

[119] P. Cheng and C. Wang. "A multiphase mixture model for multiphase, multicomponent transport in capillary porous mediaII. Numerical simulation of the transport of organic compounds in the subsurface". In: *International Journal of Heat and Mass Transfer* 39 (1996), pp. 3619 –3632.

[120] C. Wang and P. Cheng. "A multiphase mixture model for multiphase, multicomponent transport in capillary porous mediaI. Model development". In: *International Journal of Heat and Mass Transfer* 39 (1996), pp. 3607 –3618.

[121] V. Gurau, R. V. Edwards, J. A. Mann, and T. A. Zawodzinski. "A Look at the Multiphase Mixture Model for PEM Fuel Cell Simulations". In: *Electrochemical and Solid-State Letters* 11.8 (2008), B132–B135.

[122] C. Wang. "Comment on "A look at the multiphase mixture model for PEM fuel cell simulations" [Electrochemical and Solid-State Letters (2008) 11 (B132)]". English (US). In: *Electrochemical and Solid-State Letters* 12.2 (Jan. 2009).

[123] V. Gurau. "Response to Comment on A Look at the Multiphase Mixture Model for PEM Fuel Cell Simulations [Electrochem. Solid-State Lett. , 11 , B132 (2008)]". In: *Electrochemical and Solid-State Letters* 12.2 (2009), S4–S6.

[124] L. You and H. Liu. "A two-phase flow and transport model for the cathode of PEM fuel cells". In: *International Journal of Heat and Mass Transfer* 45 (2002), pp. 2277 –2287.

[125] L. You and H. Liu. "A two-phase flow and transport model for PEM fuel cells". In: *Journal of Power Sources* 155.2 (2006), pp. 219 –230.

[126] Z. Wang, C. Wang, and K. Chen. "Two-phase flow and transport in the air cathode of proton exchange membrane fuel cells". In: *Journal of Power Sources* 94 (2001), pp. 40 –50.

[127] Y. Wang and C.-Y. Wang. "A Nonisothermal, Two-Phase Model for Polymer Electrolyte Fuel Cells". In: *Journal of The Electrochemical Society* 153.6 (2006), A1193–A1200.

[128] H. Meng and C.-Y. Wang. "Model of Two-Phase Flow and Flooding Dynamics in Polymer Electrolyte Fuel Cells". In: *Journal of The Electrochemical Society* 152.9 (2005), A1733–A1741.

[129] Y. Wang. "Modeling of two-phase transport in the diffusion media of polymer electrolyte fuel cells". In: *Journal of Power Sources* 185 (2008), pp. 261 –271.

[130] A. Mahmoudi, A. Ramiar, and Q. Esmaili. "Effect of inhomogeneous compression of gas diffusion layer on the performance of PEMFC with interdigitated flow field". In: *Energy Conversion and Management* 110 (2016), pp. 78 –89.

[131] Y. Wang and K. S. Chen. "Advanced control of liquid water region in diffusion media of polymer electrolyte fuel cells through a dimensionless number". In: *Journal of Power Sources* 315 (2016), pp. 224 –235.

[132] Y. Wang and K. S. Chen. "Elucidating two-phase transport in a polymer electrolyte fuel cell, Part 1: Characterizing flow regimes with a dimensionless group". In: *Chemical Engineering Science* 66 (2011), pp. 3557 –3567.

[133] D. Natarajan and T. V. Nguyen. "Three-dimensional effects of liquid water flooding in the cathode of a PEM fuel cell". In: *Journal of Power Sources* 115.1 (2003), pp. 66 –80.

[134] D. Natarajan and T. Van Nguyen. "A Two-Dimensional, Two-Phase, Multicomponent, Transient Model for the Cathode of a Proton Exchange Membrane Fuel Cell Using Conventional Gas Distributors". In: *Journal of The Electrochemical Society* 148.12 (2001), A1324–A1335.

[135] W. He, J. S. Yi, and T. V. Nguyen. "Twophase flow model of the cathode of PEM fuel cells using interdigitated flow fields". In: *AIChE Journal* 46.10 (Oct. 2000), pp. 2053–2064.

[136] V. Gurau, J. Zawodzinski Thomas A., and J. Mann J. Adin. "Two-Phase Transport in PEM Fuel Cell Cathodes". In: *Journal of Fuel Cell Science and Technology* 5.2 (Apr. 2008). 021009.

[137] U. Pasaogullari and C. Y. Wang. "Liquid Water Transport in Gas Diffusion Layer of Polymer Electrolyte Fuel Cells". In: *Journal of The Electrochemical Society* 151.3 (2004), A399–A406.

[138] S. B. Beale, D. H. Schwarz, M. R. Malin, and D. B. Spalding. "Two-phase flow and mass transfer within the diffusion layer of a polymer electrolyte membrane fuel cell". In: *Computational Thermal Sciences: An International Journal* 1 (2009), pp. 105–120.

[139] G. Lin, W. He, and T. Van Nguyen. "Modeling Liquid Water Effects in the Gas Diffusion and Catalyst Layers of the Cathode of a PEM Fuel Cell". In: *Journal of The Electrochemical Society* 151.12 (2004), A1999–A2006.

[140] Q. Ye and T. V. Nguyen. "Three-Dimensional Simulation of Liquid Water Distribution in a PEMFC with Experimentally Measured Capillary Functions". In: *Journal of The Electrochemical Society* 154.12 (2007), B1242–B1251.

[141] X. Wang and T. V. Nguyen. "Modeling the Effects of Capillary Property of Porous Media on the Performance of the Cathode of a PEMFC". In: *Journal of The Electrochemical Society* 155.11 (2008), B1085–B1092.

[142] X. Wang and T. Van Nguyen. "Modeling the Effects of the Microporous Layer on the Net Water Transport Rate Across the Membrane in a PEM Fuel Cell". In: *Journal of The Electrochemical Society* 157.4 (2010), B496–B505.

[143] A. Z. Weber and J. Newman. "Effects of Microporous Layers in Polymer Electrolyte Fuel Cells". In: *Journal of The Electrochemical Society* 152.4 (2005), A677–A688.

[144] A. Z. Weber, R. M. Darling, and J. Newman. “Modeling Two-Phase Behavior in PEFCs”. In: *Journal of The Electrochemical Society* 151.10 (2004), A1715–A1727.

[145] A. Weber and M. Hickner. “Modeling and high-resolution-imaging studies of water-content profiles in a polymer-electrolyte-fuel-cell membrane-electrode assembly”. In: *Electrochimica Acta* 53.26 (2008), pp. 7668 –7674.

[146] A. Z. Weber and J. Newman. “Coupled Thermal and Water Management in Polymer Electrolyte Fuel Cells”. In: *Journal of The Electrochemical Society* 153.12 (2006), A2205–A2214.

[147] H. Meng. “Multi-dimensional liquid water transport in the cathode of a PEM fuel cell with consideration of the micro-porous layer (MPL)”. In: *International Journal of Hydrogen Energy* 34.13 (2009), pp. 5488 –5497.

[148] H. Meng. “Numerical studies of liquid water behaviors in PEM fuel cell cathode considering transport across different porous layers”. In: *International Journal of Hydrogen Energy* 35.11 (2010), pp. 5569 – 5579.

[149] G. He, Y. Yamazaki, and A. Abudula. “A three-dimensional analysis of the effect of anisotropic gas diffusion layer(GDL) thermal conductivity on the heat transfer and two-phase behavior in a proton exchange membrane fuel cell(PEMFC)”. In: *Journal of Power Sources* 195.6 (2010), pp. 1551 –1560.

[150] K. Kang, K. Oh, S. Park, A. Jo, and H. Ju. “Effect of spatial variation of gas diffusion layer wetting characteristics on through-plane water distribution in a polymer electrolyte fuel cell”. In: *Journal of Power Sources* 212 (2012), pp. 93 –99.

[151] I. M. Kong, A. Jung, Y. S. Kim, and M. S. Kim. “Numerical investigation on double gas diffusion backing layer functionalized on water removal in a proton exchange membrane fuel cell”. In: *Energy* 120 (2017), pp. 478 –487.

[152] P. Quan, B. Zhou, A. Sobiesiak, and Z. Liu. “Water behavior in serpentine micro-channel for proton exchange membrane fuel cell cathode”. In: *Journal of Power Sources* 152 (2005), pp. 131 –145.

[153] Y. Ding, X. Bi, and D. P. Wilkinson. “3D simulations of the impact of two-phase flow on PEM fuel cell performance”. In: *Chemical Engineering Science* 100 (2013), pp. 445 –455.

[154] W. Yuan, Y. Tang, M. Pan, Z. Li, and B. Tang. “Model prediction of effects of operating parameters on proton exchange membrane fuel cell performance”. In: *Renewable Energy* 35.3 (2010), pp. 656 –666.

[155] J. Kim, G. Luo, and C.-Y. Wang. "Modeling two-phase flow in three-dimensional complex flow-fields of proton exchange membrane fuel cells". In: *Journal of Power Sources* 365 (2017), pp. 419 –429.

[156] G. Lin and T. V. Nguyen. "A Two-Dimensional Two-Phase Model of a PEM Fuel Cell". In: *Journal of The Electrochemical Society* 153.2 (2006), A372–A382.

[157] G. He, P. Ming, Z. Zhao, A. Abudula, and Y. Xiao. "A two-fluid model for two-phase flow in PEMFCs". In: *Journal of Power Sources* 163 (2007), pp. 864 –873.

[158] P. Sui, S. Kumar, and N. Djilali. "Advanced computational tools for PEM fuel cell design: Part 2. Detailed experimental validation and parametric study". In: *Journal of Power Sources* 180.1 (2008), pp. 423 –432.

[159] P. Sui, S. Kumar, and N. Djilali. "Advanced computational tools for PEM fuel cell design: Part 1. Development and base case simulations". In: *Journal of Power Sources* 180.1 (2008), pp. 410 –422.

[160] H. Wu, P. Berg, and X. Li. "Steady and unsteady 3D non-isothermal modeling of PEM fuel cells with the effect of non-equilibrium phase transfer". In: *Applied Energy* 87 (2010), pp. 2778 –2784.

[161] H.-Y. Kim and K. Kim. "Numerical study on the effects of gas humidity on proton-exchange membrane fuel cell performance". In: *International Journal of Hydrogen Energy* 41 (2016), pp. 11776 –11783.

[162] L. Xing, S. Du, R. Chen, M. Mamlouk, and K. Scott. "Anode partial flooding modelling of proton exchange membrane fuel cells: Model development and validation". In: *Energy* 96 (2016), pp. 80 –95.

[163] L. Xing, Q. Cai, X. Liu, C. Liu, K. Scott, and Y. Yan. "Anode partial flooding modelling of proton exchange membrane fuel cells: Optimisation of electrode properties and channel geometries". In: *Chemical Engineering Science* 146 (2016), pp. 88 –103.

[164] L. Xing, Q. Cai, C. Xu, C. Liu, K. Scott, and Y. Yan. "Numerical study of the effect of relative humidity and stoichiometric flow ratio on PEM (proton exchange membrane) fuel cell performance with various channel lengths: An anode partial flooding modelling". In: *Energy* 106 (2016), pp. 631 –645.

[165] L. Fan, G. Zhang, and K. Jiao. "Characteristics of PEMFC operating at high current density with low external humidification". In: *Energy Conversion and Management* 150 (2017), pp. 763 –774.

[166] G. Zhang and K. Jiao. "Three-dimensional multi-phase simulation of PEMFC at high current density utilizing Eulerian-Eulerian model and two-fluid model". In: *Energy Conversion and Management* 176 (2018), pp. 409 –421.

[167] Y. Wang, S. Wang, G. Wang, and L. Yue. "Numerical study of a new cathode flow-field design with a sub-channel for a parallel flow-field polymer electrolyte membrane fuel cell". In: *International Journal of Hydrogen Energy* 43.4 (2018), pp. 2359 –2368.

[168] L. Chen, T.-F. Cao, Z.-H. Li, Y.-L. He, and W.-Q. Tao. "Numerical investigation of liquid water distribution in the cathode side of proton exchange membrane fuel cell and its effects on cell performance". In: *International Journal of Hydrogen Energy* 37 (2012), pp. 9155 –9170.

[169] T.-F. Cao, H. Lin, L. Chen, Y.-L. He, and W.-Q. Tao. "Numerical investigation of the coupled water and thermal management in PEM fuel cell". In: *Applied Energy* 112 (2013), pp. 1115 –1125.

[170] S.-W. Perng and H.-W. Wu. "A three-dimensional numerical investigation of trapezoid baffles effect on non-isothermal reactant transport and cell net power in a PEMFC". In: *Applied Energy* 143 (2015), pp. 81 –95.

[171] C. Pistoresi, Y. Fan, and L. Luo. "Numerical study on the improvement of flow distribution uniformity among parallel mini-channels". In: *Chemical Engineering and Processing: Process Intensification* 95 (2015), pp. 63 –71.

[172] E. Karvelas, D. Koubogiannis, A. Hatziapostolou, and I. Sarris. "The effect of anode bed geometry on the hydraulic behaviour of PEM fuel cells". In: *Renewable Energy* 93 (2016), pp. 269 –279.

[173] C. Bao and W. G. Bessler. "Two-dimensional modeling of a polymer electrolyte membrane fuel cell with long flow channel. Part I. Model development". In: *Journal of Power Sources* 275 (2015), pp. 922 – 934.

[174] W. Li, Q. Zhang, C. Wang, X. Yan, S. Shen, G. Xia, F. Zhu, and J. Zhang. "Experimental and numerical analysis of a three-dimensional flow field for PEMFCs". In: *Applied Energy* 195 (2017), pp. 278 –288.

[175] E. E. Kahveci and I. Taymaz. "Assessment of single-serpentine PEM fuel cell model developed by computational fluid dynamics". In: *Fuel* 217 (2018), pp. 51 –58.

[176] C. E. Damian-Ascencio, A. Saldaa-Robles, A. Hernandez-Guerrero, and S. Cano-Andrade. "Numerical modeling of a proton exchange membrane fuel cell with tree-like flow field channels based on an entropy generation analysis". In: *Energy* 133 (2017), pp. 306 –316.

[177] P. K. Takalloo, E. S. Nia, and M. Ghazikhani. "Numerical and experimental investigation on effects of inlet humidity and fuel flow rate and oxidant on the performance on polymer fuel cell". In: *Energy Conversion and Management* 114 (2016), pp. 290 –302.

[178] J. Park and X. Li. "An experimental and numerical investigation on the cross flow through gas diffusion layer in a PEM fuel cell with a serpentine flow channel". In: *Journal of Power Sources* 163.2 (2007), pp. 853 –863.

[179] G. Karimi, J. Baschuk, and X. Li. "Performance analysis and optimization of PEM fuel cell stacks using flow network approach". In: *Journal of Power Sources* 147.1 (2005), pp. 162 –177.

[180] J. Park and X. Li. "Effect of flow and temperature distribution on the performance of a PEM fuel cell stack". In: *Journal of Power Sources* 162.1 (2006), pp. 444 –459.

[181] Y. Zhang, A. Mawardi, and R. Pitchumani. "Numerical studies on an air-breathing proton exchange membrane (PEM) fuel cell stack". In: *Journal of Power Sources* 173.1 (2007), pp. 264 –276.

[182] J. Wang. "Pressure drop and flow distribution in parallel-channel configurations of fuel cells: U-type arrangement". In: *International Journal of Hydrogen Energy* 33.21 (2008), pp. 6339 –6350.

[183] J. Wang. "Pressure drop and flow distribution in parallel-channel configurations of fuel cells: Z-type arrangement". In: *International Journal of Hydrogen Energy* 35.11 (2010), pp. 5498 –5509.

[184] A. D. Le and B. Zhou. "A numerical investigation on multi-phase transport phenomena in a proton exchange membrane fuel cell stack". In: *Journal of Power Sources* 195.16 (2010), pp. 5278 –5291.

[185] B. Chernyavsky, P. Sui, B. Jou, and N. Djilali. "Turbulent flow in the distribution header of a PEM fuel cell stack". In: *International Journal of Hydrogen Energy* 36.12 (2011), pp. 7136 –7151.

[186] A. Amirfazli, S. Asghari, and M. Koosha. "Mathematical modeling and simulation of thermal management in polymer electrolyte membrane fuel cell stacks". In: *Journal of Power Sources* 268 (2014), pp. 533 –545.

[187] C. Robin, M. Gerard, J. dArbigny, P. Schott, L. Jabbour, and Y. Bultel. "Development and experimental validation of a PEM fuel cell 2D-model to study heterogeneities effects along large-area cell surface". In: *International Journal of Hydrogen Energy* 40.32 (2015), pp. 10211 –10230.

[188] F. Nandjou, J.-P. Poirot-Crouvezier, M. Chandesris, and Y. Bultel. "A pseudo-3D model to investigate heat and water transport in large area PEM fuel cells Part 1: Model development and validation". In: *International Journal of Hydrogen Energy* 41 (2016), pp. 15545 –15561.

[189] F. Nandjou, J.-P. Poirot-Crouvezier, M. Chandesris, and Y. Bultel. "A pseudo-3D model to investigate heat and water transport in large area PEM fuel cells Part 2: Application on an automotive driving cycle". In: *International Journal of Hydrogen Energy* 41 (2016), pp. 15545 –15561.

[190] S. Müller and Y. Stiriba. "Fully Adaptive Multiscale Schemes for Conservation Laws Employing Locally Varying Time Stepping". In: *J. Sci. Comput.* 30.3 (2007), pp. 493–531.

[191] F. H. Harlow and A. A. Amsden. "Numerical calculation of multiphase fluid flow". In: *Journal of Computational Physics* 17.1 (1975), pp. 19 –52.

[192] F. H. Harlow. "Fluid dynamics in Group T-3 Los Alamos National Laboratory: (LA-UR-03-3852)". In: *Journal of Computational Physics* 195.2 (2004), pp. 414 –433.

[193] D. B. Spalding. *Numerical computation of multi-phase fluid flow and heat transfer*. In Von Karman Inst. for Fluid Dyn. Numerical Computation of Multi-Phase Flows. 1981.

[194] M. Ishii and T. Hibiki. *Thermo-fluid dynamics of two-phase flow*. Springer Science & Business Media, 2010.

[195] H. Rusche. "Computational fluid dynamics of dispersed two-phase flows at high phase fractions". PhD thesis. Imperial College London (University of London), 2003.

[196] H. Marschall. "Towards the numerical simulation of multi-scale two-phase flows". PhD thesis. Technische Universität München, 2011.

[197] E. N. Fuller, P. D. Schettler, and J. C. Giddings. "New method for prediction of binary gas-phase diffusion coefficients". In: *Industrial & Engineering Chemistry* 58.5 (1966), pp. 18–27.

[198] B. E. Poling, J. M. Prausnitz, J. P. O'connell, et al. *The properties of gases and liquids*. Vol. 5. Mcgraw-hill New York, 2001.

[199] N. Epstein. "On tortuosity and the tortuosity factor in flow and diffusion through porous media". In: *Chemical Engineering Science* 44.3 (1989), pp. 777 –779.

[200] J. M. Zalc, S. C. Reyes, and E. Iglesia. "The effects of diffusion mechanism and void structure on transport rates and tortuosity factors in complex porous structures". In: *Chemical Engineering Science* 59.14 (2004), pp. 2947 –2960.

[201] C. R. Wilke. "Diffusional properties of multicomponent gases". In: *Chemical Engineering Progress* 46 (Feb. 1950), pp. 95–104.

[202] A. L. Buck. "New Equations for Computing Vapor Pressure and Enhancement Factor". In: *Journal of Applied Meteorology* 20.12 (1981), pp. 1527–1532.

[203] M. Roos, E. Batawi, U. Harnisch, and T. Hocker. "Efficient simulation of fuel cell stacks with the volume averaging method". In: *Journal of Power Sources* 118.1 (2003). Scientific Advances in Fuel Cell Systems, pp. 86 –95.

[204] S. B. Beale. "Calculation procedure for mass transfer in fuel cells". In: *Journal of Power Sources* 128 (2004), pp. 185–192.

[205] S. B. Beale. "Mass transfer formulation for polymer electrolyte membrane fuel cell cathode". In: *International Journal of Hydrogen Energy* 40 (2015), pp. 11641 –11650.

[206] D. Spalding. "A standard formulation of the steady convective mass transfer problem". In: *International Journal of Heat and Mass Transfer* 1.2 (1960), pp. 192 –207.

[207] S. B. Beale. "Conjugate mass transfer in gas channels and diffusion layers of fuel cells". In: *Journal of fuel cell science and technology* 4.1 (2007), pp. 1–10.

[208] The OpenFOAM Foundation. *OpenFOAM v6 User Guide*. `https://cfd.direct/openfoam/user-guide`.

[209] R. Issa. "Solution of the implicitly discretised fluid flow equations by operator-splitting". In: *Journal of Computational Physics* 62.1 (1986), pp. 40 –65.

[210] C. M. Rhie and W. L. Chow. "Numerical study of the turbulent flow past an airfoil with trailing edge separation". In: *AIAA Journal* 21.11 (1983), pp. 1525–1532.

[211] A. Bendzulla. "Von der Komponente zum Stack: Entwicklung und Auslegung von HT-PEFC-Stacks der 5 kW-Klassen". In German. PhD thesis. RWTH, 2010.

[212] C. Korte, F. Conti, J. Wackerl, and W. Lehnert. "Phosphoric Acid and its Interactions with Polybenzimidazole-Type Polymers". In: *High Temperature Polymer Electrolyte Membrane Fuel Cells: Approaches, Status, and Perspectives*. Ed. by Q. Li, D. Aili, H. A. Hjuler, and J. O. Jensen. Cham: Springer International Publishing, 2016. Chap. 9, pp. 169–194.

[213] H. Janßen, J. Supra, and W. Lehnert. "Stack Concepts for High Temperature Polymer Electrolyte Membrane Fuel Cells". In: *High Temperature Polymer Electrolyte Membrane Fuel Cells: Approaches, Status, and Perspectives*. Ed. by Q. Li, D. Aili, H. A. Hjuler, and J. O. Jensen. Cham: Springer International Publishing, 2016. Chap. 20, pp. 441–457.

[214] A. Kulikovsky, A. Kucernak, and A. Kornyshev. “Feeding PEM fuel cells”. In: *Electrochimica Acta* 50 (2005), pp. 1323 –1333.

[215] L. Lüke. “Analyse des Betriebsverhaltens von Hochtemperatur-Polymerelektrolyt-Brennstoffzellen”. In German. PhD thesis. Forschungszentrum Jülich, 2013.

[216] C. Wieser, A. Helmbold, and E. Gülzow. “A new technique for two-dimensional current distribution measurements in electrochemical cells”. In: *Journal of Applied Electrochemistry* 30.7 (2000), pp. 803–807.

[217] J. G. Pharoah. “On the permeability of gas diffusion media used in PEM fuel cells”. In: *Journal of Power Sources* 144.1 (2005), pp. 77 –82.

[218] Z. Niu, K. Jiao, Y. Wang, Q. Du, and Y. Yin. “Numerical simulation of two-phase cross flow in the gas diffusion layer microstructure of proton exchange membrane fuel cells”. In: *International Journal of Energy Research* 42.2 (2017), pp. 802–816.

[219] J. Bachman, A. Santamaria, H.-Y. Tang, and J. W. Park. “Investigation of polymer electrolyte membrane fuel cell parallel flow field with induced cross flow”. In: *Journal of Power Sources* 198 (2012), pp. 143 –148.

[220] B. Randrianarizafy, P. Schott, M. Chandesris, M. Gerard, and Y. Bultel. “Design optimization of rib/channel patterns in a PEMFC through performance heterogeneities modelling”. In: *International Journal of Hydrogen Energy* 43.18 (2018), pp. 8907 –8926.

[221] P. Berg and A. Kulikovsky. “A model for a crack or a delaminated region in a PEM fuel cell anode: analytical solutions”. In: *Electrochimica Acta* 174 (2015), pp. 424 –429.

[222] S. Kundu, M. Fowler, L. Simon, and S. Grot. “Morphological features (defects) in fuel cell membrane electrode assemblies”. In: *Journal of Power Sources* 157.2 (2006). Selected papers presented at the Ninth Grove Fuel Cell Symposium, pp. 650 –656.

[223] Q. Guo and Z. Qi. “Effect of freeze-thaw cycles on the properties and performance of membrane-electrode assemblies”. In: *Journal of Power Sources* 160.2 (2006), pp. 1269 –1274.

[224] A. Kusoglu, A. Kwong, K. T. Clark, H. P. Gunterman, and A. Z. Weber. “Water Uptake of Fuel-Cell Catalyst Layers”. In: *Journal of The Electrochemical Society* 159.9 (2012), F530–F535.

[225] Y. Shi, H. Janen, and W. Lehnert. “A Transient Behavior Study of Polymer Electrolyte Fuel Cells with Cyclic Current Profiles”. In: *Energies* 12.12 (2019).

[226] I. A. Schneider, S. von Dahlen, A. Wokaun, and G. G. Scherer. "A Segmented Microstructured Flow Field Approach for Submillimeter Resolved Local Current Measurement in Channel and Land Areas of a PEFC". In: *Journal of The Electrochemical Society* 157.3 (2010), B338–B341.

[227] F. Barbir. "CHAPTER 4 - Main Cell Components, Materials Properties and Processes". In: *PEM Fuel Cells*. Ed. by F. Barbir. Burlington: Academic Press, 2005, pp. 73 –113.

[228] T. Uchiyama, H. Kumei, and T. Yoshida. "Catalyst layer cracks by buckling deformation of membrane electrode assemblies under humidity cycles and mitigation methods". In: *Journal of Power Sources* 238 (2013), pp. 403 –412.

[229] M. Pestrak, Y. Li, S. W. Case, D. A. Dillard, M. W. Ellis, Y.-H. Lai, and C. S. Gittleman. "The effect of mechanical fatigue on the lifetimes of membrane electrode assemblies". In: *Journal of Fuel Cell Science and Technology* 7.4 (2010), p. 041009.

[230] F. Hizir, S. Ural, E. Kumbur, and M. Mench. "Characterization of interfacial morphology in polymer electrolyte fuel cells: Micro-porous layer and catalyst layer surfaces". In: *Journal of Power Sources* 195.11 (2010), pp. 3463 –3471.

[231] N. Karst, V. Faucheux, A. Martinent, P. Bouillon, and J.-P. Simonato. "Improvement of water management in polymer electrolyte membrane fuel cell thanks to cathode cracks". In: *Journal of Power Sources* 195.16 (2010), pp. 5228 –5234.

[232] S. TSUSHIMA and S. HIRAI. "An overview of cracks and interfacial voids in membrane electrode assemblies in polymer electrolyte fuel cells". In: *Journal of Thermal Science and Technology* 10.1 (2015), JTST0002–JTST0002.

[233] N. Zamel and X. Li. "Effective transport properties for polymer electrolyte membrane fuel cells With a focus on the gas diffusion layer". In: *Progress in Energy and Combustion Science* 39.1 (2013), pp. 111 –146.

[234] J. M. Morgan and R. Datta. "Understanding the gas diffusion layer in proton exchange membrane fuel cells. I. How its structural characteristics affect diffusion and performance". In: *Journal of Power Sources* 251 (2014), pp. 269 –278.

[235] S. Kim and M. Mench. "Physical degradation of membrane electrode assemblies undergoing freeze/thaw cycling: Micro-structure effects". In: *Journal of Power Sources* 174.1 (2007). Hybrid Electric Vehicles, pp. 206 –220.

[236] G. Ding, M. H. Santare, A. M. Karlsson, and A. Kusoglu. “Numerical evaluation of crack growth in polymer electrolyte fuel cell membranes based on plastically dissipated energy”. In: *Journal of Power Sources* 316 (2016), pp. 114 –123.

[237] S. Kim, M. Khandelwal, C. Chacko, and M. M. Mench. “Investigation of the Impact of Interfacial Delamination on Polymer Electrolyte Fuel Cell Performance”. In: *Journal of The Electrochemical Society* 156.1 (2009), B99–B108.

[238] W. Yoon and A. Z. Weber. “Modeling Low-Platinum-Loading Effects in Fuel-Cell Catalyst Layers”. In: *Journal of The Electrochemical Society* 158.8 (2011), B1007–B1018.

[239] S. Kamarajugadda and S. Mazumder. “Generalized flooded agglomerate model for the cathode catalyst layer of a polymer electrolyte membrane fuel cell”. In: *Journal of Power Sources* 208 (2012), pp. 328 –339.

[240] T. Suzuki, K. Kudo, and Y. Morimoto. “Model for investigation of oxygen transport limitation in a polymer electrolyte fuel cell”. In: *Journal of Power Sources* 222 (2013), pp. 379 –389.

[241] L. Xing, X. Liu, T. Alaje, R. Kumar, M. Mamlouk, and K. Scott. “A two-phase flow and non-isothermal agglomerate model for a proton exchange membrane (PEM) fuel cell”. In: *Energy* 73 (2014), pp. 618 –634.

[242] K.-M. Yin, B.-S. Cheng, and K.-W. Chiang. “Non-uniform agglomerate cathode catalyst layer model on the performance of PEMFC with consideration of water effect”. In: *Renewable Energy* 95 (2016), pp. 191 –201.

[243] T. Mashio, H. Iden, A. Ohma, and T. Tokumasu. “Modeling of local gas transport in catalyst layers of PEM fuel cells”. In: *Journal of Electroanalytical Chemistry* 790 (2017), pp. 27 –39.

[244] J. Nam, P. Chippar, W. Kim, and H. Ju. “Numerical analysis of gas crossover effects in polymer electrolyte fuel cells (PEFCs)”. In: *Applied Energy* 87 (2010), pp. 3699 –3709.

[245] P. Chippar and H. Ju. “Numerical modeling and investigation of gas crossover effects in high temperature proton exchange membrane (PEM) fuel cells”. In: *International Journal of Hydrogen Energy* 38 (2013), pp. 7704 –7714.

Acknowledgement

Time flies. It has been four years since I started to work at IEK-14, Forschungszentrum Jülich. First of all, I wish to express my sincere appreciation to my supervisors, Prof. Werner Lehnert and Prof. Steven Beale. They offered me the opportunity to study here. It is their indispensable encouragement and scientific advice that helped me to go through every difficulties, especially during the first half year. They provided me the freedom to pursue independent scientific work. Thanks to their patience, motivation, and comprehensive knowledge of physics, I finally get to the point of having this thesis. Prof. Steven Beale, who directly supervised my research, presented me many valuable insights into topics on heat and mass transfer, two phase flow, etc. Many studies in this thesis were inspired from the discussions with him. Especially, he helped me a lot during the writing of scientific publications.

My sincere thanks also go to the rest of my thesis committee: Prof. Wolfgang Schröder, and Prof. Ghaleb Natour, for their valuable time, effort and insightful comments.

The physical and technical support from Prof. Martin Andersson (Lund University) and Dr. Uwe Reimer is truly appreciated. They gave many constructive advises on the fuel cell researches and the numerical simulations. Lots of meaningful comments were shared by them during my PhD study. The valuable help from Dieter Froning is also significant and important. Without their help, I cannot conduct the research fluently. Besides, I would like to acknowledge Prof. Liangfei Xu (Tsinghua University), Prof. Meng Ni (Hong Kong Polytechnic University), and Prof. Diankai Qiu (Shanghai Jiao Tong University). They visited this institute as guest scientists. I learned a lot from them and we had many interesting discussions.

I really appreciate the help from many colleagues and friends. It is a great pleasure to meet them in this research center. The current and former colleagues in IEK-3/14: Dr. Qing Cao, Dr. Junliang Yu, Dr. Yu Lin, Dr. Yasser Rahim, Dr. Shuai Liu, Deepjyoti Borah and Yan Shi, helped me in various parts, e.g. scientific discussions, suggestions, experimental data, etc. Some friends in Jülich: Dr. Dapeng Zhou, Dr. Huimin Li, Yun Li, and Yajie Sun, also provided me numerous help. I cannot list all of those helpful and brilliant colleagues and friends, e.g. Yuan Wang, Wei Zou, etc. Some of

them left, some are working here, and the others are still fighting for their PhDs. I will keep all of them in my mind. With the best wishes to them.

The work would not be possible without the Open Source CFD toolbox OpenFOAM ®. Thanks for the opportunity from Prof. Hrvoje Jasak and Dr. Henrik Rusche to take part in the NUMAP-FOAM (Numerical Modelling of Coupled Problems in Applied Physics with OpenFOAM ®) summer school, which greatly extends my numeric and programming skills.

The study was founded by China Scholarship Council (grant number: 201506230130). Numerical calculations were performed on HPC hardware of the JARA, grant JARA0070. I would like to acknowledge all of them.

Finally, my deepest and sincerest gratitude to my parents, who always support my work and encourage me. They kept me going on and this work would not have been possible without their input.

Band / Volume 479
Morphology and Degradation of High Temperature Polymer Electrolyte Fuel Cell Electrodes
S. Liu (2019), III, 162 pp
ISBN: 978-3-95806-436-2

Band / Volume 480
Structural uptake and retention of safety relevant radionuclides by cementitious materials
S. Lange (2019), 133 pp
ISBN: 978-3-95806-437-9

Band / Volume 481
Quantifying the Impact of Inhomogeneity, Transport and Recombination in Emerging Thin-Film Solar Cells
P. Kaienburg (2019), vii, 258 pp
ISBN: 978-3-95806-440-9

Band / Volume 482
Studies of oxidation resistant tungsten alloys at temperatures of 1100K to 1475K
F. Klein (2019), 158 pp
ISBN: 978-3-95806-444-7

Band / Volume 483
Impact Assessment of Land-Use Change and Agricultural Treatments on Greenhouse Gas Emissions from Wetlands of Uganda and Tanzania
K. X. X. Wagner (2019), 144 pp
ISBN: 978-3-95806-447-8

Band / Volume 484
IEK-3 Report 2019
Tailor-Made Energy Conversion for Sustainable Fuels
D. Stolten, B. Emonts (Eds.) (2020), 162 pp
ISBN: 978-3-95806-451-5

Band / Volume 485
Multiskalare Modellierung integrierter Energie- und Elektrizitätssysteme
T. C. Pesch (2019), XXV, 384 pp
ISBN: 978-3-95806-452-2

Band / Volume 486
Quantitative Untersuchung des Laserablationsprozesses mittels Kombination von optischer Spektroskopie und Massenspektrometrie
J. Oelmann (2020), vii, 141 pp
ISBN: 978-3-95806-453-9

Band / Volume 487
Leistungssteigerung metallgestützter Festelektrolyt-Brennstoffzellen (MSCs) durch gezielte Optimierungen des Anoden/Elektrolytverbunds
C. Bischof (2020), X, 176 pp
ISBN: 978-3-95806-455-3

Band / Volume 488
Aluminiumoxiddispersionsverstärkte Haftvermittlermaterialien in Wärmedämmschichtsystemen
C. Vorkötter (2020), VIII, 99, XXXIII pp
ISBN: 978-3-95806-457-7

Band / Volume 489
The Balmer lines emission of fast hydrogen atoms at the plasma-solid interface in a low density plasma: challenges and applications
S. O. Dickheuer (2020), 117 pp
ISBN: 978-3-95806-458-4

Band / Volume 490
Micromechanical Characterization of Ceramic Solid Electrolytes for Electrochemical Storage Devices
J. F. Nonemacher (2020), xv, 131 pp
ISBN: 978-3-95806-461-4

Band / Volume 491
Nanoscale investigation of high temperature oxidation mechanisms of high-Cr ferritic steels
A. Vayyala (2020), xix, 105 pp
ISBN: 978-3-95806-467-6

Band / Volume 492
Electrolyte development for a SOFC operating at low temperature
J. Zhang (2020), vi, 121 pp
ISBN: 978-3-95806-471-3

Band / Volume 493
Modeling and Simulation of Polymer Electrolyte Fuel Cells
S. Zhang (2020), 4, xii, 214 pp
ISBN: 978-3-95806-472-0

Weitere ***Schriften des Verlags im Forschungszentrum Jülich*** unter
http://wwwzb1.fz-juelich.de/verlagextern1/index.asp

Energie & Umwelt / Energy & Environment
Band / Volume 493
ISBN 978-3-95806-472-0

Mitglied der Helmholtz-Gemeinschaft

JÜLICH
Forschungszentrum